



The
University
Of
Sheffield.

**Preparation and Characterisation of Novel Carbon
Materials for Refractory Castable Applications**

Jianke Ye

**Department of Materials Science and Engineering
The University of Sheffield**

April 2014

A thesis submitted for the degree of Doctor of Philosophy

To my family

Abstract

To overcome the difficulty of incorporation of hydrophobic carbon materials into refractory castables, TiC and SiC coatings with much better water-wettability were prepared on carbon particles from metallic powders (Ti or Si) by using a novel low temperature molten salt synthesis technique. The preparation conditions were optimized by varying processing parameters including synthesis temperature, holding time, salt assembly and metal/carbon molar ratios.

Homogeneous TiC coatings were prepared on carbon black (CB) particles by firing them with Ti powders in KCl or KCl-LiCl at 750-850 °C for 4 hours. Alternatively, TiC coatings could be prepared at a lower cost by firing the mixture of TiO₂ and Ti (in molar ratio of 1/3) with CB in KCl at 950 °C for 4 hours. High quality SiC coatings were prepared on CB spheres after firing them with Si powders in a binary NaCl-NaF salt for 6 hours at as low as 1100 °C. NaF was proven to be essential in the molten salt synthesis of SiC and its optimal amount was 2.5-5 wt% in the binary salt. In addition, graded SiC/SiO₂ composite coatings were prepared by controlled oxidation of SiC-coated CB in air at 450 °C for 90 minutes to further improve their water-wettability.

Carbide-coated CB spheres were identified as having a core-shell structure by scanning/transmission electron microscopy (SEM/TEM) and the thicknesses of TiC and SiC shells (Ti/C or Si/C = 1/8 in molar ratio) were estimated as ~10 nm and ~12 nm, respectively. Nevertheless, the coating thickness and corresponding particle density could be readily tailored by controlling the metal/carbon molar ratio in the initial batch mixture to meet practical requirements in real castable systems. The coated CB particles retained similar morphologies and sizes to as-received CB, indicating the formation of carbide coatings in molten salt at test temperatures was governed by a template growth mechanism: dissolution of Ti or Si in molten salt and subsequently fast delivery of dissolved Ti or Si species to the surface of carbon particles, forming carbide coatings on the template. The growth of carbide coatings was dependent on the inward diffusion of Ti or Si and outward diffusion of carbon through an initially formed carbide coating layer.

The water-wettability, dispersion behaviour and flowability of CB after carbide coating were evaluated by sedimentation comparison, zeta potential measurement and rheology testing. Owing to the formation of hydrophilic Ti-OH and Si-OH

groups on the surface of carbide-coated CB particles, they were able to be immediately wetted by water and well dispersed in aqueous solutions. Moreover, improved dispersivity and flowability of CB after carbide coating were verified by the increased zeta potential values (e.g. at pH=10, ~46.1 mV for TiC-coated CB, ~54.7 mV for SiC-coated CB and ~65.9 mV for SiC/SiO₂-coated CB but only ~22.6 mV for uncoated CB) and lowered apparent viscosity (e.g. the apparent viscosity of suspensions containing 25 wt% coated CB was over one order of magnitude lower than that containing as-received CB) of coated CB containing suspensions. In addition, thermogravimetric analysis (TGA) and differential scanning calorimetry (DSC) verified that the improvement in oxidation resistance of carbon after carbide coating was limited, however, the annealing treatment at 1200-1500 °C could promote the growth of carbide nanocrystals and make the carbide coating denser, thus effectively improving carbon's oxidation resistance. Both weight-loss curve (TGA) and exothermic peaks of carbon oxidation (DSC) were right shifted to higher temperatures. It was also found that annealing atmosphere and temperature were influential on the oxidation resistance of coated CB particles.

To investigate the effect of carbide coating on water demand for preparation of carbon-containing castables, both uncoated and carbide-coated carbon particles (carbon black and graphite flakes) were incorporated into model low cement Al₂O₃-C castables. The water addition was found to decrease dramatically, from 8.5-9.7 wt% required for uncoated carbon containing castables to 6.5-7.0 wt% for carbide-coated carbon containing castables when both of them reached the similar flow values. The evident decrease in water addition led to a considerable drop in apparent porosity and increase in bulk density. As a result, castables containing carbide-coated carbon particles after coking at 1500 °C showed over 6 times higher compression strength and 3-5 times higher bending strength than uncoated carbon containing castables. Furthermore, oxidation resistance of carbon-containing castables was improved as well. Uncoated CB containing castable was severely oxidised at 1000 °C for 3 hours and showed the decarbonized depth of 10.48 mm, whereas TiC-coated and SiC-coated CB containing castables showed respectively 6.82 mm and 6.35 mm decarbonized depths under the same oxidation conditions.

Key Publications

1. Ye J, Thackray, PR, Lee WE, Zhang S. Microstructure and rheological properties of titanium carbide coated carbon black particles synthesised from molten salt *Journal of Materials Science* **2013**, 48(18): 6269-75.
2. Ye J, Zhang S, Lee WE. Molten salt synthesis and characterisation of SiC coated carbon black particles for refractory castable applications *Journal of the European Ceramic Society* **2013**, 33(10): 2023-29.
3. Ye J, Zhang S, Lee WE. SiC hollow spheres fabricated on carbon black by molten salt synthesis at low temperature *Microporous and Mesoporous Materials* **2012**, 152: 25-30.
4. Ye J, Zhang S. Molten salt preparation of aluminium oxide coated graphite flake for castable applications *55th International Colloquium on Refractories* 19-20 Sept. **2012**, Aachen, Germany.
5. Zhang S, Ye J, Liu X. Low temperature preparation of carbide coated carbon for refractory castable applications *6th International Symposium on Refractories* 18-21 Oct. **2012**, Zhengzhou, China.

Invited Presentations

1. Molten salt preparation of aluminium oxide coated graphite flake for castable applications. Oral presentation at *55th International Colloquium on Refractories*, Aachen, Germany, 19-20 Sept. **2012**.
2. Low temperature molten salt synthesis of SiC hollow spheres. Oral presentation at *The 1 Day Research Meeting on Advanced Ceramics (1DRAC)*, Department of Materials, Imperial College London, UK, 13 Apr. **2011**.
3. Molten salt synthesis of carbide coating on carbon black for carbon-containing castable applications. Oral presentation at *Friday Seminar*, Centre for Advanced Structural Ceramics (CASC), Imperial College London, UK, 05 Nov. **2010**.

Acknowledgements

In the summer of 2008, I came to Sheffield starting an amazing journey of studying overseas. After one-year master course at the University of Sheffield, I decided to stay here to continue my further study in materials science and engineering. The diversity of the people and research at this prestigious university was for me the deciding factor. As I prepare to leave I would like to express my gratitude to some of many people who have made my time here so happy and productive.

I would like to express my sincere gratitude to my research advisor, Professor Shaowei Zhang, for his patience and continuous support. His guidance helped me in all the time of research and writing of this thesis. My sincere thanks also goes to Professor William E. Lee, Chair in Ceramic Engineering at the Centre for Advanced Structural Ceramics (CASC), Imperial College London, for his financial support on this research project. I would also like to thank the University of Sheffield for providing me with the University Studentship, and Professor Frank R. Jones and Materials Department for their support on my scholarship application. Last but not the least, I'm very appreciated to Dr Richard P. Thackray who is very kind to take over as 1st supervisor when Professor Shaowei Zhang decided to move to the University of Exeter in 2012. He is always willing to help and provide the best suggestions.

I am also very grateful to my colleges in Professor Zhang's research group, Dr Wei Xie, Mr Yan Wen, Miss Matthana Khangkhamano, Dr Juntong Huang, Ms Ke Bao, Mr Cheng Liu, for their help in experiments and companionship at lunch time. Thanks also go to Mr Ian P. Watts for his maintenance of tube furnaces and Dr Nik Reeves-McLaren, Dr Peng Zeng, Dr Le Ma and Ms Zhen Xu for their help in phase analysis and microstructure characterisation. Many of my friends, especially Dr Zifu Li, Mr Zhen Zhou, Mr Yiran Zhao, Miss Wei Wang, Mr Jiewei Zhang, Mr Tianbo Xu, Ms Shuming Yang, made the four years more pleasurable.

Finally, I would like express my deepest appreciation to all of my family members, especially my greatest mother Ms Caihua Yu, for their support, encourage and love. I also want to say thanks to my girlfriend, Miss Xin Xin, for her giving me the best care and love. I would never have been able to complete my PhD thesis without her companionship. This dissertation is written for all of you.

List of Abbreviations

| | | | |
|-----------------|--|--------|---|
| AP | Apparent porosity | HRTEM | High resolution transmission microscopy |
| ASTM | American Society for Testing and Materials | IPA | Isopropyl alcohol |
| BD | Bulk density | IEP | Isoelectric point |
| BEI | Backscattered electron imaging | LCCs | Low cement castables |
| BFs | Blast furnaces | MA | MgO·Al ₂ O ₃ , Spinel |
| BFA | Brown fused alumina | MSS | Molten salt synthesis |
| BOFs | Basic oxygen furnaces | Mu | Mullite, 3Al ₂ O ₃ ·2SiO ₂ |
| CA | CaO·Al ₂ O ₃ | NCF | Natural cotton fibre |
| CA ₂ | CaO·2Al ₂ O ₃ | PLC | Permanent linear change |
| CA ₆ | CaO·6Al ₂ O ₃ | PVC | Permanent volume change |
| CACs | Calcium aluminate cements | SAED | Selected area electron diffraction |
| CAS | CaO·Al ₂ O ₃ ·SiO ₂ | SEI | Secondary electron imaging |
| CCRBs | Carbon-containing refractory bricks | SEM | Scanning electron microscopy |
| CCRCs | Carbon-containing refractory castables | SHMP | sodium hexametaphosphate |
| CCS | Cold crushing strength | SiC-CB | SiC-coated carbon black |
| CF | Carbon fibre | SS | Sodium sulfonate-based carbon dispersant |
| CMOR | Cold modulus of rupture | STPP | Sodium triphosphate |
| CNT | Carbon nanotube | TA | Tabular alumina |
| CPFT | Cumulative percent finer than | TEM | Transmission electron microscopy |
| DSC | Differential scanning calorimetry | TGA | Thermogravimetry analysis |
| EDS | Energy-dispersive X-ray spectroscopy | TiC-CB | TiC-coated carbon black |
| EAFs | Electric arc furnaces | TiC-GF | TiC-coated graphite flake |
| FTIR | Fourier transform infrared spectroscopy | ULCCs | Ultra-low cement castables |
| HA | Hydratable alumina | WFA | White fused alumina |
| | | XRD | X-ray diffraction |

Table of Contents

| | |
|---|------|
| Abstract | iii |
| Publications & Presentations | v |
| Acknowledgements | vi |
| List of Abbreviations | vii |
| Table of Contents | viii |
| Chapter 1 Introduction | 1 |
| 1.1 Background of the project | 1 |
| 1.2 Objectives | 2 |
| 1.3 Main content of the thesis | 3 |
| Chapter 2 Literature review | 5 |
| 2.1 Refractory composites | 5 |
| 2.1.1 Classification and Composition | 5 |
| 2.1.2 Manufacturing process | 8 |
| 2.1.3 Applications of refractory composites | 10 |
| 2.1.4 Development of carbon-containing refractory castables | 13 |
| 2.2 Carbon-containing refractory castables | 15 |
| 2.2.1 Carbon source | 15 |
| 2.2.2 Aggregates | 18 |
| 2.2.3 Superfines | 20 |
| 2.2.4 Binders | 22 |
| 2.2.5 Additives | 25 |
| 2.3 Solutions for improving carbon's water-wettability | 29 |
| 2.3.1 Poor water-wettability of carbon materials | 29 |
| 2.3.2 Surfactants | 30 |
| 2.3.3 Micropellet /briquette techniques | 31 |
| 2.3.4 Surface coating | 33 |
| 2.4 Molten salt synthesis (MSS) | 42 |
| 2.4.1 Principle of MSS | 42 |
| 2.4.2 Mechanism of MSS | 43 |
| 2.4.3 Carbide synthesis via MSS | 45 |
| 2.5 Motivation and objectives of present work | 50 |
| Chapter 3 Experimental details | 51 |
| 3.1 Raw materials | 51 |

Table of Contents

| | |
|--|------------|
| 3.1.1 Raw materials for carbide coating synthesis | 51 |
| 3.1.2 Raw materials for castable preparation | 52 |
| 3.2 Experimental procedure | 57 |
| 3.2.1 Carbide coating synthesis..... | 57 |
| 3.2.2 Castable preparation | 64 |
| 3.3 Characterisation and Testing..... | 69 |
| 3.3.1 Phase identification and microstructural observation..... | 69 |
| 3.3.2 Property measurements | 74 |
| 3.3.3 Testing methods for castable samples | 78 |
| Chapter 4 Molten salt synthesis of TiC coatings on CB | 83 |
| 4.1 Preparation of TiC coatings on CB using Ti..... | 83 |
| 4.1.1 Synthesis temperature..... | 83 |
| 4.1.2 Microstructure characterisation | 84 |
| 4.1.3 Effect of Ti/C molar ratio on TiC formation | 88 |
| 4.1.4 Effect of CB particle size on TiC formation..... | 90 |
| 4.1.5 Effect of molten salt on TiC formation..... | 92 |
| 4.2 Preparation of TiC coatings on CB using TiO ₂ /Ti..... | 95 |
| 4.2.1 Using TiO ₂ | 95 |
| 4.2.2 Using TiO ₂ and Ti..... | 98 |
| Chapter 5 Molten salt synthesis of SiC coatings on CB..... | 102 |
| 5.1 Preparation of SiC coatings on CB | 102 |
| 5.1.1 Optimisation of SiC coating formation | 102 |
| 5.1.2 Morphological changes of Si-CB mixtures after firing | 105 |
| 5.1.3 Microstructural characterisation of SiC-coated CB spheres | 108 |
| 5.1.4 Effect of Si/C ratio on SiC formation..... | 112 |
| 5.1.5 Effect of molten salt on SiC formation | 119 |
| 5.1.6 Void formation at higher Si/C molar ratio..... | 121 |
| 5.2 Preparation of SiC/SiO ₂ composite coating..... | 124 |
| 5.2.1 Phase analysis of SiC/SiO ₂ composite coatings | 124 |
| 5.2.2 Microstructural characterisation of SiC/SiO ₂ composite coating..... | 126 |
| Chapter 6 Water-wettability and oxidation resistance of carbide-coated carbon materials | 128 |
| 6.1 Zeta potential | 128 |
| 6.2 Sedimentation testing..... | 131 |
| 6.3 Rheological behaviour..... | 132 |
| 6.3.1 TiC coated CBs..... | 132 |
| 6.3.2 SiC-coated CBs | 134 |

Table of Contents

| | |
|---|------------|
| 6.4 Oxidation resistance..... | 137 |
| 6.4.1 Post-treatment of carbide coated CB (Annealing)..... | 137 |
| 6.4.2 Thermogravimetry analysis (TGA)..... | 140 |
| 6.4.3 Oxidation process | 144 |
| Chapter 7 Al₂O₃-C castables | 147 |
| 7.1 Kg-scale production of carbide-coated CB and GF..... | 147 |
| 7.2 Water demand and flowability | 149 |
| 7.3 Physical and mechanical properties..... | 152 |
| 7.3.1 Bulk density, Apparent porosity and Permanent linear change..... | 152 |
| 7.3.2 Cold crushing strength and cold modulus of rupture..... | 154 |
| 7.4 Oxidation resistance..... | 157 |
| 7.5 Microstructural examination | 160 |
| 7.5.1 Castable specimens after coking at 1500 °C | 160 |
| 7.5.2 Castable specimens after oxidation test..... | 163 |
| Chapter 8 Further discussions..... | 170 |
| 8.1 Factors affecting molten salt synthesis of carbide coatings | 170 |
| 8.1.1 Synthesis temperature..... | 170 |
| 8.1.2 Metal/Carbon ratio | 173 |
| 8.1.3 Molten salt..... | 175 |
| 8.1.4 Template growth mechanism..... | 178 |
| 8.2 Water-wettability and oxidation resistance of carbide-coated carbon materials | 182 |
| 8.2.1 Effects of carbide coatings on wettability, dispersivity and flowability..... | 182 |
| 8.2.2 Effect of carbide coatings on oxidation resistance | 186 |
| 8.3 Carbon-containing high alumina castables | 190 |
| 8.3.1 Effects of carbide coatings on water demand and flowability | 190 |
| 8.3.2 Effect of carbide coatings on oxidation resistance | 191 |
| 8.3.3 Effect of phase evolution on mechanical properties..... | 192 |
| Chapter 9 Conclusions and Future work | 194 |
| 9.1 Conclusions | 194 |
| 9.1.1 Preparation of carbide-coated CB | 194 |
| 9.1.2 Water-wettability and oxidation resistance of carbide-coated CB..... | 195 |
| 9.1.3 Application of carbide-coated carbon in castables..... | 196 |
| 9.2 Future work | 197 |
| References | 199 |

Chapter 1 Introduction

1.1 Background of the project

Refractories are inorganic non-metallic materials which can be resistant to heat and retain sufficient physical and chemical stability for structural purposes when they are exposed to high temperature environments.[1-3] They are normally used in massive quantities to line vessels and furnaces in which other materials such as metals, glass, and cements are manufactured at high temperature in the range of 600 °C to as high as 2000 °C.[4] In a harsh environment, they are subject to mechanical abrasion, thermal stress/strain, corrosion/erosion from molten solids, hot liquids and gases. The refractory industry is considered to be the fundamental industry behind other manufacturing industries. Without refractories, other manufacturing activities would not be possibly realized.[5]

Refractories are classified primarily on the basis of their chemical compositions and the forms in which they are used.[4, 6-8]. Chemically, the majority of them are based on six single oxides (Al_2O_3 , MgO , SiO_2 , CaO , ZrO_2 , Cr_2O_3) or their combinations. They may be fabricated and sold in shaped or unshaped (monolithic) forms. For shaped refractories, they go through mixing, shaping and firing before delivering to customers. Compared with refractory bricks or blocks, there has been a significant increase in the use of monolithic refractories (e.g. castables, mouldables and rammables) worldwide, which now, in many countries, account for more than 50% of world total production [9], owing to their quicker and cheaper preparation and installation and to their properties approaching those of shaped refractories.

However, conventional oxide-based refractories suffer, for example, from poor resistance to slag corrosion and penetration (especially in a basic slag environment) and structural spalling.[10-12] All these problems have been significantly alleviated since the 1970s when carbon was incorporated into oxide-based refractory bricks. Thanks to carbon's high thermal conductivity, low thermal expansion coefficient and non-wettability by molten metal/slag, carbon-containing refractory bricks (CCRBs) show much better physicochemical properties and performance than their carbon-free oxide-based counterparts, resulting in increased lining lifetimes and reduced specific consumption.[5, 13] Therefore, a range of CCRBs with improved properties were developed and produced such as MgO-C , $\text{Al}_2\text{O}_3\text{-C}$, $\text{ZrO}_2\text{-C}$,

$\text{Al}_2\text{O}_3\text{-SiC-C}$ and $\text{Al}_2\text{O}_3\text{-MgO-C}$.

The benefits from incorporating of carbon and making castable-formed refractories have stimulated development and commercialization of the so-called carbon-containing refractory castables (CCRCs). In the past two decades considerable R&D work has been carried out worldwide in this area, but with only limited success. Several technical difficulties are considered to be responsible for this, including carbon's poor water-wettability and dispersivity [14]. These technical problems lead to high demand of water during casting and placement of castables. After drying, high porosity of CCRCs caused by evaporation of excess water results in low mechanical properties, poor oxidation resistance and high permeability to molten slag. These would adversely decrease service lives of refractory linings. Therefore, it is necessary to improve wettability and dispersion property of carbon materials in order to reduce the water addition for castable making and applications.

To overcome these problems, several techniques have been attempted, for example, using a surfactant (dispersing agent) to improve carbon's water affinity [15], making micropellets/briquettes to reduce carbon exposure to water [16] and coating carbon with more water-wettable carbon, oxides or carbides [17-27]. (All these techniques will be reviewed in Section 2.3 in more detail.) However, it is still not possible to prepare carbon materials economically with satisfactory water-wettability and dispersive properties, and consequently realize scaled-up production and applications in industry. So the aim of the present work is to find an effective and economic way to tackle these problems.

1.2 Objectives

In the present study, a molten salt synthesis technique was further developed and employed to prepare carbide coatings (TiC and SiC) on carbon to increase its water-wettability and dispersion ability, and as well as flowability. A model alumina-carbon ($\text{Al}_2\text{O}_3\text{-C}$) low cement castable was used as a work tool to evaluate the effect of carbide coating on castable's water demand and flowability, and relevant refractory properties.

The main objectives of this thesis can be defined as follows:

- 1) To prepare TiC and SiC coatings on carbon particles by using molten salt synthesis technique and to characterise the microstructure of coated carbon

particles.

- 2) To optimise processing parameters for coating preparation, such as synthesis temperature, holding time, initial ratio of reactants and salt selection.
- 3) To investigate wettability and dispersion property of uncoated and carbide coated carbon in water, and their oxidation resistance.
- 4) To compare and evaluate the flowability and water demand for $\text{Al}_2\text{O}_3\text{-C}$ low cement castables containing uncoated and coated carbon materials.
- 5) To investigate the physical and mechanical properties, and oxidation resistance of castables at elevated temperature.
- 6) To examine microstructures of the model castable after casting, firing and oxidation at high temperature.

1.3 Main content of the thesis

This PhD thesis consists of 9 chapters in total. Chapter 1 gives a brief introduction of the research background, and objectives of the project.

Chapter 2 introduces the development of refractory composites, in particular, development of carbon-containing refractory castables and reviews the work in the literature on the possible solutions to improve the water-wettability of graphite. In addition, molten salt synthesis of carbides is highlighted.

In Chapter 3, the details of raw materials, experimental procedure and characterisation for phase analysis and microstructure are documented. In addition, testing methods for flowability, apparent porosity, cold crushing strength, cold rupture of modulus, oxidation resistance are comprehensively presented.

Chapter 4 documents the work of preparation of TiC coatings on carbon black (CB) surfaces. The synthesis condition was optimized by varying heating temperature, selecting the appropriate chloride salt and ratios of Ti/C. The feasibility of replacing part of the metallic Ti powders by TiO_2 was also discussed with details of XRD phase analysis and morphological changes.

Chapter 5 focuses on the molten salt synthesis of SiC coatings on CB surface. In addition to optimization of synthesis conditions, the core-shell microstructure formed after SiC coating was characterised in detail. In addition, SiC/SiO₂ composite

coatings were prepared by slight oxidation of SiC in air to further increase water-wettability SiC coated CB.

The investigation of wettability and oxidation resistance of carbide coated carbon materials is presented in Chapter 6. To characterise the changes of these properties after carbide coating, zeta potential measurement, sediment test, apparent viscosity, and TGA-DSC thermal tests were employed.

In Chapter 7, carbon materials (graphite flakes (GF), TiC-coated GF, SiC-coated GF, CB, TiC-coated CB, and SiC-coated CB) were incorporated into model high alumina low cement castables. Comparisons were made between the effects of uncoated and coated carbon on their flowability, water addition, physical and mechanical properties, and oxidation resistance.

Further discussions are made in Chapter 8 on molten salt synthesis of carbide coatings, mechanism of improvement in carbon's wettability, and the effects of carbide coating on flowability, physical and mechanical properties, and oxidation resistance of carbon-containing castables.

Chapter 9 concludes all the findings in the studies and gives some suggestions for further work.

Chapter 2 Literature review

This chapter introduces the development and applications of refractory composites, in particular, carbon-containing refractory castables. The techniques for improving water-wettability and dispersion property of carbon materials are reviewed in detail. In addition, molten salt synthesis (MSS) of carbides and relevant applications in refractory castables are highlighted.

2.1 Refractory composites

2.1.1 Classification and Composition

There are several classification methods for refractories, mainly based on their chemical composition and physical form. For instance, according to their chemical nature, they are grouped as acidic, basic and neutral (Table 2.1).[4] In terms of shapes and installation methods, they are classified as shaped refractories (bricks or blocks) and unshaped or monolithic refractories (e.g. castables, ramming mix, gunning mix and mortars).[6, 8] To a lesser extent, refractories may be identified by association with a particular function such as thermal insulation, or a special manufacturing process, for example, fusion casting.

Table 2.1 Classification according to their chemical composition.[4]

| term | reaction | refractory material |
|----------------|---|---|
| acidic | $\text{oxide} + \text{H}_2\text{O} \Rightarrow \text{acid}$ | silica, Al_2O_3 - SiO_2 -products, zircon silicate |
| basic | $\text{oxide} + \text{H}_2\text{O} \Rightarrow \text{base (hydroxide)}$ | products with magnesia and doloma base |
| almost neutral | reacts neither acidic nor basic | alumina, chromite, picrochromite, spinel, forsterite |

Despite the various classifications, only a few chemical elements are involved to form refractory compounds, including: Aluminium(Al), Silicon(Si), Magnesium(Mg), Chromium (Cr), Calcium(Ca) and Zirconium(Zr), and their corresponding oxides : Al_2O_3 , SiO_2 , MgO , Cr_2O_3 , CaO and ZrO_2 . Refractory materials are based on these six single oxides or their combinations; and more recently, often in combination with carbon materials [28] (Fig. 2.1).

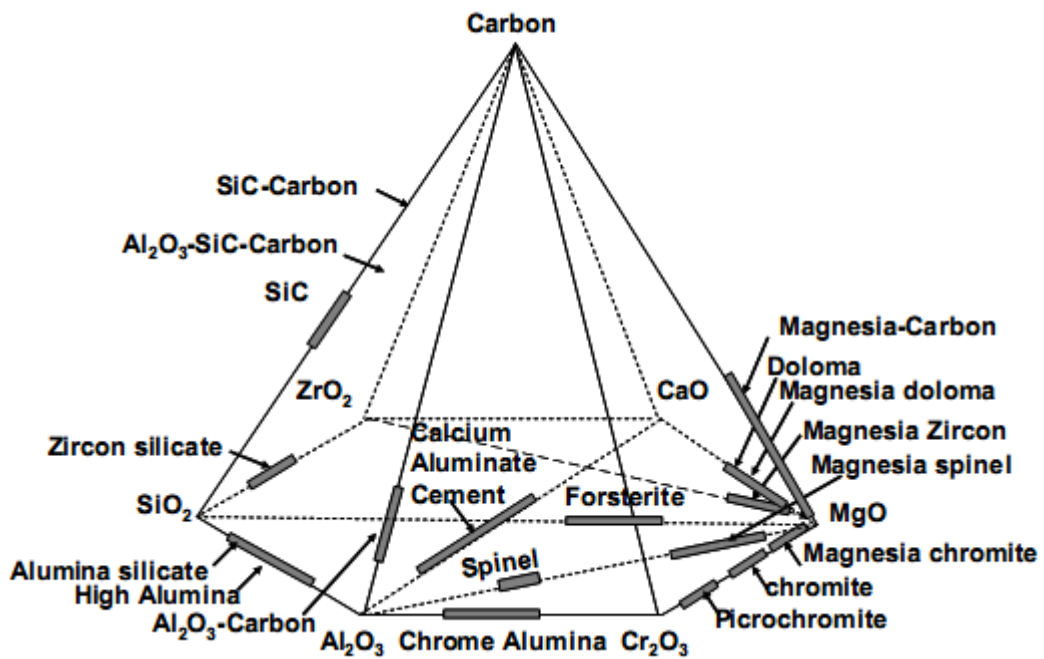


Fig. 2.1 Base material pyramid with the location of the refractory materials.[28]

Due to the high melting temperature of these oxides and their binary compounds (Table 2.2) and their inert nature in oxidizing atmosphere, they can remain stable chemically and physically at very high temperature. In addition, all these oxides are readily available in nature so they are ideal raw materials to manufacture refractory composite products used for other industrial activities. Compared with other materials, refractory composites usually do not have an intrinsic melting point. However, they melt or soften within a more or less narrow temperature range. Therefore, the end point only indicates the extreme temperature that can stay stable. The application-specific property data of main refractory oxides and their compounds are listed in Table 2.2.

Table 2.2 Application-specific property data of main refractory oxides and their compounds.[28]

| formula | abbr. designation | name | melting point | density | thermal expansion up to 1,000 °C | thermal conductivity at | | mean specific heat |
|--|-------------------------------|-----------------------------|---------------------|-----------|----------------------------------|-------------------------|-----|--------------------|
| | | | °C | | | g/cm ³ | % | |
| SiO ₂ | S | β-quartz | – | 2.65 | – | 8 | – | – |
| | | crystalite | 1,725 | 2.29–2.32 | 1-1.4 ⁴⁾ | – | – | 1.15 |
| | | fused silica | | 2.20 | 0.06 | 1.4 | 4.5 | |
| Al ₂ O ₃ | A | corundum | 2,050 | 3.99 | 0.8 | 53 | 9 | 1.1 |
| MgO | M | periclase | 2,840 | 3.58 | 1.4 | 61 | 10 | 1.2 |
| CaO | C | | 2,580 | 3.32 | 1.3 | 25 | 9 | 0.95 |
| ZrO ₂ | Z | baddeleyite | 2,680 | 5.56 | 0.8 ⁴⁾ | 19 | 21 | 0.7 |
| Cr ₂ O ₃ | Cr | eskolaite | 2,275 | 5.22 | 0.75 | – | – | 0.75 |
| 3Al ₂ O ₃ ·2SiO ₂ (Al ₆ Si ₄ O ₁₃) | A ₃ S ₂ | mullite | 1,840 ²⁾ | 3.16 | 0.45 | 9 | 5 | 1.1 |
| 2MgO·SiO ₂ (Mg ₂ SiO ₄) | M ₂ S | forsterite | 1,890 | 3.21 | 1.1 | 9 | 3 | 1.05 |
| ZrO ₂ ·SiO ₂ (ZrSiO ₄) | ZS | zircon | 1,775 ²⁾ | 4.60 | 0.45 | 6 | 4 | 0.75 |
| MgO·Al ₂ O ₃ (MgAl ₂ O ₄) | MA | spinel | 2,135 | 3.58 | 0.85 | 21 | 7 | 1.1 |
| MgO·Cr ₂ O ₃ (MgCr ₂ O ₄) | MCr | microchromite | 2,350 | 4.42 | 0.7 | – | – | 0.9 |
| CaO·Al ₂ O ₃ (CaAl ₂ O ₄) | CA | | 1,600 ²⁾ | 2.98 | 0.76 | – | – | 1.0 |
| CaO·2Al ₂ O ₃ (CaAl ₄ O ₇) | CA ₂ | | 1,750 ²⁾ | 2.91 | 0.62 | – | – | 1.05 |
| C | (α-C) (amorphous) | graphite carbon black | 3,600 ³⁾ | 2.26 | 0.3/0.5 ³⁾ | > 400 | – | 1.5 |
| | | | 3,600 ³⁾ | 1.7-1.8 | 0.4 | – | – | 2 |
| SiC | | | 2,300 ²⁾ | 3.21 | 0.5 | 130 | 26 | 1.1 |
| Si ₃ N ₄ | | | 1,900 ³⁾ | 3.18 | 0.27 | 35 | 20 | 0.7 |
| B ₄ C | | | 2,450 ³⁾ | 2.51 | 0.44 | 35 | 16 | 0.94 |
| BN | | | 3,000 ³⁾ | 2.25 | 0.37 | 50 | 20 | 0.8 |

¹⁾ the counts refer to material without pores

²⁾ incongruent melting point

³⁾ reducing atmosphere, sublimation or decomposition

⁴⁾ expansion anomalies

⁵⁾ intensive anisotropy

A typical refractory composite generally consists of aggregate with a size up to centimetres and fine powders to fill the void between large grains and to increase packing efficiency. In some cases, additives such as antioxidants and sintering aids are added to improve the densification and high temperature properties. Binders could be carbon derived from pyrolysed pitches and phenolic resins for carbon-containing refractories, mullite and glass from decomposed clays for other shaped refractories, and calcium aluminate cement, hydraulic alumina or silica sol-gel for monolithic refractories.[29] The microstructure after powder processing is schematically illustrated in Fig. 2.2. In addition to main aggregates, fine powders and bonding phases, impurities from raw materials and porosity generated during mixing and processing are also present.

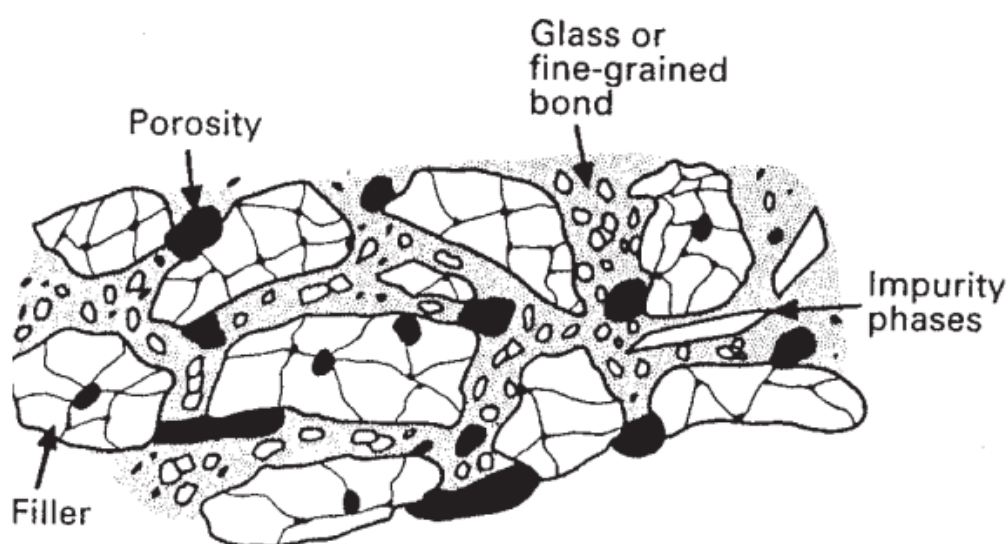


Fig. 2.2 Schematic microstructure of refractory composites.[30]

2.1.2 Manufacturing process

In general, four stages are involved with refractory manufacturing, e.g. raw material processing, forming, firing and machining [31] (Fig. 2.3). Raw materials, both ores and synthetics, are crushed and ground, and classified into different groups according to their particle sizes (e.g. coarse (>1.2 mm), intermediate (0.25-1.2 mm), and fine (<0.25 mm)). The correctly sized powders are mixed together with binders and other additives under wet or moist conditions, and shaped in designed moulds. The shaped green materials are then dried and fired to high temperatures to obtain the final products. In order to keep the products in the correct shape and size after firing, milling, grinding, and sandblasting of the finished product are carried out, since the changes in shape and size after firing always occur.

However, the manufacturing process for monolithic refractories is different, because they do not need to be pre-shaped and pre-fired before delivering to customers, and monolithic refractory products are generally made at the working site. For example, castables are mainly installed by vibration casting. Raw materials with certain compositions are mixed with water and binders, and then pumped via a hose into a furnace or ladle, inside which a mould is placed so as to provide a shape. The mixture is then vibrated to remove air bubbles. The shaped mixtures develop a hydraulic or mineral bond at room temperature which converts to a ceramic bond on firing *in-situ* in a furnace.

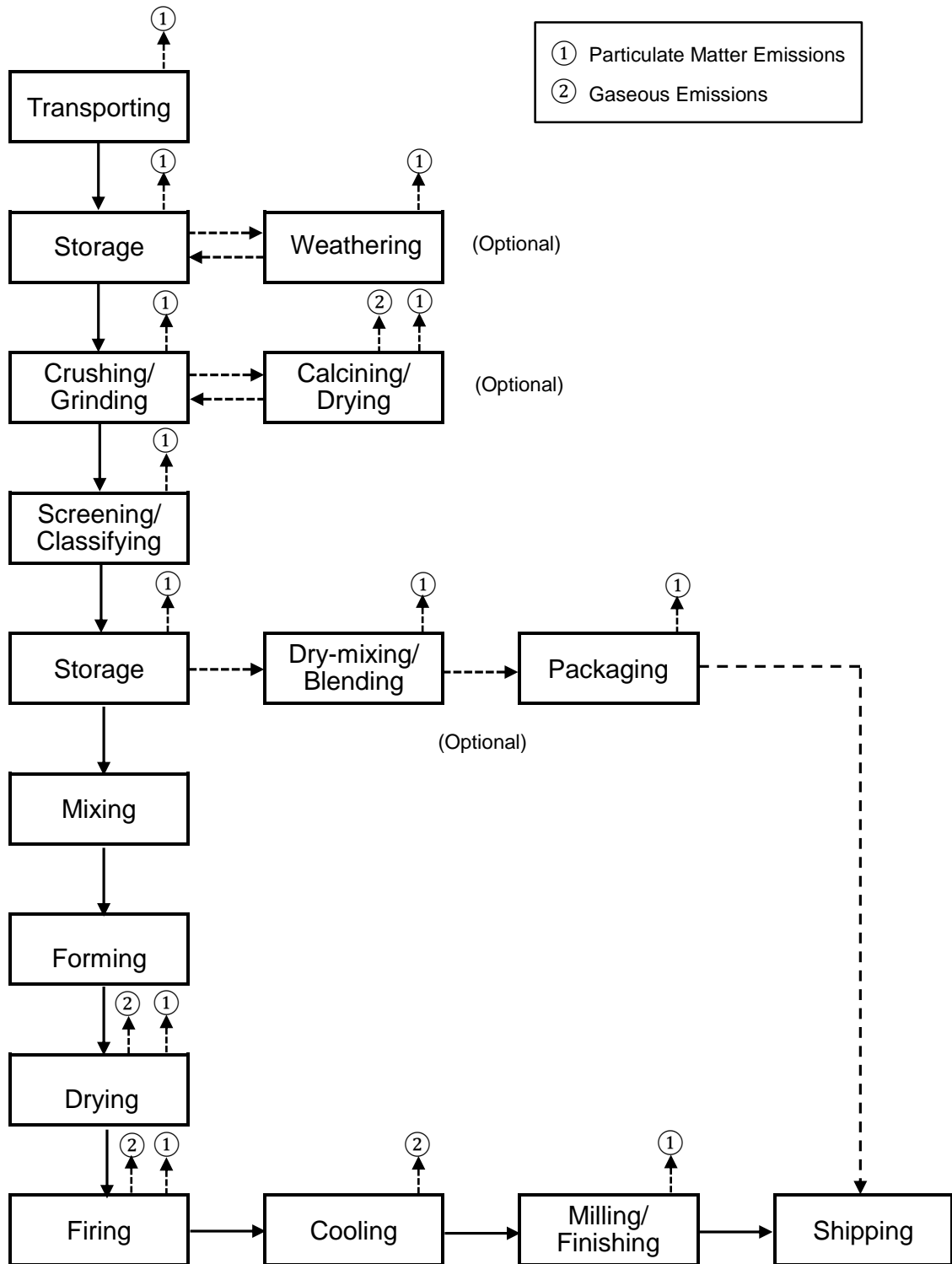


Fig. 2.3 Flow chart of refractory manufacturing process.[31]

2.1.3 Applications of refractory composites

Refractories are extensively used in the manufacture of metals, glass, cement, ceramic and petroleum products, as well as in aerospace and nuclear industries. However, the iron and steel-making industry is refractories' main consumer, uses

~70% of the total production of refractory materials worldwide.[32]

Fig. 2.4 shows schematically the steps in the production of refined steel from iron ore. The choice of refractories used to line various furnaces, ladles and vessels is governed by the operating condition at each stage in the process.[30, 33]

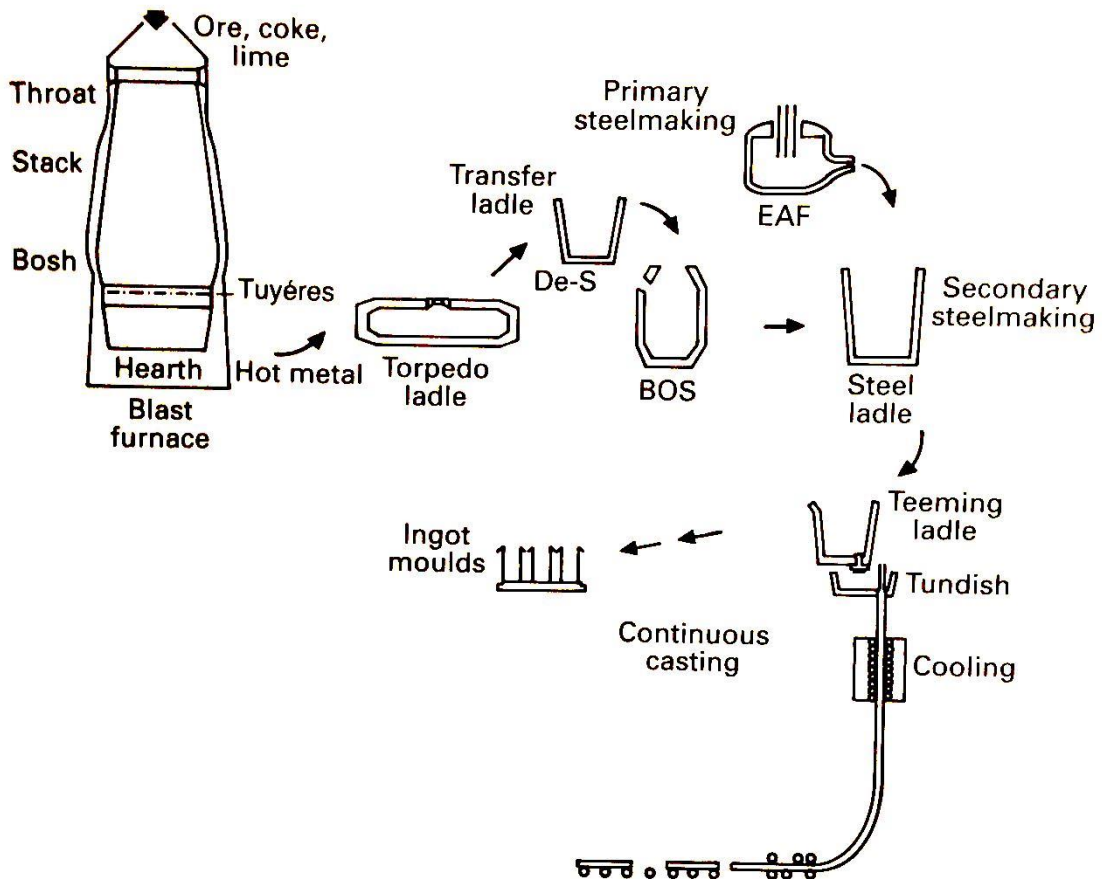


Fig. 2.4 Schematic of iron and steel- making processes.[30]

1) Blast furnaces (BFs)

Modern BFs produce hot metals from reduction of iron ore by carbon and limestone and operate in a reducing CO-rich atmosphere at 200-2000 °C, with molten fluxes, metals and slags. So BF refractories must be able to tolerate severe conditions of temperature and corrosion as well as erosion and abrasion from the loading of ore. The operating conditions vary in a tower up to 70 m tall with a hearth diameter 10-14 m so that various refractories are used depending on positions in the BF. For example, on the hearth pad flint clay bricks and low cement corundum (or chrome-alumina) castables are used to resist severe erosion. High alumina faced with SiC are used as the linings of the upper stack of a BF to resist abrasion and thermal shock.

2) Torpedo ladles

Torpedo ladles are used to transport hot metals from the BF to the primary steel works. Desulphurization metal treatment may also be carried out in torpedo ladles and other transfer ladles. Ladles which are simply for transport purposes are generally lined with flint clay, andalucite or bauxite bricks. However, High quality refractories such as unfired resin-bonded alumina-graphite can impart improved slag resistance and be used for the linings of ladles in which metal treatments are carried out.

3) Basic oxygen furnaces (BOFs)

BOFs, accounting for 70% of world steel production, are mainly used to remove carbon (C) and other unwanted elements such as P, Mn, Ti. High-purity oxygen is blown on to the metal and combines with these impurities, forming the slag. The typical BOF lining refractory material is magnesia-graphite. Higher graphite contents are added for the area which is subject to severe slag attack. Additionally, fused magnesia is added to increase corrosion resistance in the most severe wear areas.

4) Electric arc furnaces (EAFs)

EAFs are now used just for melting of steel scrap, and steel refining is carried out in a secondary steel-making process. MgO-graphite is the main slag line material and high levels of graphite are used to maximize the thermal conductivity and take full advantage of water cooling.

5) Steel ladles

Modern steel ladle linings must withstand increasingly severe conditions associated with secondary steel-making in the ladles before continuous casting, since various alloying, stirring and degassing procedures occur in the ladles. So high alumina, magnesia-carbon or zircon brick or monolithic materials of similar compositions are prepared and used to resist extensive wear.

6) Continuous casting

During the continuous casting process, various casting hollowares are used, including ladle shrouds, stopper rods, submerged entry nozzles, rotary valves, and submerged entry shrouds. All these parts of a continuous caster are made of different refractory materials. For example, alumina-graphite is used to prepare ladle shrouds providing sufficiently thermal shock resistance to withstand rapid heating

from the steel stream. In addition, stopper tips which are subject to erosion and corrosion are generally made of MgO-graphite and ZrO₂-graphite.

With continuous increase of steel production worldwide (rising to 1.55 billion tonnes in 2012 [34]), more refractories were consumed. It was estimated that total world production of refractories reached 41.5 million tonnes in 2012 and would rise to 46 million tonnes in 2017. However, specific consumption of refractories per tonne of steel has been falling since 1975. The demand for refractories in kg per tonne of steel (kg/t) decreases in the range of 1 to 2% per year, reaching ~7.8 kg/t in Japan and ~10 kg/t in Europe and North America in 2012. Further declines are likely to be slow and modest in these countries/regions.[4, 32]

Overall, there are two main reasons attributed to the declining trend. The first reason is that with the development and advancement of manufacturing technologies both in refractory and iron and steel-making industries, productivity increase and manufacturing process improvement lead to lower consumption of refractories in practice. For example, improvement in the technology of hot gunning repair has notably reduced replacement cycles and helped make full use of refractories, hence decreasing the consumption of refractories.[35, 36] In addition, the development and application of the continuous casting process further reduces refractory consumptions. Another reason is due to dramatic improvement on refractory quality and increase in service performance. One of the typical examples is the development and application of carbon-containing refractories with significantly improved thermal shock resistance and slag corrosion resistance.

2.1.4 Development of carbon-containing refractory castables

The most significant trend in refractories technology in the last three decades has been the ever increasing use of unshaped (monolithic) refractories such as castables. More than 50% of the refractories were produced and used as monolithics in some countries, for example, ~64% in Japan and ~52% in United States.[9] This is attributed to the advantages of unshaped refractories such as faster, easier and cheaper installation, and fewer corrosion-susceptible lining joints.[37, 38] For example, castables can be installed 10 times more efficiently than their brick counterparts and thus their energy consumption can be reduced by up to 90%.[39] In addition, they can be used to make complicated shapes and repair the furnaces in a short time. Taking energy consumption and environment protection

into consideration, the unshaped refractories (including castables) will replace shaped counterparts to a larger extent in the future.

However, most of the castables mainly comprise oxides so that they suffer the same drawbacks as oxide-based refractory bricks. For example, Al_2O_3 based castables have poor resistance to corrosion and spalling. MgO based castables exhibited poor slag penetration and spalling resistance. These problems lead to decreased lining lifetimes and hinder the application of oxide-based castables in the linings of various furnaces and ladles.[40]

Incorporation of free carbon into oxide-based refractory bricks (or CCRBs) (e.g. burned and impregnated MgO-C bricks) since the 1970s has led to significant improvements in their performance and thus greatly extended their service lives and reduced their specific consumption, which is mainly attributed to carbon's superior thermal properties (in particular, thermal shock resistance) and excellent slag resistance.[5, 41]

The successful development of CCRBs suggested that introducing carbon into current oxide-based castables would give improved properties. For example, by adding 5 wt% pitch to an MgO castable, the lifetime of the MgO-C castable in slag test was doubled compared to that of an Al_2O_3 -MgO castable.[42] Sakamoto [25] prepared Al_2O_3 -SiC-C castables and bricks and compared their performance at the same high temperature. It was found that the physical and mechanical properties of castable were competitive to those of brick. Similar corrosion and oxidation resistance were obtained for both forms of Al_2O_3 -SiC-C refractories, but with treated graphite incorporated in the castable, it exhibited even better performance than shaped refractories.

2.2 Carbon-containing refractory castables

2.2.1 Carbon source

As in CCRBs, there are several carbon materials that can be used as carbon source for carbon-containing refractory castables (CCRCs), including graphite, carbon black, pitch, resin, coke (coal or petroleum coke), tar (metallurgical or pitch tar). However, graphite is the favourite carbon source, due to its unique structure and thermal properties. Carbon black is also incorporated in castables as its nano-scaled size is able to help reduce the overall carbon content in carbon-containing refractories.[43, 44]

2.2.1.1 Graphite

There are two types of graphite, natural graphite and synthetic graphite. The former can be subdivided into 3 sub-groups, known as amorphous, flake and high crystalline graphite.[45] Natural flake graphite is a favourite carbon material that is used to make carbon-containing refractories, due to its ordered structure, high crystallinity, appropriate carbon content and abundant graphite supply compared with the other two natural graphites. Synthetic graphite is produced from calcined petroleum coke or coal tar pitch after a high temperature heat-treating process. The cost of synthetic graphite is very high and with a lot of pores in the final products.

Graphite has a planar structure with an infinite two dimensional array of carbon atoms arranged in hexagonal networks in the form of a giant aromatic molecule (Fig. 2.5). The covalent carbon-carbon bonds connect the carbon atoms within the parallel plane and therefore they are strongly bonded. However in the perpendicular direction, the planes are bonded by weak Van der Waal forces. Thus, graphite has a layered structure and shows preferred orientation of crystallites. It is the reason why graphite has anisotropic properties.[46]

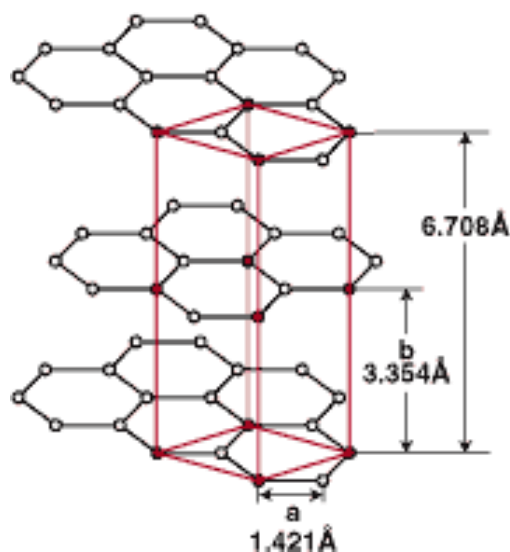


Fig. 2.5 Planar structure of graphite.

Because of the unique structure of graphite, it has some unique properties which can be used to improve thermal shock resistance and slag corrosion resistance. The detailed properties are outlined below.[46, 47]

1) Planar structure with no reactivity and wettability

The carbon atoms in a planar are in sp^2 bonding with no bonding directed out of the layer, but each layer is bonded to its neighbour by weak Van der Waal's force. So there is no propensity to bond or react in the direction at right angles to the plane. Any reactivity must be seen as deriving from the crystal edges. It is very difficult to bond to a basal surface other than through some physical mechanism. So the surface of graphite has no wetting ability. Thus graphite containing refractories cannot be readily corroded and penetrated by molten slag. The lifetimes of linings for furnaces, ladles or vessels thus can be extensively extended.

2) High thermal stability, conductivity and flexibility

Graphite has a very high melting temperature, over 3500 °C, and does not melt at normal pressure. The thermal conductivity of graphite (96.3 W/mK at 1000 °C) is about 10 times higher than refractory oxides (10.1 W/mK at 1000 °C for MgO, 9.5 W/mK at 1000 °C for Al_2O_3). As consequence of the cleavage on the basal plane and the lack of any directional bonding in the plane, graphite is extremely flexible. This makes graphite a very tough material and fracture across the flake is very difficult.

2.2.1.2 Carbon black

Carbon black refers to a group of industrial carbon materials which are also called thermal black, furnace black, acetylene black and channel blacks. They mainly consist of elemental carbon in spherical form but with different content of ash which depends on the manufacturing process. Carbon black is produced by the incomplete combustion of heavy petroleum products such as coal tar, ethylene cracking tar, and a small amount from vegetable oil. It is normally classified in terms of manufacturing process, because its characteristics and properties are very dependent on that process. For example, furnace black, most commonly used now, is produced with a furnace process. Carbon black was used as pigment in black ink in the early century, but is now widely used as filler or reinforcement for elastomers, plastics and other materials to improve thermal, mechanical or electrical properties.[48]

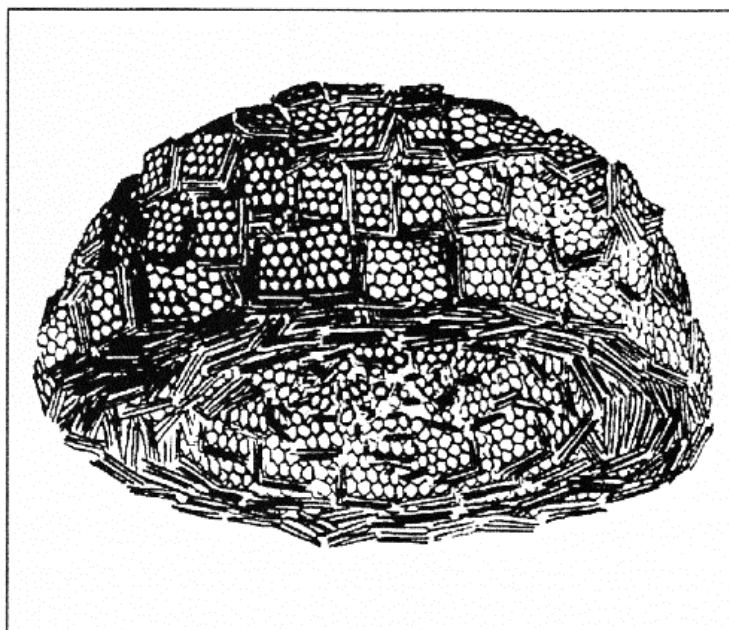


Fig. 2.6 Model microstructure of carbon black with random crystallite orientation.[49]

Carbon black is a form of amorphous carbon which is totally different from graphite and so there are no characteristic peaks appear on its X-ray diffraction pattern. But a model microstructure [49, 50] based on XRD was proposed which shows random crystallite orientation within a single carbon black particle (Fig. 2.6). As can be seen, the single carbon black particle is made of crystallites with an average of four graphite layers. The layer planes are roughly parallel and equidistant. Carbon black particles are generally aggregated, forming pellets with different size. There are

several different types of carbon black according to their particle size and specific surface area (Table 2.3).

Table 2.3 Carbon black with various particle size and surface area values.[51]

| ASTM number | Mean ^a | | EMSA ^a m ² /g | BET ^b | | Tinting ^d strength |
|-------------|----------------------|-----------------|--|--|--|----------------------------------|
| | particle dia., nm | HI ^a | | N ₂ SA m ² /g | CTAB ^c m ² /g | |
| N110 | 18 | 1.59 | 138 | 138 | 127 | 124 |
| N121 | 19 | 1.58 | 131 | 132 | 123 | 122 |
| N220 | 21 | 1.51 | 121 | 116 | 111 | 116 |
| N234 | 20 | 1.57 | 124 | 125 | 118 | 120 |
| N299 | 24 | 1.44 | 107 | 106 | 101 | 112 |
| N326 | 27 | 1.44 | 87 | 85 | 84 | 114 |
| N330 | 30 | 1.59 | 80 | 83 | 84 | 102 |
| N339 | 26 | 1.56 | 96 | 95 | 94 | 109 |
| N351 | 32 | 1.44 | 77 | 74 | 74 | 100 |
| N358 | 30 | 1.49 | 84 | 85 | 82 | 97 |
| N472 | 21 | 2.32 | 91 | 230 | 129 | 93 |
| N550 | 56 | 1.67 | 41 | 41 | 43 | 61 |
| N630 | 58 | 1.76 | 35 | 36 | 37 | 62 |
| N650 | 61 | 1.65 | 39 | 38 | 38 | 56 |
| N660 | 67 | 1.65 | 35 | 36 | 35 | 58 |
| N762 | 107 | 1.57 | 24 | 26 | 28 | 49 |
| N774 | 79 | 1.68 | 29 | 29 | 30 | 52 |
| N990 | 285 | 1.63 | 9 | 9 | 9 | 24 |

^a ASTM D 3849, Dispersion Procedure D (CAB).

^b ASTM D 3037.

^c ASTM D 3765.

^d ASTM D 3265.

2.2.2 Aggregates

Aggregate is the main matrix component in castable refractories and normally comprises 60-85 wt% of the castable mix. The aggregate selection is important and critical, as the final properties of castable products, in particular, thermal shock and corrosion resistance, are determined by aggregates' chemical composition and physical characteristics.[29] In practice, any natural or synthetic refractory oxides can be used in castable composites as aggregates for low cost purpose, similar to the case of refractory bricks.

2.2.2.1 Alumina (Al₂O₃)

Alumina is one of the most favourable oxides used in castable systems, due to its

high strength, relatively low thermal expansion coefficient, and good resistance to chemical attack. In the past, natural alumina resources such as chamotte (grog >40%, Al_2O_3 >30% SiO_2 <4%, Fe_2O_3 <2% $\text{CaO}+\text{MgO}$ [52]) and bauxite (Al_2O_3 >80%, SiO_2 <10%, with small amounts of TiO_2 , Fe_2O_3 , CaO and MgO [53]) were used mainly for castables' aggregates for low cost purposes. In the recent years, more synthesized high purity and performing alumina materials, for example, calcined, fused alumina and sintered alumina have been used.

Calcined alumina is produced from bauxite by the Bayer process in which sodium aluminate is extracted by soda (NaOH). After hydrolysis and calcination of $\text{Al}(\text{OH})_3$ in a rotary kiln at 1200 °C, calcined alumina powders are formed. Soda exists in small amounts as the major impurity. White fused alumina (WFA) is produced by fusion of calcined alumina in an electric arc furnace (EAF). The characteristic microstructure of WFA is in the form of sharp and fractured corundum grains. WFA usually contains impurities such as Na, K, Fe_2O_3 , TiO_2 , and CaO . In contrast, brown fused alumina (BFA) is prepared by fusion of bauxite and has a greater amount of impurities than WFA. Sintered alumina is produced by firing calcined alumina above 1900 °C. After sintering, sintered aluminas having flat table-like $\alpha\text{-Al}_2\text{O}_3$ crystals, usually averaging 50 μm or greater, are termed 'tabular' alumina (TA). The particle bulk density of TA is in the range of 3.40-3.65 g/cm^3 , due to grain boundary porosity entrapped during rapid sintering.[54]

2.2.2.2 Magnesia (MgO)

Magnesium oxide (MgO) is also one of the main aggregates for preparation of refractory composites (normally accounting for 70-95 wt% in MgO -C bricks). The natural sources of MgO are either from magnesium carbonate (MgCO_3) ores or from magnesium salts in sea water. To obtain MgO from both precursors, calcination and further heat-treatments are required. For the former precursor, a double burning process is usually used: i.e. start with low-temperature (~200 °C) treatment, followed by briquetting, and finish with high temperature (500~700 °C) sintering of MgO in a shaft kiln/furnace. For the latter, the following treatments are essential: the magnesium salts in sea water react first with hydrated CaO (from dolomite or limestone) to produce $\text{Mg}(\text{OH})_2$. The $\text{Mg}(\text{OH})_2$ is then washed, filter pressed, dried and calcined at 750~1000 °C. To prevent active MgO from reacting with CO_2 and H_2O , it has to be dead burned at >1500 °C in a rotary kiln/furnace or be treated by

melting calcined MgO in an EAF at a temperature above its melting point (>2800 °C). The properties of MgO are governed by such key factors as CaO/SiO₂ ratios, purity, grain size and bulk density.

MgO-C brick is an important shaped refractory composite used as BOF and EAF lining material. However, the hydration of MgO has dramatically influenced the development of MgO-C castables for the same applications. The formation of Mg(OH)₂ after hydration worsens the flowability and setting behaviour of castables. The release of water from dehydration of Mg(OH)₂ on heating also causes cracks, reducing mechanical properties of MgO containing castables.[55, 56] Extensive studies revealed that the hydration of MgO was related to the magnesia source (particle size, specific surface area, purity, CaO/SiO₂ ratio, production route, magnesite calcination temperature) [57-60], the pH and temperature of the liquid medium [61, 62], the interactions of MgO with other castables' raw materials (such as calcium aluminate cement, hydratable alumina and silica fume) and the additives [63-66].

2.2.3 Superfines

Apart from large-sized aggregates, superfines are also an important part of a refractory matrix. The superfines are normally below 45 µm and can even be smaller than 1 µm. They are added into castables to reach reasonable particle size distribution and fill the void spaces between the larger particles, so that the densest packing is possibly achieved.[29] Among superfines, silica fume and calcined alumina (or reactive alumina) are the most commonly used in both low cement castables (LCCs) and ultralow cement castables (ULCCs).

2.2.3.1 Microsilica

Microsilica, also called silica fume, is an amorphous silicon dioxide consisting of sub-micron spherical primary particles with average diameter of 0.15 µm. It has no internal porosity and its specific gravity is about 2.3 g/cm³. The specific surface area may vary between 15 and 30 m²/g.[67] The primary function of microsilica in the refractory castable is to act as filler. When microsilica particles are dispersed in castables, they fill the voids between aggregate grains and release entrapped water, thus reducing water demand and decreasing porosity of castables. It was found that the use of microsilica reduced open porosity of castable composite after firing at

1000 °C from 20-30% to 8-16%. [68, 69] In the meantime, the addition of microsilica can help achieve a reasonable particle size distribution and improve flowability and workability during the castable making process (Fig. 2.7). In addition, in a refractory castable using calcium aluminate cement (CAC) as a binder, microsilica could influence hydration of cement and delay the settings of castable by sequestering the multivalent cations Ca^{2+} and Al^{3+} . [70] Upon heating, microsilica would also react with CAC, forming eutectic liquid phase, C-A-S ternary phase which would deteriorate the hot strength at above 1200 °C. [71] However, it was claimed that in high alumina-based castables, formation of needle-shaped mullite crystals from the reaction of microsilica and alumina could significantly increase the hot strength at 1300-1400 °C. [72]

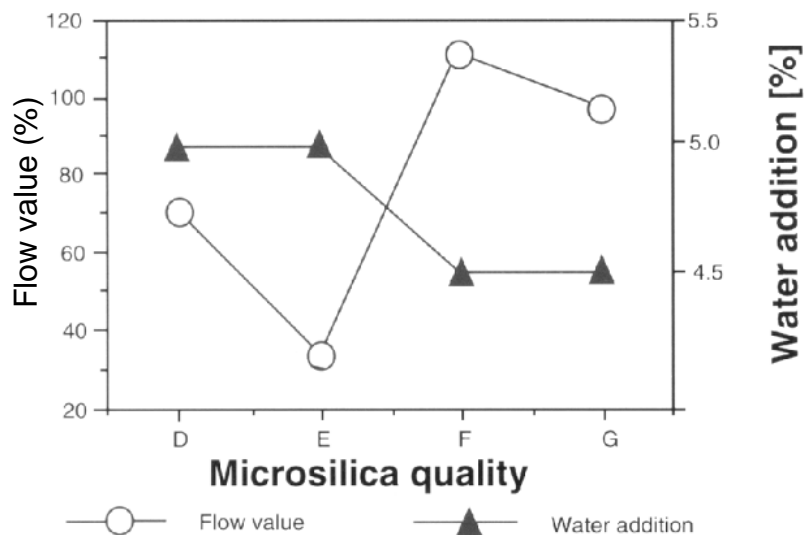


Fig. 2.7 The effect of microsilica content on flow and water addition to a tabular alumina based refractory castable. [73]

Since microsilica would form a liquid phase with cement at high temperature which is detrimental to mechanical properties of castables, the ratio of microsilica and cement content should be carefully controlled. To avoid the negative impact of microsilica, calcined and reactive alumina are added to improve packing density and enhance the development of ceramic bonding phases at low temperature. [74]

2.2.3.2 Calcined/Reactive alumina

Calcined alumina is obtained by milling calcined alumina aggregates to smaller sizes, normally below 44 μm (95-99%). Reactive alumina is the superground alumina with relatively high surface area, exhibiting higher densification and reaction rates. The use of fine reactive aluminas results in LCCs with excellent hot properties

and very low mixing water requirements for placement.

2.2.4 Binders

Unlike oxide-carbon bricks in which pitch and phenolic resin are used to bind aggregates together, refractory castables usually are bonded by calcium alumina cement, hydratable alumina and colloidal silica/alumina.

2.2.4.1 Calcium alumina cement (CAC)

CAC is the most popular binder used in castable systems. Based on lime (CaO) content, cement containing castable is divided into three types: conventional cement (CaO >2.5%), low cement (2.5 >CaO >1.0%), ultra-low cement (1.0% >CaO >0.2%), and cement free (CaO <0.2%).[54, 75] With development of cement containing castables, cement content has been dramatically reduced from conventional addition of ~30%, because high cement would cause high water addition, lower strength after dehydration process and heating at high temperature. Thus, low cement castables (LCCs) and ultralow cement castables (ULCCs) have been widely used since the 1970s.[76]

CACs are produced by reaction of alumina and lime either via a clinker sintering process at 1315-1425 °C or fusion at 1450-1550 °C.[54] The calcium aluminate phases are governed by the lime/alumina ratio and firing temperature. As predicted by the CaO-Al₂O₃ binary phase diagram [29], lime and alumina react with each other until completely combined as follows.



The hydration mechanism of CACs has been extensively investigated and discussed previously.[29, 77, 78] In the presence of water, the main calcium aluminate phases, CA, CA₂ and C₁₂A₇, begin to dissolve quickly forming a saturated solution of ions (Ca²⁺ and Al(OH)₄⁻). The subsequent nucleation and precipitation would produce an interlocked network which provides strength for green castables. The formation of hydrates is largely dependent on temperature. As shown in Fig. 2.8, CAH₁₀ and AH₃ gel are formed at low temperature (<21 °C), C₂AH₈ formed at intermediate temperature (21-35 °C), and more stable compounds C₃H₆ and AH₃ crystals formed at relatively high temperature (>35 °C). Upon firing, the hydrates experience dehydration forming anhydrous phases. On heating to 200 °C

dehydration occurs and by 400 °C $C_{12}A_7$ starts to form. Elongated CA forms at 900 °C from reaction of alumina with $C_{12}A_7$. At 1000-1200 °C CA reacts with alumina to form coarse and globular CA_2 while at >1300 °C CA_2 reacts with alumina to form hexagonal platelets of CA_6 which is able to improve mechanical properties and thermal shock resistance of alumina castables.[79]

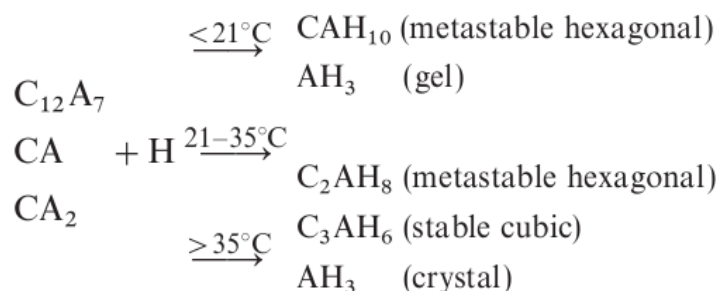


Fig. 2.8 Calcium aluminate hydrates formation as a function of temperature.[80]

2.2.4.2 Hydratable alumina (HA)

HA has been used as a CaO-free binding agent for refractory castables to avoid the unfavourable influences of CAC on high-temperature properties.[81, 82] In addition, CAC is not compatible with MgO, as low melting phases formed from CAC and MgO would decrease the refractoriness of MgO and corrosion resistance of MgO-C castables.[83] HA is mainly in a high surface area transition phase, $\rho\text{-Al}_2\text{O}_3$, generally produced by flash calcination of gibbsite ($\gamma\text{-Al(OH)}_3$). Similar to CAC, the binding ability of HA is derived from its rehydration. During hydration, a thick layer of gel is formed, which consists of major quantities of bayerite ($\alpha\text{-Al(OH)}_3$) and small amount of boehmite ($\gamma\text{-AlO(OH)}$). The mechanical strength is provided by interlocking bayerite crystals and gels through forming honeycomb structures on the surface of aggregates.[81] The evidence shows that formation of bayerite gel is strongly dependent on hydration temperature.[84, 85] High temperature is beneficial to bayerite formation. The hydration of HA is quite slow at room temperature but could be completed at ~55 °C for 24 hours.[86] However, the presence of reactive magnesia accelerates the hydration of HA and promotes the formation of hydrotalcite-like compound which increases the strength of the castables after frying at 110 °C and firing at 816 °C.[87] Although the castable with HA does not suffer from low-melting phases as formed in microsilica containing CAC castables, it has higher risks of explosive spalling, due to its less permeable structure after drying.[88]

2.2.4.3 Colloidal silica/alumina

In the recent years, colloidal silica or alumina have been used as nano-binders for refractory castables.[89-91] High reactive silica sol could lower the formation temperature of Mullite for alumina-rich systems (1100 °C). In addition, the use of colloidal silica binder does not result in generation of hydrated phases, making castable processing and placement safer and quicker. The mechanical strength provided by colloidal silica is obtained by gelling and coagulation through condensation of siloxane groups on the particle surface as expressed in the following equation.[92]



The properties of three types of castable binders are listed in Table 2.4, providing a general principle of binder selection before use. As stated above, each binder has both advantages and disadvantages. The function and developed binding strength are highly dependent on the practical use of a specific castable system. So it is essential to make an appropriate decision on choosing the best binder for actual castable production.

Table 2.4 Properties of three types of binders, colloidal silica/alumina, hydratable alumina and calcium aluminate cement.[93]

| Binder type | Chemical specification (wt%) | Surface area (m ² /g) | Aggregate size | Surface charge | pH range | Stabilizer | BD (g/cm ³) |
|--------------------|---|----------------------------------|------------------------------|----------------|----------|---------------|-------------------------|
| Colloidal alumina | Al ₂ O ₃ : 40 | 100 | 80 nm | Anionic | 6-9 | Citric acid | 1.5 |
| Colloidal silica | SiO ₂ : 40 N ₂ O <0.4 | 200 | 15 nm | Anionic | 10 | Na-stabilized | 1.3 > |
| Calcium aluminate | Al ₂ O ₃ >69 CaO <30 SiO ₂ >0.3 Fe ₂ O ₃ <0.3 | 0.4 | -45 μm: 82 wt% D50= 13 μm | — | — | — | 2.9-3.05 |
| Hydratable alumina | Al ₂ O ₃ : 90 Na ₂ O: 0.5 LOI: 6.5 | 270 | D50= 2.5 μm | — | — | — | 3.2 |

2.2.5 Additives

To improve castable processing and maximize their high temperature performance, a small amount of additives are added during raw materials mixing. For different functions and purposes, different additives are added, such as dispersants, accelerators, retarders, plasticizers, deflocculants or water reducers, explosion inhibitors, and antioxidants. Herein, the special focus is made on three important additives for carbon-containing castables, which are deflocculants, carbon dispersants, and antioxidants.

2.2.5.1 Deflocculants

In many studies, microsilica and calcium cement are used at the same time. Microsilica with negative charges on the surface is prone to be attacked by abundant cations, Ca²⁺ and Al³⁺ from dissolution of cement in water.[94] Thus, the gelling and coagulation occur before completion of mixing and casting, increasing viscosity and making the castable mixture difficult to flow freely. Therefore, deflocculants added to prevent the absorption of calcium on microsilica surface so

as to improve flowability of castables and reduce water additions at the same time. Currently, there are three main commercial deflocculants used for castable applications, Calgon (sodium polyphosphate), Darvan (sodium polyacrylate) and Castaman FS20 (polycarboxylate ether (PCE)). As shown in Fig. 2.9a, both Darvan and Calgon are able to increase negative charges of microsilica, but Castaman FS20 is not. However, PCE with a negatively charged backbone and non-ionic side chains exhibits an excellent function to improve workability of high cement castables (Fig. 2.9b), due to both steric and electrostatic stabilization.[95-97] For ultralow cement castables, investigation carried out by Otraj [98] suggested that sodium polyacrylate helped castables obtain the best flowability. However, for zero cement castables, dispersants rather than deflocculants are required. Studart and Pandolfelli [99] suggested that short-chain molecules with high density of dissociable sites such as 3,4,5-Trihydroxybenzoic acid (Gallic acid) and 2-phosphonobutane-1,2,4-tricarboxylic acid (PBTCA) were suitable for basic pH environment (high alumina castables, $8 < \text{pH} < 10$), but citric acid for acid pH conditions.

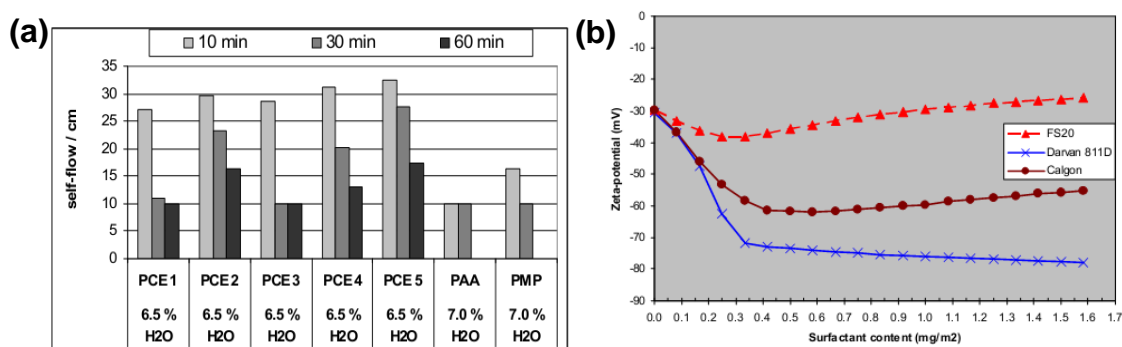


Fig. 2.9 (a) Zeta potential of microsilica as a function of deflocculant addition (expressed as addition per surface area) [94], (b) Self-flow of basic high alumina castable containing various deflocculants.[96]

2.2.5.2 Carbon dispersants

Due to poor wettability of carbon materials, a carbon dispersant is added to improve water-wettability of carbon surfaces and enhance the dispersion of carbon particles in a castable matrix. The organic dispersant normally has a structure of hydrophobic and hydrophilic functional groups on two ends [100] as schematically shown in Fig. 2.10. The hydrophobic end is attached to the surface of carbon particles, and the hydrophilic end interacts with water, generating steric/electrostatic repulsions between carbon particles.[101] The use of dispersants is one of the methods to improve wettability of carbon materials. The details are given in Section 2.3.2.

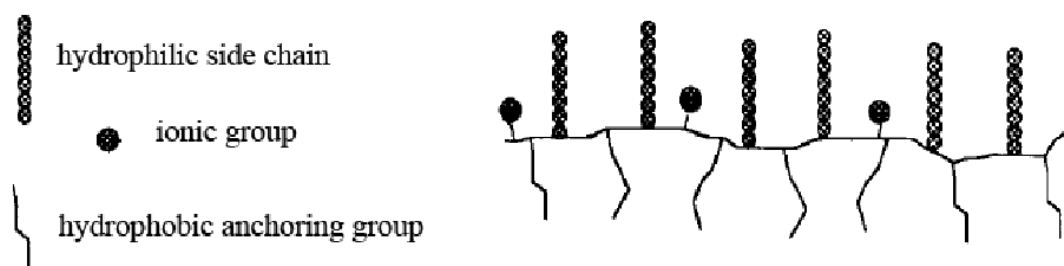


Fig. 2.10 Polyfunctional surfactants for aqueous systems.[100]

2.2.5.3 Antioxidants

The incorporation of carbon materials brings another problem. That is the carbon's high susceptibility to oxidation in oxidising atmospheres. So highly effective antioxidants are required in carbon-containing refractories. The antioxidants developed in the past include metals powders such as Al, Mg, Si, or Al-Mg and Al-Si, carbides (mainly SiC), and boron-based compounds such as B₄C, ZrB₂, CaB₂. [40] Metal powders can react with carbon monoxide prior to oxidation of carbon materials. The formed carbon and oxides decrease porosity and block the penetration of oxidizing gases. [5] SiC is able to prevent carbon oxidation by reacting with CO at high temperatures. The comparison of the effects of these antioxidants on carbon oxidation losses is shown in Fig. 2.11. B₄C is the most effective antioxidant for MgO-C refractories, since liquid phase magnesium borate (Mg₃B₂O₆) is formed upon heating and effectively fills up the open pores and forms a protective layer on the surface. [102, 103] However, liquid phase would significantly reduce the mechanical properties and refractoriness. So the amount of B₄C needs to be controlled and it is normally used with Al. All these studies of antioxidants were carried out in refractory bricks, however, metal powders should be carefully used in castables, due to evident hydration in water. [104] So attempts have been made to improve hydration resistance of Al powder in water by using inorganic-organic hybrid coatings. [105] Recently, two complex carbides, Al₄SiC₄ and Al₈B₄C₇ have been used as antioxidants with excellent hydration resistances [106, 107] However, it has been proved that the effect of Al₄SiC₄ on improving oxidation resistance of Al₂O₃-SiC-SiO₂-C castable was limited, because the carbon source was oxidised earlier before Al₄SiC₄ functioned. [108] Luz and Pandolfelli's work [109] suggested that a blend of antioxidant (Si, B₄C and sodium borosilicate glass) was effective to improve oxidation resistance and increase mechanical strength of carbon-containing castables.

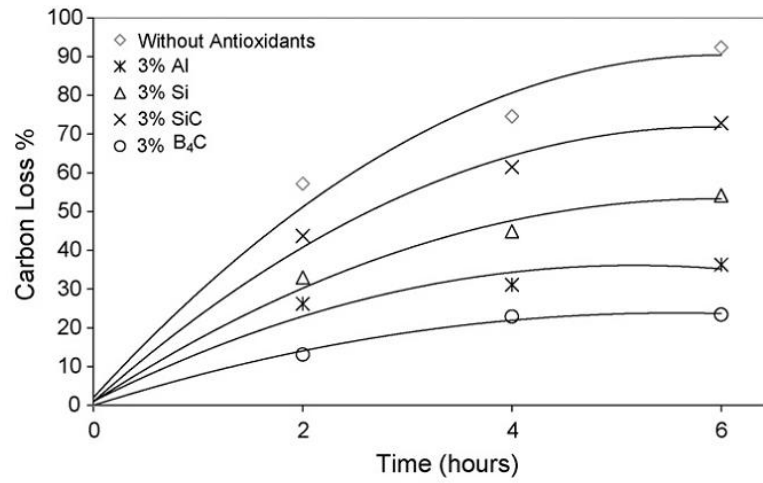


Fig. 2.11 Carbon losses of MgO-C specimens with/without 3 wt% antioxidant at 1500 °C.[102]

2.3 Solutions for improving carbon's water-wettability

2.3.1 Poor water-wettability of carbon materials

Trying to make carbon-containing refractory castables (CCRCs) introduces many new **c** arising from the hydration tendency of MgO fines and aluminium based antioxidants (reviewed in Section 2.2.2.2 and 2.2.5.3), and poor water-wettability and dispersion property of carbon materials. The latter technical problem is fatal, because it directly leads to high water demand for casting castables, and consequently high apparent porosity and low mechanical property of CCRCs, making it difficult to add carbon into castables to acquire equivalent refractory properties of carbon-containing refractory bricks (CCRBs).[40]

The water-wettability and dispersion behaviour of carbon materials is associated with their intrinsic nature of water affinity and the presence of hydrophilic functional groups on their surface, such as $-OH$ and $-COOH$. This can be reflected in their Zeta (ζ) potential in water. A higher ζ value leads to better water-wettability and dispersion property. For example, compared with oxides such as alumina and silica (Fig. 2.12a), both flake graphite and grain graphite (Fig. 2.12b) show much lower ζ potential over a wide range of pH.[110] As for carbon black, it was reported carbon black contained oxygen-containing functional groups on its surface [111], however, limited amount of hydrophilic groups were not able to impart carbon black with desirable water-wettability and dispersivity.

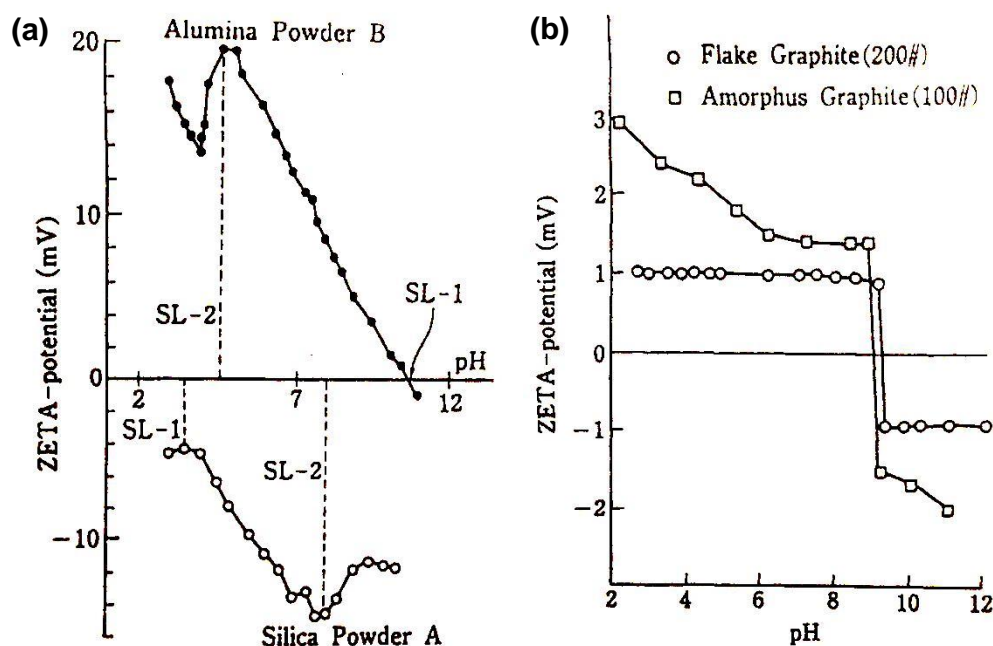


Fig. 2.12 Zeta potential (ζ) of (a) graphite, and (b) alumina and silica in 0.01 M KCl as function of pH.[110]

Therefore, to improve water-wettability and dispersion property of carbon materials and promote their application in CCRCs, various methods have been investigated, including using surfactants, making graphite micropellets or briquettes and coating carbon with other materials.

2.3.2 Surfactants

Surfactants (or surface active agents) have been used to improve aqueous wettability and dispersion of graphite since they can increase its water affinity through physical absorption.[112, 113] However, the surfactants specially designed for graphite seem not be commercially available. Thus Kawasaki et al [114, 115] prepared a surfactant which could be used to improve the wettability of graphite. This is the first method that has ever been developed to tackle the problem. In this method, a water soluble polymer (cationic cellulose) was used to coat graphite as the first ionic layer and sodium silicate (Na_2SiO_3) as the second ionic layer. (Fig. 2.13)

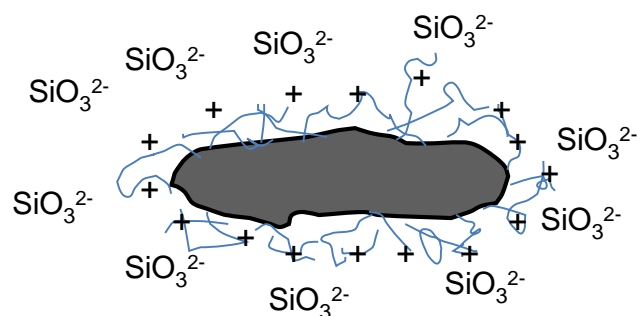


Fig. 2.13 Schematic drawing of surfactants coated graphite.

The wettability and dispersion property of graphite were slightly improved by simple absorption of double ionic layers. Nevertheless, the system of ionic layers was not stable, as excessive adsorption of anions would remove the polymeric adsorption layer. A self-developed dispersant was prepared thereafter by Isomura et al [116]. Some organic acids such as polycarboxylic acid, polyacrylic acid and naphthalenesulfone acid were used, however, no further details were reported on the dispersant.

Although these surface active agents are cheap and easy to prepare, the main problem is that the simple physical adsorption is not always stable so that the improvement in wettability and dispersion is limited. Therefore, it is difficult to incorporate a large amount of graphite into a castable system. Surfactants also often interfere with other additives, such as deflocculants. In addition, carbonization of polymer agents upon firing at high temperature will adversely increase porosity and decrease mechanical strength of castables.

2.3.3 Micropellet /briquette techniques

Instead of straightforward incorporation of flake graphite into castables, Zhou and Rigaud [117, 118] prepared micro-pelletized graphite and briquetted alumina-graphite and tried them in $\text{Al}_2\text{O}_3\text{-SiC-C}$ and $\text{Al}_2\text{O}_3\text{-MgO-C}$ castables .

Micro-pelletized graphite was mainly composed of flake graphite, antioxidants and liquid binder. Two metal powders (Al and Si) and two boron bearing powders (B_4C and ZrB_2) were included as antioxidants. Fine alumina powers were added to adjust graphite content and balance the density of the pellets. Organic binders such as polyvinyl alcohol, phenolic resin and molasses were used to bind all raw materials. After homogeneous mixing and shaping, heat treatment was done to cure the resin and form carbon bonding.

The detailed process of fabricating micro-pelletized graphite comprised four steps: mixing all the raw materials in Horbart N50 mixer; extruding from a screw-press extruder with different diameters of orifice; curing at room temperature and heated at 200 °C; breaking up into the designed pellet size. The resultant graphite micro-pellets were in diameter of ~0.5 mm and length up to 5 mm as seen in following figure.

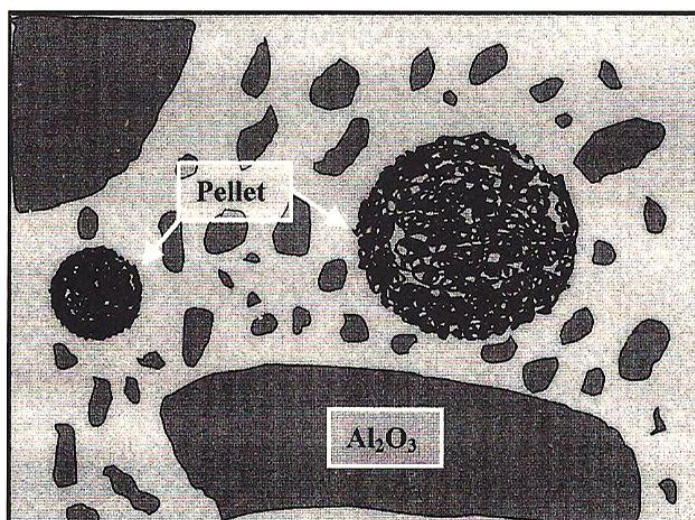


Fig. 2.14 Graphite micro-pellets in carbon-containing castable.[118]

Briquetted alumina-graphite was actually a mixture of 70% alumina and 30% graphite, in which phenolic resin was used as binder. Raw materials were mixed and blended in a mixer and then briquetted under a pressure of 70 MPa into 204×52×62 mm prisms. After heat treatment at 180 °C for 24 hours, they were crushed into different size fractions between 0.074 and 3.36 mm.

The resultant graphite-containing pellets were incorporated into a Al₂O₃-SiC-C castable system to examine their actual effectiveness. Fig. 2.15 compares flow value and water demand of the castables containing different graphite sources. It shows that the castable with unmodified graphite required the highest water level but exhibited the lowest flow value. However, water demand for making castables containing micro-pelletized graphite and briquetted alumina-graphite decreased by about 1.5%.

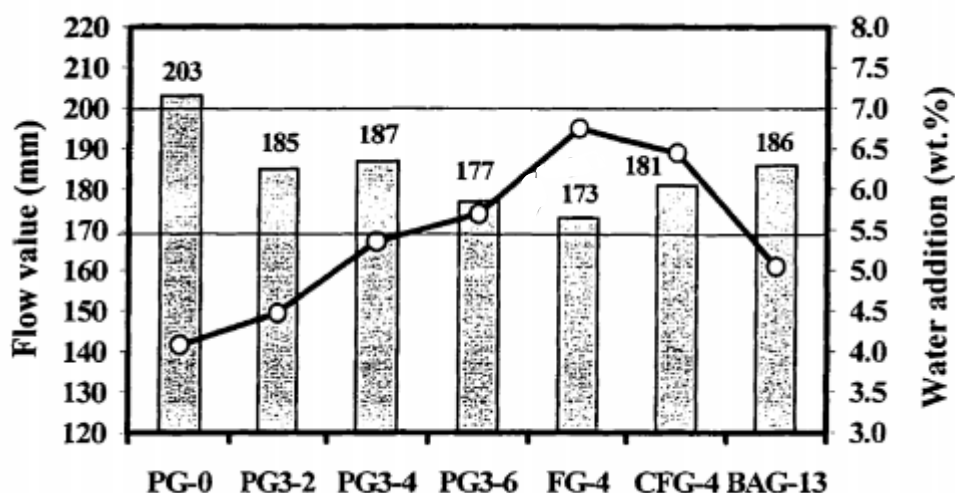


Fig. 2.15 Flow value and water demand of $\text{Al}_2\text{O}_3\text{-SiC-C}$ castables containing different types of carbon listed in Table 2.5.[117]

Table 2.5 The weight percentage of carbon source in $\text{Al}_2\text{O}_3\text{-SiC-C}$ castables.[117]

| | PG-0 | PG3-2 | PG3-4 | PG3-6 | FG-4 | CFG-4 | BAG-13 |
|----------------------------|---------------------------|-------|-------|-------|----------------|---------------------------------|-----------------------------|
| Carbon type | Micro-pelletized graphite | | | | Flake graphite | TiO_2 -coated graphite | Briquetted alumina-graphite |
| Carbon-oxide mixture (wt%) | 0 | 2 | 4 | 6 | 4 | 4 | 13 |
| Carbon content (wt%) | 0 | 1.7 | 3.4 | 5.1 | 4 | ~4 | 3.9 |

Micropellet/briquette methods appear to decrease water demand effectively and are experimentally straightforward. However, it is difficult to achieve a homogeneous distribution of graphite in the castable microstructure, because graphite is prefixed in the micropellets or briquettes prior to incorporation into castables. This will weaken the corrosion resistance and decrease mechanical strength. In addition, micropellets and briquettes bonded by resin are easily disintegrated during vigorous mixing with aggregates.

2.3.4 Surface coating

2.3.4.1 Carbon coating

Zhang [40] summarized that depending on crystallinity and surface activity of carbon

materials (e.g. graphite flakes, carbon black and carbon from pitch, resin and coke, etc.), they show different aqueous wettability and dispersion. The lower the crystallinity or the more active the surface, the better the wettability and dispersion. Thus, some work has been done to coat graphite flakes with active amorphous carbon materials.

Pitch was initially used to coat graphite flakes, due to its low melting point (100-200 °C) and easy preparation procedure.[17] Graphite flakes were mixed with 10-60 wt% of a pitch (coal tar) and heated over 100 °C to soften pitch. After cooling, the bulk mixture was subsequently crushed to produce carbon granules. However, the improvement in wettability is limited, because pitch has only slightly better aqueous wettability than graphite. Furthermore, pitch is undesirable from an environmental standpoint. Toxic vapours would also be released from pitch decomposition, causing environmental concerns.

Sharifsh [18] prepared a coating layer of 50 nm on graphite flakes using carbon black in the assistance of an ink colloid. In the study, nanosized carbon black N220 was dispersed in ink by stirring and ultrasonic vibration, forming colloidal suspensions. Graphite flakes were then immersed into carbon black-containing suspensions and the absorption was enhanced by vigorously stirring. In this way, graphite flakes was coated with carbon black (Fig. 2.16a). The surface of graphite flakes became rough and a lower contact angle was obtained (Fig. 2.16 a&b), indicating the improvement in wettability. However, the coatings were discontinuous and weak physical attached carbon black would lead to peeling off during mixing and casting.

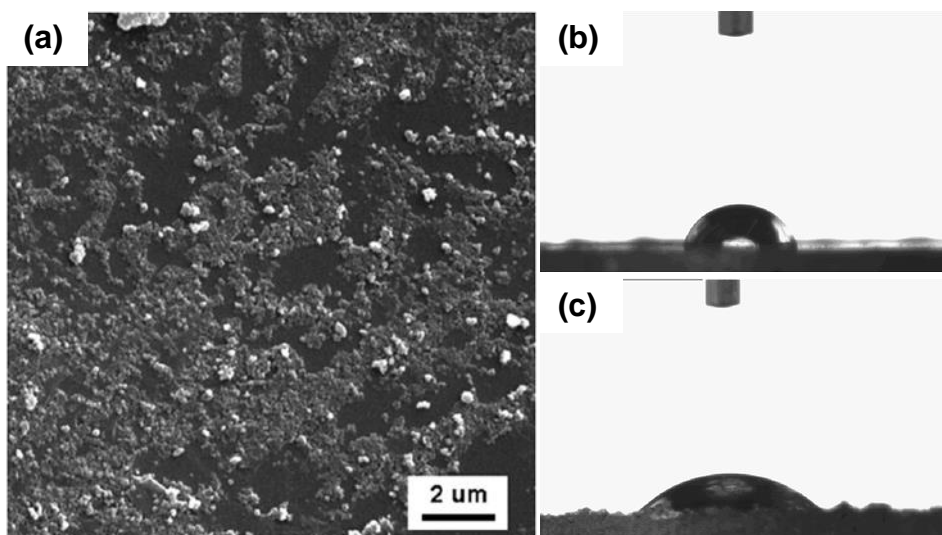


Fig. 2.16 (a) SEM image of carbon black coated graphite flake, and contact angle of a water drop on (b) uncoated and (c) coated graphite.[18]

Other carbon coating methods are mainly based on chemical vapour deposition (CVD).[119, 120] Amorphous carbon was deposited on a graphite surface from gaseous carbon precursors such as methane CH_4 and ethane C_2H_2 when they were heated up to around $1000\text{ }^\circ\text{C}$ under Ar flow. The method has widely been used to modify natural graphite to prevent it from electrolyte attack in the application of lithium-ion batteries.[121, 122] The electrochemical performance of pyrolytic carbon-coated graphite was studied but the water-wettability of coated graphite was not yet reported. Another concern arises from its high cost when it finds its application in refractory industry

2.3.4.2 Oxide coating

Among the coatings, oxide coatings are of most interest to modify the hydrophobic surface of graphite flakes. As for preparation of oxide coatings, sol-gel process is the most favourite method. Sol-gel process initially referred to the production of inorganic oxides, either from colloidal dispersion or from metal alkoxides, however, currently it is also used to synthesise some other components such as nitrides, sulphides and hybrid organic-inorganic materials.[123, 124]

The synthesis of ceramic materials via the sol-gel process goes through four main steps, which are 1) selection of appropriate sol precursor, 2) gelation, 3) hydrolysis and 4) sintering (Fig. 2.17).

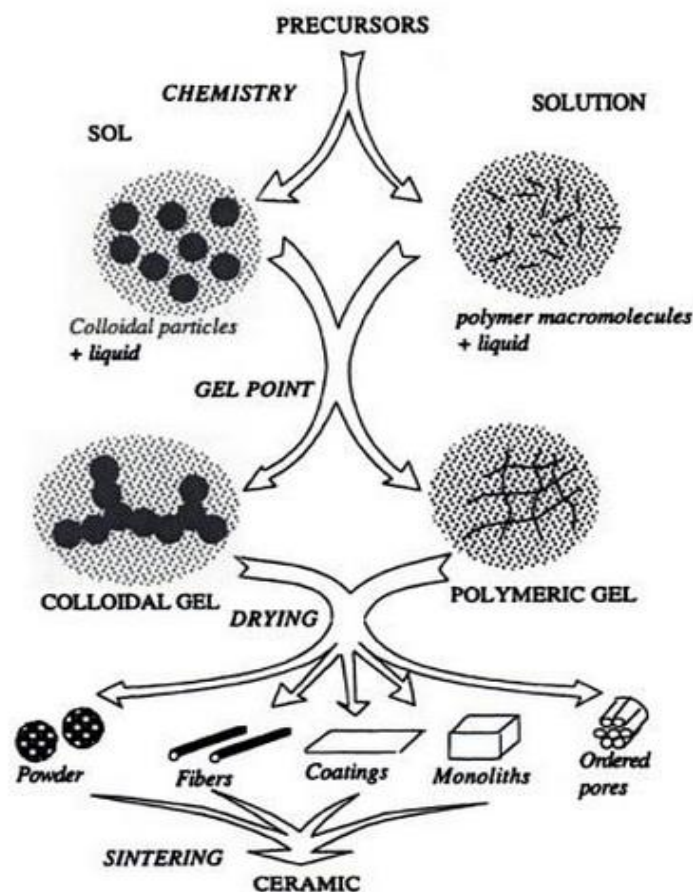


Fig. 2.17 Flow chart of sol-gel process.[124]

Sol-gel processes could be used to prepare oxide coatings from two types of molecular precursors, metal alkoxides in organic solvents and metal salts in aqueous solutions. The mechanism of sol-gel preparation of oxides were well documented in many books [125-127] and review papers [128-130].

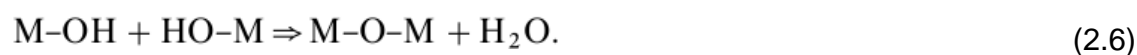
Starting with metal alkoxides, parent alcohol is used to dissolve the precursors prior to hydrolysis, as metal alkoxides are normally not miscible with water. The first step is hydrolysis for formation of reactive M-OH groups.

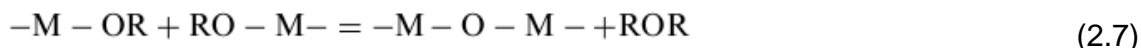


Or partially hydrolysed

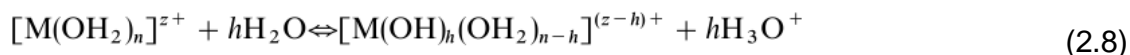


which is followed by condensation and network formation.

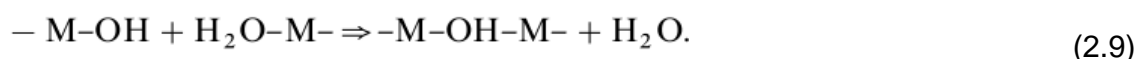




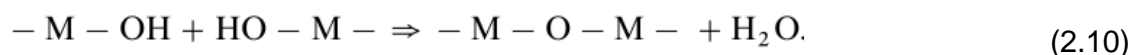
When metal salt dissolves in aqueous solution, $[M(OH_2)_n]^{z+}$ species are formed by interacting with dipolar water. Spontaneous deprotonation also occurs as follows:



Condensation is usually initiated by adding a base to aquo-cations $[M(OH_2)_n]^{z+}$. Depending on the oxidation state of cations, two condensation mechanisms are proposed. For cations of low oxidation state ($z < 4$), oxolation reactions occur.



For cations of high oxidation state ($z > 4$), an 'oxo' bridge is formed via oxolation reactions



Due to better water affinity of oxides, various oxides coatings were prepared via sol-gel process on graphite flakes from alkoxide precursors. For example, Yoshimatsu [131] was the first to use a sol-gel technique to prepare Al_2O_3 coatings on graphite flakes. Mixing with various content of Al_2O_3 gel in a mixer spinning, graphite flakes were coated with Al_2O_3 coating after subsequent drying at $100\text{ }^\circ\text{C}$ for 3h and calcination up to $500\text{ }^\circ\text{C}$. After coating, wettability of graphite flakes was improved (Fig. 2.18a) and it led to less water addition when incorporated into castables.[132] In addition, Yilmaz's work [133] showed that the oxidation resistance of coated graphite flakes was also improved (Fig. 2.18b).

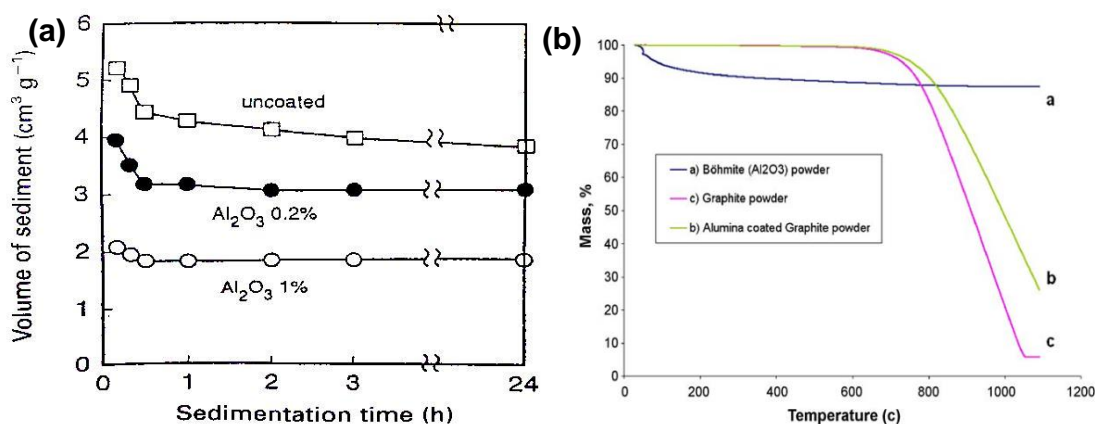


Fig. 2.18 (a) Sediment volume of graphite coated with various amounts of Al_2O_3 , [131] (b) TG results of uncoated and coated graphite flakes. [133]

Similarly, Yu et al [134] mixed graphite with various amounts of titanium alkoxide

($\text{Ti}(\text{OC}_4\text{H}_9)_4$). TiO_2 was consequently formed when heating the mixture in air where alkoxide reacted with water and then decomposed. The effect of TiO_2 on wettability was reflected in the change of the floating ratio of graphite in water. When the TiO_2 content was increased to above 0.5%, it showed much better wettability as expected (Fig. 2.19a). ZrO_2 coating was also attempted from hydrolysis of zirconium oxychloride.[20] In this case, a surfactant, polyvinyl alcohol (PVA), was added to enhance ZrO_2 absorption, due to low wettability of ZrO_2 for graphite. However, the as-prepared ZrO_2 coating was low quality and the zeta potential results (Fig. 2.19b) did not show much improvement on the wettability of graphite. SiO_2 coating on graphite prepared by Zhang [21] showed the better water-wettability and oxidation resistance than Al_2O_3 coated graphite.

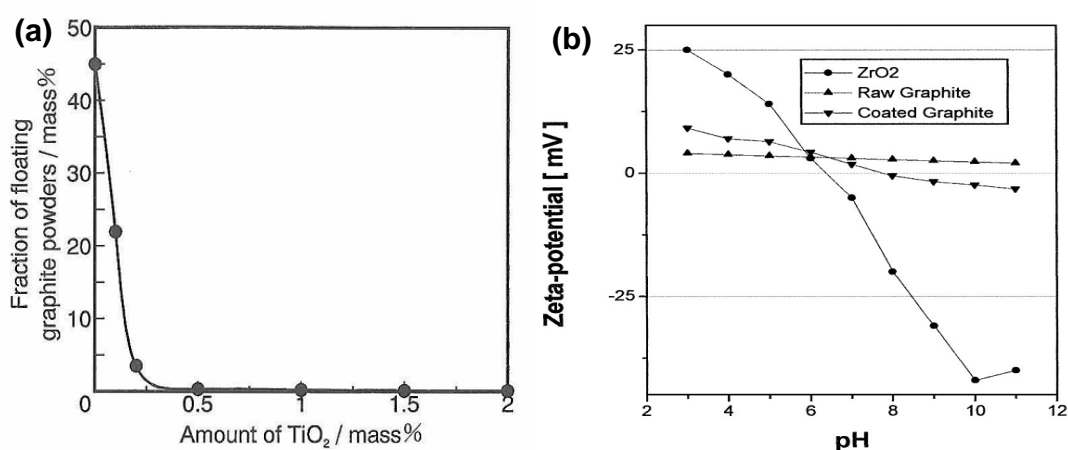


Fig. 2.19 (a) Fraction of the floating graphite powders as a function of the amount of TiO_2 coating,[134] (b) Zeta potential of ZrO_2 , raw graphite and ZrO_2 coated graphite as a function of pH.[20]

Beside single oxide coatings, binary oxide coatings such as $\text{Al}_2\text{O}_3\text{-SiO}_2$, $\text{Al}_2\text{O}_3\text{-ZrO}_2$ were prepared.[21, 135, 136] They all show similar wettability and oxidation resistance, indicating that binary oxide coatings did not further enhance the effect on graphite's wetting behaviour. Unlike simply preparing a $\text{Al}_2\text{O}_3\text{-SiO}_2$ composite oxide coating at around 500 °C, Mukhopadhyay [22] fabricated mullite ($3\text{Al}_2\text{O}_3\cdot 2\text{SiO}_2$) by firing a hybrid polymeric precursor at high temperature where mullitization of Al_2O_3 and SiO_2 took place. Mullite formation from sol-gel precursors initiated at above 940 °C [137] and showed poor crystallinity at 1000 °C, whereas at 1200 °C and above, the orthorhombic mullite phases became prominent. The wettability of Mullite coated graphite was not solely demonstrated, but water demand for castable containing mullite coated graphite could be reduced to 7.8–8.2% which was lower in comparison with that of castable containing uncoated graphite (11.0%).[138] It also

showed that castables containing mullite-coated graphite were more resistant to thermal shock.

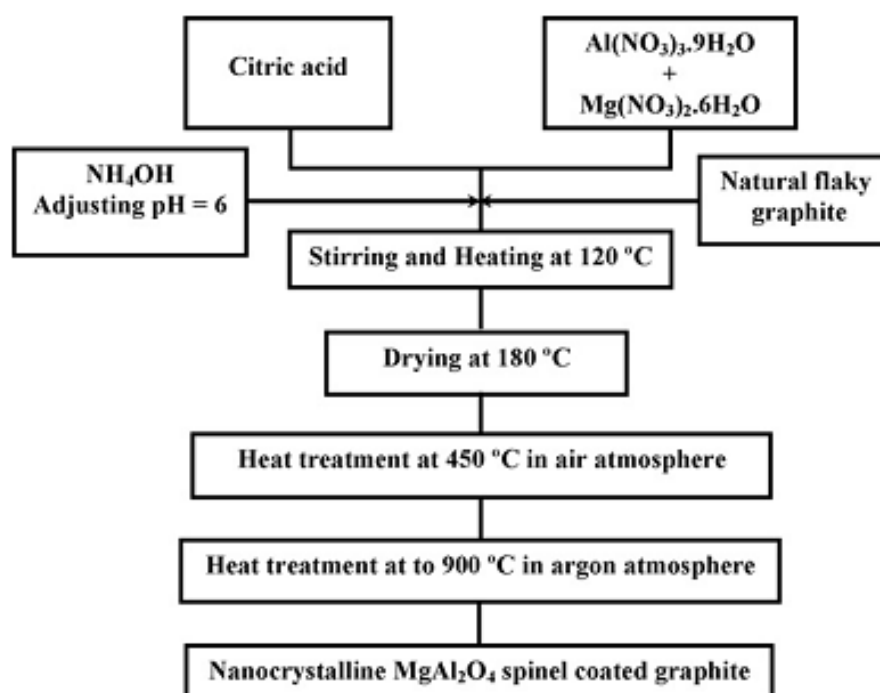


Fig. 2.20 Flowchart of preparation of MgAl₂O₄ spinel coated graphite particles.[23]

Due to excellent chemical resistance and refractoriness of MgAl₂O₄ spinel, Saberi [23, 139] and Mukhopadhyay [140, 141] prepared spinel coating on graphite by using magnesium nitrate (Mg(NO₃)₂·6H₂O) and aluminium nitrate (Al(NO₃)₃·9H₂O). Following a complicated process (Fig. 2.20), crystalline spinel was completely converted at 900 °C from an amorphous intermediate phase which was formed at 450 °C. With spinel coating on graphite surface, the zeta potential was increased but not significantly (Fig. 2.21a), showing a certain improvement in wettability. However, the water demand for casting spinel coated graphite containing castable was at 8.5%, lower than 11.0% for uncoated graphite containing counterpart.[140] The reduction in water addition resulted in much lowered apparent porosity and higher bulk density at elevated temperature (Fig. 2.21b). It shows the importance of wettability of carbon materials on the physical and mechanical properties of castables.

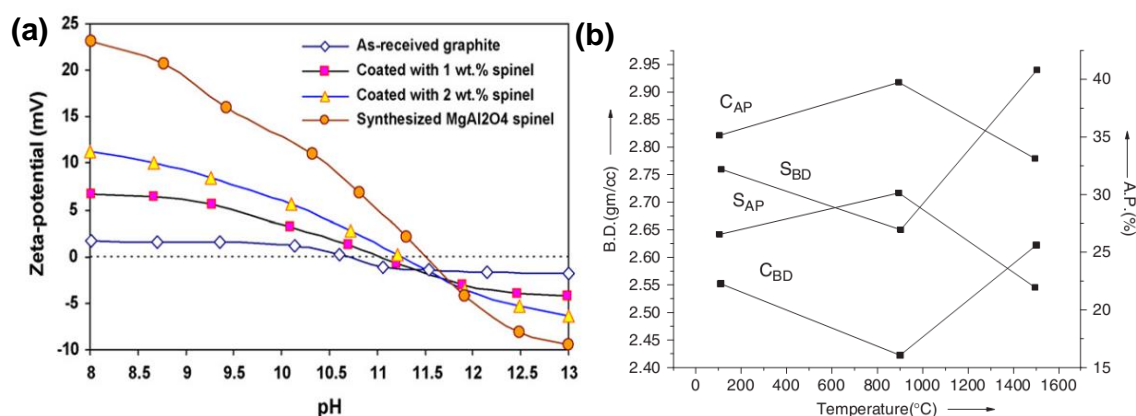


Fig. 2.21 (a) Zeta potential of uncoated graphite, spinel coated graphite and spinel powder as a function of pH,[23] (b) Comparison of bulk density and apparent porosity of castables containing uncoated graphite and spinel graphite after firing at 110, 900, 1500 °C, respectively.[140]

To further reduce water demand and enhance the compatibility of the castable matrix with binding materials, calcium aluminate (CaAl_2O_4) was prepared on graphite via a sol-gel process.[142] CaAl_2O_4 coatings were originated from aluminum-sec-butoxide and hydrated calcium nitrate and formed after calcination at above 900 °C. With more functional groups such as $-\text{OH}$, hydrophilicity of graphite was significantly improved. The water addition in castable placement was reduced to 7.5% from original 10.8%. In addition, improvement in oxidation resistance of carbon was also remarkable. For example, only 10% weight loss was found for coated graphite after firing in air to 1000 °C, compared with nearly 100% weight loss for uncoated graphite in the same condition.

Overall, the aqueous wettability and dispersivity of graphite is improved to various extents by the oxide coatings discussed above. Sol-gel coating technique allows the coating preparation to be carried out at low temperature for a short time. However, the main drawback is that it is difficult to prepare thick coatings so as to further improve carbon's wettability and oxidation resistance. Secondly, oxide coatings readily crack after hydrolysis, condensation and drying of their alkoxide precursors. In addition, the high cost of raw materials makes this method uncompetitive for the mass production and not affordable for the refractory industry.

2.3.4.3 Carbide coating

Due to good water affinity of carbide materials, SiC coatings were also attempted on graphite flakes to improve their wettability and dispersion property. With development of (Chemical Vapour Deposition) CVD technique, SiC coatings could

be prepared on various carbon substrates including bulk C/C composite [143] and carbon fibres [144] from gaseous mixture of H_2 and methyltrichlorosilane (CH_3SiCl_3). However, it is difficult to homogeneously coat carbon powders (e.g. graphite flakes and carbon black nanoparticles) with SiC by this method. The high cost of this technique will limit its application and development in the refractory industry. To prepare SiC coatings at low cost, Ono and co-authors [110, 145] proposed a high speed impact treatment. In their research, graphite and SiC powders were mixed in a container with assistance of high speed gas. The high speed spinning activated the graphite surface and enabled SiC to be absorbed on the graphite surface. The wettability of resultant hybrid SiC/C powders were examined by zeta potential which showed a higher zeta potential value than that of as-received graphite. Unfortunately, the resultant coating was not continuous, and SiC particles were only physically and loosely absorbed on the graphite and would easily peel off on prolonged mixing.

Recently, molten salt synthesis technique has been developed by Zhang's group to prepare *in-situ* carbide coatings on various carbon templates. In addition to successful fabrication of TiC [146] and SiC [147] coating on carbon fibre, template growth of carbide materials could be realised on carbon nanotubes [148, 149]. Inspired by this, the preparation of carbide coatings can be extended to carbon particles to improve their wettability and oxidation resistance.

2.4 Molten salt synthesis (MSS)

2.4.1 Principle of MSS

MSS was initially used in preparing ceramic powders, in particular complex oxide powders. A low melting water-soluble salt (or a salt assembly) is used to form a reaction medium to accelerate the synthesis from constituent materials (e.g. single oxides and carbonates).[150] Similarly to wet chemical reactions in aqueous solution or organic solvent assisted reactions, the salt-solution medium facilitates the dissolution of the reactants; thus enabling the achievement of a more homogeneous mixing in the liquid medium. In addition, mobility of reactant species in molten salt is remarkably increased, for example, the mobility of oxide species is >10 orders of magnitude faster in molten salt than in the solid state [151]. Therefore, compared with conventional high temperature solid-solid reaction, reaction in molten salt can be completed at relatively low temperature and in a short time. In addition, MSS has many other advantages as summarized by Zhang [152], including:

- 1) In principle any kinds of precursor can be used as starting materials, including cheap natural raw materials.
- 2) The resulting powders are homogeneous and in high purity, and have high surface reactivity.
- 3) Particle shapes (spheroidal, platelet-shaped or lath/needle-shaped) and sizes (nano-scale to micro-scale) can be tailored.
- 4) The process is easy to perform and economical.

To take full advantages of MSS, a salt or salt assembly needs to be carefully chosen to meet the following: 1) does not react with reactants and resulting products; 2) have low melting temperature and low viscosity at reaction temperature so as to facilitate the diffusion of species; 3) the reactants should have high enough solubilities in the selected salt; 4) have high solubility in water so as to be readily removed from resultant powders.

A typical MSS process is shown in Fig. 2.22, including raw materials mixing with salts, firing at target temperature, washing and separating from salt, and drying finally.

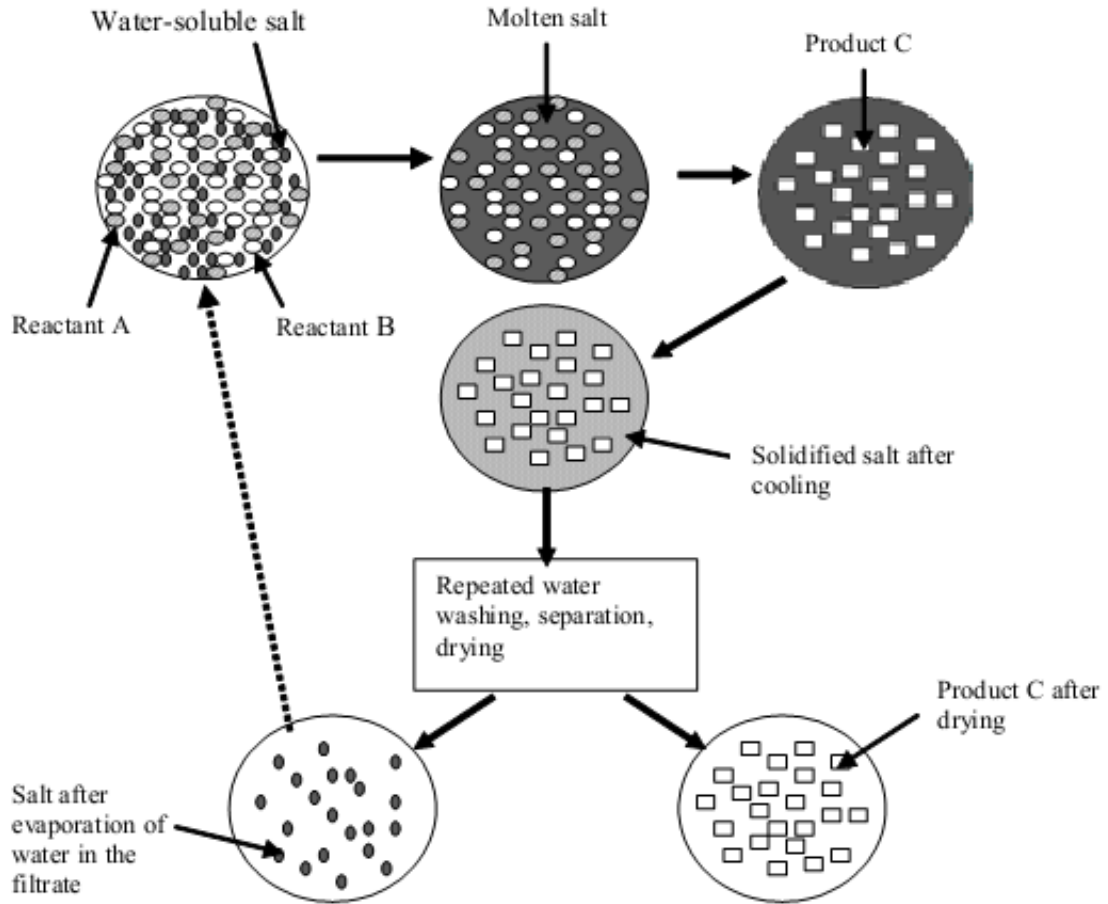


Fig. 2.22 Flow chart of preparation procedure of molten salt synthesis.[152]

2.4.2 Mechanism of MSS

Two reaction mechanisms, “dissolution-precipitation” and “dissolution-diffusion” (or “template –growth”), are involved in MSS.[150, 152] The difference of these two mechanism results in different particle size and shape (Fig. 2.23). The relative dissolution rate (solubility) of reactants determines the dominant formation mechanism.

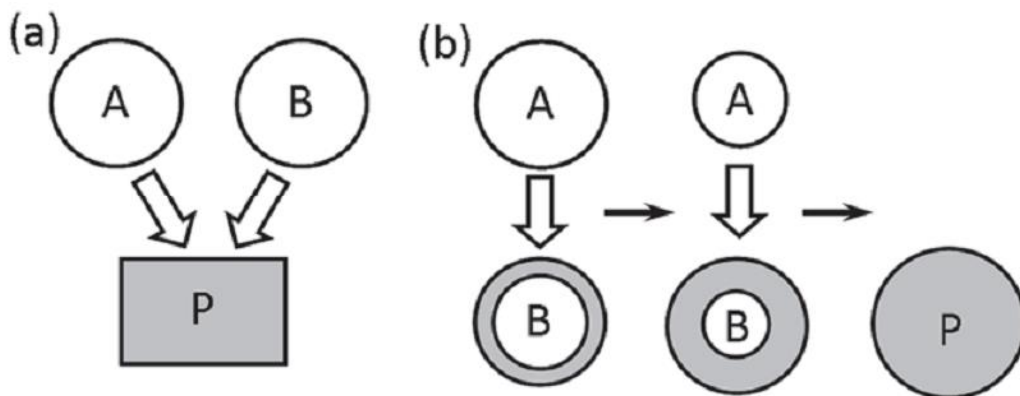


Fig. 2.23 Schematic diagram of mechanisms of particle formation in molten salt, (a) dissolution-precipitation and (b) dissolution-diffusion.[150]

When the dissolution rate of the two reactants in molten salt, A and B (Fig. 2.23a), are comparable, the MSS process will be dominated by the “dissolution-precipitation” mechanism. As a result, the resultant powder, P, precipitates from the salt oversaturated with the two reactants. In this case, the reaction rate is fast and synthesis temperature is relatively low, due to dissolution of both of reactants in molten salt. In addition, the morphology and size of products are usually different from the reactants. A typical example is the MSS of LaAlO_3 in the KCl-KF eutectic salt in which both La_2O_3 and Al_2O_3 are soluble. The synthesis temperature was reduced to as low as $630\text{ }^\circ\text{C}$, $\sim 1000\text{ }^\circ\text{C}$ lower than by conventional synthesis methods. As shown in Fig. 2.24, unlike spheroidal La_2O_3 and Al_2O_3 powders, rhombohedral LaAlO_3 were synthesized.[153]

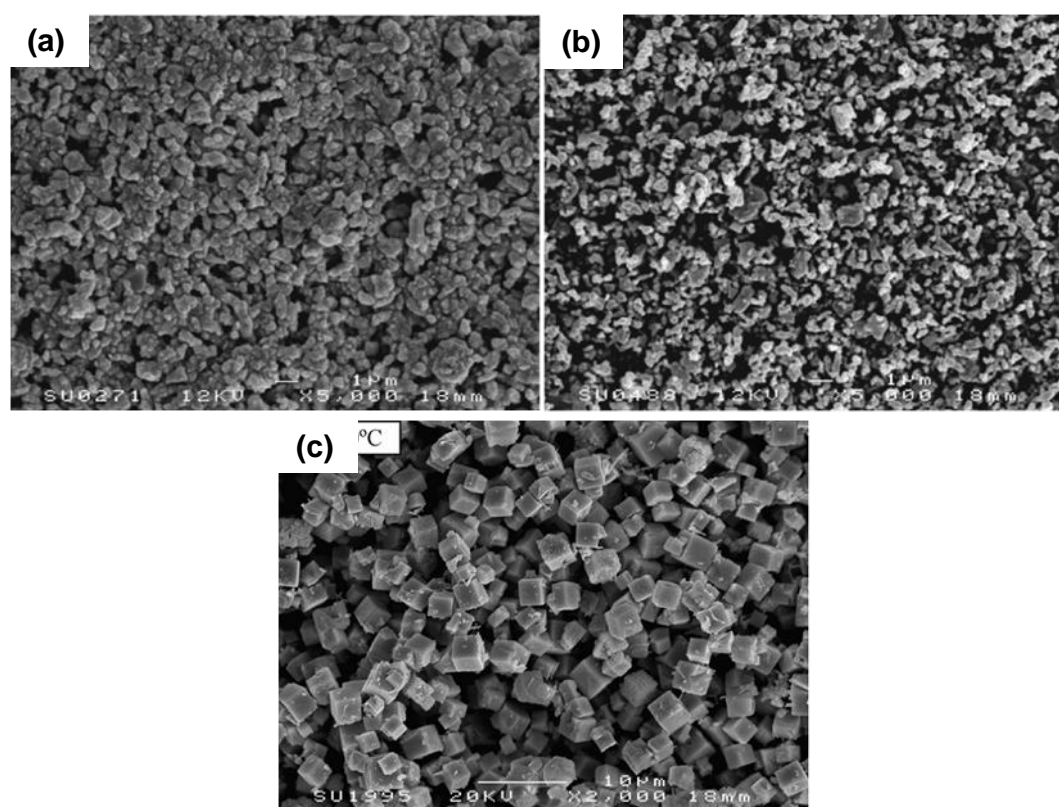


Fig. 2.24 SEM images of (a) La_2O_3 , and (b) Al_2O_3 , (c) LaAlO_3 prepared in KF-KCl eutectic salt at $630\text{ }^\circ\text{C}$ [153]

However, the reaction dominated by “dissolution-diffusion” requires much higher temperature and the reaction rate is slower compared with that of “dissolution-precipitation”. As the dissolution rate of reactant A (Fig. 2.23b) is considerably higher than that of B in molten salt, the product P will form on the surface of B by diffusion of A through molten salt. The initial formation of product P is fast but becomes slower with the build-up of a product layer on the less-soluble

reactant. This is because A and B species have to diffuse through the barrier layer to continue the reaction. Following this manner of reaction, the shape of product P is almost the same as the less-soluble particle B. So “dissolution-diffusion” mechanism is also called “template-growth”. For example, MgAl_2O_4 (MA) microplatelets were prepared from $\alpha\text{-Al}_2\text{O}_3$ platelets with MgO or $\text{Mg}(\text{NO}_3)_2$ powders in KCl.[154] MgO powder had much high solubility than $\alpha\text{-Al}_2\text{O}_3$, so the formation of MA initiated at the surface of $\alpha\text{-Al}_2\text{O}_3$ platelets and consequently MA retained the morphology and size of Al_2O_3 (Fig. 2.25).

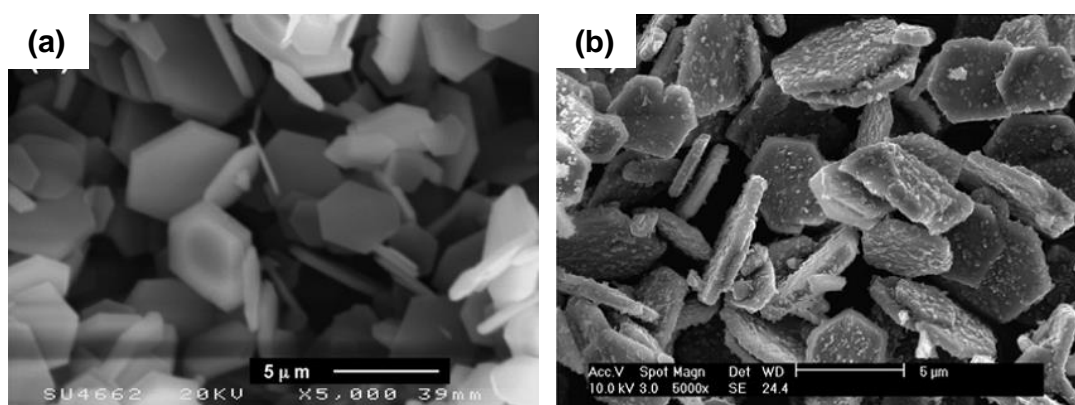


Fig. 2.25 SEM images of (a) Al_2O_3 , and (b) MgAl_2O_4 prepared from Al_2O_3 and MgO in KCl at 1150°C . [154]

2.4.3 Carbide synthesis via MSS

2.4.3.1 TiC and SiC synthesis

Based on “template-growth” mechanism, carbide materials (e.g. TiC and SiC) can also be prepared on various carbon templates.[26, 146-149] Since Ti and Si are more soluble in molten salt than carbon, the resulting carbides retain the morphologies and sizes of carbon templates. Although the exact solubility of Ti/Si is not clear, the size and microstructure changes of Ti and Si after interaction with molten salt (as reported by Liu [155] and Xie [156]) indicate that Ti and Si did dissociate into mobile cations and delocalized electrons, a state intermediate between ionic and metallic.[157] However, carbon templates from micron-sized carbon fibre to nano-sized carbon nanotube are both physical and chemical stable in molten salt at reaction temperatures. Thus, dissolved Ti and Si species rapidly diffuses onto the surface of carbon and consequently the reaction begins and continues until they are completely consumed. So the obtained carbides retain the size and morphology of carbon substrates. In addition, the synthesis temperature for carbide formation is significantly reduced. For example, compared with commercial

preparation of TiC and SiC by carbothermal reduction of TiO₂ and SiO₂ with carbon at relatively high temperatures, 1700-2100 °C for TiC [158] and 1400-1600 °C for SiC [159], the synthesis temperature for TiC and SiC by MSS was remarkably reduced to 850-950 °C for TiC [26, 146] and 1100-1200 °C for SiC [147, 160]. The advantage of lower synthesis temperature indicates that MSS of TiC and SiC will be commercialized in the future.

Following “template growth” mechanism, carbide materials were prepared from metallic Ti and Si with various templates, such as carbon nanotubes (CNT), natural cotton fibres (NCF), carbon fibre (CF), and graphite flakes (GF) (Fig. 2.26). For example, TiC nanofibres were synthesized from multi-walled CNTs at 950-960 °C in LiCl-KCl-KF ternary salt.[148] The resultant TiC nanofibres (Fig. 2.26a) appeared curved and entangled, similar to their CNT templates. The diameters of these fibres were about 40-90 nm, slightly larger than their CNT precursors. In addition, Xie and Zhang [149] prepared SiC nanorods (Fig. 2.26b) from multi-walled carbon nanotubes (CNTs) and Si particles in NaCl-NaF binary salt at 1200 °C, which was 200-250 °C lower than that required by conventional vapour-solid formation of SiC nanorods. They completely followed the morphologies of unreacted CNTs. Similarly, TiC and SiC fibres were prepared from a natural cotton derived carbon template using the same synthesis conditions (Fig. 2.26 c, d), indicating it is possible to prepare carbides with various size, shape and morphology from natural carbon precursors at low cost.[156, 161]

In addition to complete conversion of carbon substrates to carbide, carbide coatings (Fig. 2.26 e, f) could also be realised. Li [146] mixed titanium powders and carbon fibre at weight ratio of 1/1.5 and fired in the molten salt of KCl-LiCl-KF at 900-950 °C for 5h. After reaction, the carbon fibre was coated with TiC coating with thickness of ~800 nm. Xie [147] prepared SiC coatings on carbon fibre in NaCl-NaF. By changing Si/C weight ratios (1/5 and 1/10), both “thick” (300 –350 nm) coatings and “thin” coatings were obtained. Using MSS process, Liu [26, 27] also prepared TiC coatings on carbon particles (graphite flakes) in KCl (or KCl-LiCl, or KCl-LiCl-KF) at 950 °C. The coating quality was examined by high magnification SEM and AFM, revealing the resultant TiC coatings consisted of nanoparticles on graphite were uniform, continuous and crack-free. Liu’s work [155] also tried to coat graphite flakes with SiC coatings, however, SiC coatings consisted of loosely connected nanorods and they did not fully cover each graphite flake.

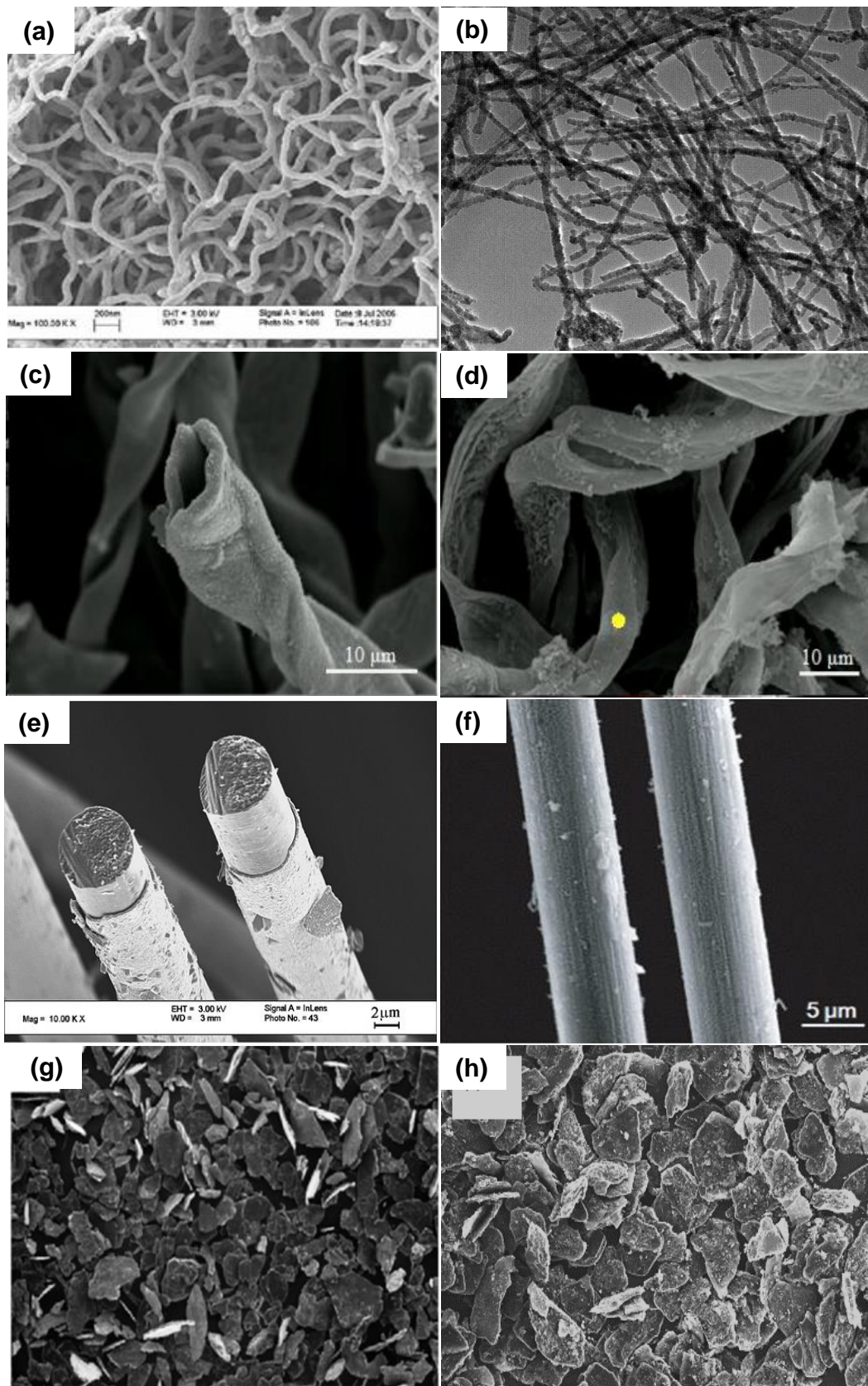


Fig. 2.26 (a)TiC nanofibres [148], (b) SiC nanorods [149], (c) TiC fibres from natural cotton [156], (d) SiC fibres from natural cotton [156], (e) TiC-coated carbon fibre [146], (f) SiC-coated carbon fibre [147], (g) TiC-coated graphite flakes [26], (h) SiC-coated graphite flakes.[155]

2.4.3.2 TiC or SiC coated carbons for refractory castable applications

TiC and SiC are considered to be important high-temperature structural materials, due to their superior physical and chemical properties, high melting point, high thermal conductivity, high hardness and Young's modulus, and high chemical stability.[162, 163] As for their refractory applications, TiC (or TiCN) powders were added into MgO-C bricks [164] and Al₂O₃ based castables [165], and it has been proven that they were beneficial to mechanical properties, oxidation and slag resistance of refractory composites. SiC were used in carbon-containing refractories as antioxidants to prevent carbon from oxidation at early stage [102] and also used in Al₂O₃-SiC-C bricks/castables as an aggregate to provide them with high thermal shock resistance.[166] On the other hand, since coating carbon with carbide materials is an effective way to improve wettability and dispersion properties of carbon materials (as introduced in Section 2.3.4.3), TiC and SiC are ideal candidates of the coating materials for surface modifications of carbon particles (e.g. graphite flakes and carbon black nanoparticles).

The investigation on wettability, dispersion property and flowability of uncoated, and TiC or SiC coated graphite flakes prepared by MSS showed that the improvement after coating had been achieved.[155] The contact angle for uncoated graphite was ~101°, in contrast, it was reduced to <60° for both TiC and SiC coated graphite. In addition, as shown in Fig. 2.27a, zeta potential values of graphite after coating with TiC and SiC were significantly increased, indicating better dispersion of graphite in aqueous solution was obtained. The decrease in apparent viscosity (Fig. 2.27b) of graphite after coating (one order of magnitude) implies better flowability of castables could be achieved when coated graphite was used. The preliminary results indicate TiC and SiC coated carbon particles prepared by using a MSS technique for castable refractory applications are promising, however, the actual use of them in castable systems has not yet been reported. So application studies on this aspect will be conducted in this work.

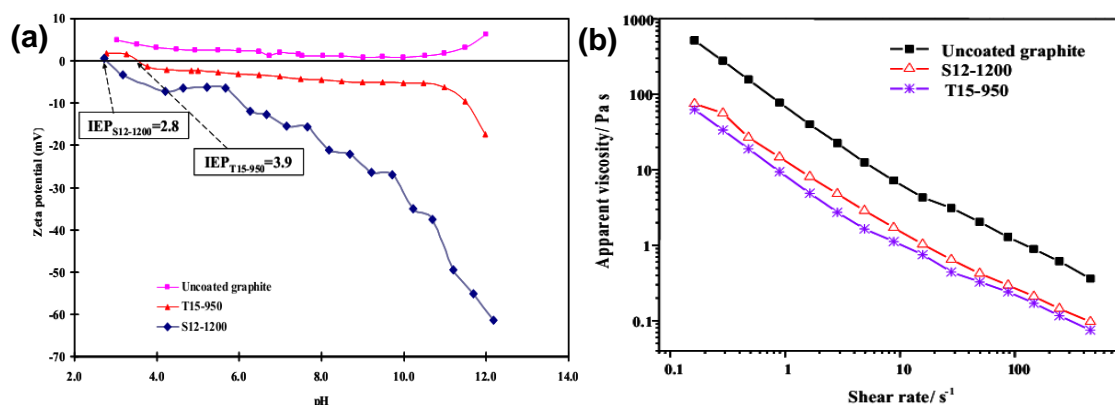


Fig. 2.27 (a) Zeta potential and (b) apparent viscosity of suspensions (slurries) containing uncoated, TiC coated (T15-950) or SiC coated (S12-1200) graphite flakes.[155]

In addition to natural graphite flakes, the use of amorphous nano carbon black has been of increasing interest to researchers [44, 167, 168] as much lower levels of carbon content and lower water addition were pursued. The reasons for this trend is as discussed below.

- 1) To reduce carbon content in carbon-containing refractories (CCRs). As high level of carbon in CCRs (>25% carbon in commercial CCRs) causes several serious problems, such as great heat loss, contamination in clean steel making and emission of green house gases, lower carbon additions are needed. In this case, nano-scale carbon with high specific surface area is required. The research conducted by Bag [44] shows that MgO-C refractories containing a combination of 0.9 wt% nano carbon black and 3 wt% graphite flakes exhibited better performance (low porosity, high mechanical strength and high thermal shock resistance) than that containing 10 wt% graphite. In Ochiai's experiments [168], 1.5% nano carbon containing MgO-C refractories showed thermal spalling resistance equivalent to that of conventional refractories containing 18% graphite.
- 2) To further reduce water additions for castable making. With characteristics of nano-scale size and spherical shape, carbon black shows better water-wettability and flowability than graphite. As shown in Fig. 2.28, to achieve the same flow value, carbon black (before surface coating) containing MgO-C castables required lower water addition compared with graphite and coke.[42]

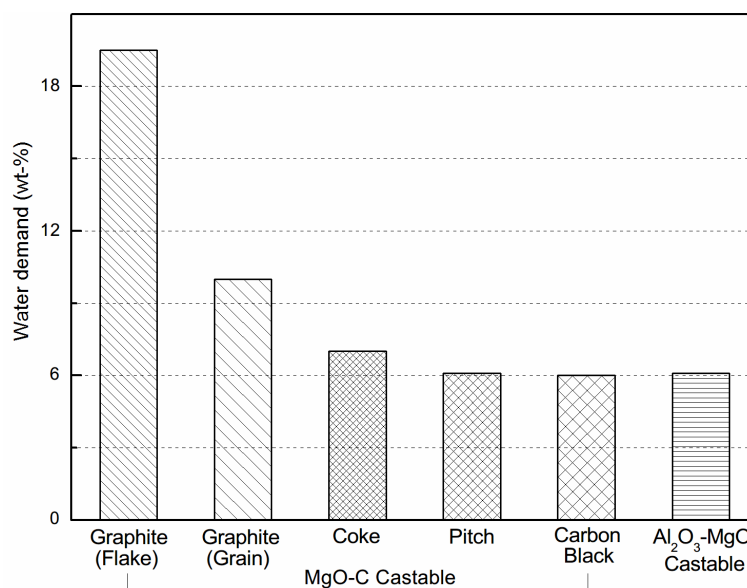


Fig. 2.28 Water demand of MgO-C castable using various forms of carbon.[42]

2.5 Motivation and objectives of present work

In summary, the development and commercialization of high performance carbon-containing refractory castables have been hindered in the past two decades mainly by carbon's poor water-wettability and dispersivity. Although considerable research work were carried out worldwide, the success achieved on this aspect was limited. However, the recent development of molten salt synthesis indicates carbide coatings can be prepared on carbon particles to improve their water-wettability and dispersive properties. As a result, the water demand for preparing carbon-containing castables will be reduced and refractory properties of castables improved correspondingly.

The objectives of present project are: 1) to prepare high quality TiC and SiC coatings on carbon black particles (from sub-micron to nano scale) under optimal conditions by using the MSS technique; 2) to improve water-wettability, dispersivity and oxidation resistance of carbon particles by carbide coating on them; 3) to reduce water addition and improve flowability, physical/mechanical properties and oxidation resistance of castables by incorporating carbide-coated carbon particles.

Chapter 3 Experimental details

3.1 Raw materials

3.1.1 Raw materials for carbide coating synthesis

TiC and SiC coatings were prepared from metallic Ti or Si powders on carbon black (CB) spheres, and on graphite flakes (GF) as well for comparison. Chloride and fluoride salts were used to form reaction media at test temperatures. Particle size, purity and physical properties of all raw materials are listed in Table 3.1 and the salts are given in Table 3.2.

Table 3.1 Raw materials for molten salt synthesis of TiC and SiC coatings

| Materials | Particle size | Purity (wt %) | Density (g/cm ³) | Provided by |
|-----------------|-------------------------|---------------|------------------------------|------------------------------|
| GF | ~149 μm | 94% | 2.23 | Vesuvius, UK |
| CB * (N990/991) | ~280 nm (100-700 nm) | 99.9% | 1.8-1.9 | Cancarb Ltd, Canada |
| CB (N660) | ~62 nm on average | >99.2% | 1.7-1.9 | Makrochem, Poland |
| CB (N330) | ~30 nm on average | >99% | 1.7-1.9 | Socachim fine chemicals, USA |
| Micron-Si | ~44 μm | 99% | 2.33 | |
| Nano-Si | < 100 nm | >98% | 0.08 | Sigma-Aldrich |
| Ti | ~149 μm | 99.7% | 4.50 | |

*Trade name of CB N990/N991 is Thermax® medium thermal carbon black

Table 3.2 Chloride and fluoride salts for molten salt synthesis of TiC and SiC coatings

| Salts | Purity (wt %) | Density (g/cm ³) | Melting point (°C) | Boiling point (°C) | Provided by |
|-------|---------------|------------------------------|--------------------|--------------------|---------------|
| KCl | >99% | 1.98 | 790 | 1420 | Sigma-Aldrich |
| LiCl | 99% | 2.07 | 605 | 1382 | |
| NaCl | >99% | 2.17 | 801 | 1413 | |
| NaF | >99% | 2.56 | 993 | 1695 | |

3.1.2 Raw materials for castable preparation

3.1.2.1 Castable matrix

1) Al₂O₃

Two types of alumina were used for the preparation of model castables. Tabular alumina (T-64) provided by Almatis with different size fractions from 3 mm to smaller than 0.02 mm were used as the aggregates. Reactive and calcined aluminas, CT3000SG and Nabalox 315 (<5 μm), were also added as ultrafines to improve packing efficiency of the aggregates. Their detailed information are given in Table 3.3 and described below.

Table 3.3 Chemical composition and physical properties of alumina materials.[169-171]

| | Tabular Al ₂ O ₃ | Reactive Al ₂ O ₃ | Calcined Al ₂ O ₃ | |
|---------------------------------------|--|---|---|------|
| | T64 | CT3000SG | Nabalox 315 | |
| Chemical composition | Al ₂ O ₃ | 99.5 | 99.7 | 99.6 |
| | Na ₂ O | ≤ 0.40 | 0.08 | 0.3 |
| | SiO ₂ | ≤ 0.09 | 0.03 | 0.03 |
| | Fe ₂ O ₃ | ≤ 0.02 | 0.02 | 0.03 |
| | CaO | — | 0.03 | — |
| | MgO | — | 0.07 | — |
| Specific surface (BET) | — | 7.5 m ² /g | 1.5 m ² /g | |
| Particle size (d ₅₀) | ≤ 3mm, wide range | 0.5 μm | 4 μm | |
| Specific density (g/cm ³) | ≥ 3.50 | 3.90 | 3.90 | |
| Supplier company | Almatis | | Nabaltec | |

Tabular alumina T64 is a pure sintered α -alumina material that has been converted to corundum form from aluminium oxide by rapid-sintering in excess of 1800 °C just below the fusion point of Al₂O₃ (2035 °C). The nomination of ‘tabular’ is because of its well developed hexagonal tablet shaped crystals of 40 to 200 μm diameter. Due to overall low open porosity and large crystals with closed pores entrapped during rapid sintering, tabular alumina possesses excellent thermal volume stability and thermal shock resistance. In combination with its high refractoriness, high mechanical strength and abrasion resistance, Tabular alumina is commonly used as an aggregate in unshaped and shaped refractory composites.[169] Reactive alumina (γ -Al₂O₃) is produced by calcining aluminium trihydroxide obtained by the Bayer process at 140-150 °C. Its excellent sintering reactivity and highly controlled particle size distribution enables monolithic refractories to have better particle packing, reduced water demand and increased mechanical strength by forming strong ceramic bonds. Calcined alumina in the alpha phase obtained after calcination of aluminium hydroxide at 1200 °C is used for enhancing castables’

refractoriness, mechanical strength and abrasion resistance.[171]

2) Microsilica

Microsilica, also called fumed silica, is amorphous silicon dioxide consisting of 0.1-0.3 μm diameter spherical particles. It is commonly used in low or ultra-low cement castables and gel-bonded castable systems. Microsilica has no internal porosity, and has a specific gravity of about 2.3 g/cm^3 . Its specific surface area may vary between 15 and 30 m^2/g . [67] Elkem Microsilica with chemical compositions shown in Table 3.4 was used in this work.

Table 3.4 Chemical composition of microsilica 971U.[172]

| Oxide/Element | SiO ₂ | C | Fe ₂ O ₃ | Al ₂ O ₃ | CaO | MgO |
|---------------|------------------|-------------------|--------------------------------|--------------------------------|------|--------------------|
| Weight % * | 98.4 | 0.50 | 0.01 | 0.20 | 0.20 | 0.10 |
| Oxide/Element | K ₂ O | Na ₂ O | P ₂ O ₅ | SO ₃ | Cl | H ₂ O** |
| Weight % | 0.20 | 0.15 | 0.03 | 0.10 | 0.01 | 0.20 |

**Typical content; ** when packed*

3) Calcium aluminate cement

SECAR®71, one type of calcium aluminate cements (CAC) supplied by Kerneos, was employed as the main binder for castable preparation. It is a hydraulic binder containing approximately 70% alumina and 30% lime (Table 3.5). It possesses the general properties of high refractoriness and can help achieve exceptional flow and high early compressive strength via interacting with most organic and mineral additives. In addition, it is very compatible in all types of deflocculated castable systems.[173, 174] Thus, it has been used extensively in alumina based castables. As shown in Table 3.6, the main phases in CAC are CA and CA₂.

Table 3.5 Chemical composition of calcium aluminate cement SECAR®71.[173, 174]

| Chemical composition | Content (wt%) |
|------------------------------------|---------------|
| Al ₂ O ₃ | 68.7-70.5 |
| CaO | 28.5-30.5 |
| SiO ₂ | 0.2-0.6 |
| Fe ₂ O ₃ | 0.1-0.3 |
| TiO ₂ | <0.4 |
| MgO | <0.5 |
| Na ₂ O+K ₂ O | <0.5 |
| SO ₃ | <0.3 |

Table 3.6 Typical physical properties and mineralogical composition of calcium aluminate cement SECAR®71.[173, 174]

| Physical properties | |
|-----------------------------------|--------------------------------------|
| Bulk density (g/cm ³) | 1.04-1.23 |
| Specific gravity | 2.90-3.05 |
| Specific surface area* | 3800-4400 |
| Laser PSD – d ₅₀ (μm) | 12 |
| Laser PSD – d ₉₀ (μm) | 50 |
| Mineralogical composition | |
| Principal phases | CA, CA ₂ |
| Secondary phases | C ₁₂ A ₇ , α-A |

*Blaine specific surface area (cm²/g) –EN 196-6

3.1.2.2 Additives

1) Carbon materials

Two types of carbon materials, CB and GF, were used for preparing

carbon-containing castables. To investigate the effect of carbide coating, both uncoated and coated CBs or GFs were incorporated into castables, respectively.

Natural GFs usually contain some impurities. As-received graphite flakes were oxidized in air at 1000 °C for 45 minutes for phase analysis. XRD of the ash (6 wt% as indicated by supplier) was illustrated in Fig. 3.1, showing the impurities comprise SiO_2 , Fe_2O_3 and Al_2O_3 .

CB is also called medium thermal carbon black. CB used by this work was supplied by Cancarb Ltd, which is specially produced for refractory applications because of its high purity (low ash (0.1 wt%), low sulphur content (150 ppm) and low surface area ($9.5 \text{ m}^2/\text{g}$)). It has wide particle size distribution, 100-700 nm, but the average size is $\sim 280 \text{ nm}$. [175]

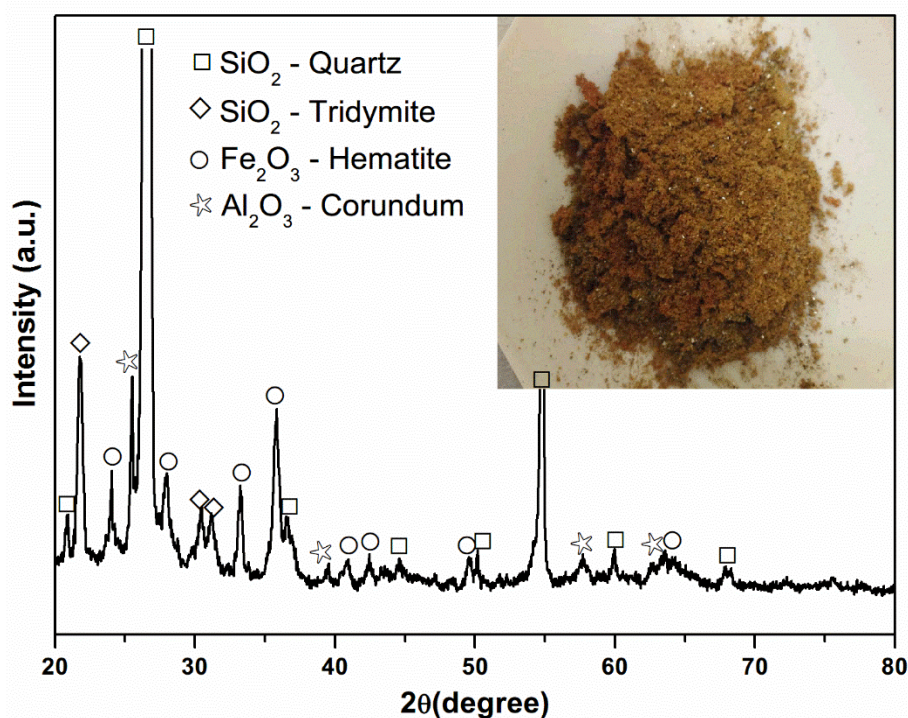


Fig. 3.1 XRD pattern of the residual powders after oxidation of as-received GFs at 1000 °C for 45 minutes in air. The insert are the impurities obtained after combustion of GFs.

2) Carbon dispersant

To compare the effects of commercial carbon dispersant and water-wettable carbide coatings on water demand and flowability of carbon-containing castables, a sodium sulfonate-based carbon dispersant was used.

3) Deflocculant

Sodium triphosphate (STPP), $\text{Na}_5\text{P}_3\text{O}_{10}$, was used as a deflocculant to enhance the

flowability of castables. The function of STPP is similar to that of sodium hexametaphosphate (SHMP) for castable applications. Being a highly charged chelating agent, TPP^{5-} anions bind with dications such as Ca^{2+} and Mg^{2+} preventing of coagulation or flocculation of particles as described in Section 2.2.5.1.

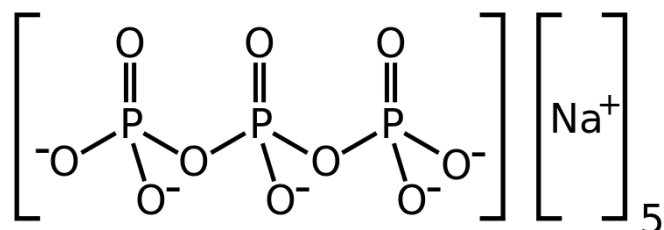


Fig. 3.2 Molecular structure of STPP.

3.2 Experimental procedure

3.2.1 Carbide coating synthesis

The typical sample preparation process for preparation of carbide coatings on CB was demonstrated in Fig. 3.3 and described below.

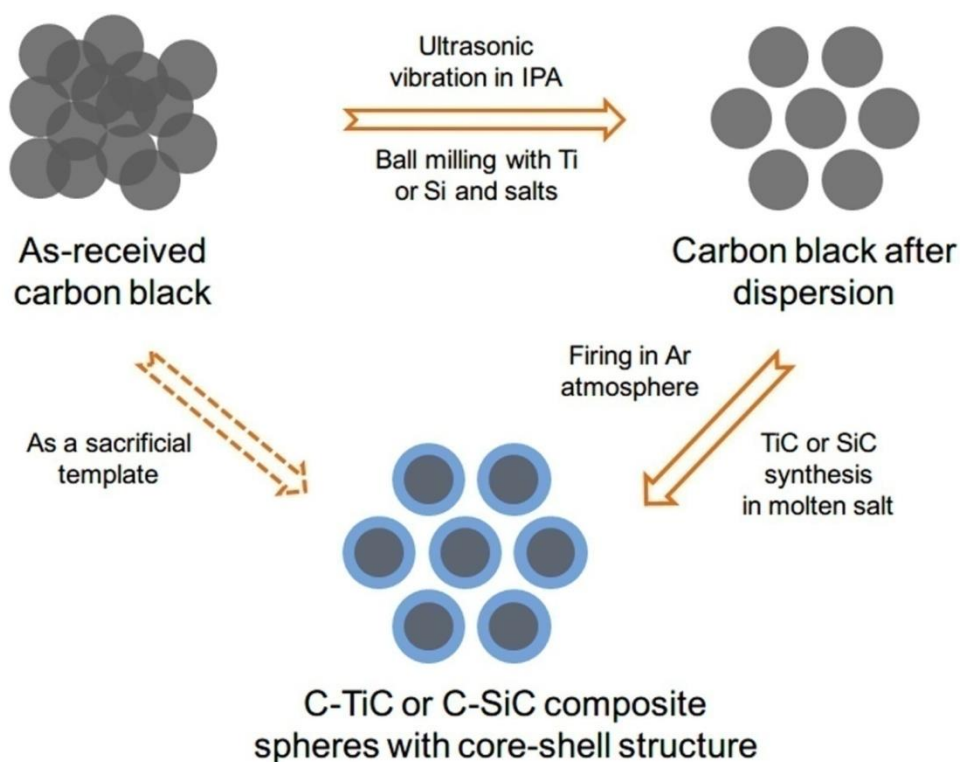


Fig. 3.3 A flow chart of experimental procedure for preparing carbide coating on carbon black spheres.

1) Mixing

The carbide coating synthesis started with dry mixing of starting materials with solid salts using a ball milling at low speed or by mixing and grinding in an agate mortar. The dosage of chloride salts was 10-20 times higher than reactants by weight. As for submicron-sized CB particles, they were ultrasonically dispersed in isopropyl alcohol (IPA) for 2 hours. IPA was later removed by evaporation in an oven.

2) Firing

The powder mixture of raw materials was placed in an Al_2O_3 or graphite crucible with a lid and fired in a tube furnace under Ar protection at high temperature. The required synthesis temperature varied depending on starting materials, 750-950 °C for TiC synthesis and 1100-1200 °C for SiC formation. After cooling to room temperature, samples were collected from the tube furnace.

3) Washing

The solidified mass was washed with hot distilled water to remove any residual salts. This process was repeated several times until no Cl^- was detected in the filtrate by an AgNO_3 solution (i.e., no AgCl precipitation was observed when an AgNO_3 solution was added dropwise to the filtrate). The resulting coated CB powders were oven-dried over-night at 110 °C before further characterisation.

3.2.1.1 Preparation of TiC coatings

The processing parameters for TiC coating formation such as initial Ti/C ratio, salt composition and synthesis temperature are detailed in Table 3.7.

Table 3.7 Synthesis conditions for TiC coating formation on CB.

| Sample No. | Ti/C molar ratio | Salt assemble (wt%) | | Temperature (°C) |
|------------|------------------|---------------------|------|----------------------|
| | | KCl | LiCl | -Holding time (hour) |
| 1 | 1/8 | 100 | 0 | 950-4 |
| 2 | 1/8 | 100 | 0 | 850-4 |
| 3 | 1/8 | 55 | 45 | 850-4 |
| 4 | 1/8 | 55 | 45 | 750-4 |
| 5 | 1/8 | 55 | 45 | 650-4 |
| 6 | 1/4 | 100 | 0 | 850-4 |
| 7 | 1/2 | 100 | 0 | 850-4 |
| 8 | 1/8 | 0 | 0 | 850-4 |
| 9 | 1/8 | 100 | 0 | 850-4 |
| 10 | 1/8 | 100 | 0 | 850-4 |
| 11 | Only Ti | 100 | 0 | 850-4 |

Note: No. 1-8: TiC coating on CB N990/N991; No.9: TiC coating on CB N660; No. 10: TiC coating on CB N220.

In order to reduce the cost in the TiC coating formation on carbon black, Ti was completely or partially replaced with TiO₂. The corresponding synthesis conditions are listed in Table 3.8. The final molar ratio of Ti/C was determined as 1/8 (which is equivalent to the TiC coatings obtained from metallic Ti powders in initial Ti/C molar ratio of 1/8), assuming all initial titanium sources (TiO₂ or Ti+TiO₂) were converted to TiC after the reactions were completed.

Table 3.8 Synthesis conditions for TiC coating on CB from only TiO₂ or combination of Ti and TiO₂.

| (1) TiC coating using TiO ₂ as titanium source | | | |
|---|------------------------------------|------|--|
| Sample No. | TiO ₂ /C molar ratio | Salt | Temperature (°C) -Holding time (hour) |
| 1 | 1/10 | — | 950-4 |
| 2 | 1/10 | KCl | 950-4 |
| 3 | 1/10 | KCl | 1200-4 |
| 4 | 1/10 | KCl | 950-4-1200-4 |
| (2) TiC coating using TiO ₂ +Ti as titanium source | | | |
| Sample No. | Ti/TiO ₂ /C molar ratio | Salt | Temperature (°C) -Holding time (hour) |
| 5 | 1/2/28 | KCl | 950-4 |
| 6 | 1/1/18 | KCl | 950-4 |
| 7 | 2/1/26 | KCl | 950-4 |
| 8 | 3/1/34 | KCl | 950-4 |
| 9 | 1/2/28 | KCl | 1050-4 |
| 10 | 1/1/18 | KCl | 1050-4 |
| 11 | 2/1/26 | KCl | 1050-4 |

3.2.1.2 Preparation of SiC and SiC/SiO₂ composite coatings

NaCl-NaF binary salt instead of KCl or KCl-LiCl was used for SiC formation on CB. Synthesis parameters such as temperature, holding time, the mass ratio of two sodium salts, and particle size of Si powders were varied to optimize the SiC synthesis conditions. In addition, SiC coatings with different thicknesses on CB were prepared by changing the initial molar ratio of Si/C before firing. The detailed parameters are listed in Table 3.9. To assist in verifying the formation of SiC coating, as-prepared particles were also heated at 600 °C for 60 min in air to oxidize their carbon cores.

Table 3.9 Synthesis conditions for SiC coating formation on CB.

| Sample No. | Si/C molar ratio | Salt ratio (wt%) | | Temperature (°C) |
|------------|------------------|------------------|------|----------------------|
| | | NaCl | NaF | -Holding time (hour) |
| 1 | 1/8 | 80 | 20 | 1200-8 |
| 2 | 1/8 | 80 | 20 | 1200-8 |
| 3 | 1/12 | 80 | 20 | 1200-8 |
| 4 | 1/4 | 80 | 20 | 1200-8 |
| 5 | 1/2 | 80 | 20 | 1200-8 |
| 6 | 1/8 | 80 | 20 | 1100-6 |
| 7 | 1/8 | 80 | 20 | 1000-6 |
| 8 | 1/8 | 80 | 20 | 900-6 |
| 9 | 1/8 | 95 | 5 | 1100-6 |
| 10 | 1/8 | 97.5 | 2.5 | 1100-6 |
| 11 | 1/8 | 98.75 | 1.25 | 1100-6 |
| 12 | 1/8 | 100 | 0 | 1100-6 |
| 13 | 1/8 | 0 | 0 | 1100-6 |
| 14 | Only Si | 100 | 0 | 1100-6 |
| 15 | Only Si | 95 | 5 | 1100-6 |
| 16 | Only Si | 80 | 20 | 1100-6 |
| 17 | Only Si | 0 | 100 | 1100-6 |

Note: No.1: SiC coatings were prepared using nano-sized Si powders (<100 nm), and the rest of the samples were prepared using micro-sized Si powders (~44 μm).

To further enhance the water affinity of SiC-coated CB, pre-oxidation was carried out in order to form a thin layer of SiO₂ on the SiC surface. In this case, the oxidation conditions were critical, since severe oxidation would cause damage to SiC coatings and carbon burning off. So SiC-coated CB particles were exposed to air at different

temperatures for a certain time as shown in Table 3.10.

Table 3.10 Oxidation conditions for preparation of SiO₂/SiC composite coatings on CB.

| Sample No. | Oxidation temperature (°C) | Oxidation time (minutes) |
|------------|----------------------------|--------------------------|
| 1 | 400 | 30 |
| 2 | 450 | 30 |
| 3 | 500 | 30 |
| 4 | 400 | 90 |
| 5 | 450 | 90 |
| 6 | 500 | 90 |
| 7 | 450 | 60 |

3.2.1.3 Kg-scale production of carbide-coated CB and GF

For large scale trials of carbide-coated carbon materials in practical castable systems, a large vertical tube furnace with two sealable ends (Fig. 3.4) was used to prepare the materials. In this case, a graphite crucible was used. To avoid reaction between the graphite crucible and Ti or Si, the graphite crucible was pre-fired with a small amount of Si in NaCl-NaF at 1200 °C to create an interior SiC protective coating layer.



Fig. 3.4 The experimental set-up for molten salt preparation of kg-scale carbide-coated CB and GF particles.

To maximize the production of TiC or SiC coated CB and GF (TiC-CB, SiC-CB, TiC-GF, SiC-GF) and to save energy and labour, salt usage was reduced to just two times higher than the reactants by weight, as this barrel-shaped graphite crucible could enable all reactants to be immersed in smaller amounts of molten salt. About 100g samples were prepared for each run and more details are given in Table 3.11.

Table 3.11 Composition and synthesis conditions for preparation of kg-scale carbide-coated CBs and GFs.

| Raw materials (g) | TiC-GF | TiC-CB | SiC-GF | SiC-CB |
|----------------------|--------|--------|--------|--------|
| Molar ratio Ti(Si)/C | 1/8 | 1/8 | 1/8 | 1/8 |
| Ti | 33.3 | 33.3 | | |
| Si | | | 21.9 | 21.9 |
| GF | 66.7 | | 75.1 | |
| CB | | 66.7 | | 75.1 |
| KCl | 200 | 200 | | |
| NaCl | | | 156 | 156 |
| NaF | | | 29 | 29 |
| Temperature (°C) | 950 | 850 | 1200 | 1100 |
| Holding time (hour) | 4 | 4 | 8 | 6 |

3.2.2 Castable preparation

3.2.2.1 Composition of castables

A model carbon-containing castable was prepared by incorporating 5 wt% carbon into a commercial high alumina low cement castable as reported in Ref [176, 177]. Such a carbon-containing alumina castable ($\text{Al}_2\text{O}_3\text{-C}$) contained tabular Al_2O_3 (≤ 3 mm), along with reactive and calcined Al_2O_3 fines. About 4 wt% ultrafine microsilica particles were added to improve flowability and particle packing. Only 4 wt% Secar 71 calcium aluminate cement (CAC) was used as the binder. The detailed composition and notation for $\text{Al}_2\text{O}_3\text{-C}$ low cement castables are listed in Table 3.12.

Table 3.12 Composition and notation of Al₂O₃-C low cement castables.

| Notation | GF | TiC-GF | SiC-GF | CB | TiC-CB | SiC-CB | SiC-CB-8 |
|--|-----|--------|--------|-----|--------|--------|----------|
| T64 Al ₂ O ₃ | 76 | 76 | 76 | 76 | 76 | 76 | 76 |
| Reactive+Calcined Al ₂ O ₃ | 11 | 11 | 11 | 11 | 11 | 11 | 11 |
| Microsilica (Elkem 971) | 4 | 4 | 4 | 4 | 4 | 4 | 4 |
| CAC (Sear 71) | 4 | 4 | 4 | 4 | 4 | 4 | 4 |
| Carbon materials (wt%) | GF | TiC-GF | SiC-GF | CB | TiC-CB | SiC-CB | SiC-CB |
| | 5 | 5 | 5 | 5 | 5 | 5 | 8 |
| STPP (wt%) | 0.1 | 0.1 | 0.1 | 0.1 | 0.1 | 0.1 | 0.1 |

Before applying uncoated and coated carbon particles into the castable systems, particle size distribution (PSD) analysis was carried out to ensure high packing density could be achieved for specific Al₂O₃-C castable compositions. The objective is to get as dense refractory structure as possible, but suitable flow is also required for casting after wet mixing of raw materials. Since the added water left porosity upon its evaporation, its amount has to be carefully controlled. PSD analysis has proven to be an effective tool to help achieve a dense structure and minimize water addition as well.[178, 179] By adjusting the fractions of different particle sizes based on a reference castable model -Al₂O₃ low cement castable [176, 177], the optimal compositions for the Al₂O₃-C castables were obtained (Table 7.1).

Table 3.13 Compositions of Al₂O₃-C castables (wt%).

| Raw materials | Grain size | Content |
|------------------|----------------------------|--------------|
| Tabular Alumina | 1-3 mm | 28% |
| | 0.5-1 mm | 17% |
| | 0.2-0.6 mm | 13% |
| | 0-0.2 mm | 18% |
| Reactive Alumina | d ₅₀ =0.5 μm | 6% |
| Calcined Alumina | d ₅₀ =4.1 μm | 5% |
| Microsilica | d ₅₀ =0.15 μm | 4% |
| CAC | d ₅₀ = 12.05 μm | 4% |
| Carbon | Uncoated/Coated GF | ~149 μm |
| | Uncoated/Coated CB | ~ 100-700 nm |

PSD analysis was performed by using the well-known Andreassen's model which is a semi-empirical equation, but has advantage of only requiring different particles to have similar shapes.[179, 180]The Andreassen equation is expressed as

$$\text{CPFT} = (d/D)^q * 100 \quad (3.1)$$

where CPFT is cumulative percent finer than (in vol%), d refers to particle size and D the maximum particle size. In the case, q was set at 0.29 (relatively high q-value, close to 0.3) for vibratable castables, which is suitable for low cement high alumina castable system. PSD analysis was realized by numerical simulation based on the software EMMA developed by Elkem, so as to optimise and refine the refractory mix designs.[181]

After adjusting the amounts of particles with different sizes, the cumulative percentage (vol%) for GF containing alumina castable (Al₂O₃-GF) was determined (Fig. 3.5). It can be seen that experimental curve (blue line) almost matches with theoretical Andreassen curve (red line), indicating the particle size distribution of castable model shown in Table 3.13 is reasonable, and therefore it is able to achieve the highest packing efficiency for vibrate flow castables.

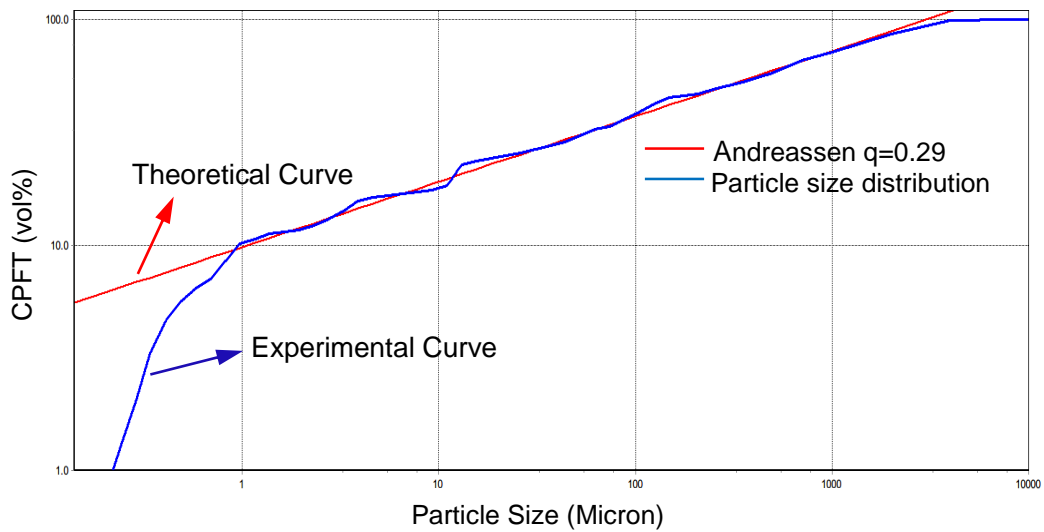


Fig. 3.5 Particle size distribution and q -value of Al_2O_3 -GF castable.

When micron-sized GF were replaced with submicron-sized CB particles, the experimental curve changed, as the percentage of particles less than 1 micron increased. It could still be considered to be reasonable particle size distribution, however, the flow pattern of castables changed, as the actual curve fits well with the theoretical curve at $q=0.22$ (Fig. 3.6). If relatively a low q -value is used (i.e. less than 0.25) then self-flow will be dominant. However, in this case, due to the poor water-wettability of CB, self-flow was not likely to occur and external vibration force had to be used to help casting.

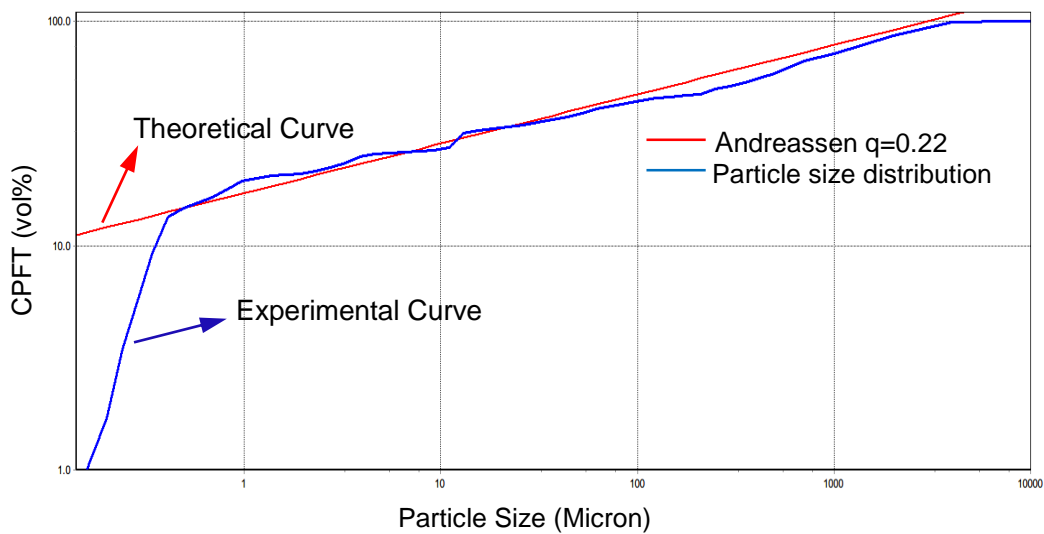


Fig. 3.6 Particle size distribution and q -value of Al_2O_3 -CB castable.

3.2.2.2 Castable specimens preparation

The specimen preparation went through three steps: mixing, casting and drying. All raw materials were dry mixed for 5 minutes and wet mixed for another 5 minutes after adding water in a Hobart mixer (Fig. 3.7a). Around 5.5 kg castables were made for sample casting for each formula. Before casting, the flow value of castable of each formula was measured and recorded. All these well-mixed and flowable castable materials were cast in moulds with assistance of a vibration table (Fig. 3.7b). Vibration with frequency of 66 Hz lasted (~5 minutes) until no gas bubbles were seen coming out of the castable. All these castable specimens were left in the moulds (Fig. 3.7c) for 24 hours at room temperature followed by demoulding and drying at 110 °C for another 24 hours in an oven.

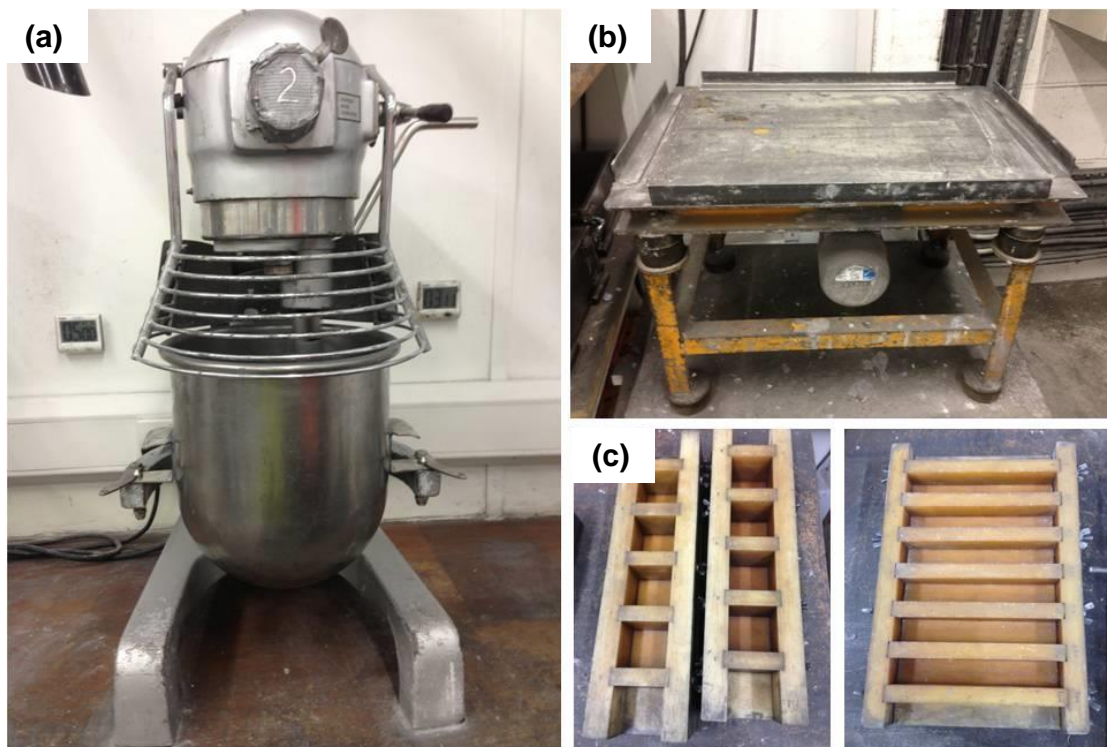


Fig. 3.7 Photos of (a) Hobart mixer, (b) vibration table and (c) moulds for casting specimens (bars and cubes).

Cubes (50×50×50 mm) were made for measurements of bulk density (BD), apparent porosity (AP), permanent linear (volume) change (PLC/PVC), crushing strength and oxidation resistance. Prism bars (25×25×150 mm) were made for evaluation of rupture failure under a load.

3.3 Characterisation and Testing

3.3.1 Phase identification and microstructural observation

3.3.1.1 X-ray Diffraction (XRD)

XRD is a non-destructive analytical technique which can yield the unique fingerprint of Bragg reflections associated with a crystal structure. It is widely used to identify crystalline phases and orientation, and to determine atomic arrangement, lattice parameters, residual stress and strain, and grain size.[182]

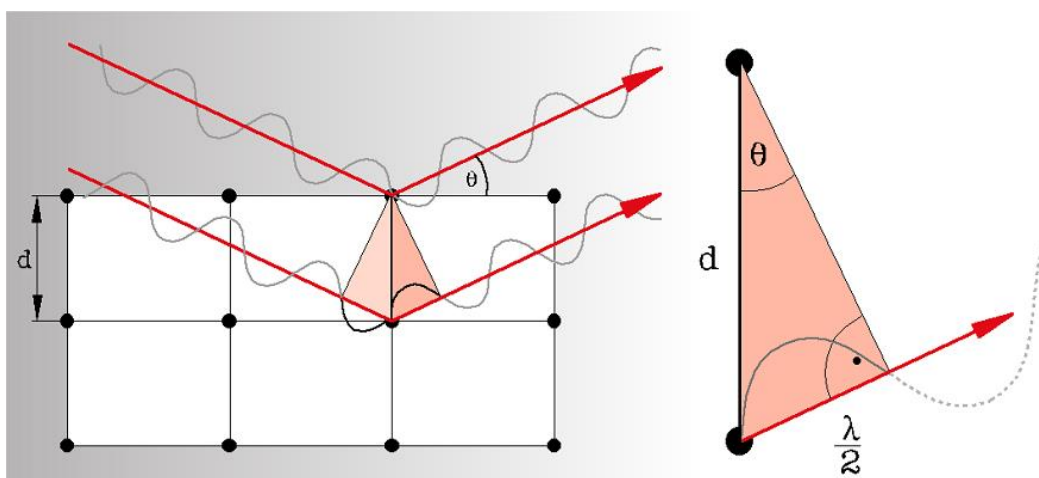


Fig. 3.8 A schematic diagram of interaction of X-rays with a crystal structure.

An X-ray tube is the most important component of X-ray diffractometer. In an X-ray tube, the electron beam from the cathode provided by a heated tungsten filament is accelerated towards an anode by a potential difference of $\sim 30\text{kV}$. When electrons strike the metal target (normally Cu or Co), X-rays are emitted. For most diffraction experiments, a monochromatic beam of X-rays is desirable. Crystals consist of planes of atoms that are spaced a distance, d , apart, but can be resolved into many atomic planes, each with a different d -spacing. X-rays with a wavelength (λ) similar to the distances between these planes can be reflected such that the angle of reflection is equal to the angle of incidence, θ , as shown in Fig. 3.8. When diffraction occurs, it must follow the Bragg's Law:

$$2d\sin\theta = n\lambda \quad (3.2)$$

The X-rays after 'Bragg reflection' will be picked up by a detector scanning at this angle. Thanks to Bragg's Law, the inter-layer spacings of atoms in the crystal structure can be identified by the positions of these reflections. The obtained X-ray diffraction pattern corresponds to a unique crystal structure. Thus, the crystal

phases can be identified. It is also possible to quantify each phase present in the sample. It has to be noted that for amorphous materials, there are no characteristic XRD peaks in the obtained patterns.

In this study, phases present in the samples obtained from different processing stages were identified by powder X-ray diffraction (XRD) analysis (Siemens D500 reflection diffractometer). ICDD cards used for identification were TiC (65–242), SiC (29-1129), TiO₂ (21-1272), C (graphite) (75-2078), Ti (44–1294) and Si (27-1402). Spectra were recorded at 30 mA and 40 kV using Ni-filtered Cu K α radiation ($\lambda = 1.54178 \text{ \AA}$). The scan rate (2θ) was $2^\circ / \text{min}$ at a step size of 0.05° .

3.3.1.2 Scanning Electron Microscopy (SEM)

SEM is a type of electron microscopy technique for studying the texture, topography and surface features of powders or solid pieces. The SEM images are produced by scanning the specimens with a focused beam of electrons. The electron-matter interactions result in a number of different particles or waves being emitted (e.g. secondary electrons, back-scattered electrons, X-rays, photons and Auger electrons).

Secondary electrons (SE) are produced through inelastic scattering that results in the ejection of loosely bound electrons from the specimen. Imaging with secondary electrons provides information about morphology and surface topography. In contrast, back-scattered electrons (BE) are beam electrons that are reflected from the sample by elastic scattering. BE images can provide information about the distribution of different elements in the sample, since the intensity of the BE signal is strongly related to the atomic number (Z). X-rays give characteristic chemical information of the emitting atoms. The probed depth in EDS analysis is around 1-3 μm (Fig. 3.9). All these electrons and waves are collected by corresponding detectors equipped with a specimen chamber, and then images and spectra can be presented after signal processing.

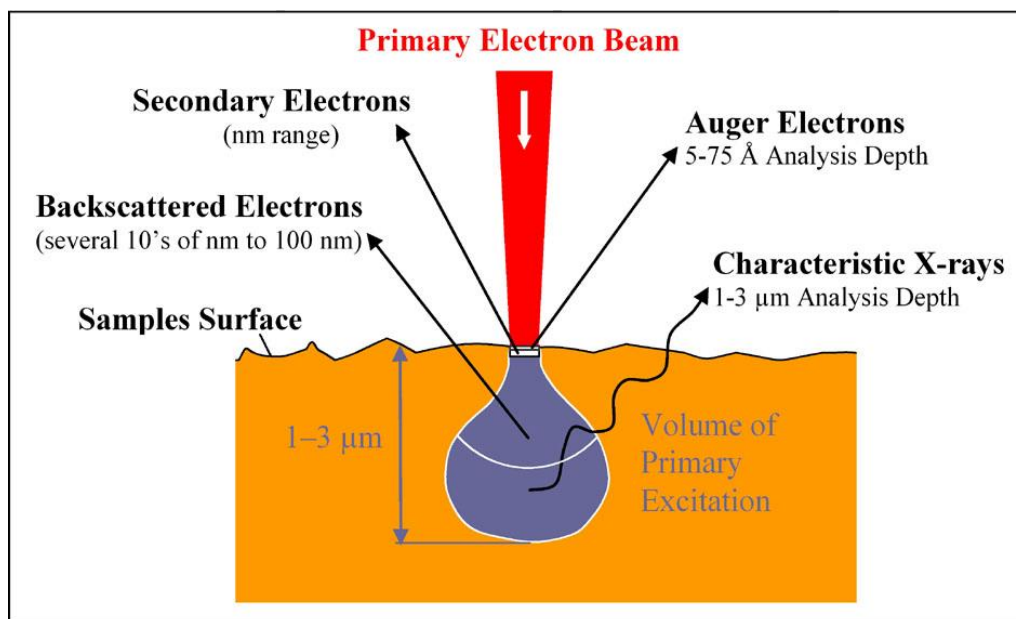


Fig. 3.9 A schematic diagram of electron-matter interactions for SEM.[183]

In the present study, microstructures and morphologies were observed by using a field emission gun scanning electron microscope (SEM) (Inspect F, FEI Company) equipped with an energy-dispersive spectroscope (EDS) (Oxford instrument) to identify the local chemical composition. Powder samples were directly dropped onto conductive sticky carbon films and characterised after gold coating. However, for nano-sized particles, they were dispersed in isopropyl alcohol (IPA) to avoid agglomeration. One drop from the suspension was then put on the sticky carbon film, followed by drying IPA in air and gold coating. For bulk castable samples, they were sectioned and mounted in cold setting resin. Standard ceramographic grinding and polishing techniques were then used, after which all samples were coated with carbon and examined by backscattered electron imaging (BEI) and secondary electron imaging (SEI).

3.3.1.3 Transmission Electron Microscopy (TEM)

TEM is an electron microscopy technique allowing visualisation and analysis of specimens in the realms of microspace to nanospace. It is commonly used to investigate crystal structures, specimen orientations and chemical compositions. Unlike an optical microscope, a focused beam of high energy electrons is used in TEM. As shown in Fig. 3.10, an electron beam is emitted from a filament in electron gun and passes through condenser lenses (which is used to control how strongly beam is focused onto specimen). An image is formed from the interaction of the electrons transmitted through the specimen. The image can be magnified by

objective lenses and projected on an imaging device (e.g. a fluorescent screen). TEMs are capable of imaging at a significantly higher resolution than light microscopes, owing to the small de Broglie wavelength of electrons. As the wavelength of high-energy electrons is far smaller than the spacing between atoms in a solid, diffraction also occurs when an electron beam is transmitted through specimens. Selected area electron diffraction (SAED) can be used to determine the crystal structure of samples.

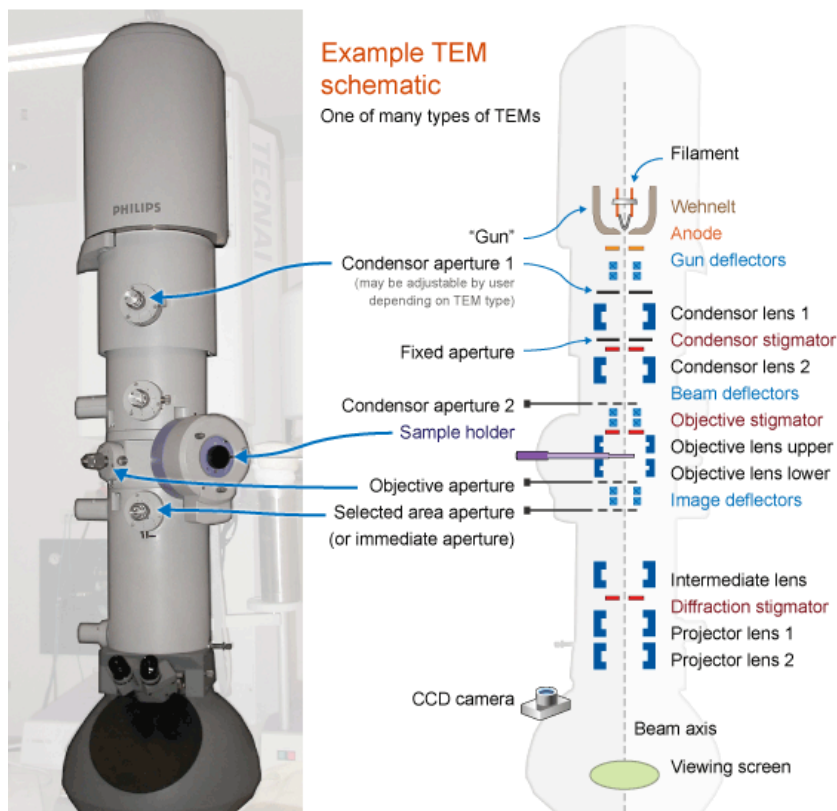


Fig. 3.10 A generalised cut-away diagram of the internal structure of a transmission electron microscope alongside an example of a modern instrument.[184]

In this study, microstructure of carbide coated CB was observed by using a transmission electron microscope (TEM) (Philips EM 420T instrument). Selected area electron diffraction (SAED) was used to assist identifying local phases. A high resolution TEM (HRTEM, JEOL 2010F microscope) was also applied for lattice-resolved imaging to identify the atomic structure of carbide shells. Based on mass-thickness contrast, regions of specimen which are thicker, or of higher density, will scatter more strongly and will appear darker in the image. So the thickness of carbide coatings could be estimated by measuring the darker shells. As for TEM specimen preparation, fine powders were dispersed in IPA with assistance of ultrasonic vibration for 15 minutes. One drop from the suspension was put on a

carbon film with Cu grids. IPA was evaporated in air prior to TEM characterisation.

3.3.1.4 Fourier Transform Infrared Spectroscopy (FTIR)

FTIR is a chemically-specific analysis technique. It can be used to identify chemical compounds, and constituent groups. When an infrared beam with continuous frequencies passes through a sample, the interaction between beam and sample causes the absorption of specific frequencies of the infrared wave. Since the vibration frequencies of the atomic bonds of materials are unique, the obtained infrared spectrum containing characteristic absorption peaks can be used for identification of chemical bonds. However, the infrared absorption only occurs when infrared radiation interacts with a molecule undergoing a change in dipole. On the other hand, the incoming infrared photon should have sufficient energy for the transition to the next allowed vibrational energy state. If these two rules are not met, no absorption will occur.[185]

The normal instrumental process is shown in Fig. 3.11. The interferometer is the most important component, which is used to produce an interferogram with information about every infrared frequency. The signals after collection by detectors and decoding via Fourier transformation are presented in an infrared spectrum for analysis.

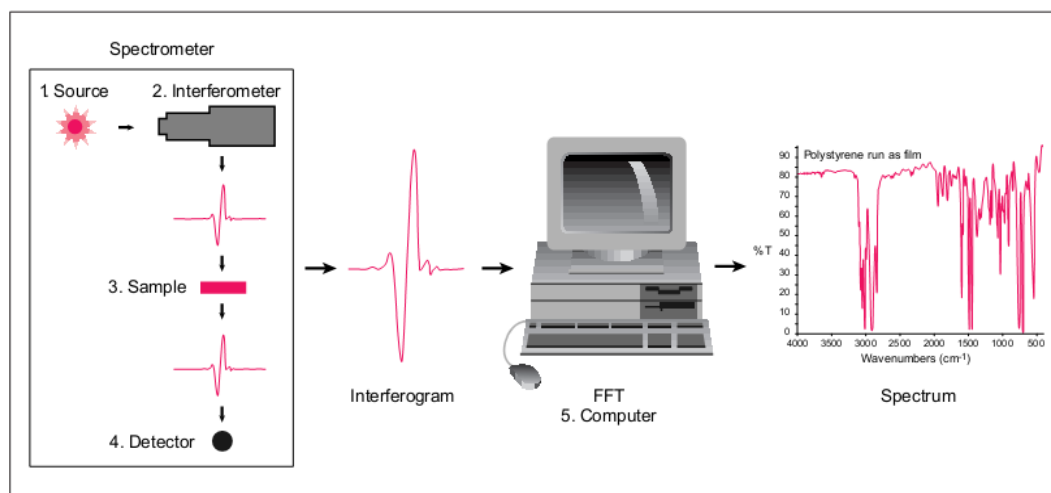


Fig. 3.11 Schematic diagram of the sample analysis process.[186]

FTIR measurements were carried out on a Spectrum 2000 (Perkin Elmer, USA) to identify atomic bonds in the phases. For better transmittance, ~5 mg as-prepared powders were mixed with 200 mg KBr powders and pressed into a thin pellet. The pellet samples were scanned from 4000 cm⁻¹ to 400 cm⁻¹ at an interval of 1 cm⁻¹.

The spectrum was recorded as a function of wavelength of the incident radiation.

3.3.2 Property measurements

3.3.2.1 Particle density

Density is merely calculated as the ratio of mass to volume. For a regular shape e.g. cubic or prim, the volume of the bulk object can be readily measured by a ruler, because the substance in the bulk is closely packed. However, for sub-micron or nano-sized particles, they exist in a form of loose packing. To determine the true density of particles (not packing density), the true volume of particles needs to be measured precisely, excluding the void space between particles and internal or open porosity. Thus, gas pycnometry needs to be used to measure the volume and true density of solid particles without damaging the samples.[187] The basic procedure of this method is putting a sample of known mass into a cell of known volume. Then helium gas is introduced into the cell which is at a vacuum, so helium occupies the space in the cell that is not occupied by the sample. The volume difference is determined by pressure change before and after gas filling. The calculation is based on gas displacement and well-known Boyle's Law ($P_1V_1=P_2V_2$).

In this study, true densities of as-received uncoated CB and as-prepared TiC or SiC coated CB after ultrasonic dispersion were determined using a Helium Pycnometer (AccuPyc II 1340, Micromeritics Instruments (Fig. 3.12)). Before testing, a proper amount (~0.1-0.2 g), m , of powders was weighted and placed in a 1 cm³ sample chamber. Their absolute volume was measured as ΔV . So true densities of particles were obtained according to Equation 3.3.

$$\rho_t = m/\Delta V \quad (3.3)$$



Fig. 3.12 A helium Pycnometer (AccuPyc II 1340) supplied by Micromeritics Instruments.

3.3.2.2 Zeta potential

Zeta potential is a physical property exhibited by particles in suspensions. The magnitude of zeta potential gives an indication of the potential stability of the colloidal or suspension system. Herein, it is used to characterise corresponding dispersion ability of uncoated and coated carbon particles in water.

When a particle is immersed in an electrolyte or water, the surface charge is developed by dissociation of ionogenic groups on the particle surface or by differential adsorption from solution of ions of different charges into the surface region. In addition, an electrical double layer (Fig. 3.13) is formed around each particle. In the inner region (also called stern layer), the ions with opposite charge of particle surface are strongly bonded. Next to the stern layer is the diffusion region (diffusion layer) where the ions are less firmly attached. There is a notional boundary called the slipping plane. When a particle moves, ions within the boundary move with it, but any ions beyond the boundary do not travel with the particle. Thus, the potential detected at this boundary is known as the zeta potential.[188] The large negative or positive zeta potential indicates particles in colloidal or suspension are stable due to a high repelling force between each other. On the other hand, low zeta potential values are obtained, showing there is no sufficient force to prevent particles from coming together or flocculating.

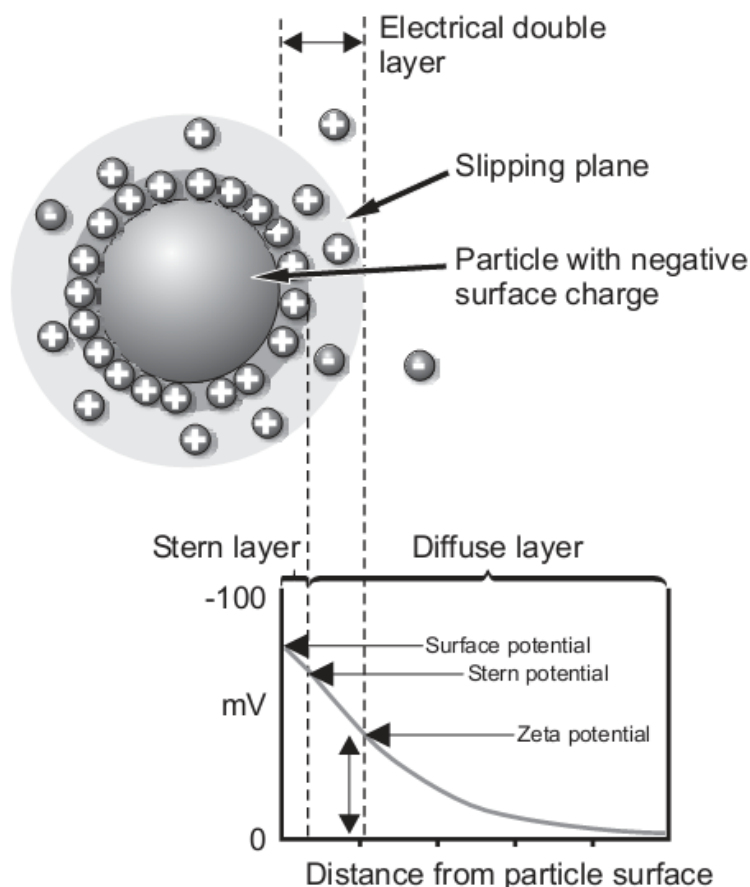


Fig. 3.13 A schematic diagram of electrical double layer.[188]

Zeta potential measurements were performed on a ZetaProbe Analyzer (Colloidal Dynamics Pty Ltd, USA) based on the multi-frequency electroacoustic principle. The sample used in this case was a water suspension containing 2 wt% ultrasonically dispersed uncoated or coated CB powders. 1 mol/L HCl and KOH solutions were used for pH titration from 3 to 12.

3.3.2.3 Sedimentation testing

Sedimentation testing was done to visually demonstrate the improvement in water-wettability and dispersivity of CB after coating. 1 gram as-received or coated CB powders were put in water and agitated violently for 1 minute. After setting aside for 5 min, their wetting behaviours were observed and photos of the suspensions were taken for comparison.

3.3.2.4 Rheological behaviour

Rheology is the study of the flow of matter, primarily in the liquid state, but also as 'soft solids' or solids under conditions in which they respond with plastic flow rather

than deforming elastically in response to an applied force. It is important for industrial production processes, such as in the fields of resin, cement, paintings, and food systems, etc. As for castable production, the study on rheological behaviour of oxide pastes or carbon materials in water is necessary, as the workability of castables is normally governed by flowability of fine powders.

According to the Newton's law of viscosity, the strain rate is proportional to the applied stress (Equation 3.4).

$$\sigma = \eta \cdot \dot{\gamma} \quad (3.4)$$

where η (Pa·s) is the viscosity which is independent of the applied stress and strain, σ is shear stress and $\dot{\gamma}$ refers to the rate of shear strain. The fluids that obey the Newton's law of viscosity are called Newtonian fluids. Their characteristic is that the viscosity is constant with time of shearing and does not vary with shear rate. However, for a large number of fluids, the viscosity changes with the shear rate. These fluids such as slurries, pastes, gels and polymer are called non-Newtonian and the typical relationship of viscosity and shear rate is shown in Fig. 3.14.

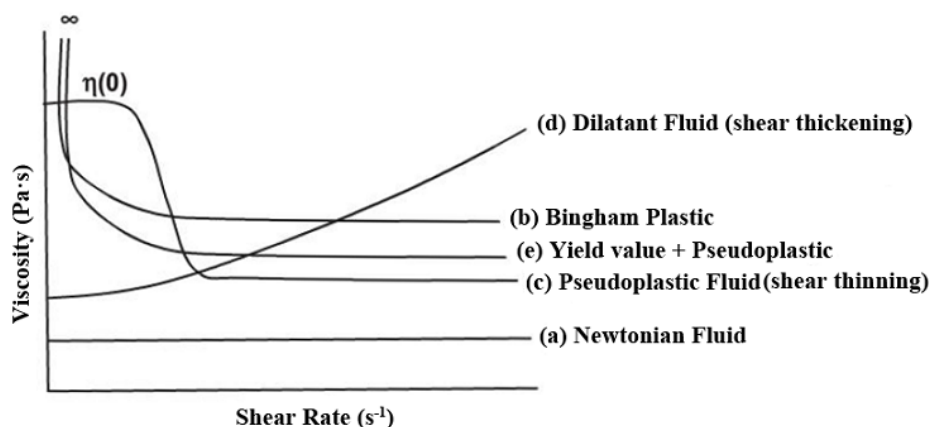


Fig. 3.14 Viscosity-Shear rate relationship.[189]

To investigate the flowability of carbon materials before and after surface modification, a strain-controlled rheometer (TA instruments AR 2000, USA) was used to investigate rheological properties of water suspensions containing 25 wt% of uncoated or TiC (or SiC)-coated CBs at room temperature (20 °C, pH= 6 or 10). A flat plate geometry with 60 mm diameter was used for the steady rate sweep ranging from 0.01 to 500 s⁻¹.

3.3.2.5 Thermal analysis (TGA+DSC)

Thermogravimetry (TG) measures the change in mass of a substance as a function

of temperature or time. A sample is heated at a constant rate and has a varying mass when the decomposition or oxidation takes place over a range of temperatures. The changes in mass are fundamental properties of the sample and can be used for quantitative calculations of compositional changes. Differential scanning calorimetry (DSC), a thermoanalytical technique, is used to determine glass transition temperature and to study crystallization, oxidation and other chemical reactions. The enthalpy changes could be measured directly by maintaining the sample and an inert reference at the same temperature. The extra heat is input to the reference when the sample undergoes an exothermic change, and vice versa.[190]

In this study, TG and DSC analysis were carried out simultaneously to examine the oxidation behaviour of uncoated and carbide-coated carbon materials in air at elevated temperature by using SDT-Q600 (TA instruments, Fig. 3.15) The sample (~10 mg) was put in an alumina crucible and heated in a sealed furnace chamber from room temperature to 1000 °C at heating rate of 10 °C/min. The air flow was set at 100 mL/min.

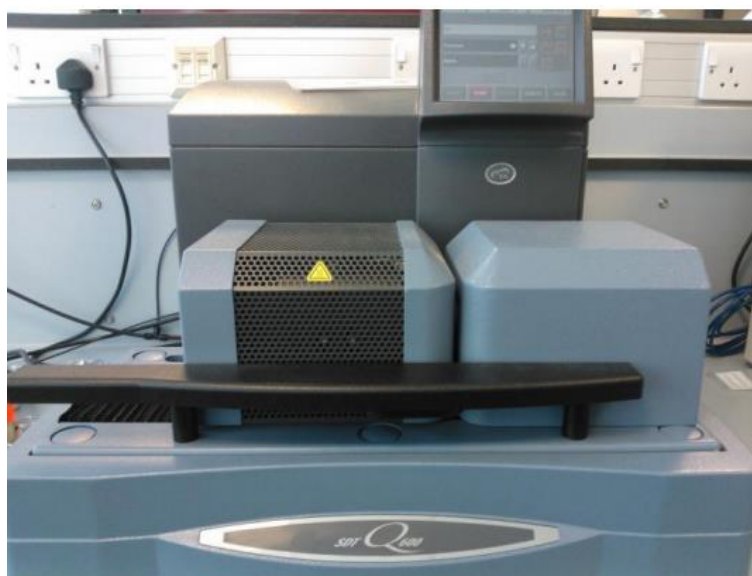


Fig. 3.15 SDT-Q600 simultaneous TGA/DSC supplied by TA instruments.

3.3.3 Testing methods for castable samples

3.3.3.1 Water demand and flowability

The water demand was determined by the amount of water required for castables to achieve a certain flow value under vibration. It is meaningful when both the water addition and flow value are considered together. In the present work, they were

measured based on ASTM C1445-99.[191] The well-mixed castables (as described in Section 3.2.2.2) were filled into a bronze cone ($\phi 70 \times \phi 100 \times 50$ mm) and then pre-vibrated for 2 or 3 up-and-down stands while holding firmly on vibration table as shown in Fig. 3.16. After levelling the surface to the top of the cone, the cone was carefully removed. The castable in a cone shape was then flowed freely under up-and-down vibration. The diameter of the spread mass was measured at the ends of 6 arbitrary diameters after 15 cycles of vibration. The average diameter was taken as the flow value of castable at the certain water addition. In this study, water was added until the castable reached a flow value between 140 to 150 mm.

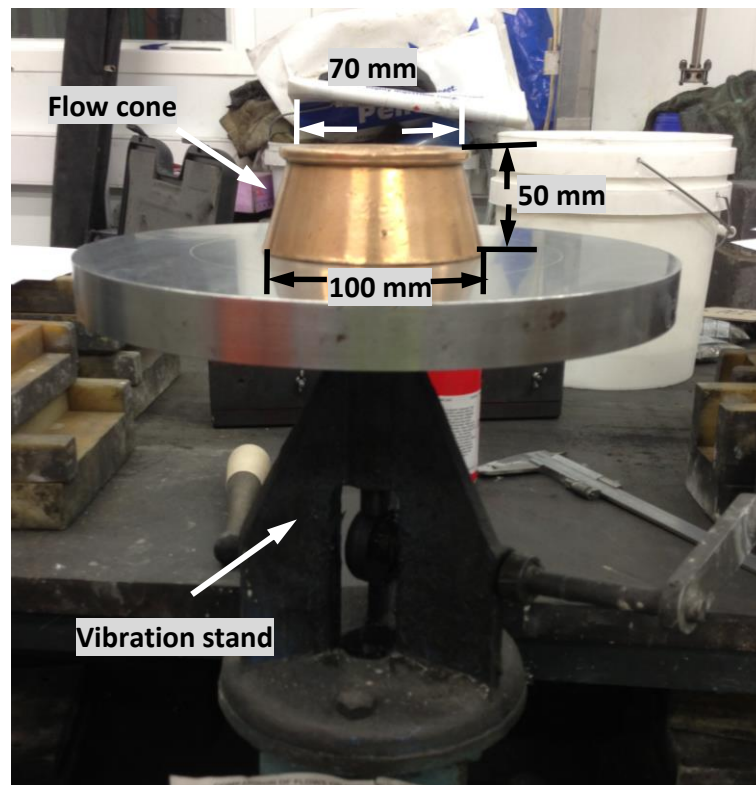


Fig. 3.16 A photo of bronze flow cone and simplified vibration stand.

3.3.3.2 Bulk density, apparent porosity and permanent linear change

Apparent porosity (AP) and bulk density (BD) were measured according to ASTM C830-00.[192] A castable test specimen ($50 \times 50 \times 50$ mm cube) was dried to constant weight by heating at 110°C for 24 hours. The dry weight, m_d , was determined using a balance before it was placed in a vacuum-pressure vessel and fully impregnated with water under pressure for a certain time. Following this, the suspended weight, m_s , was measured when the saturated specimen was suspended in water. Finally, a blotting operation was performed to slightly remove all drops of liquid on the surface of the test specimen and then the saturated weight, m_w , was measured in air.

According to ASTM C830-00, AP is the percentage ratio of the volume of open pores in the refractory specimen to its exterior volume and calculated using Equation 3.5.

$$AP (\%) = \frac{m_w - m_d}{m_w - m_s} \times 100\% \quad (3.5)$$

Bulk density of the test specimen is calculated as follows

$$BD (g/cm^3) = \frac{m_d}{m_w - m_s} \times \rho_{H_2O} \quad (3.6)$$

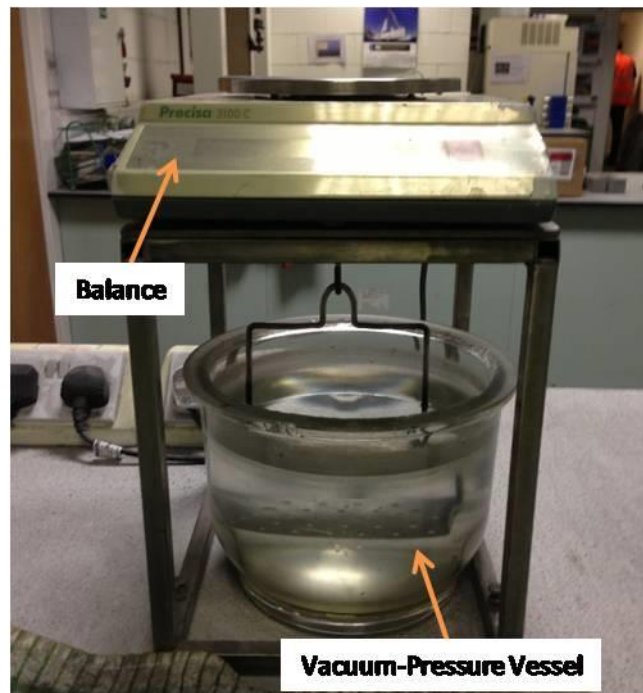


Fig. 3.17 A setup for bulk density and apparent porosity measurement.

AP and BD values were measured for both types of castable specimens (uncoated or coated carbon containing castables) after drying at 110 °C and after coking in graphite powders at 1500 °C respectively to investigate the changes of physical properties before and after high temperature heating.

In addition, permanent linear and volume changes before and after firing were also examined based on standard test method ASTM C1407-98 [193] to characterise the dimensional stability of castables. The lengths of three sides of the cube before coking were measured and labelled as L_a , L_b and L_c . The corresponding length after coking are referred as L'_a , L'_b and L'_c , respectively. PLC and PVC are calculated according to the following equations.

$$\Delta L_a = \frac{L'_a - L_a}{L_a} \quad (3.7)$$

$$\Delta L_b = \frac{L'_b - L_b}{L_b} \quad (3.8)$$

$$\Delta L_c = \frac{L'_c - L_c}{L_c} \quad (3.9)$$

$$PLC(\%) = \frac{\Delta L_a + \Delta L_b + \Delta L_c}{3} \times 100\% \quad (3.10)$$

$$PVC(\%) = \frac{L'_a * L'_b * L'_c - L_a * L_b * L_c}{L_a * L_b * L_c} \times 100\% \quad (3.11)$$

3.3.3.3 Cold crushing strength and cold modulus of rupture

Cold crushing strength (CCS) and cold modulus of rupture (CMOR) were determined by using the standard testing method ASTM C133-97.[194] For the crushing testing, a cubic specimen (50×50×50 mm) after drying was placed in the centre of sample holding platform, and subject to a load until collapse or reduction of specimen height to 90% of its original value. It should be noted that the selected compression test section must be free of cracks, chipped surfaces, and other obvious defects. The loaded surfaces should be approximately parallel planes. The CCS was calculated as

$$CCS = \frac{F_{max}}{A_0} \quad (3.12)$$

Where:

CSS = cold crushing strength, N/mm²=MPa

F_{max} = maximum load at failure, N

A₀ = surface area where subjected to load, mm²

CMOR testing was performed on a three bending strength tester. The testing bar (150×25×25 mm) was positioned flat on bearing cylinders with a span of 100 mm and a load applied at mid-span, as illustrated in Fig. 3.18. The loading rate for the CMOR was controlled by the speed of the cross head. It was set as 1.3 mm/min in this work.

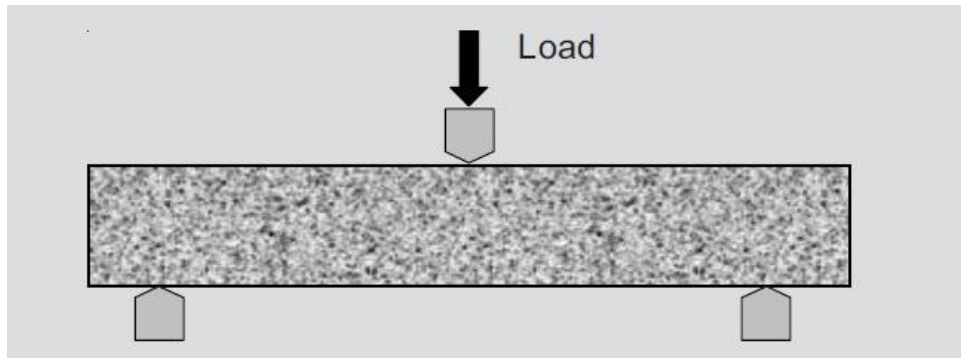


Fig. 3.18 A schematic diagram of three point bending test.

The CMOR value was calculated by the following equation,

$$\text{MOR} = 3FL/(2bd^2) \quad (3.13)$$

MOR = modulus of rupture, $\text{N/mm}^2 = \text{MPa}$,

Where F is the maximum load applied at rupture (N); L is the span between two bottom bearing cylinders (100mm for all the tests in this work); b is the width of the test specimen (25 mm in this work); d is the depth or height of specimen (also 25 mm in this work). Each value is the average of three parallel specimen.

3.3.3.4 Oxidation resistance

Oxidation resistance of carbon-containing castables was evaluated by two main parameters: the depth of decarbonized layer and oxidation area. Since no antioxidants were added into investigated castables in this study, the oxidation test was carried out at 1000 °C in air for 30 minutes and 3 hours, respectively. Cubic samples were placed into a hot chamber furnace prefixed at 1000 °C. For unidirectional oxidation for each face of cube, a layer of coarse fused magnesia grains were placed at the bottom of the cube to expose the bottom face of the cube to air flow.

After oxidation test, castable specimens were sectioned from the middle, and the average depth of the decarbonized layer was measured as one of the indexes for evaluation of oxidation resistance. The oxidation area of each specimen was also calculated. The oxidized samples were also characterised by using SEM, to assist understanding the oxidation mechanism of the samples in air at high temperature.

Chapter 4 Molten salt synthesis of TiC coatings on CB

In this chapter, a molten salt synthesis technique was developed and employed for preparation of TiC coatings on CB. The synthesis parameters such as temperature, Ti/C molar ratios, CB particle size and salt assembly were optimised. Microstructures of TiC coated CB particles were characterised by SEM, EDS, TEM, and SAED. Apart from Ti, TiO₂ was used as an alternative Ti source for preparing TiC coatings on CB in order to reduce their fabrication cost.

4.1 Preparation of TiC coatings on CB using Ti

4.1.1 Synthesis temperature

Fig. 4.1 shows XRD of products of firing the mixtures of Ti and CB (in the molar ratio of 1/8) (referred to as the CB-Ti mixtures hereafter) for 4 hours in KCl-LiCl at 650-750 °C and in KCl at 800-850 °C. The reaction between CB and Ti initiated at as low as 650 °C, as indicated by the small TiC peaks. However, intensive Ti peaks (shifted slightly to the left probably due to formation of Ti(C) solid solution [195, 196]) still remained, indicating that the reaction was not complete. On increasing the temperature to 750 °C, Ti disappeared and only TiC was detected along with unreacted CB (indicated by the broad peak centred at about 25.6°), indicating that Ti was completely consumed to form TiC. This preparation temperature was 100-200 °C lower than that used in the preparation of TiC coated graphite [26], which is attributable to the higher reactivity of submicron-sized amorphous CB. On further increasing temperature to >800 °C, no further phase changes were seen, but the TiC peaks became slightly higher and sharper, indicating a slight increase in its crystallinity and/or crystal size. The results indicate that the optimal reaction temperature for the MSS was 750-850 °C.

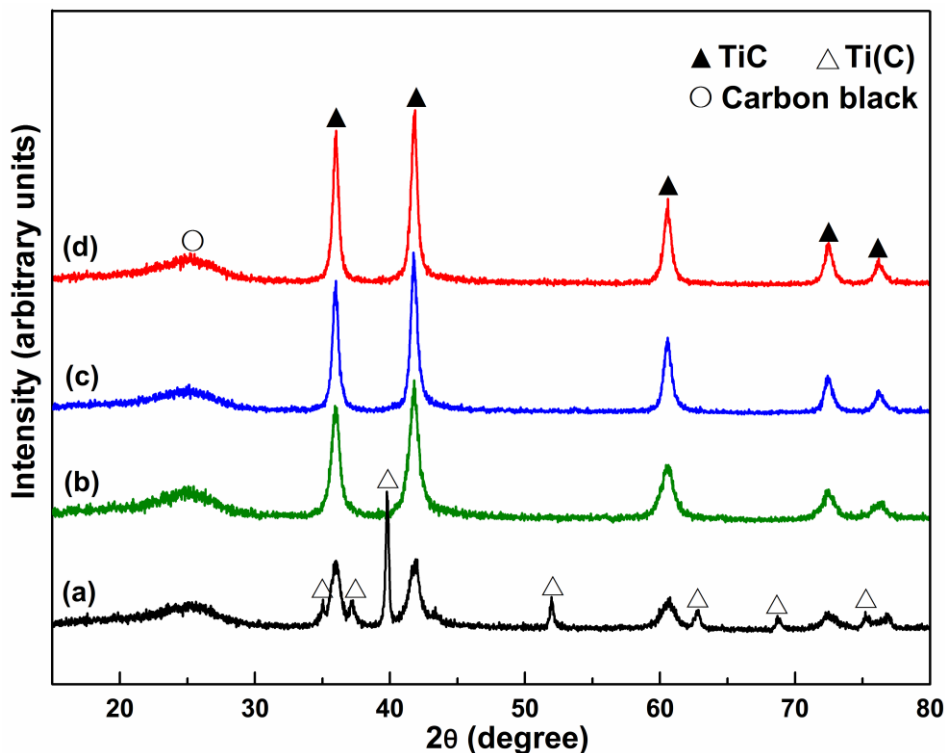


Fig. 4.1 XRD of product powders of firing the mixtures of Ti and CB (with Ti/C=1/8) for 4 hours at (a) 650 °C and (b) 750 °C in KCl-LiCl, and (c) 800 °C and (d) 850 °C in KCl.

4.1.2 Microstructure characterisation

4.1.2.1 Morphological changes of CB-Ti mixtures after firing

Figs. 4.2a and b illustrate typical SEM images of raw materials, spherical CB particles (~280 nm in average diameter) and micron-sized Ti powders (~44 μm). However, after firing the CB-Ti mixtures in molten salt at 750-850 °C Ti disappeared and only spherical particles were seen (Fig. 4.2c, d). These particles showed similar morphologies and sizes to the unreacted CB particles (Fig. 4.2a), but exhibited rougher surfaces, indicating new phase formation on their surfaces. Fig. 4.2c and d also compare the microstructures of product powders after firing the CB-Ti mixtures for 4 hours in KCl at 850 °C and in KCl-LiCl at 750 °C. The latter was similar to the former but showed slightly heavier agglomeration. The reason for this was not clear, but could be related to the difference in the salt properties (e.g. viscosity, wettability and surface tension) which might have affected the dispersion of CB particles. A higher magnification SEM image (Fig. 4.3a) further reveals the presence of many nanosized grains on their surfaces. These particles contained C and Ti (Fig. 4.3b). This, along with the XRD pattern shown in Fig. 4.1d, verified the formation of TiC coatings on the original CB particles.

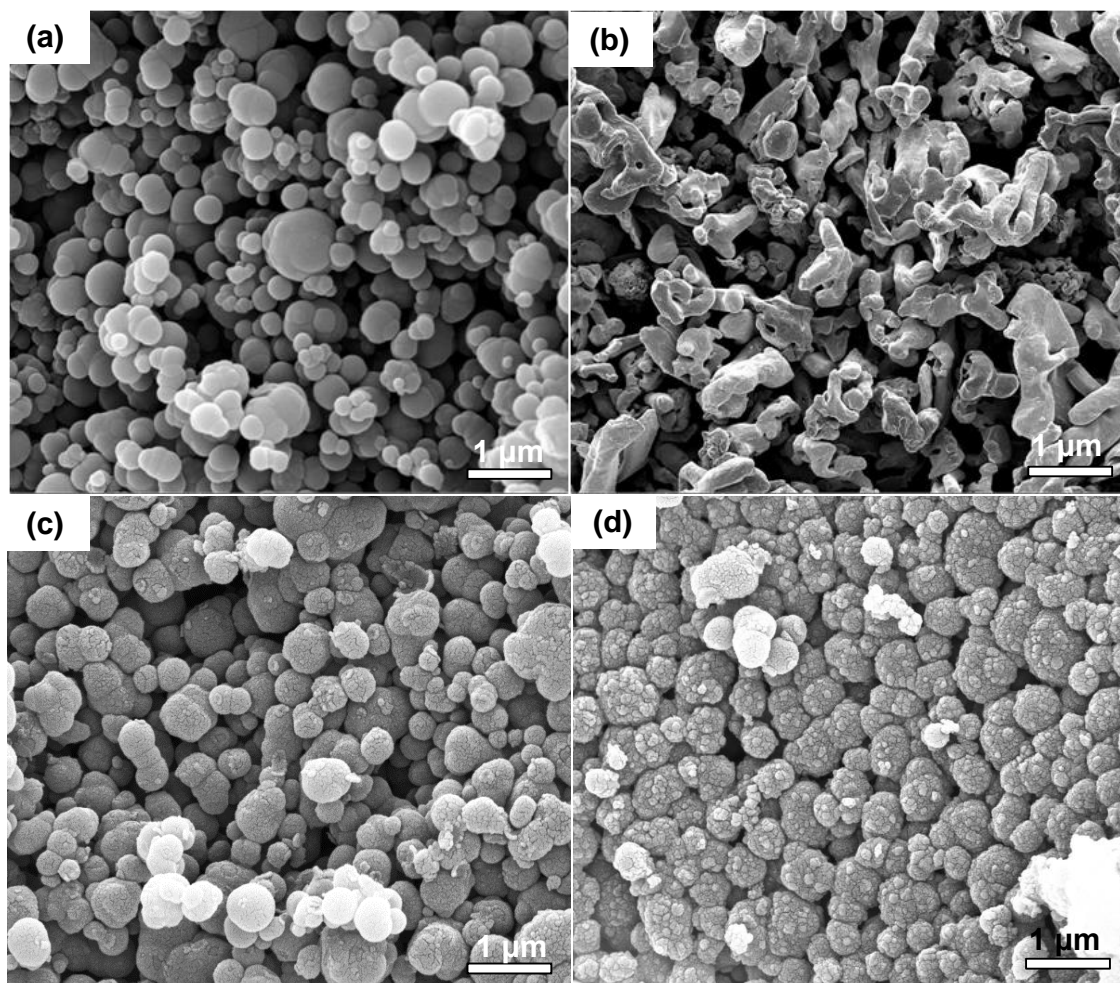


Fig. 4.2 Typical SEM images of (a) as-received uncoated CB particles and (b) Ti powders, and product powders of firing the mixtures of CB and Ti (with Ti/C = 1/8) for 4 hours in (c) KCl at 850 °C and (d) KCl-LiCl at 750 °C.

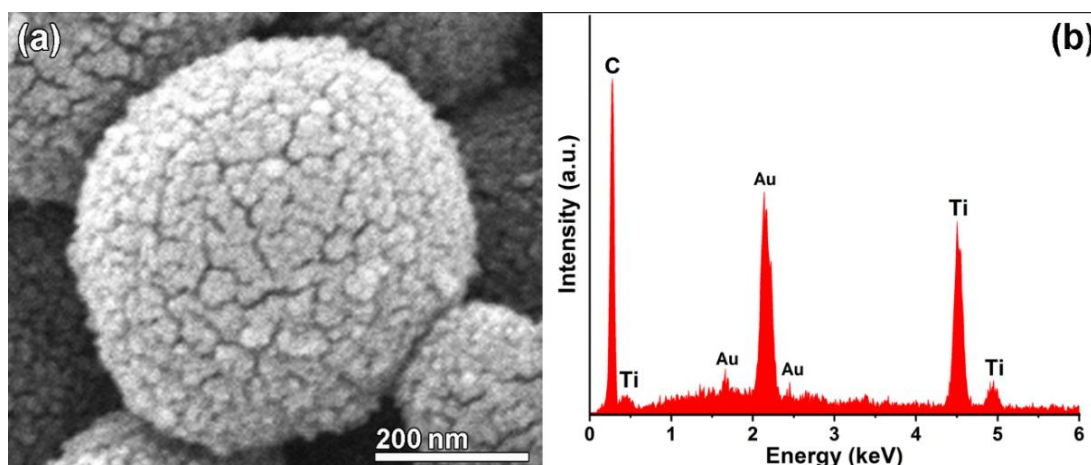


Fig. 4.3 (a) Higher magnification SEM image of a typical individual CB particle shown in Fig. 4.2c, and (b) EDS of the surface of the particle shown in (a).

Fig. 4.4 presents together back-scattered electron images (BEI) of as-received CB and as-prepared TiC-coated CB particles (synthesised at 850 °C for 4 hours in KCl).

Compared to uncoated CB particles with dark contrast (Fig. 4.4a), as-prepared CB particles showed homogeneous brighter contrast, additionally indicating the homogeneous distribution of Ti and the formation of TiC coatings.

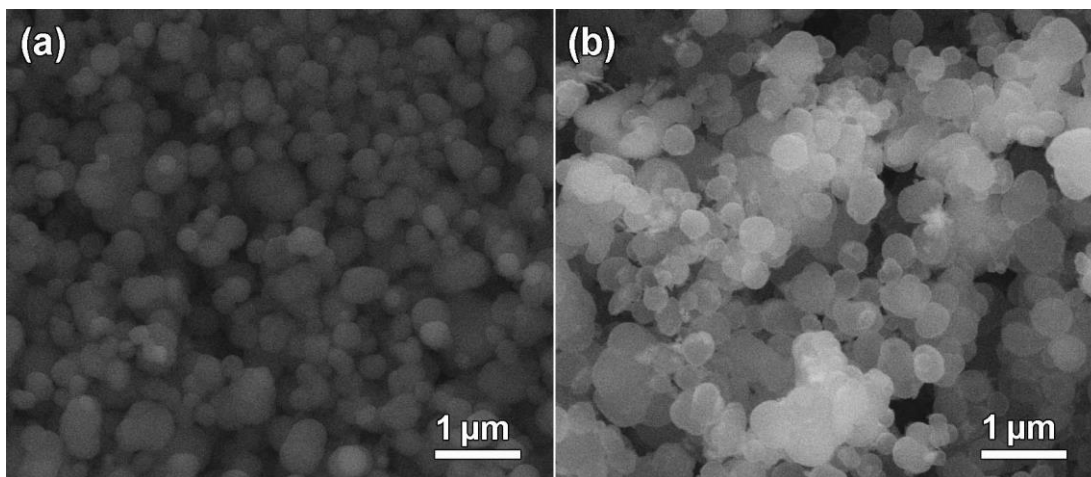


Fig. 4.4 BEI images of (a) as-received carbon black and (b) TiC coated carbon black (with Ti/C = 1/8) prepared from KCl at 850 °C for 4 hours.

4.1.2.2 Core/shell structure of TiC coated CB

The core/shell structure of TiC coated CB was confirmed directly by TEM observations. As shown in Fig. 4.5a, the surfaces of as-received uncoated CB particles appeared to be smooth, with identical contrast over the whole particles (apart from the overlapped areas). However, in the case of coated CB particles, a slightly darker-contrast shell was seen, covering each individual particle core (Fig. 4.5b, c). The SAED pattern of the shell shows three diffraction rings corresponding respectively to the (111), (200) and (220) planes of the cubic TiC, which further verifies the formation of TiC coatings. In terms of the TEM image in Fig. 4.5c, the thickness of the shell corresponding to Ti/C = 1/8 was estimated to be 11.09 nm.

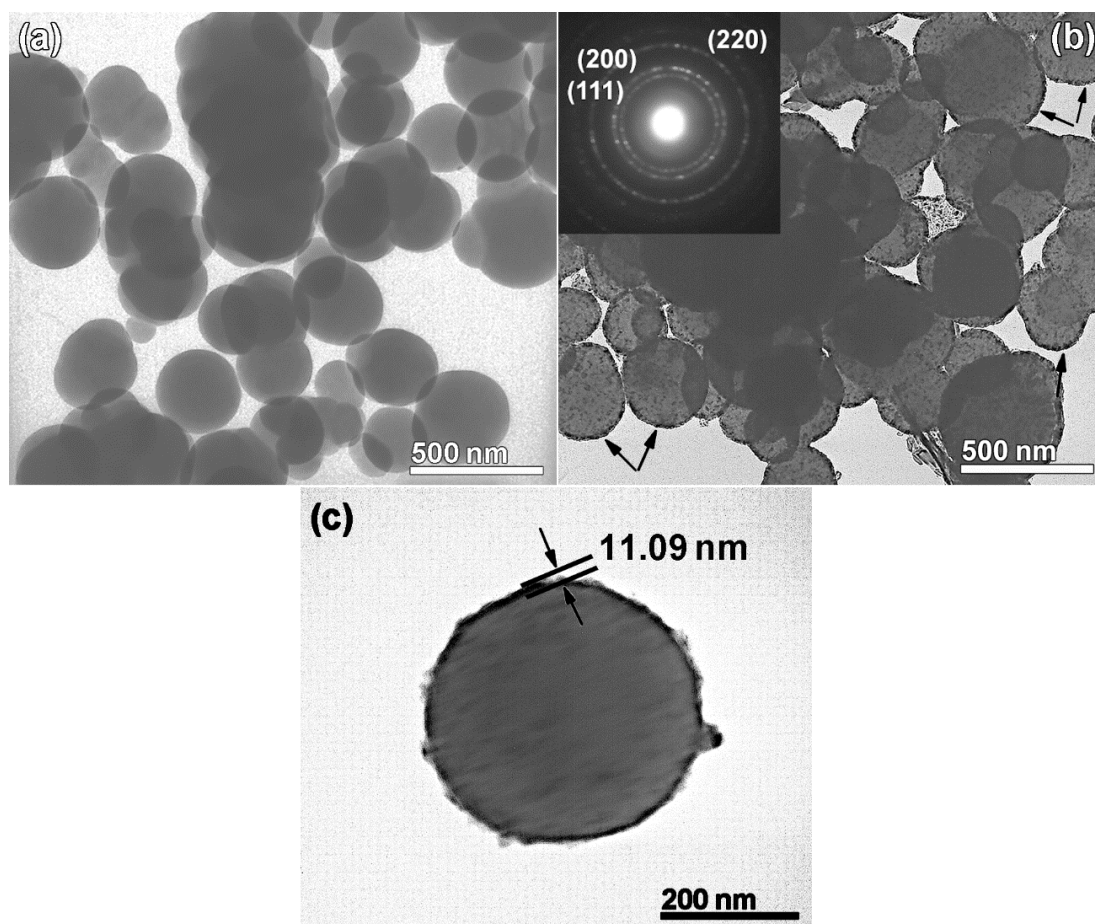


Fig. 4.5 TEM images of (a) uncoated CB, (b) TiC coated CB (with Ti/C=1/8) prepared at 850 °C for 4 hours in KCl, and (c) an individual TiC coated CB particle from (b). The insert in (b) is the SAED pattern of the shell, showing the (1 1 1), (2 0 0) and (2 2 0) diffraction planes of TiC.

To further reveal core/shell structure of TiC-C composite spheres, carbon was removed by combustion of them in air at 500 °C for 30 minutes. Fig. 4.6a shows XRD of TiC-coated CB particles after oxidation, in which TiO_2 phase was detected along with a small amount of TiC remained in the resulting powders. The disappearance of carbon peak (broad peak centred at about 25.6° as shown in Fig. 4.1) confirmed the removal of carbon at this oxidation temperature. As can be seen from Fig. 4.6b, spherical shape of the resulting particles still remained and some broken spheres (e.g. indicated by the black arrows) shows the obviously hollow structure. Despite TiC shells were oxidised and converted to TiO_2 shells during oxidation treatment, the hollow structure verified the formation of TiC coatings on carbon cores.

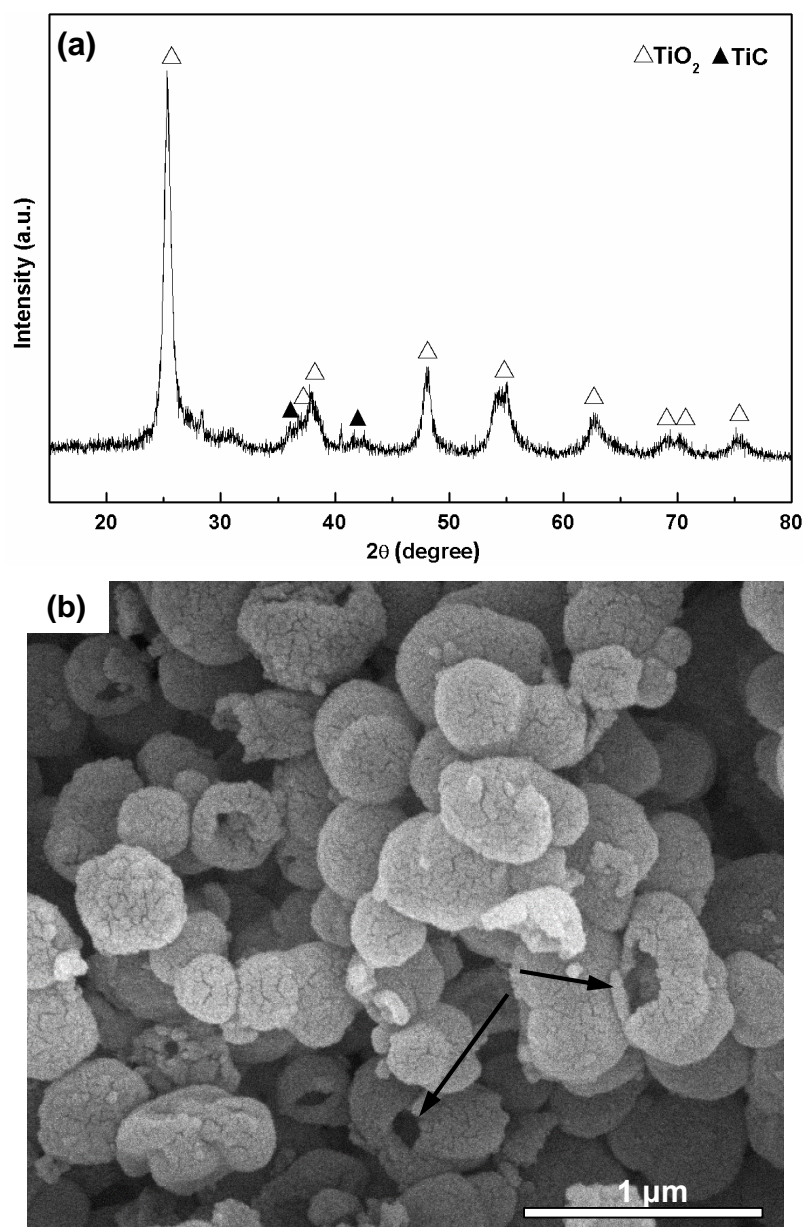


Fig. 4.6 (a) XRD pattern and (b) SEM image of TiC-coated CB particles after oxidation in air at 550 °C for 30 minutes, showing their hollow structure after oxidation removal of the carbon cores in air.

4.1.3 Effect of Ti/C molar ratio on TiC formation

To reveal the controllability of TiC coating thickness, the mixtures of Ti and CB in other molar ratios (1/4-1/2) were also fired under the identical conditions. The formation of TiC coatings on the original CB particles was also verified by XRD and SEM. Fig. 4.7 shows XRD of product powders of firing the mixture of Ti and CB in the molar ratio of 1/4 and 1/2. Only TiC crystalline phase was detected after reaction, indicating all Ti powders were completely converted to TiC coatings at 850 °C in KCl though the proportion of Ti in starting materials was increased. Furthermore, the

intensity of TiC peaks increased, concurrent with a decrease in the broad CB peak, indicating the formation of more TiC or thicker TiC coatings. SEM images (Fig. 4.8) of as-prepared CB particles prepared from higher initial Ti/CB molar ratios shows thicker TiC coatings retain as high quality as the thin counterparts (prepared in low Ti/CB molar ratio (1/8)).

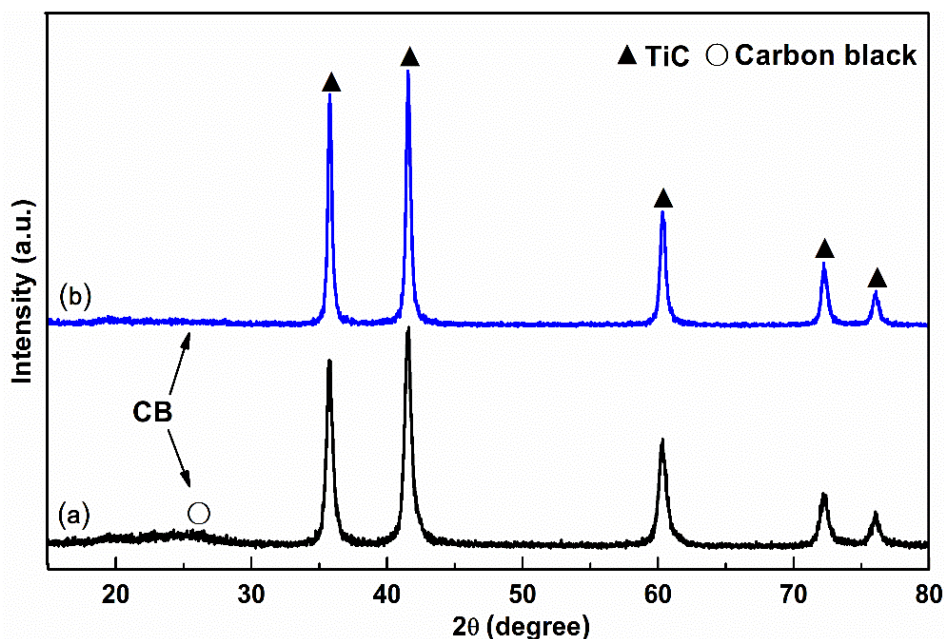


Fig. 4.7 XRD of product powders of firing the mixture of Ti and CB in the molar ratio of (a) 1/4 and (b) 1/2 for 4 hours at 850 °C in KCl.

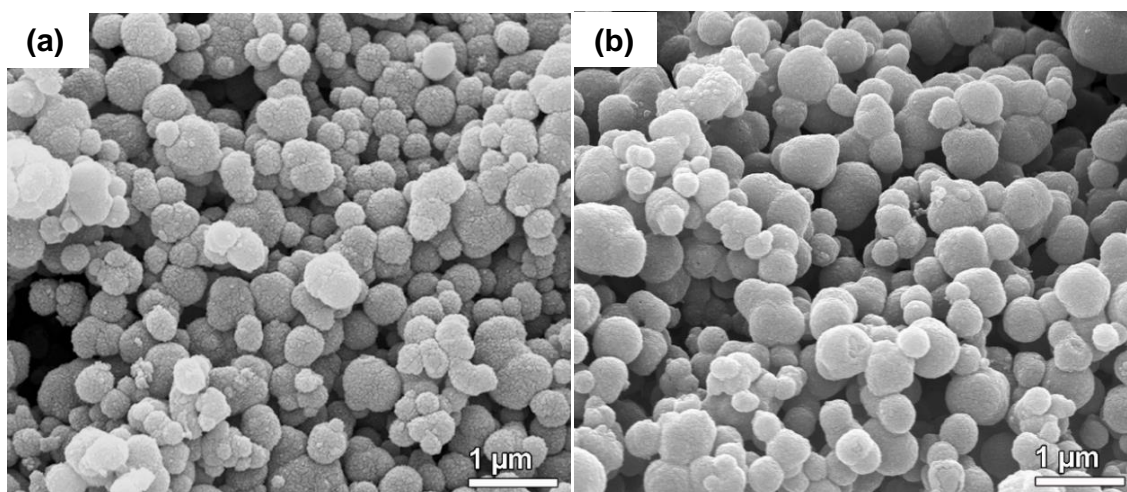


Fig. 4.8 SEM images of product powders of firing the mixture of Ti and CB in the molar ratio of (a) 1/4 and (b) 1/2 for 4 hours at 850 °C in KCl.

Unfortunately, with increasing coating thickness, it became more difficult for the accelerating electrons to be transmitted through the coatings. Consequently, it became almost impossible to take clear TEM images for estimating the coating

thickness. Nevertheless, considering the difference in the densities of CB and TiC, the TiC coating thicknesses could be roughly estimated based on the true densities of CB particles after coating. As shown in Fig. 4.9, the density of as-received CB was 1.89 g/cm^3 , whereas that of TiC coated CB when $\text{Ti/C} = 1/8$ was 2.59 g/cm^3 , and further increased to 3.70 g/cm^3 upon increasing Ti/C to $1/2$. Such an increase in the density of TiC-coated CB particles could narrow the density difference between them and other grains (e.g. MgO and Al_2O_3) used in castable systems, thus assisting more homogeneous distribution/dispersion of carbon in the castable systems. Based on the true densities, the coating thickness was estimated to be $\sim 10 \text{ nm}$ when $\text{Ti/C} = 1/8$, which is close to that ($\sim 11 \text{ nm}$) estimated from TEM images (e.g., Fig. 4.5c). Upon increasing the Ti/C ratio to $1/2$, the estimated TiC coating thickness increased to $\sim 50 \text{ nm}$. These results indicate that the TiC coating thickness and true density of CB could be readily tailored to meet practical requirements simply *via* adjusting the Ti/C ratio of the starting mixture.

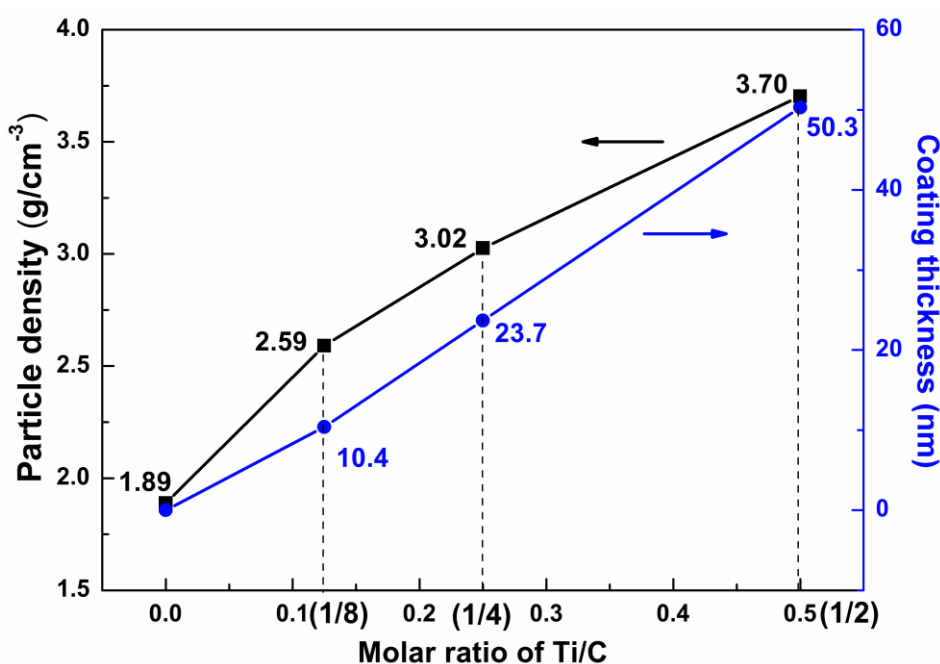


Fig. 4.9 True density of CB particles and corresponding TiC coating thickness as a function of Ti/C.

4.1.4 Effect of CB particle size on TiC formation

To study the feasibility of molten salt preparation of TiC coatings on smaller carbon particles, two types of CB particles, N660 ($\sim 62 \text{ nm}$) and N330 ($\sim 30 \text{ nm}$), were used as carbon templates. After firing CB-Ti mixtures ($\text{Ti/CB} = 1/8$ in molar ratio) in KCl at $850 \text{ }^\circ\text{C}$ for 4 hours, the produced particles, as shown in Fig. 4.10, to a large extent,

appeared to retain the morphologies and sizes of their corresponding uncoated CB particles. To confirm the formation of TiC coatings on nano-sized CB particles (<100 nm), the approach of removal of carbon cores in air was also employed. As indicated by black arrows in Fig. 4.11, the hollow structure of nano-particles (< 50 nm) was obtained after completely oxidizing carbon cores (CB N330), indicating TiC coatings could even be prepared on nano-sized CB particles (30-60 nm diameter) by using the MSS technique.

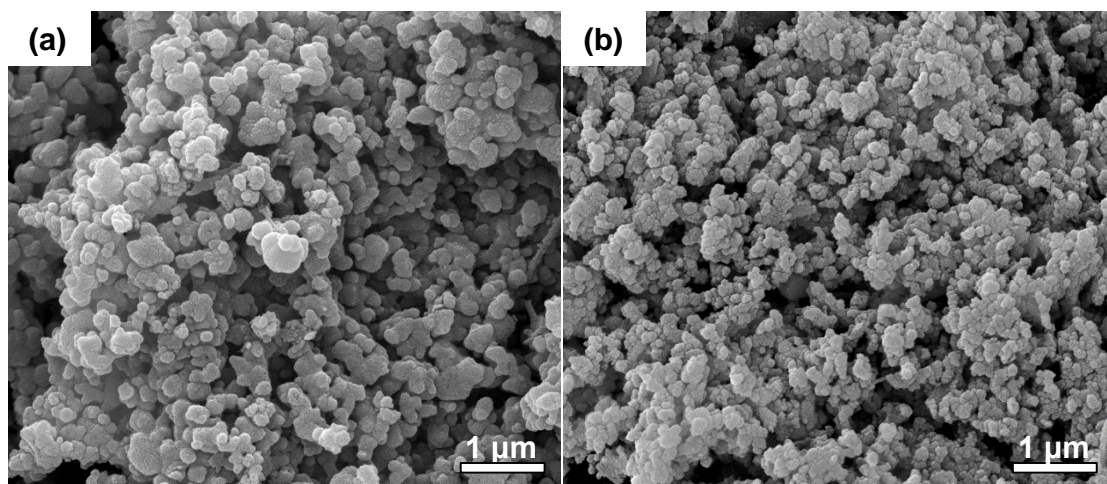


Fig. 4.10 SEM images of TiC-coated CB particles (Ti/C = 1/8 in molar ratio) prepared in KCl at 850 °C for 4 hours using (a) CB N660 and (b) CB N330.

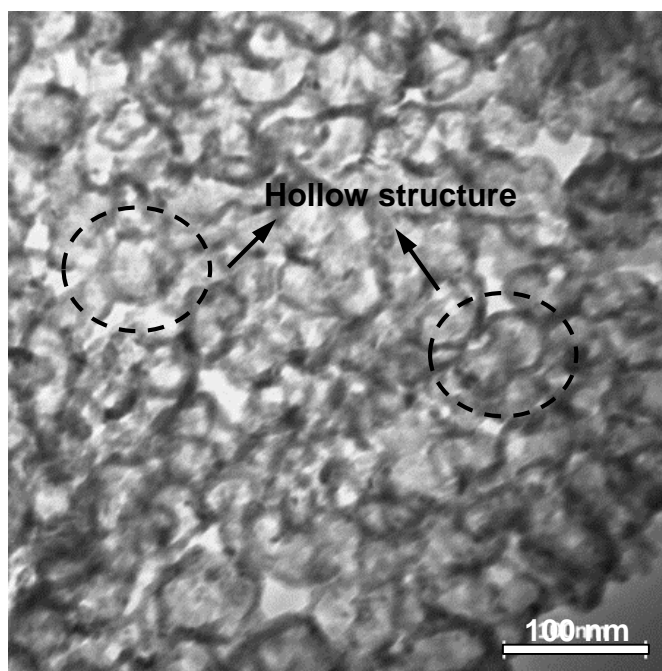


Fig. 4.11 TEM image of hollow particles after firing as-prepared TiC-coated CB (N330) in air at 500 °C for 30 minutes.

4.1.5 Effect of molten salt on TiC formation

Based on above experimental results, it can be concluded that high quality TiC coatings were successfully prepared on CB particles with the assistance of molten salt at a low temperature. To demonstrate the role of molten salt played in TiC coating preparation, the synthesis was also conducted under conditions without using a salt. Fig. 4.12b shows XRD of the products resultant from firing the CB-Ti mixture (Ti/C = 1/8 in molar ratio) at 850 °C for 4 hours in the absence of salt. The appearance of TiC peaks indicates CB was able to directly react with Ti in salt-free condition, however, a certain amount of unreacted Ti (or Ti(C)) as indicated in Fig. 4.12b, formed due to solid solution of C in unreacted Ti) still remained, which was further verified by SEM (indicated by white arrow in Fig. 4.13a). Differently from the morphology of TiC coated CB particles prepared from the molten salt (Fig. 4.2c), micron-sized TiC/C powders (~20-100 μm) rather than dispersive submicron-sized particles were obtained in the product powders (Fig. 4.13a). A high magnification SEM image (Fig. 4.13b) revealed that these TiC/C powders' surface was consisted of sintered micron-sized TiC crystals. These results indicate solid-solid reaction (without molten salt media) of CB and Ti could not produce TiC coatings on CB, which further indicates the important role played by the molten salt in the TiC coating formation.

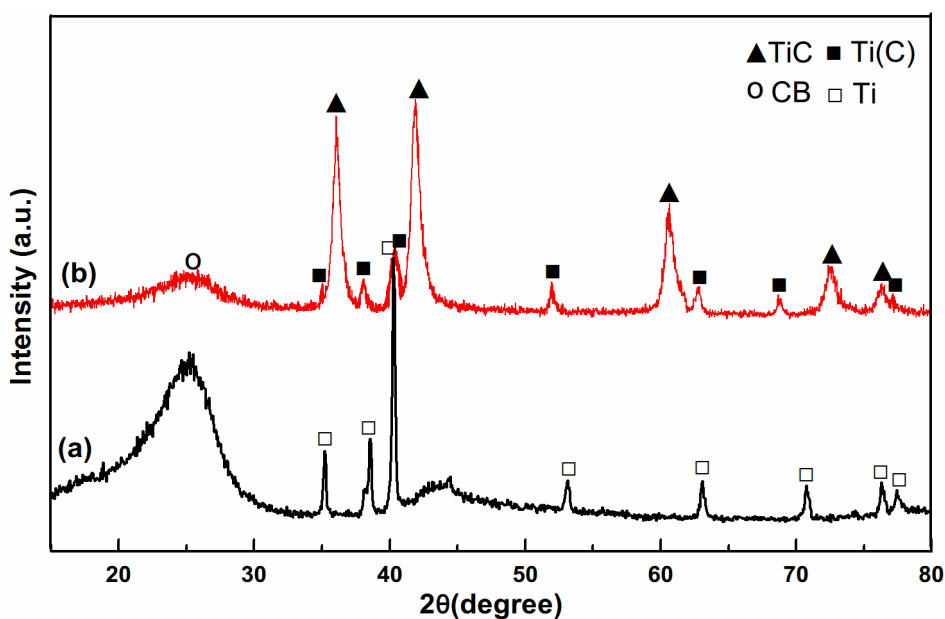


Fig. 4.12 XRD of the powders of (a) before and (b) after firing the CB-Ti mixture (Ti/C = 1/8 in molar ratio) in the absence of KCl at 850 °C for 4 hours.

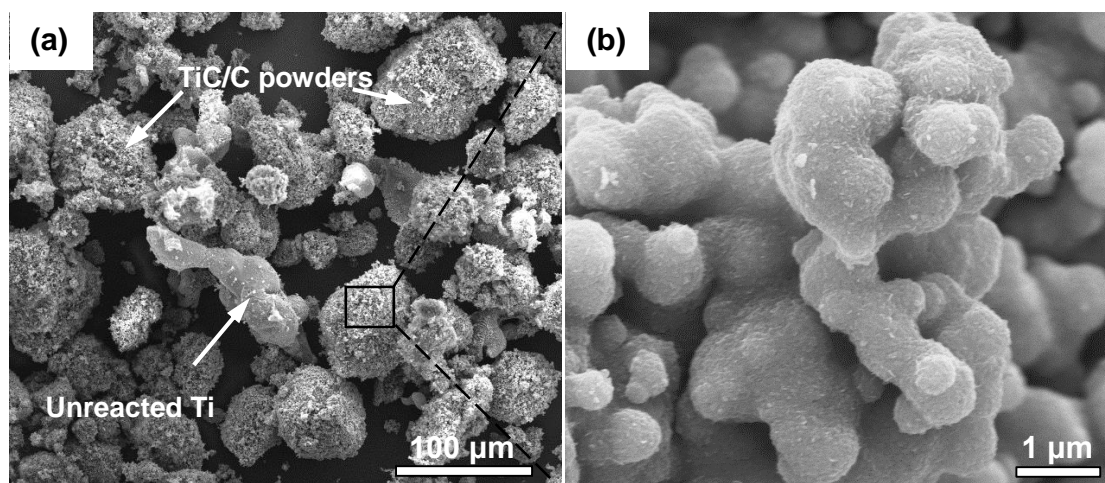


Fig. 4.13 (a) Low magnification and (b) high magnification SEM images of the resulting powders of firing the CB-Ti mixture (Ti/C = 1/8 in molar ratio) in the absence of KCl at 850 °C for 4 hours.

This is attributed to the interaction between metallic Ti powders and molten salt at the reaction temperature. Fig. 4.14 shows the microstructure of the Ti powders after firing in KCl at 850 °C for 4 hours. As shown in Fig. 4.2b, as-received Ti powders had irregular shapes with a micron-size (~44 μm), however, after firing in the molten salt at 850 °C for 4 hours, the size was reduced evidently, and some nano-sized particles (indicated by white arrows) were seen. Based on these results, it can be reasonable to speculate that the changes in shapes and size of Ti powders are attributed to dissolution of Ti in molten salt, although the solubility of Ti in KCl is unclear. Micron-sized Ti were partially dissolved into molten salt at high temperature, and then re-precipitated out of the salts upon cooling. Such a 'dissolution-precipitation' process was verified by the appearance of nano-sized Ti particles as shown in Fig. 4.14. The dissolved Ti would be readily diffused through the salt onto CB particles and then reacted with CB forming TiC coatings. This mechanism will be detailed in Chapter 8.

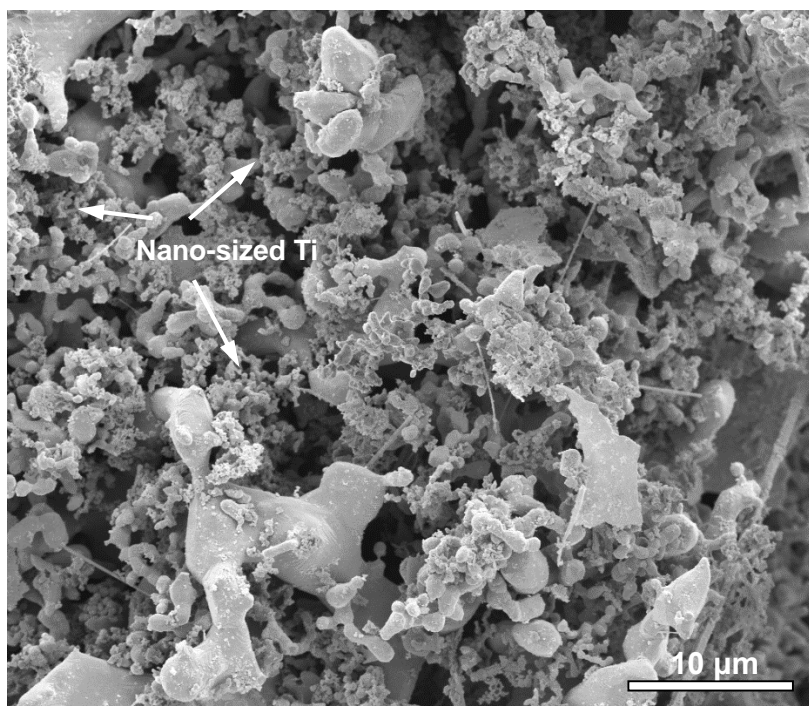


Fig. 4.14 SEM image of as-received Ti powders after firing in KCl at 850 °C for 4 hours.

4.2 Preparation of TiC coatings on CB using TiO₂/Ti

To further reduce the cost of preparing TiC coatings, relatively cheap TiO₂ was used as an alternative titanium source in molten salt synthesis. According to Razavi's study [197], the carbothermal reduction of TiO₂ and formation of TiC go through three stages:



TiO₂ will be reduced gradually by carbon, forming sub-oxides such as Ti₄O₇, Ti₃O₅ and Ti₂O₃. With carbothermal reduction progressing, part of oxygen in Ti_nO_{2n-1} will be replaced by carbon and intermediates with different O/C ratios in form of TiC_xO_y are formed before completely converting to TiC. So The overall process of the carbothermal reduction of TiO₂ is shown as follows:



4.2.1 Using TiO₂

TiO₂ was initially mixed with CB in molar ratio of 1/10 which is equivalent to 1/8 of Ti/C if the carbothermal reaction (Reaction 4.4) is completed. Fig. 4.15 shows XRD of the product powders of firing the mixtures of TiO₂ and CB (in the molar ratio of 1/10) (referred to as the CB-TiO₂ mixtures hereafter) at 950 °C with or without KCl. No TiC crystalline phase was detected by XRD after firing in the absence of KCl whereas phase transition of TiO₂ from anatase to rutile occurred (Fig. 4.15b). In contrast, in the presence of KCl, the intensity of TiO₂ peaks (Fig. 4.15c) decreased dramatically and some intermediate phases (TiO_x, x=1.83-1.89) were formed, indicating TiO₂ was slightly reduced by carbon in KCl. The fact shows that molten salt is beneficial to carbothermal reduction of TiO₂. Unfortunately, TiC was not obtained either, although the carbothermal reduction was initiated in KCl at 950 °C.

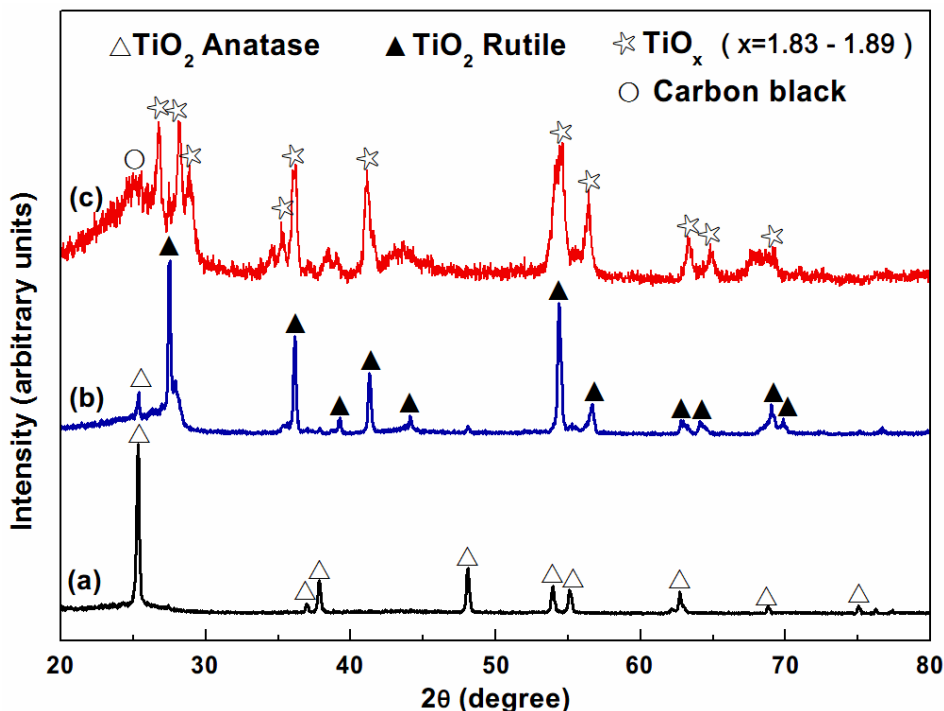


Fig. 4.15 XRD of the product powders of the CB- TiO_2 mixtures (with $\text{TiO}_2/\text{C} = 1/10$ in molar ratio) (a) before, and after firing at 950 °C for 4 hours (b) in the absence of KCl, and (c) in the presence of KCl.

When increasing temperature to 1200 °C, the carbothermal reduction of TiO_2 was accelerated in molten salt. As shown in Fig. 4.16a, the main phase of the product of firing the CB- TiO_2 mixture at 1200 °C for 4 hours in KCl was Ti_3O_5 (TiO_x , $x=1.67$), along with a small amount of Ti_2O_3 (TiO_x , $x=1.5$). When the holding time was extended to 8 hours, the intensity of Ti_2O_3 peak increased evidently, indicating a higher reduction extent. Comparison between Fig. 4.15c and Figs. 4.16a, b reveals that increasing reaction temperature and time can lead to a further reduction of TiO_2 to sub-oxides with lower O/Ti ratios. Nevertheless, in all cases, complete reduction of TiO_2 to TiC was still not achieved. However, TiC could be obtained (Fig. 4.16c) when a double stage heating schedule (950 °C-4 hours-1200 °C-4 hours) was employed. Furthermore, all titanium oxides disappeared, indicating TiO_2 was completely reduced and relatively pure TiC was formed. This is because the first stage (heating at 950 °C) significantly improved the mixing of TiO_2 and CB in a liquid medium (molten salt) so that carbothermal reduction could be completed at higher temperature (1200 °C) in the second stage.

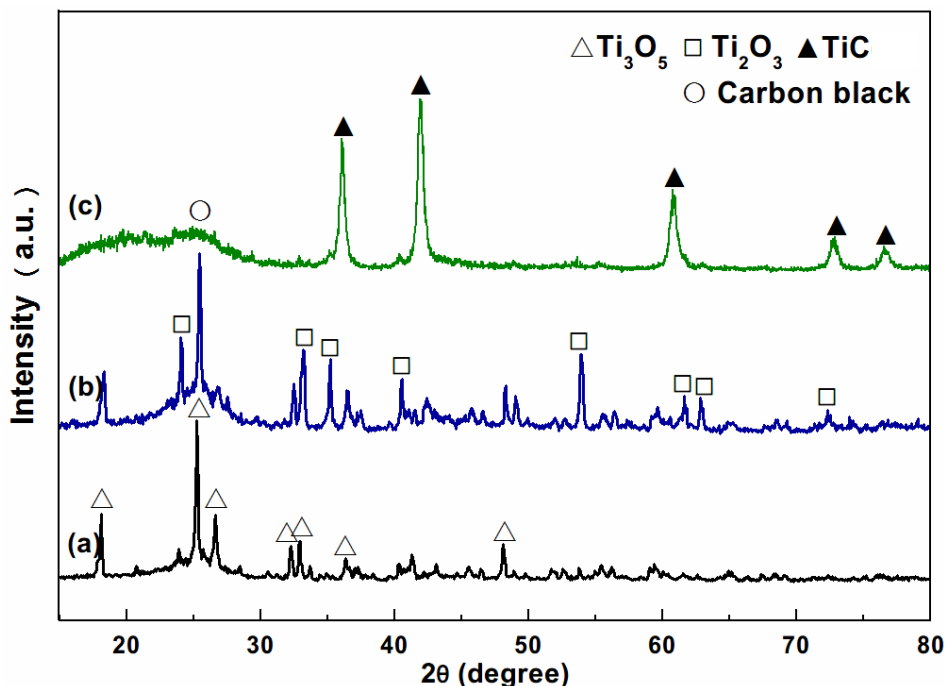


Fig. 4.16 XRD of product powders of firing the CB- TiO_2 mixtures (with $\text{TiO}_2/\text{C} = 1/10$ in molar ratio) in KCl (a) at 1200 °C for 4 hours, (b) at 1200 °C for 8 hours, and (c) at 950 °C for 4 hours and then 1200 °C for 4 hours.

The microstructures of the product powders of firing the CB- TiO_2 mixtures in molten salt were characterised by SEM, along with EDS analysis. Fig. 4.17a and b show the morphologies of the resulting powders prepared at 950 and 1200 °C, respectively. Micron-sized titanium oxide crystals such as TiO_x ($x=1.83-1.89$) and Ti_3O_5 confirmed by XRD (Fig. 4.15a and Fig. 4.16b) were found (as indicated by black arrows in Fig. 4.17a, b) in the resulting powders. However, as shown in Fig. 4.17c, they disappeared after the double stage heating process in KCl (at 950 °C for 4 hours and 1200 °C for 4 hours). EDS (Fig. 4.17e) did not detect any oxygen, indicating TiO_2 was completely reduced to TiC and none of the titanium oxide intermediate phases remained. A higher magnification SEM image (Fig. 4.17d) revealed that not all CB particles were coated with TiC. As indicated by the black arrows, TiC nanocrystals were observed on some of the CB particles, however, the surface of the rest of CB particles (indicated by the white arrows) remained smooth, which was similar to the surface of uncoated CB. Apparently, TiC coatings were not prepared on every individual CB particles, although a pure TiC was formed by the carbothermal reduction in KCl via the double stage heating process (950+1200 °C).

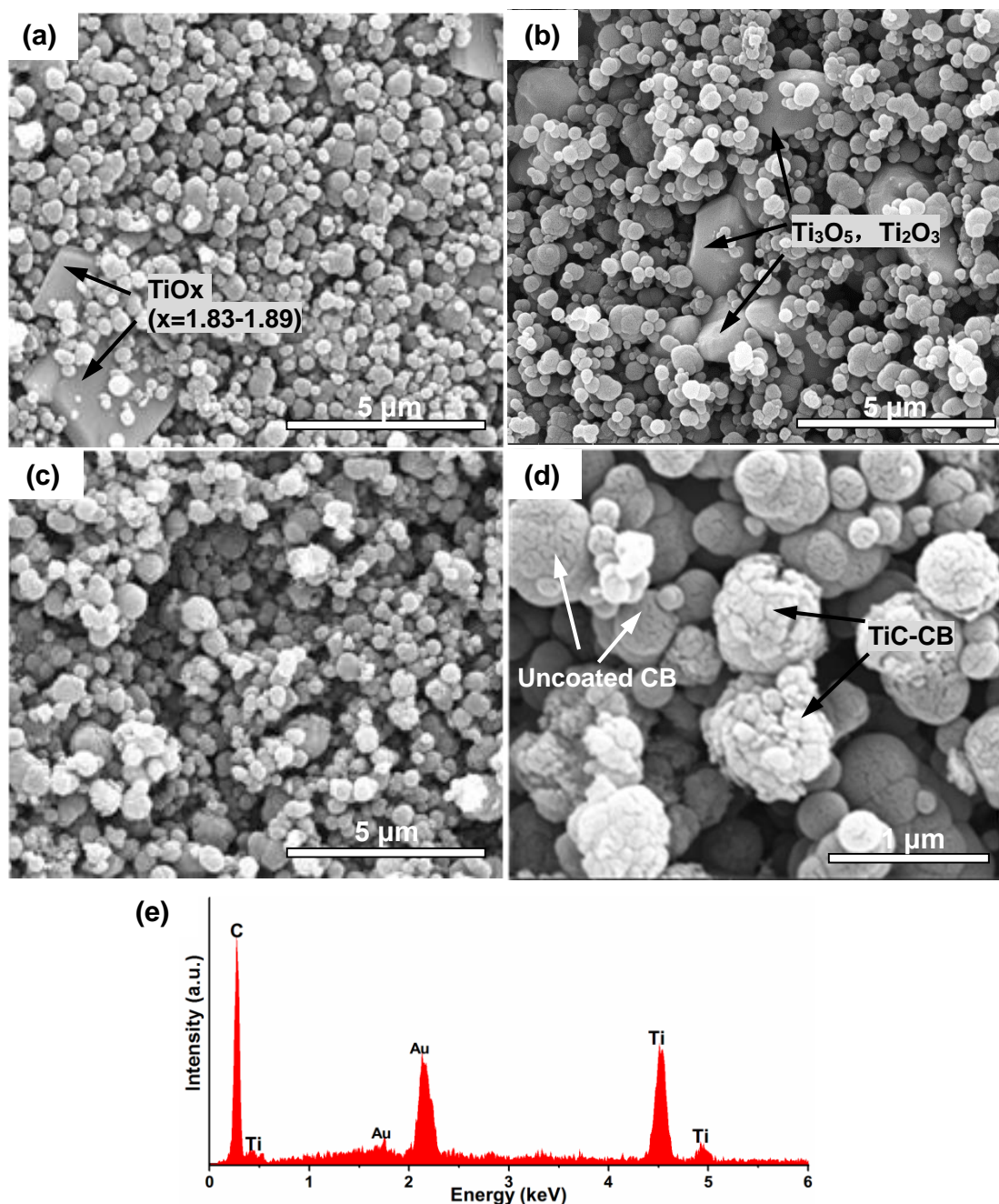


Fig. 4.17 SEM images of product powders of firing the CB-TiO₂ mixtures (with TiO₂/C = 1/10 in molar ratio) in KCl (a) at 950 °C for 4 hours, (b) at 1200 °C for 8 hours, and (c) and (d) at 950 °C for 4 hours and then 1200 °C for 4 hours; (e) Typical EDS spectrum of the coating shown in (d).

4.2.2 Using TiO₂ and Ti

Another attempt was made to prepare TiC coatings by using a combination of TiO₂ and Ti as the titanium source. To produce equivalent high quality TiC coatings on CB, the final molar ratio of Ti/C was set at 1/8, assuming all TiO₂ and Ti were converted to TiC after the reaction completed. Since the molar ratio of TiO₂/Ti is crucial to the

formation of TiC coatings in molten salt, the mixtures of TiO_2 , Ti and CB (referred to as the CB-Ti- TiO_2 mixtures hereafter) with different TiO_2/Ti molar ratios were prepared and fired in KCl at 950 °C. As shown in Fig. 4.18, only Ti_2O_3 was found after firing the mixture containing TiO_2 and Ti in molar ratio of 2/1. TiC formation was initiated at TiO_2/Ti molar ratio of 1/1. Upon decreasing to 1/3, titanium oxides (e.g. Ti_2O_3 and Ti_3O_5) disappeared and only TiC was detected along with unreacted CB (labelled by a small empty circle in Fig. 4.18d), indicating TiO_2 and Ti were completely consumed to form TiC. The phase evolution reveals pure TiC can be obtained from firing CB- TiO_2 -Ti in KCl at as low as 950 °C when the TiO_2/Ti molar ratio is strictly controlled $<1/3$.

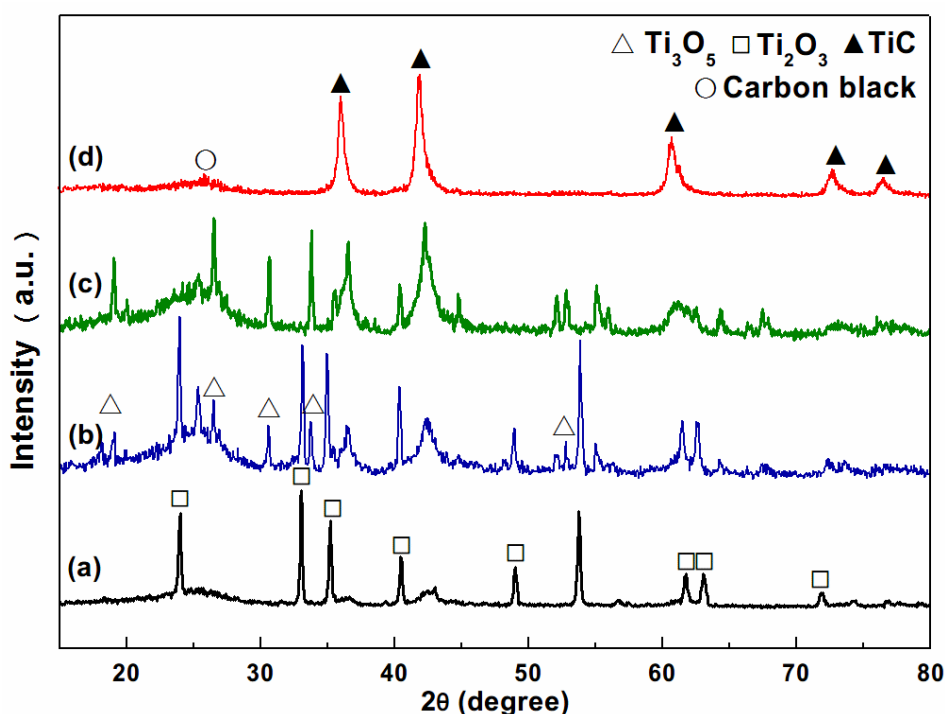


Fig. 4.18 XRD of the product powder of firing mixtures of TiO_2 , Ti and CB at 950 °C in KCl in TiO_2/Ti molar ratio of (a) 2/1, (b) 1/1, (c) 1/2, and (d) 1/3.

As concluded in Section 4.2.1, a high temperature is beneficial to carbothermal reduction of TiO_2 in molten salt. In order to prepare TiC by using TiO_2 and Ti in a higher molar ratio, the synthesis temperature was increased to 1050 °C. As shown in Fig. 4.19c, nearly a pure TiC was obtained, along with small amounts of titanium oxide intermediates when firing CB-Ti- TiO_2 mixture (with a TiO_2/Ti molar ratio of 1/2) in KCl at 1050 °C. The TiC peaks were shifted slightly to the right due to a small amount of oxygen remaining in TiC nanocrystals, thus they were assigned to TiC(O). In contrast, when TiO_2/Ti molar ratio increased to 1/1 and 2/1, sub-oxides after reduction of TiO_2 such as Ti_3O_5 was the main crystalline phase in the product

powders.

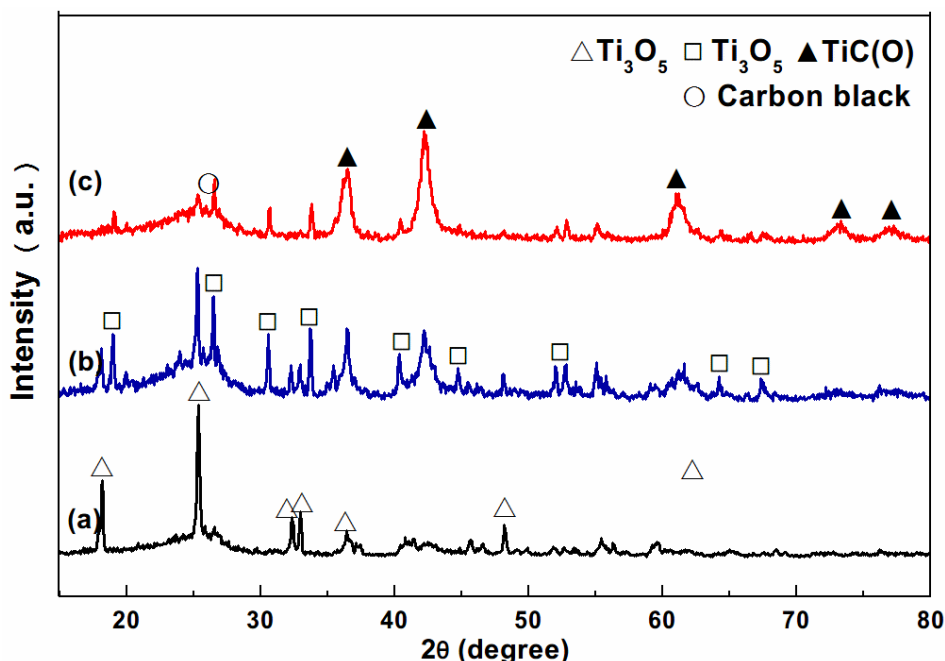


Fig. 4.19 XRD of the powders of firing mixtures of TiO_2 , Ti and CB at 1050°C in KCl in TiO_2/Ti molar ratio of (a) 2/1, (b) 1/1, (c) 1/2

As-prepared TiC/CB mixtures were further characterised and analyzed by SEM and EDS. Fig. 4.20a show the resulting powders of firing CB- TiO_2 -Ti mixture ($\text{TiO}_2/\text{Ti} = 1/3$ in molar ratio) at 950°C in KCl. The rough surface was clearly seen on spherical particles, indicating TiC phase was formed on CB. The as-prepared TiC coatings were in high quality (uniform, crack-free), similar to that prepared from Ti and CB. Elemental analysis (Fig. 4.20c) confirmed no titanium oxide remained in the resulting powders. However, upon increasing TiO_2/Ti molar ratio from 1/3 to 1/2 in the starting materials, TiC coatings cracked (Fig. 4.20b), although they were tightly attached on the CB surfaces. A minor amount of oxygen (Fig. 4.20d) was detected, showing minor amounts of titanium oxides still remained in the obtained powders, which was also confirmed by XRD (Fig. 4.19c). Therefore, the upper limit for replacing TiO_2 with Ti for the formation of TiC coatings is 25% mole percentage. When the molar ratio of TiO_2/Ti is $>1/3$, a higher temperature ($> 1050^\circ\text{C}$) will be required, but the TiC coatings will not be as high quality as expected.

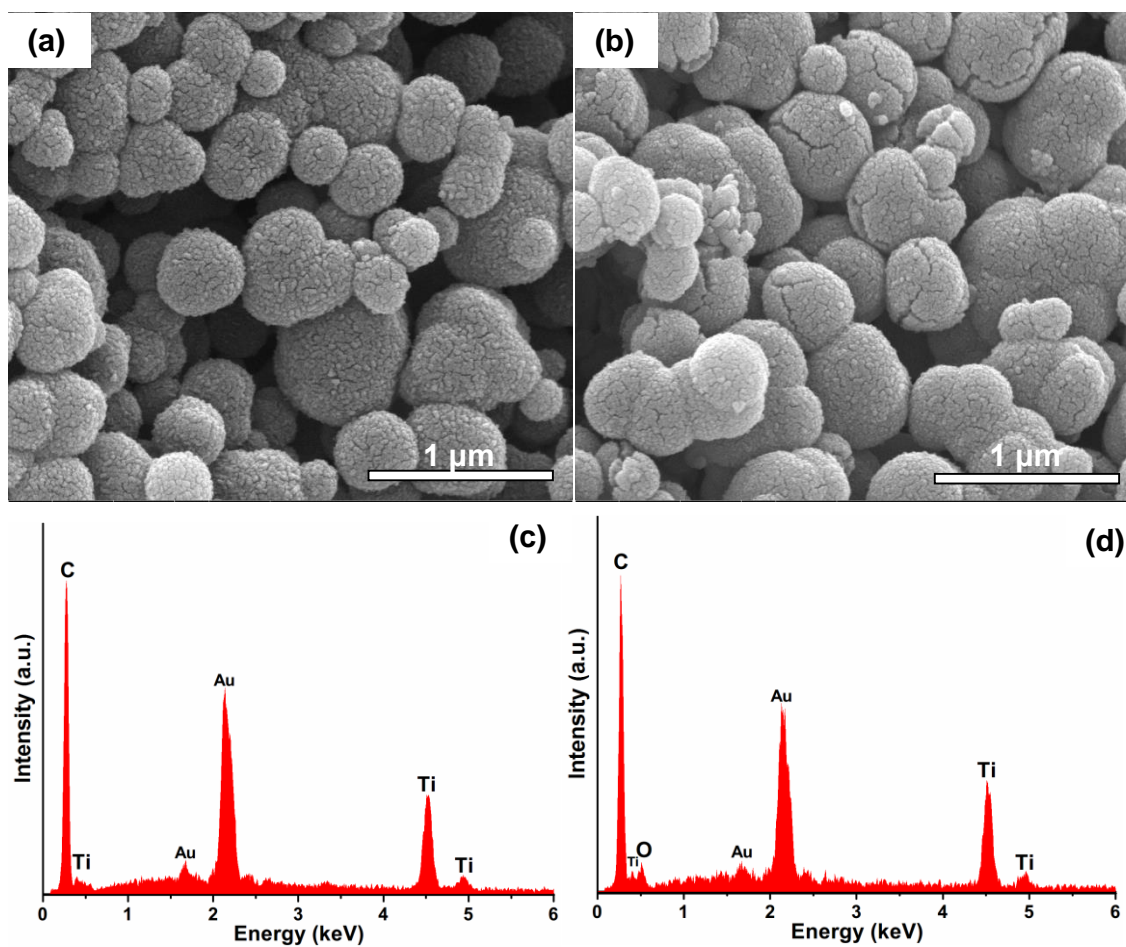


Fig. 4.20 SEM images of the resultant powders after firing TiO_2/Ti mixture in KCl at molar ratio of (a) and (b) 1/3 at 950 °C, (c) and (d) 1/2 at 1050 °C. Typical EDS spectra of the coatings, (e) shown in (b), and (f) shown in (d).

Chapter 5 Molten salt synthesis of SiC coatings on CB

In this chapter, SiC coatings were prepared on CB by using a molten salt synthesis technique. The effects of the size of Si powders, synthesis temperature, NaF-NaCl assembly, and Si/C molar ratios on SiC coating formation were investigated. The microstructure of SiC coated CB particles were characterised by SEM, EDS, TEM and SEAD. In addition, graded SiC/SiO₂ composite coatings were prepared by controlled oxidation of SiC-coated CB in air to further improve their water-wettability.

5.1 Preparation of SiC coatings on CB

5.1.1 Optimisation of SiC coating formation

To study the effect of the size of Si powders on SiC formation, CB particles were mixed with micron-sized Si (~44 μm) or nano-sized Si powders (<100 nm) in the Si/C molar ratio of 1/8 and fired under the same conditions. Fig. 5.1 shows XRD of the product powders of firing the mixtures of micron-sized Si and CB (micron-Si-CB) and nano-sized Si and CB (nano-Si-CB) respectively at 1200 °C for 8 hours in a NaF-NaCl binary salt containing 20 wt% NaF (referred to as 20%NaF-NaCl hereafter). In these two fired samples, Si peaks were absent and apart from the broad peak (centred at about 25.6°) attributed to the residual CB, only β-SiC peaks were seen. These results indicated that under this firing condition both micron-sized and nano-sized Si had completely reacted with CB to form β-SiC, which further indicated that cheaper micron-sized Si powders instead of expensive nano-sized Si powders (which were used to react with carbon nanotubes forming SiC nanorods [149]) could be used to prepare SiC. Therefore, micron-sized Si powders were used as the main silicon source in the following experiments.

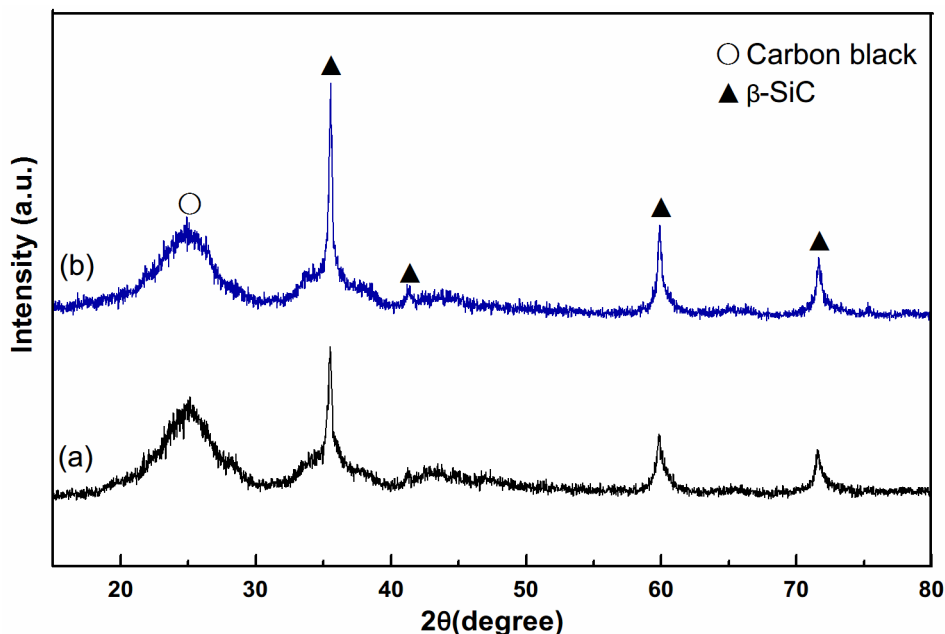


Fig. 5.1 XRD of the powders of firing the mixtures of (a) micron-sized Si and CB, and (b) nano-sized Si and CB at 1200 °C for 8 hours in 20%NaF-NaCl.

Fig. 5.2 shows phase evolution in the mixtures of Si and CB (with the molar ratio of 1/8) (referred to as the 1/8 Si-CB mixture hereafter) after 6 hours firing in 20%NaF-NaCl, at various temperatures. At 900 °C, no SiC was formed and only unreacted carbon (indicated by the broad peak) and Si remained, whereas at 1000 °C, SiC started to appear and Si peaks concurrently decreased. On increasing the temperature to 1100 °C, Si disappeared and only SiC was seen along with unreacted carbon. On further increasing the temperature to 1200 °C, no further phase changes were seen, though the peaks of SiC became slightly sharper, indicating its enhanced crystallinity or increased size.

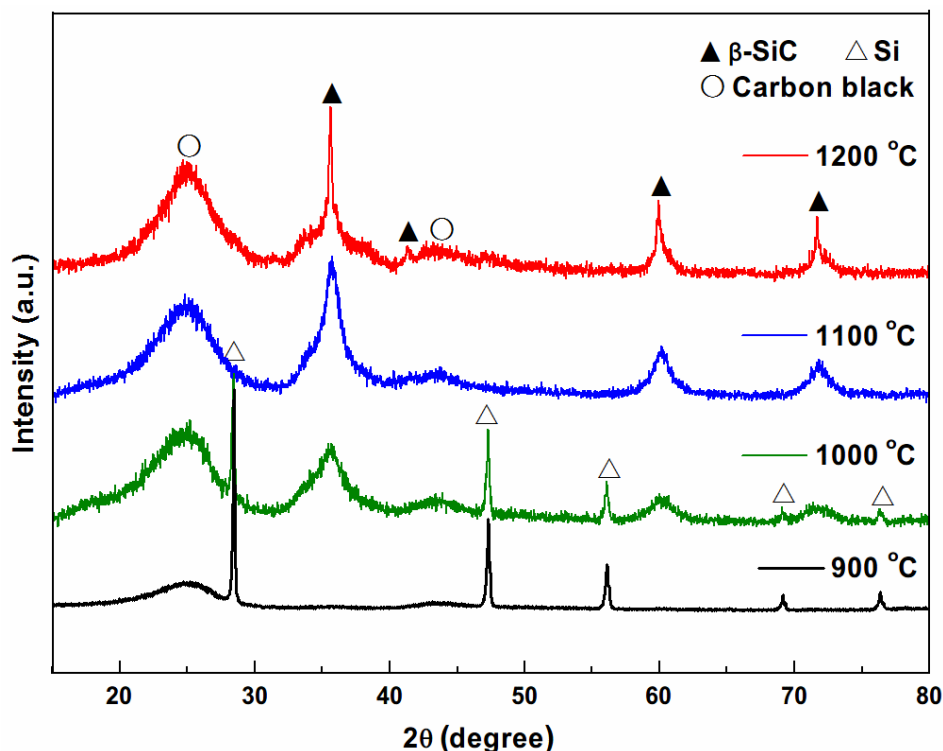


Fig. 5.2 XRD patterns of the product of firing mixtures of Si and CB (in the molar ratio of 1/8) for 6 hours in 20%NaF-NaCl at 900, 1000, 1100 and 1200 °C.

To investigate the effect of NaF on the SiC synthesis, the 1/8 Si-CB mixtures were also fired in NaCl-based salt containing different amounts of NaF. Fig. 5.3 presents XRD patterns of products of firing the 1/8 Si-CB mixtures after 6h at 1100 °C in a NaCl-based salt containing 0, 1.25, 2.5 or 5 wt% NaF. Almost no SiC was detected in the absence of NaF. However, when 1.25 wt% NaF was used in the salt, SiC peaks started to appear and Si peaks decreased concurrently. On further increasing the NaF content to 2.5 wt%, Si disappeared and only SiC along with unreacted carbon was present. In addition to the primary SiC peaks, two tiny shoulder peaks at $2\theta \approx 33.78^\circ$ and 38.01° (marked as black stars) were seen, in particular, in the case of using 1.25 wt% NaF. They are believed to arise from the stacking faults commonly existing in β -SiC.[198, 199] Further increasing the NaF content to 5 wt% did not result in any further phase changes, but the two small shoulder peaks almost disappeared. The XRD pattern in this case was almost identical to that when using 20 wt% NaF (Fig. 5.2), indicating that 2.5-5 wt% NaF in the binary salt was sufficient for the MSS process of SiC.

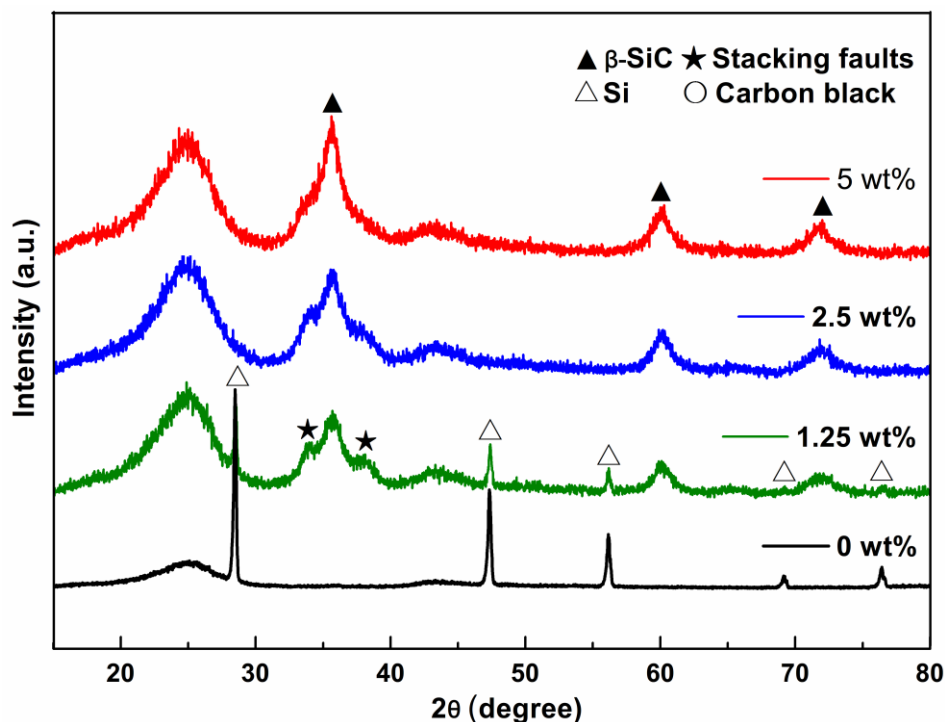


Fig. 5.3 XRD patterns of the product of firing mixtures of Si and CB (in the molar ratio of 1/8) at 1100 °C for 6 hours in a NaCl-based salt containing 0, 1.25, 2.5 and 5 wt% NaF.

5.1.2 Morphological changes of Si-CB mixtures after firing

Figs. 5.4 a and b show respectively typical SEM images of micron-Si-CB mixture and nano-Si-CB mixture. The difference in Si particle size was clearly demonstrated (indicated by white arrows). Micron-sized Si particle is ~ 440 times larger than nano-sized Si particle. After dispersion treatment, the agglomeration of nano-sized particles was not observed (indicated as the insert in Fig. 5.4b). However, after firing starting material mixtures at 1200 °C, the resultant powders in both cases exhibited almost the same morphologies. Si powders in micron-scale or nano-scale disappeared and spheres similar to CB particles were seen (Figs. 5.4c, d), which was consistent with the phase analysis (Fig. 5.1). Furthermore, it also verified that it was feasible to replace nano-sized Si with micron-sized Si to synthesize SiC on CB.

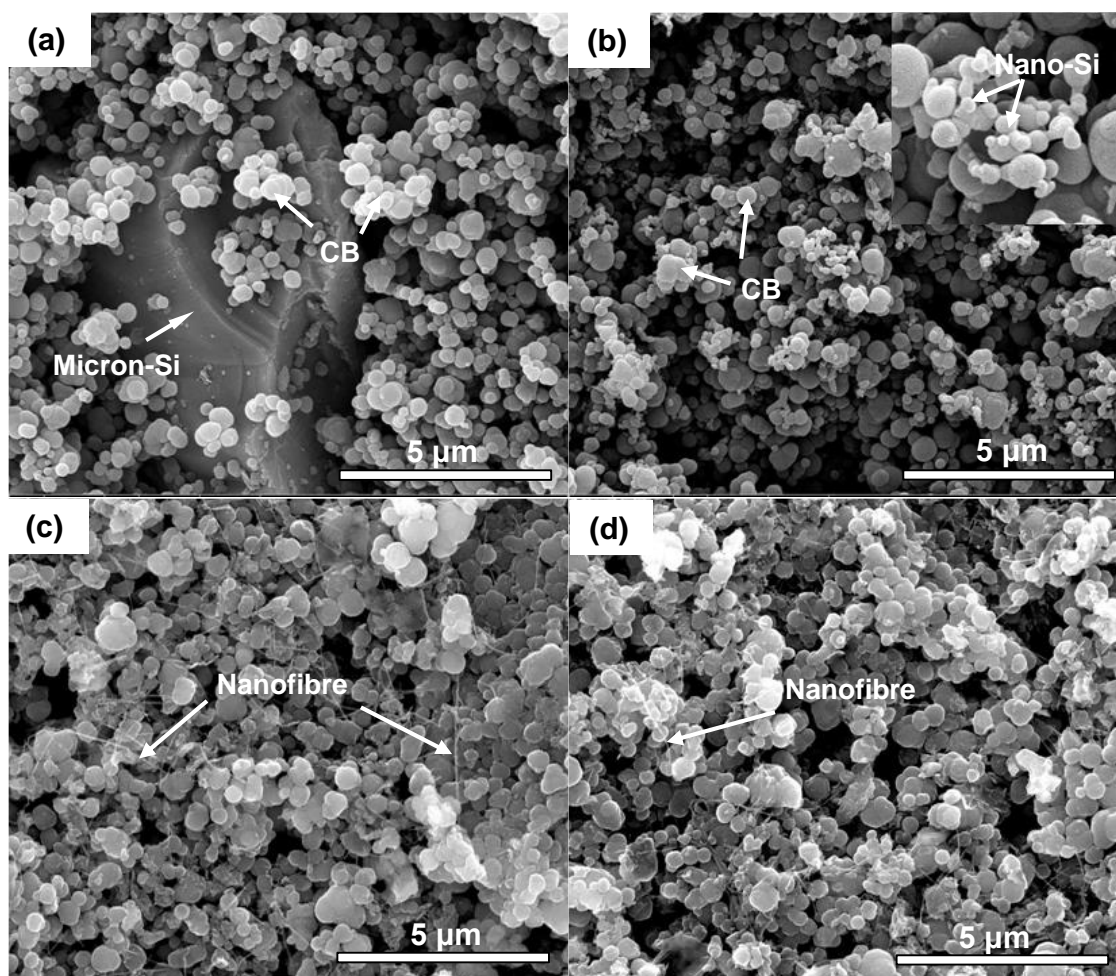


Fig. 5.4 SEM images of the micron-Si-CB mixture (a) before and (c) after firing at 1200 °C for 8 hours in 20%NaF-NaCl; the nano-Si-CB mixture (b) and (d) after firing under the same firing conditions.

In addition, a small amount of nanofibres were also seen in the fired samples (indicated by white arrows in Figs. 5.4c, d). To identify these nanofibres, further characterisations were carried out. As shown in high resolution SEM images (Fig. 5.5a, b), the nanofibres were distributed in the gaps of C/SiC composite spheres, and had high length/diameter ratios and the average diameter of ~40 nm (Fig. 5.5b). TEM images (Fig. 5.5c) further revealed that these nanofibres were bamboo-like. Their crystal structure was determined by selected area electron diffraction (SAED). Both these nanofibres and C/SiC spheres showed similar diffraction patterns (Fig. 5.5e, f) which were assigned to the (111), (220), (311) planes of 3C-SiC (also called β -SiC). These results confirmed that the nanofibres were SiC, and also revealed polycrystalline nature of the formed SiC phase.

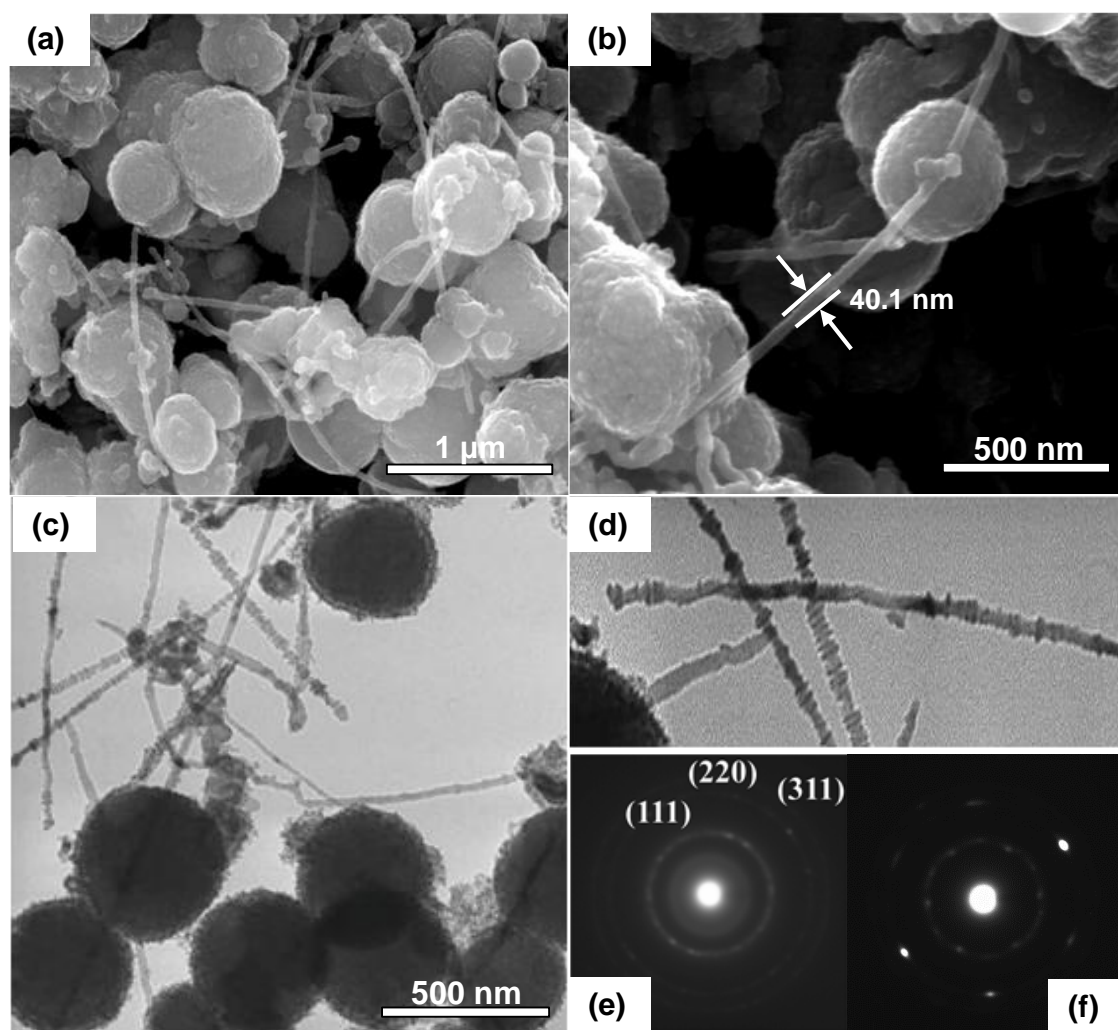


Fig. 5.5 (a) and (b) magnified SEM images, and (c) and (d) TEM images of nanofibres and C/SiC composite spheres in resulting powders of firing micron-Si-CB mixture at 1200 °C for 8h in 20%NaF-NaCl; (e) An SAED pattern from C/SiC composite spheres shown in (c); (f) An SAED pattern from nanofibres shown in (d).

The morphologies of the resulting powders prepared at lower temperature (1100 °C) were also examined by SEM. Phase analysis in Fig. 5.2c confirmed that the reaction of Si and CB (in molar ratio of 1/8) was completed at 1100 °C, even in a NaCl-based salt containing less NaF (2.5-5 wt%) (Fig. 5.3c, d). Fig. 5.6 shows SEM images of the resulting powders prepared at 1100 °C in NaCl-based salts containing respectively 20 wt% and 5 wt% NaF, exhibiting almost the same morphologies in both cases. Only spheres with rough surface were presented, indicating the reduction in NaF content in the binary salts had no negative effect on the SiC formation and products' morphologies.

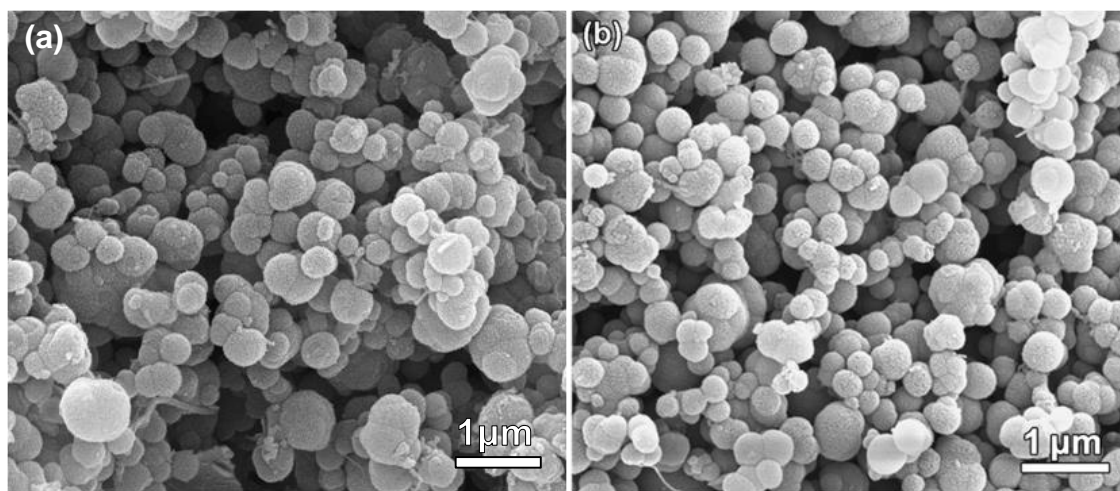


Fig. 5.6 SEM images of the product powders of firing 1/8 Si-CB mixtures at 1100 °C for 6 hours in NaCl based salt containing (a) 20 wt% and (b) 5 wt% NaF.

5.1.3 Microstructural characterisation of SiC-coated CB spheres

5.1.3.1 Core-shell structure of CB-SiC spheres

To reveal the microstructure of CB/SiC composite spheres, characterisation on individual particles were performed by using high resolution SEM and TEM. As shown in Fig. 5.6b, Si disappeared after firing at 1100 °C for 6 hours in 5%NaF-NaCl and only spherical particles were seen. These particles showed similar morphologies and sizes to the unreacted CB particles, but exhibited rougher surfaces, indicating new phase formation on their surfaces. Incomplete coverage was occasionally seen on some of these spherical particles (Fig. 5.7a), seemingly revealing the formation of a core-shell structure. EDS (Fig. 5.7b) further reveals that the shell contained mainly carbon and silicon, along with minor oxygen arising from some contamination [200]. This, along with the corresponding XRD (Fig. 5.3) verified the formation of SiC coatings (containing minor oxygen) on CB particles. The core-shell structure of the spherical particles shown in Fig. 5.6b can be more directly revealed by TEM (Fig. 5.8a). The black contrast shells with fairly consistent thicknesses were identified as SiC by SAED (not shown). High resolution TEM (Fig. 5.8b) reveals that the SiC shells were composed of nanocrystals about 10 nm in size. Furthermore, the main lattice interlayer distance was identified as ~0.25 nm which corresponds to the (111) plane of β -SiC.

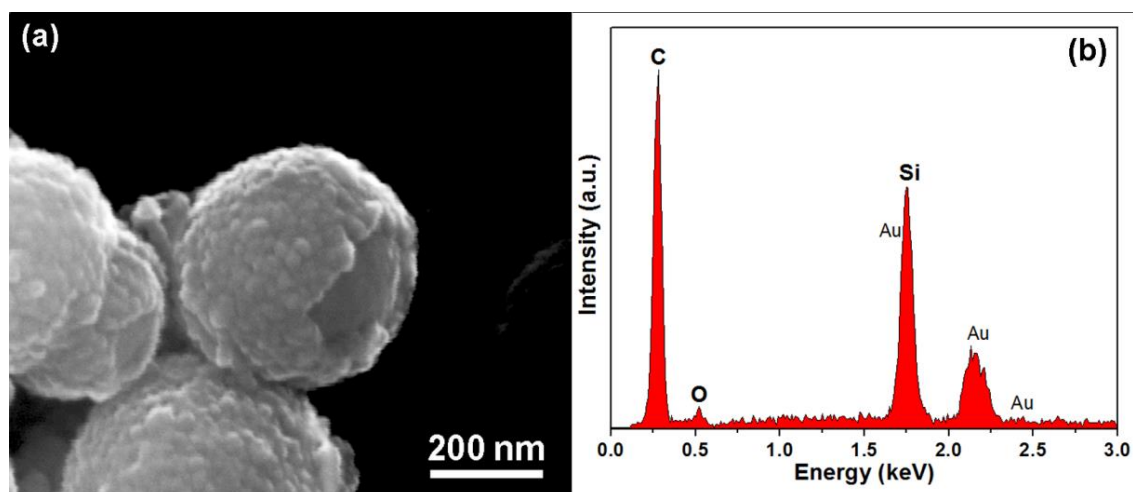


Fig. 5.7 (a) SEM image of CB particles showing some incomplete SiC coverage, which were occasionally found in the microstructure shown in Fig. 5.6b. (b) Typical EDS spectrum of the coating shown in (a).

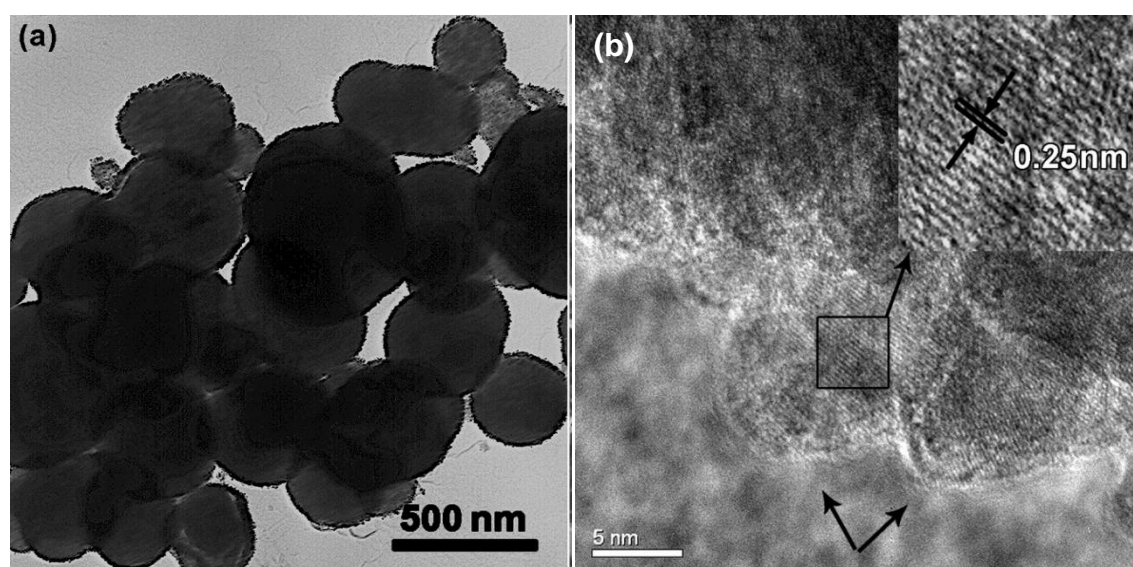


Fig. 5.8 TEM images of (a) SiC coated carbon black particles, and (b) High resolution TEM image of a typical SiC coating on a carbon black particle. The inset reveals the regular stacking sequence of β -SiC.

5.1.3.2 Hollow SiC spheres

Since CB is more vulnerable to oxidation than SiC, the carbon cores could be removed by oxidation in air at an appropriate temperature (in this case 600 °C) to further reveal the formation of SiC coatings. Nevertheless, the oxidation temperature and time are crucial and so need to be carefully optimised. If the oxidation temperature is too low or the time is too short, carbon cores will not be completely removed. On the other hand, if the temperature is too high or the time is too long, although carbon cores can be removed completely, part of the SiC shell might also be oxidised to silica (SiO_2). Trials under different conditions (500-700 °C

for 30-90 minutes) revealed that the optimal oxidation condition was 90 minutes at 600 °C. This condition was slightly different from that (600-700 °C for 2 hours) used by Zhang et al [201] and Liu et al [202]. However, even under this optimal oxidation condition, there was still some minor oxidation of SiC. Consequently, a small amount of amorphous SiO₂ were always detected in the samples after the oxidation treatment. As shown in Fig. 5.9 (Curve a), after oxidation under the optimal condition, the two broad peaks of CB disappeared, but a new broad peak (around $2\theta = 22.01^\circ$) attributable to amorphous SiO₂ appeared. The presence of SiO₂ in the sample after oxidation treatment was also revealed by FTIR (Fig. 5.10a). As shown in Fig. 5.10a, in addition to the intensive sharp peak at around 820 cm⁻¹ arising from the fundamental stretching vibration of SiC, two other absorption bands at 1095 and 471 cm⁻¹ respectively were found. These two bands were attributed to the antisymmetric and symmetric stretching vibrations of Si-O-Si bonds, respectively. [203]

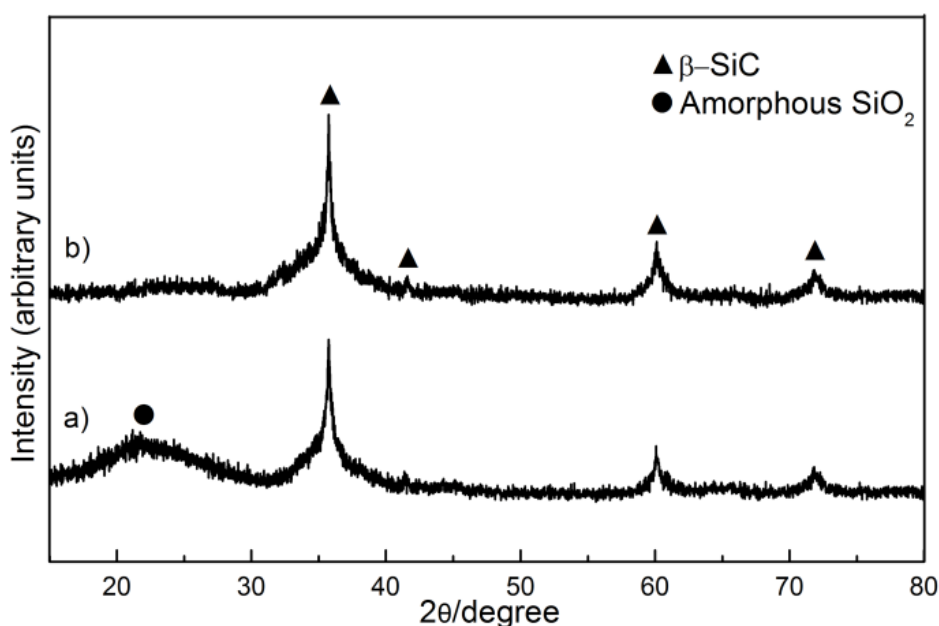


Fig. 5.9 XRD of (a) hollow SiC spheres obtained after oxidizing SiC coated CB spheres in air at 600 °C for 90 minutes and (b) final hollow SiC spheres obtained after the NaOH treatment.

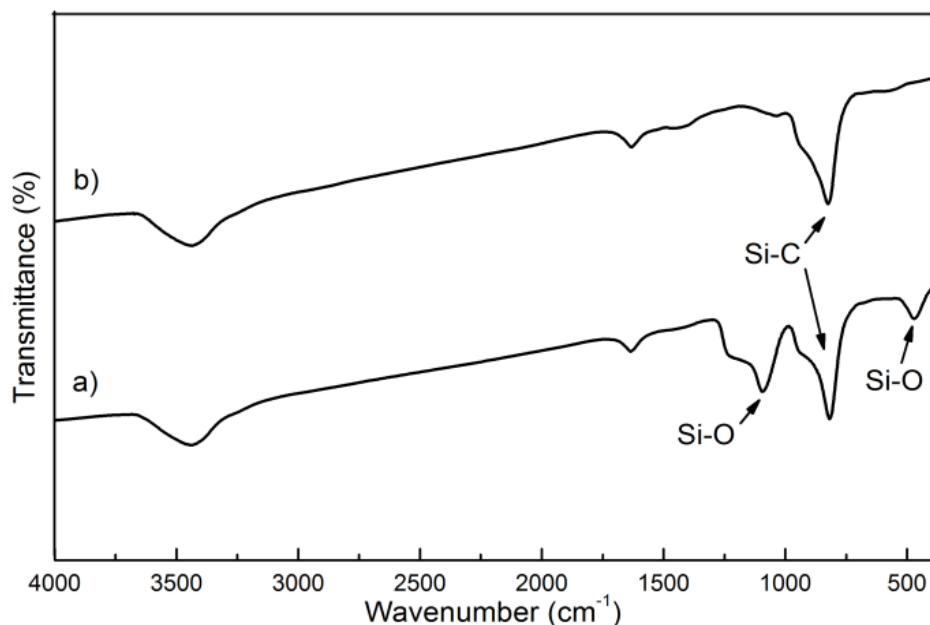


Fig. 5.10 FTIR spectra of SiC hollow spheres: (a) before and (b) after the NaOH treatment.

A 40 wt% NaOH solution was used to etch out the amorphous SiO₂ present in the samples. As shown in Fig. 5.9 (Curve b), the broad SiO₂ peak disappeared after such treatment. The absence of amorphous SiO₂ after the NaOH treatment was also confirmed by FTIR (Fig. 5.10b) which shows that while the absorption band of SiC still remained, the Si-O absorption bands disappeared.

After such oxidation removal of carbon cores, hollow SiC spheres remained, which were demonstrated by SEM and TEM characterisation. Fig. 5.11a shows that spherical particles were obtained and their surfaces were rough and composed of nanosized SiC particles (Fig. 5.11b). Occasionally some broken SiC spheres or spheres with small holes (up to ~100 nm) were seen, indirectly indicating their hollow structures. The hollow structure can be seen more clearly and directly from TEM images (Figs. 5.11 c, d). Near-spherical hollow spheres were observed (Fig. 5.11c). Some small (20-100 nm) holes (bright contrast areas indicated by the arrows) were also seen in some of the shells (Fig. 5.11d), which might be created during the oxidation treatment, although further work is needed to clarify this.

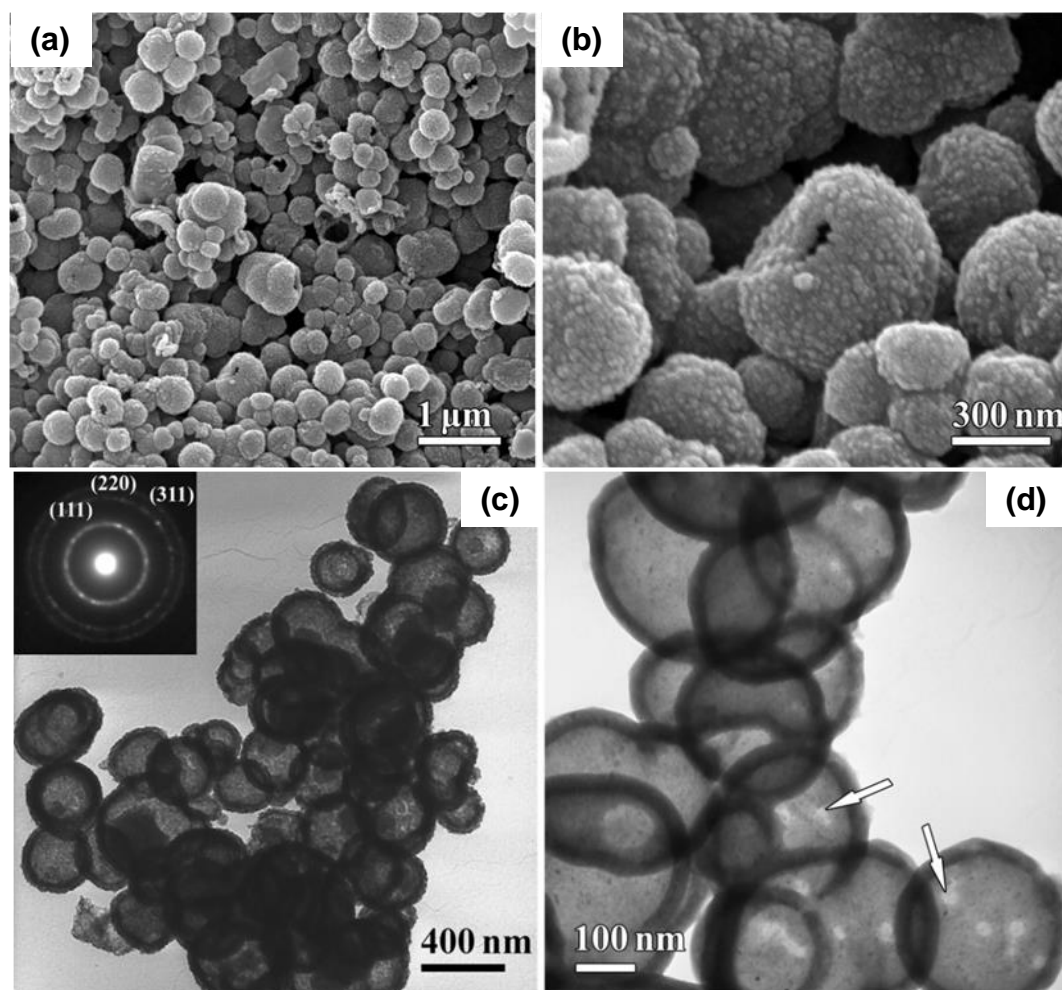


Fig. 5.11 (a) and (b) SEM images, and (c) and (d) bright field TEM images of hollow SiC spheres after carbon core removal, followed by the NaOH treatment: The insert in (c) is an SAED pattern from SiC shell.

5.1.4 Effect of Si/C ratio on SiC formation

5.1.4.1 Preparation of 'thicker' SiC coatings on CB

Fig. 5.12 shows XRD patterns of the powders resulting from firing Si-CB mixtures in molar ratio of 1/4 and 1/2, respectively at 1100-1150 °C in molten salt. At 1100 °C, small Si peaks in addition to intensive SiC peaks were detected in the fired sample with Si/C molar ratio of 1/4, indicating not all Si powders were completely reacted to form SiC. However, when the heating temperature was increased to 1150 °C, only SiC crystalline phase was present in the fired samples (in molar ratio of 1/4 and 1/2). These results showed that the increase in the molar ratio of Si/C would require slightly higher temperature to complete the reaction within the same reaction time. Meanwhile, compared with XRD of SiC coated CB prepared from Si/C molar ratio of 1/8 (Fig. 5.3), the intensity of SiC peaks increased with higher Si/C molar ratio, and

carbon peaks decreased concurrently, indicating more SiC were formed. SEM images (Fig. 5.13) show that the resultant particles appeared similar morphologies and sizes to unreacted CB particles and SiC-coated CB prepared in lower Si/C molar ratio (1/8) (Fig. 5.6). In this case, more Si was consumed and converted to SiC coatings on CB, indicating the coating thickness was most likely increased with Si/C molar ratio. This will be verified by TEM in the later section.

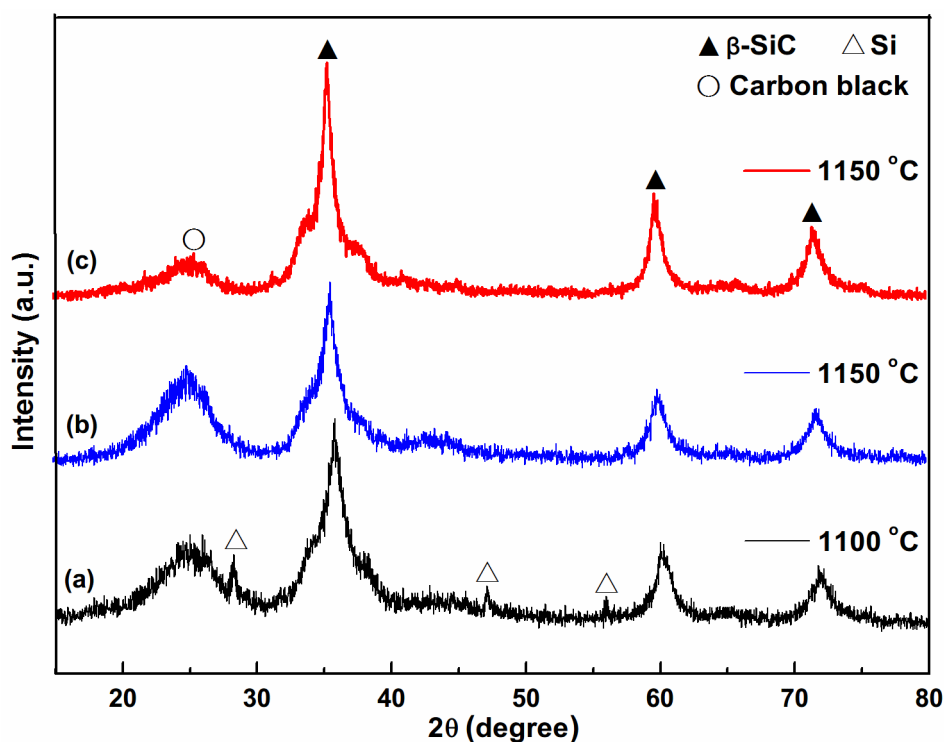


Fig. 5.12 XRD of the product powders of firing Si-CB mixtures in molar ratio of (a) 1/4 at 1100 °C, (b) 1/4 at 1150 °C, and (c) 1/2 at 1150 °C in NaCl-based salt containing 5 wt% NaF.

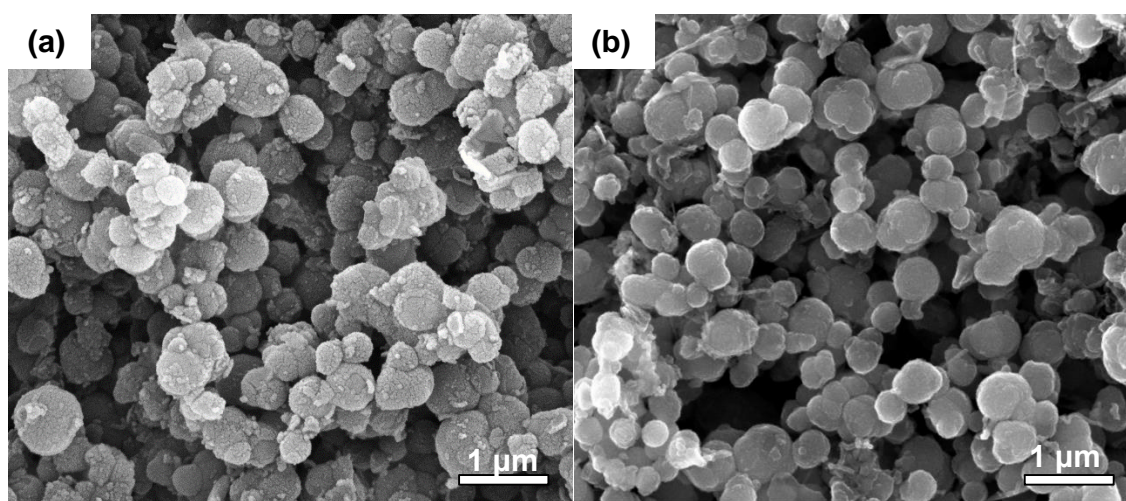


Fig. 5.13 SEM images of the powder of firing Si-CB mixtures in molar ratio of (a) 1/4 (b) 1/2 at 1150 °C for 6 hours in NaCl-based salt containing 5 wt% NaF.

5.1.4.2 SiC coating thickness

Based on above results, it can be concluded that the SiC coating thinness could be readily tailored by controlling the molar ratio of Si to CB (Si/C). The different thicknesses of SiC coatings prepared in different molar ratios of Si/C were both theoretically calculated and experimentally determined.

1) Theoretical calculation of SiC coating thickness

A SiC-coated CB sphere model shown in Fig. 5.14 was built up for theoretical calculation of thickness of coating layer, based on the following two main assumptions.

- i. The volume expansion of the CB sphere does not occur after reaction.
- ii. The formed SiC nanocrystals are closely packed and SiC coatings are firmly bonded on the carbon core. In other words, the true density of the formed SiC coating is 3.21 g/cm^3 which is as same as that of the bulk SiC.

The initial diameter of CB sphere is supposed to be D_0 , the diameter of CB sphere after reaction D_1 , and the diameter of SiC-coated CB sphere D_2 . Furthermore, the mole number of an individual CB sphere is supposed to be n_0 and the mole number be reduced to n after molten salt reaction completes. In addition, it is assumed that the model SiC-coated CB sphere is prepared from an initial mixture of Si and C in the molar ratio of $1/x$ (i.e., 1 mole silicon and x mole CB were mixed for preparation of SiC-coated CB). As we know, the density of CB is $\rho = 1.89 \text{ g/cm}^3$, and its molar mass is $M = 12 \text{ g/mol}$.

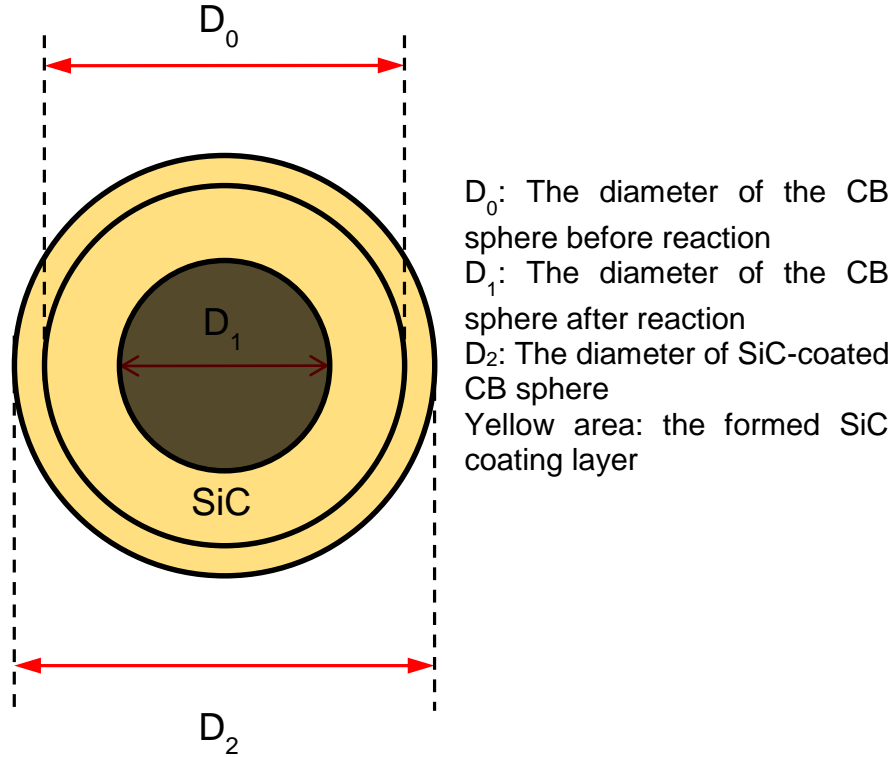


Fig. 5.14 A schematic diagram of a typical SiC-coated CB sphere.

The volume of CB particle before reaction is calculated as

$$V_0 = \frac{4}{3} \pi \left(\frac{D_0}{2} \right)^3 \quad (5.1)$$

If all of Si completely react with CB after reaction, the volume of residual CB should be

$$V_1 = \frac{4}{3} \pi \left(\frac{D_1}{2} \right)^3 \quad (5.2)$$

The volume of SiC-coated CB sphere is

$$V_2 = \frac{4}{3} \pi \left(\frac{D_2}{2} \right)^3 \quad (5.3)$$

Based on $V=m/\rho$, $m= M \cdot n$, the ratio of carbon volume before and after reaction is expressed as

$$\frac{V_1}{V_0} = \frac{m_1/\rho}{m_0/\rho} = \frac{m_1}{m_0} = \frac{M \cdot n_1}{M \cdot n_0} = \frac{n_1}{n_0} = \frac{x-1}{x} \quad (5.4)$$

Or

$$\frac{V_1}{V_0} = \frac{\frac{4}{3} \pi \left(\frac{D_1}{2} \right)^3}{\frac{4}{3} \pi \left(\frac{D_0}{2} \right)^3} = \left(\frac{D_1}{D_0} \right)^3 \quad (5.5)$$

By combining Equations 5.4 and 5.5, D_1 can be written as a function of x ,

$$D_1 = D_0 \sqrt[3]{\frac{x-1}{x}} \quad (5.6)$$

After 1 mole Si completely reacts with 1 mole CB, 1 mole SiC will be produced, thus,

$$n_{\text{SiC}} = n_{\text{Si}} = n_{(\text{consumed C})} \quad (5.7)$$

The ratio of the volume of SiC to consumed CB is

$$\frac{V_{\text{SiC}}}{V_{\text{consumed C}}} = \frac{m_{\text{SiC}}/\rho_{\text{SiC}}}{m_{\text{C}}/\rho_{\text{C}}} = \frac{n_{\text{SiC}}M_{\text{SiC}}/\rho_{\text{SiC}}}{n_{\text{consumed C}}M_{\text{C}}/\rho_{\text{C}}} = \frac{M_{\text{SiC}}\rho_{\text{C}}}{M_{\text{C}}\rho_{\text{SiC}}} = \frac{40 \times 1.88}{12 \times 3.21} = 1.96 \quad (5.8)$$

Also, we have

$$V_{\text{SiC}} = V_2 - V_1 \quad (5.9)$$

$$V_{\text{consumed C}} = V_0 - V_1 \quad (5.10)$$

By combining Equations 5.5, 5.6, 5.8, 5.9 and 5.10, we can have,

$$V_2 = V_0 \left[1.96 - \frac{0.96(x-1)}{x} \right] \quad (5.11)$$

$$D_2 = D_0 \sqrt[3]{1.96 - \frac{0.96(x-1)}{x}} \quad (5.12)$$

Therefore, the thickness of SiC coating, t , on the surface of carbon black is

$$t = \frac{D_2 - D_1}{2} = \frac{D_0}{2} \left[\sqrt[3]{1.96 - \frac{0.96(x-1)}{x}} - \sqrt[3]{\frac{x-1}{x}} \right] \quad (5.13)$$

Clearly, the thickness of SiC coatings is a function of the initial diameter of CB sphere and Si/C molar ratio. When D_0 is set as 300 nm, the corresponding SiC coating thicknesses corresponding to various Si/C molar ratios can be calculated and listed in Table 5.1.

Table 5.1 Thickness of SiC coating as a function of molar ratio of Si/C=1/x.

| Molar ratio of Si/C | 1/12 | 1/10 | 1/8 | 1/6 | 1/4 | 1/2 |
|----------------------------|------|------|------|------|------|------|
| x | 12 | 10 | 8 | 6 | 4 | 2 |
| SiC coating thickness (nm) | 8.2 | 9.8 | 12.3 | 16.4 | 24.9 | 51.9 |

2) Experimental measurement of SiC coating thickness

Due to mass-thickness contrast and Bragg contrast of TEM image formation, SiC shell and carbon core were distinguished by different contrasts. So the thickness of

SiC shell can be estimated by measuring the width of dark ring over the carbon core. Fig. 5.15 shows TEM images of four individual SiC-coated CB spheres prepared using different molar ratios of Si/C from 1/12 to 1/2. The thicknesses of SiC coatings were estimated based on these TEM images. As shown in Fig. 5.16, with increasing Si/C from 1/12 to 1/2, the SiC coating thickness continuously increased, from ~12 nm to ~66 nm. These results are closed to the ones obtained from the theoretical calculations, indicating that the theoretical calculation based on specific Si/C molar ratio can be used to predict the SiC coating thickness.

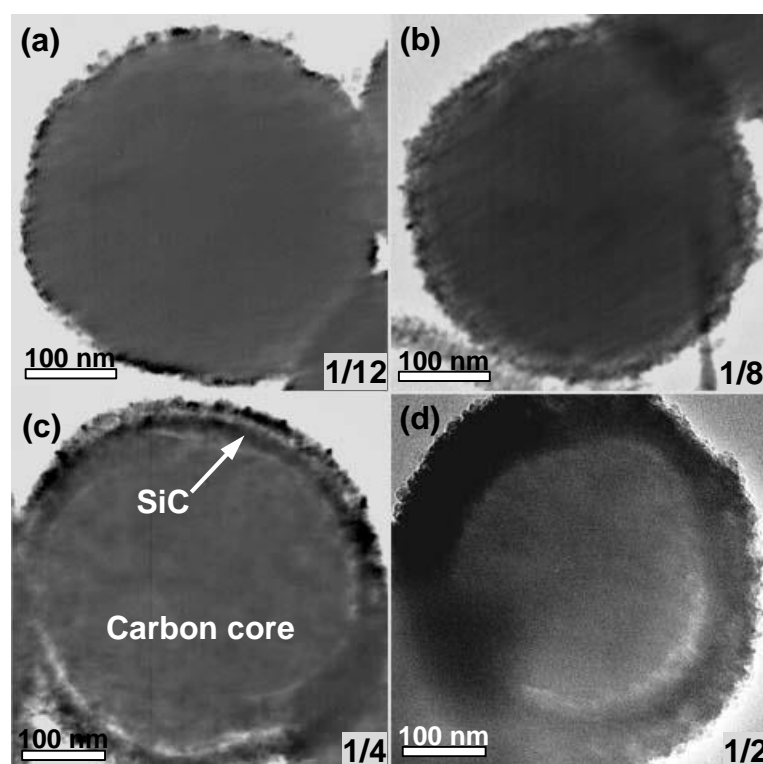


Fig. 5.15 Typical TEM images of individual SiC-coated CB particles prepared using various molar ratios of Si/C: (a) 1/12; (b) 1/8; (c) 1/4 and (d) 1/2, respectively.

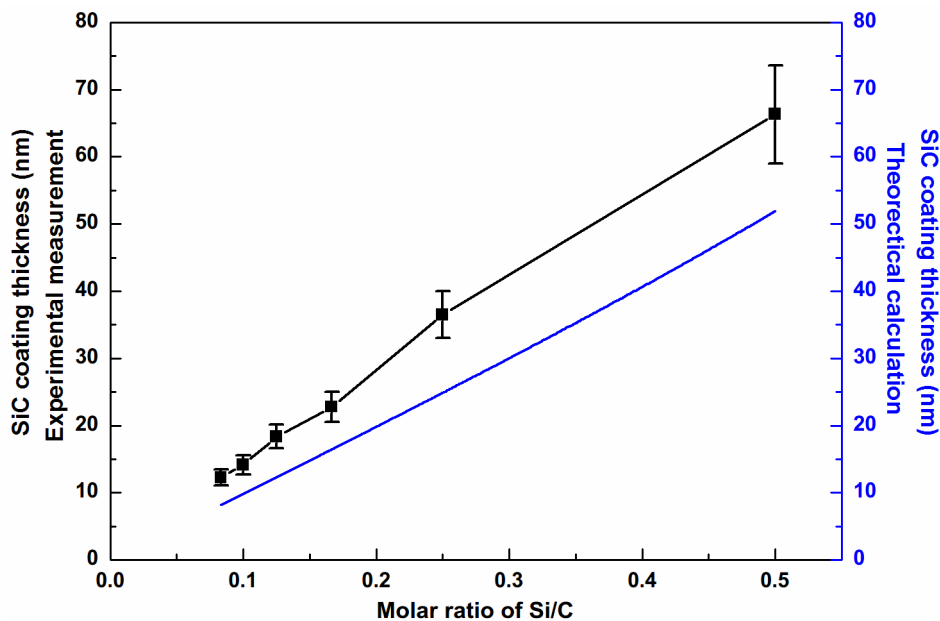


Fig. 5.16 Thickness of SiC coatings corresponding to different molar ratios of Si to C.

5.1.4.3 Particle density

When the thickness of formed SiC coating was varied with molar ratio of CB and Si, the particle density of SiC-coated CB sphere also changed. As shown in Fig. 5.17, the density of as-received CB was 1.89 g/cm^3 , whereas that of SiC coated CB increased to 2.14 g/cm^3 (13% increment) and 2.78 g/cm^3 (47% increment) upon increasing Si/C to 1/12 and 1/2, respectively. Such increases in density would narrow the density gap between carbon and other oxide grains in future castable systems, which could avoid or alleviate segregation, thus additionally improving the dispersion/distribution of carbon.

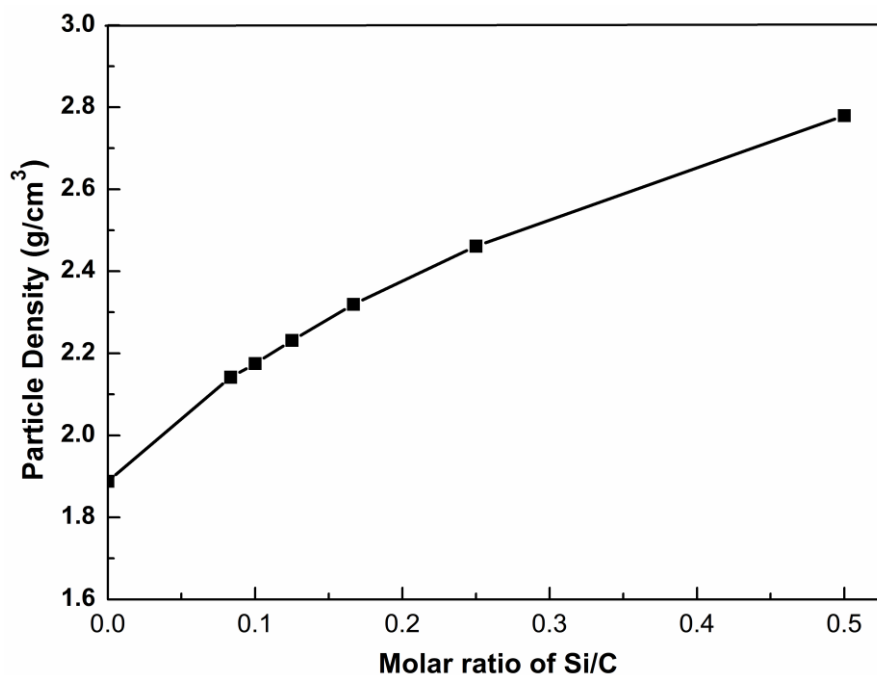


Fig. 5.17 Particle densities of SiC coated CB particles prepared using different Si/C molar ratios.

5.1.5 Effect of molten salt on SiC formation

As indicated by above results, SiC coatings were prepared on CB at as low as 1100 °C in molten salt, which is 200 °C lower than that (1300 °C) required by the conventional vapour–solid reaction technique [201, 202]. To further demonstrate the effect of molten salt on SiC formation, the micron-Si-CB mixture (in molar ratio of 1/8) was fired at 1100 °C in the absence of NaF-NaCl. Fig. 5.18 shows almost the same XRD patterns of the micron-Si-CB mixture before and after firing at the target temperature, indicating no SiC was formed from reaction of Si and CB in the absence of molten salt, indicating that molten salt (NaF-NaCl in this case) is key to synthesize SiC coating at a relatively low temperature. Fig. 5.19 shows typical SEM images of the micron-Si-CB mixture after firing at 1100 °C without molten salt. Unreacted Si and CB particles were still seen (Fig. 5.19b), and many particles of the former were loosely attached to the latter.

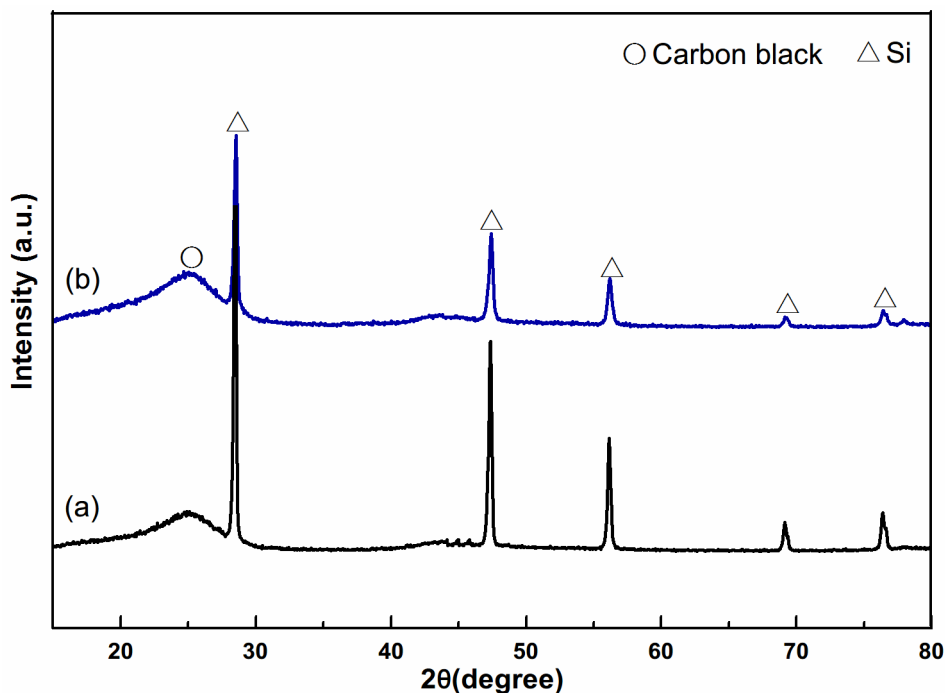


Fig. 5.18 XRD of the mixture of micron-sized Si and CB in molar ratio of 1/8 (a) before and (b) after firing at 1100 °C for 6 hours in the absence of molten salt.

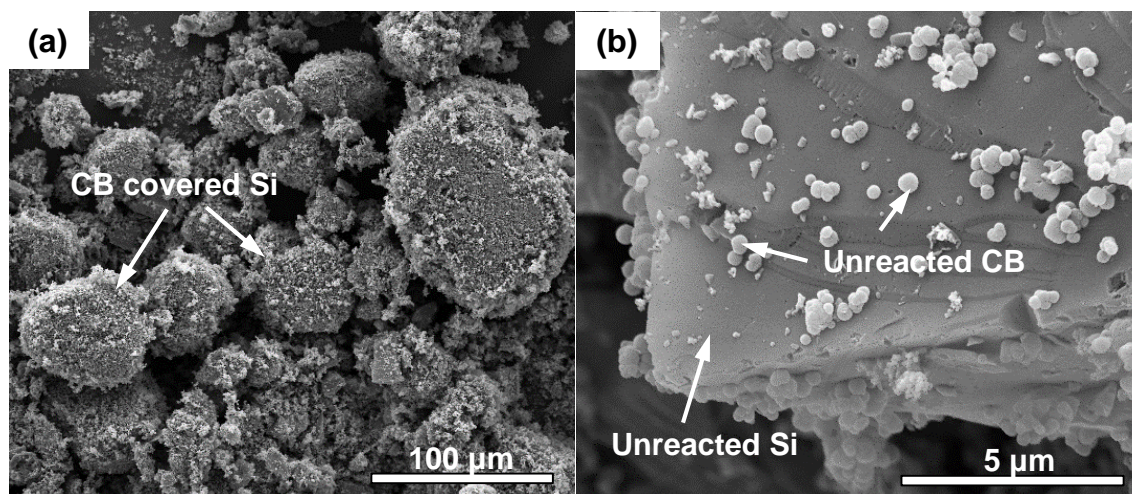


Fig. 5.19 Low magnification and (b) high magnification SEM images of the resulting powders of firing the micron-Si-CB (Si/C = 1/8 in molar ratio) at 1100 °C for 6 hours in the absence of molten salt.

In order to further investigate the role of the molten salt and the corresponding reaction mechanisms, Si powders alone (without CB) were mixed with NaCl-NaF salts, followed by firing in Ar at the SiC formation temperature. Fig. 5.20, as an example, shows together SEM images of Si before (Fig. 5.20a) and after firing in a single NaCl (Fig. 5.20b), a binary NaCl-NaF salt containing 5 wt% NaF (Fig. 5.20c) and a single NaF (Fig. 5.20d). The original sharp edges of Si grains (Fig. 5.20a) appeared to be rounded and their sizes became evidently smaller after firing in the

NaCl based salt containing NaF (Fig. 5.20c). Furthermore, after firing in a single NaF salt, significant nano-sized Si particles were seen along with some small Si dendrites (Fig. 5.20d). On the other hand, after firing in a single NaCl salt, the morphologies and sizes of Si changed very little (Fig. 5.20b). These results indicate that Si did not dissolve significantly in a molten NaCl salt, but had some solubility in a NaF-containing NaCl salt. This explained the more significant formation of SiC in the sample fired in a NaF containing salt than in a single NaCl salt without NaF, and the lower synthesis temperature in the case of the former (Fig. 5.2 and Fig. 5.3).

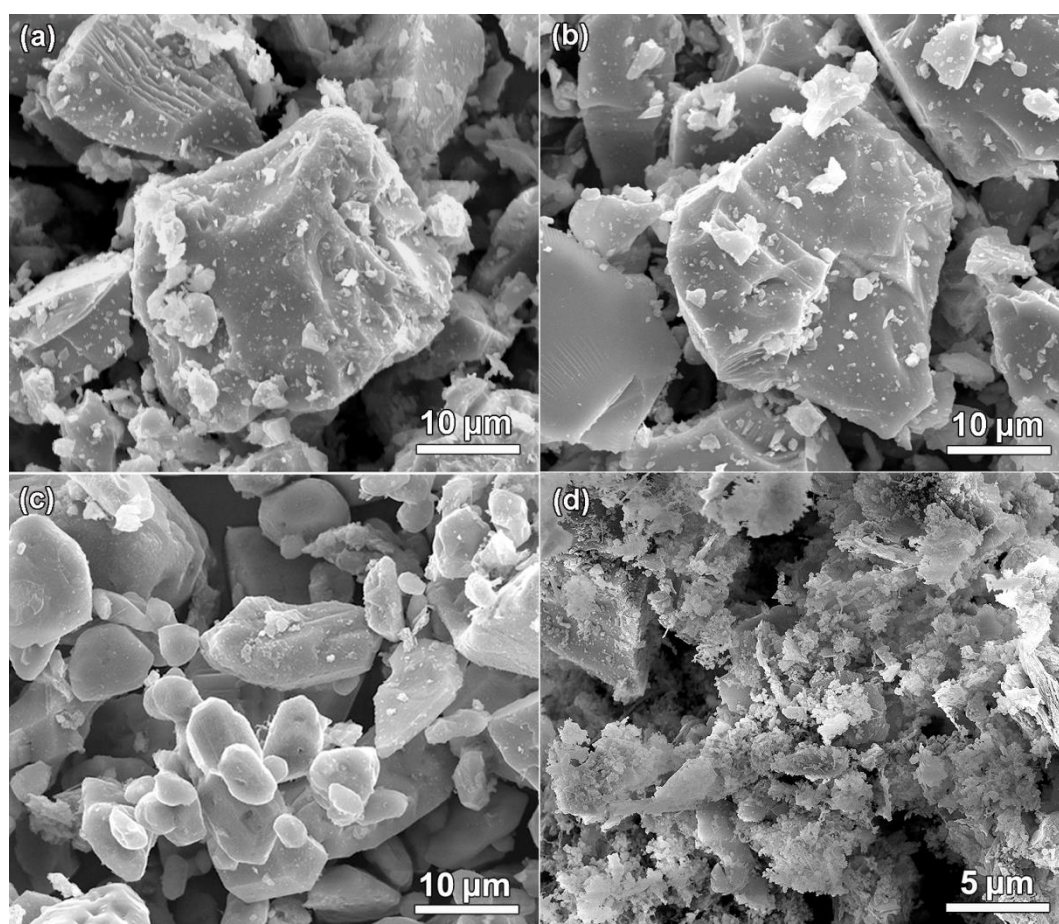



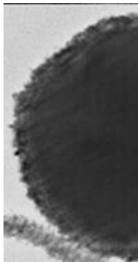
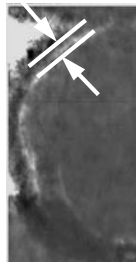
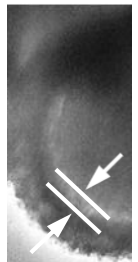
Fig. 5.20 SEM images of (a) as-received Si powders, and after 6h firing in (b) a single NaCl salt, (c) a binary salt containing 5 wt% NaF and (d) a single NaF salt, respectively.

5.1.6 Void formation at higher Si/C molar ratio

In this study, a void or gap at the interface between SiC shell and carbon core was observed under TEM (Fig. 5.15). It was hard to find the void in the particles coated with thin SiC ($\text{Si/C} \leq 1/8$), however, it appeared when the thickness of SiC coating increased to ~ 36.5 nm (at which $\text{Si/C} = 1/4$). The void formation became more evident in the SiC coated CB sphere prepared from Si/C molar ratio of $1/2$. As

shown in the inserts in Table 5.2, the widths of the labelled voids or gaps were measured as ~8.4 nm at Si/C molar ratio of 1/4 and ~18.4 nm at 1/2.

Table 5.2 The void formed at interface of SiC shell and carbon core.

| Si/C | 1/12 | 1/8 | 1/4 | 1/2 |
|---|---|--|---|---|
| Individual SiC-coated CB sphere (TEM images shown in Fig. 5.15) |  |  |  |  |
| Width of the void (nm) | 0 | 0 | 8.4 | 18.4 |
| Thickness of SiC coating (nm) | 12.2 | 18.4 | 36.5 | 66.3 |

The above results indicated that the void formation was associated with Si/C molar ratio or thickness of the formed SiC coatings. Based on this, the hollow void could be formed by increasing the Si/C to 1/1. This was verified by firing Si and CB (two sizes, ~280 nm and ~100 nm) in molar ratio of 1/1 at 1150-1200 °C for 12-16 hours in NaF-NaCl. As revealed by Fig. 5.21, carbon cores disappeared in both cases, however, the hollow structure of the resulting particles became more evident and visible (Fig. 5.21b) when CB sphere in smaller size (~100 nm) was used. The formation of void and hollow structure is attributed to different diffusion rates of the reagents, Si and C in this case, at the fired temperatures. This phenomenon is also called Kirkendall effect [204, 205] which will be detailed in Chapter 8. In addition, the above observations suggest that the Si/C molar ratio should be reasonably controlled ($\text{Si/C} \leq 1/8$) to avoid the formation of voids.

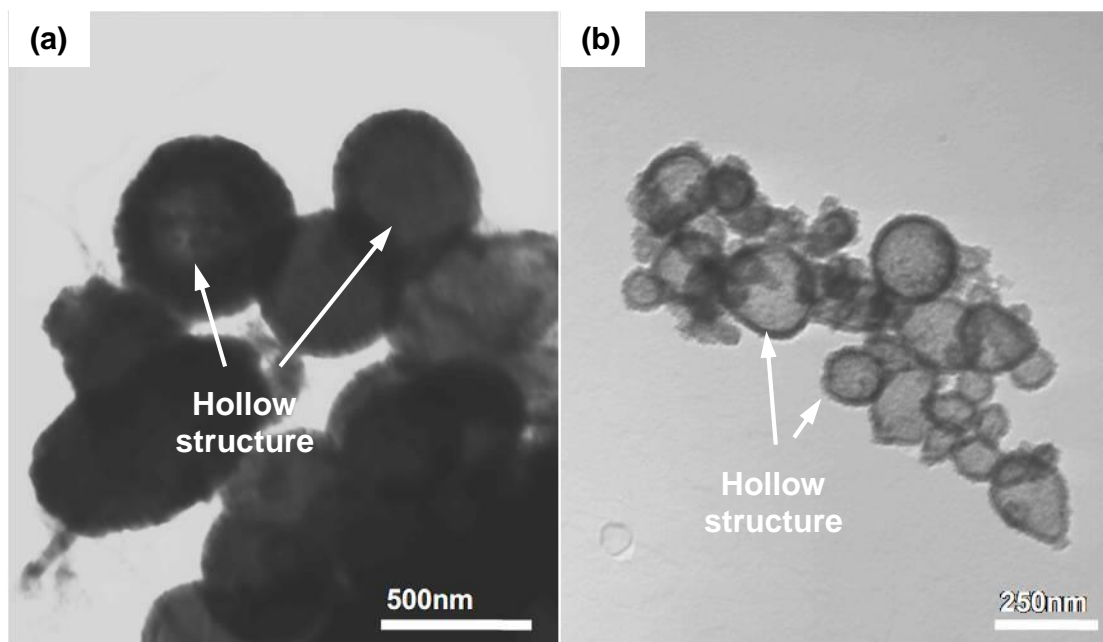


Fig. 5.21 TEM images of the resultant SiC hollow spheres prepared from (a) Si and CB (N991, ~ 280 nm), and (b) Si and CB (N660, ~100 nm) (Si/C=1/1 in both cases) in NaF-NaCl.

5.2 Preparation of SiC/SiO₂ composite coating

SiC coatings were prepared on CB to improve water-wettability of CB particles, due to their excellent water affinity. Nevertheless, the fundamental studies [200] revealed that good wettability of SiC was mainly attributed to formation of SiO₂ thin film when SiC was exposed to air (see more details about this in the Discussion chapter). So it can be reasonably speculated that the water-wettability of SiC coatings will be enhanced if more SiO₂ (thicker SiO₂ films) is formed on the surface of SiC. For this reason, a graded SiC/SiO₂ composite coating was attempted by controlled oxidation of as-prepared SiC coated CB in air at optimised low temperatures.

Since CB is more vulnerable to oxidation than SiC at low temperature, the pre-oxidation conditions have to be carefully controlled. As demonstrated in Section 5.1.3.2, carbon core was etched out from SiC shell by combustion at 600 °C for 90 minutes. But in this case, to avoid carbon combustion, as-prepared SiC-coated CB particles (with Si/C molar ratio of 1/8) were fired in air at a lower temperature between 400-500 °C for a shorter time period (30-60 minutes).

5.2.1 Phase analysis of SiC/SiO₂ composite coatings

Preliminary examination by XRD (Fig. 5.22) shows no new crystalline phases were detected after firing SiC-coated CB under various pre-oxidation conditions, but the intensity of broad carbon peak (centred at ~25.5°) and SiC peak ((111) plane) decreased slightly with increasing oxidation temperature from 400 and 500 °C. The weakening in peak intensity is most likely due to formation of amorphous SiO₂ from SiC coatings.

The phase evolution was further verified by using FTIR. Fig. 5.23 shows infrared spectra of as-prepared SiC coated CB particles after pre-oxidation at various firing conditions. The absorption at 1640 cm⁻¹ was assigned to water which was absorbed while making KBr pellets in the ambient environment. The fundamental stretching vibration of SiC was observed at absorption at ~820 cm⁻¹. In addition, the obvious change was the appearance of absorption peaks at 1080 cm⁻¹ and 440 cm⁻¹ (which were attributed to the antisymmetric and sym-metric stretching vibrations of Si–O–Si bond, respectively) after pre-oxidation. Si-O-Si bonding peaks started becoming sharp and clear after firing in air at 450 °C for 30 min, indicating small amounts of

SiO₂ were formed at above 450 °C. When increasing oxidation temperature to 500 °C (for 30 minutes) or extending oxidation time to 60 minutes at 450 °C, SiO₂ absorption peaks appeared shaper and the transmittance ratio of SiO₂/SiC decreased concurrently, indicating more SiO₂ was formed.

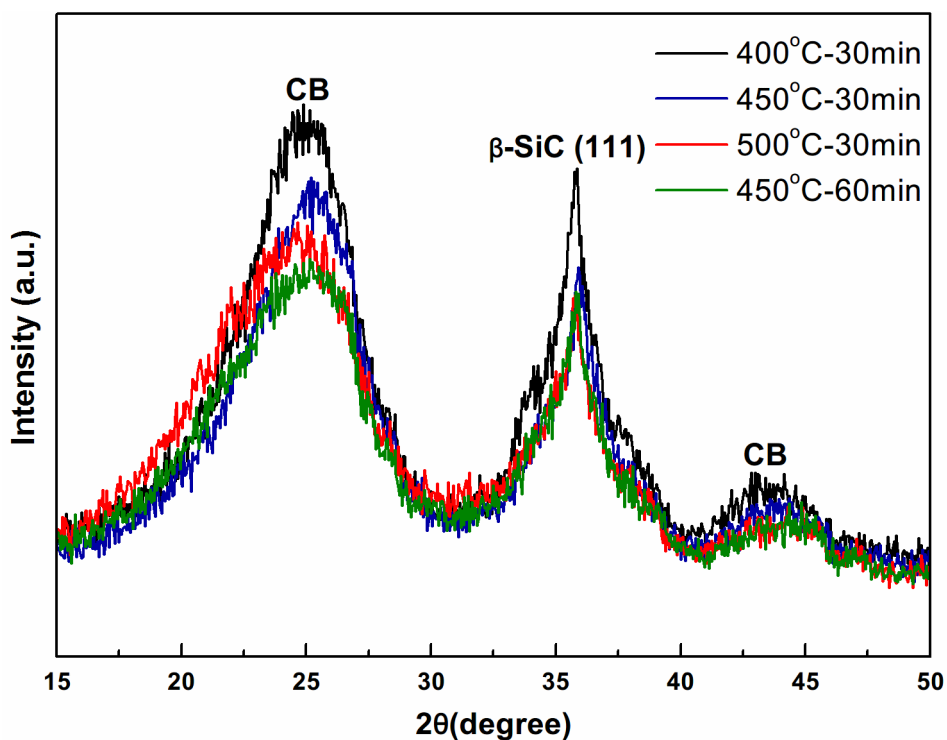


Fig. 5.22 XRD of the resulting powders after firing SiC-coated CB particles (Si/C = 1/8) in air at 400, 450 and 500 °C for 30 minutes, and 450 °C for 90 minutes.

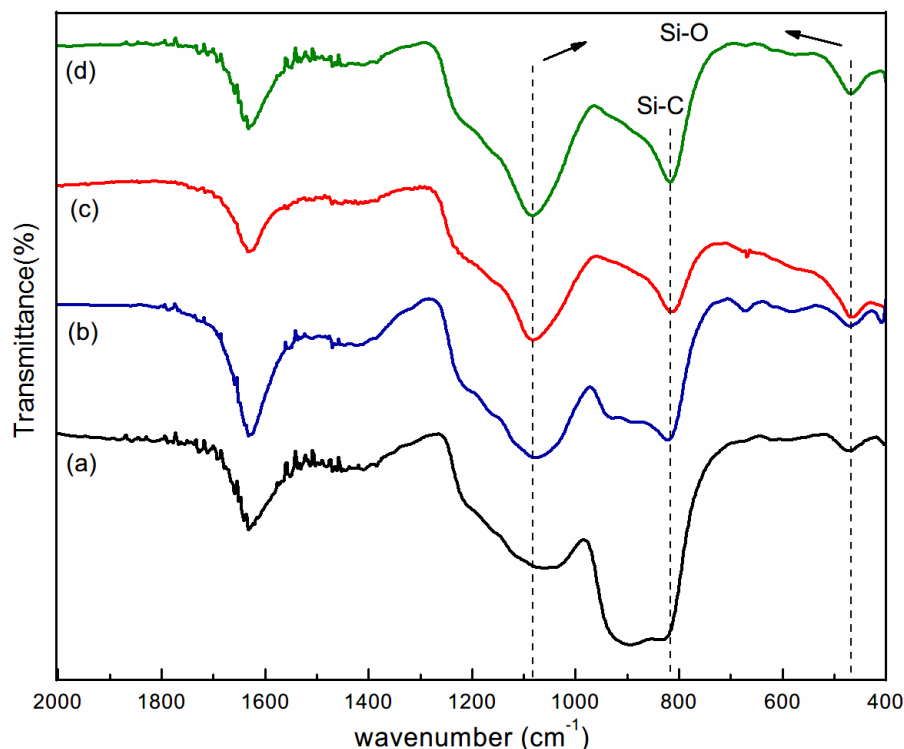


Fig. 5.23 FTIR spectra of the resulting powders after firing SiC-coated CB particles (Si/C = 1/8) in air at 400, 450 and 500 °C for 30 minutes, and 450 °C for 90 minutes.

5.2.2 Microstructural characterisation of SiC/SiO₂ composite coating

Microstructural characterisations by using SEM and EDS were carried out to probe the surface changes before and after pre-oxidation of SiC-coated CB particles. Fig. 5.24 a and b show SEM images of SiC-coated CB particles after pre-oxidation at 500 °C for 30 minutes and 450 °C for 60 minutes. Clearly, the particles before and after oxidation treatment in both conditions changed very little in their morphologies and sizes (Fig. 5.6), indicating SiC-coated CB particles did not suffer severe damage during this process. So the appropriate pre-oxidation temperature for preparing SiC/SiO₂ composite coating was at 450-500 °C. However, some cracked SiC-coated CB particles were occasionally seen in the sample fired at 500 °C for 30 minutes (indicated by white arrows in the insert in Fig. 5.24a).

The typical EDS spectrum (Fig. 5.24c) on the sample (after pre-oxidation at 450 °C for 60 minutes) shows a significant increase in oxygen content compared with that of SiC-coated CB before oxidation (Fig. 5.7b) in which very minor quantities of oxygen were detected on SiC surface. The oxygen content on particle surface treated under different conditions was roughly estimated and compared by the net intensity of oxygen presented in their corresponding EDS spectra. Fig. 5.24d shows

that the oxygen content increased considerably after increasing oxidation temperature from 400 to 450 °C, and continued rising to 500 °C, which is consistent with the result detected by FTIR. However, the highest level of SiO₂ was obtained in the sample oxidised at 450 °C for 60 minutes. This, along with microstructural observation (Fig. 5.24a, b) shows that high quality SiC/SiO₂ composite coatings on CB were prepared by controlled oxidation at 450 °C for 60 minutes.

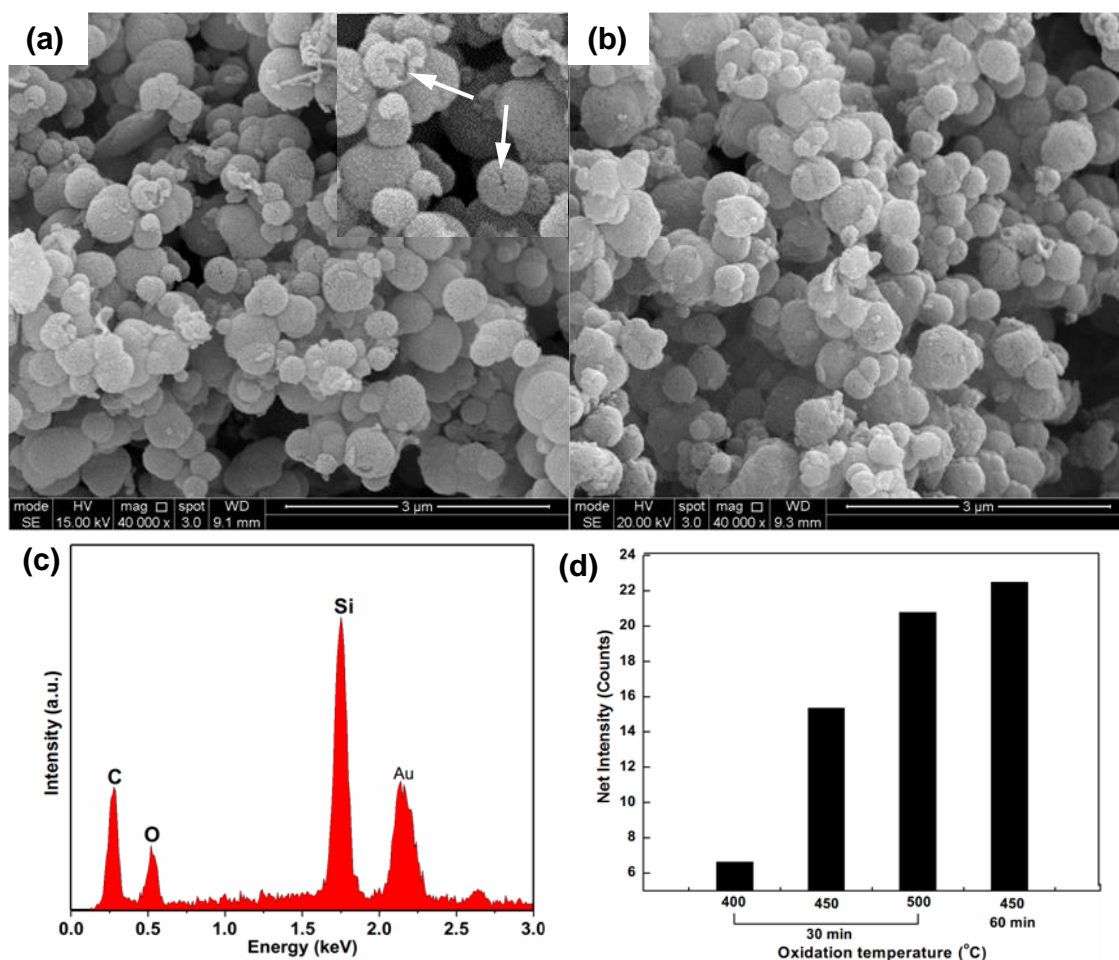


Fig. 5.24 SEM images of SiC-coated CB after pre-oxidation at (a) 500 °C for 30 minutes and (b) 450 °C for 60 minutes. (c) Typical EDS spectrum on SiC-coated CB after pre-oxidation at 450 °C or 60 minutes as shown in (b). (d) Net intensity of oxygen element detected by EDS as a function of different pre-oxidation conditions.

Chapter 6 Water-wettability and oxidation resistance of carbide-coated carbon materials

In this chapter, the wettability and dispersion ability of uncoated and carbide coated CB particles in aqueous solutions were evaluated and compared by zeta potential measurement and sedimentation testing. The effect of carbide coatings on rheological behaviour of CB containing suspensions was investigated. In addition, thermogravimetry (TG) analysis were performed to examine the oxidation resistances of uncoated and carbide coated CB particles. The effect of annealing treatment of as-prepared coated CB particles on their oxidation resistance was also examined.

6.1 Zeta potential

Shown in Fig. 6.1 are zeta potentials of as-received and TiC-coated CB particles in water at pH = 3-12. Zeta potential (absolute value) in all cases generally increased with pH, in particular when pH>8. Nevertheless, at a given pH, zeta potential in the case of TiC-coated CB was much greater than that in the case of uncoated CB. Furthermore, an isoelectric point (IEP) appeared at pH=3.96 in the latter, but was absent in the former. These results indicated that TiC-coated CB particles had more negative charges on their surfaces than uncoated CB particles. The much increased zeta potential in the case of TiC-coated CB particles would improve their water wettability and dispersivity.

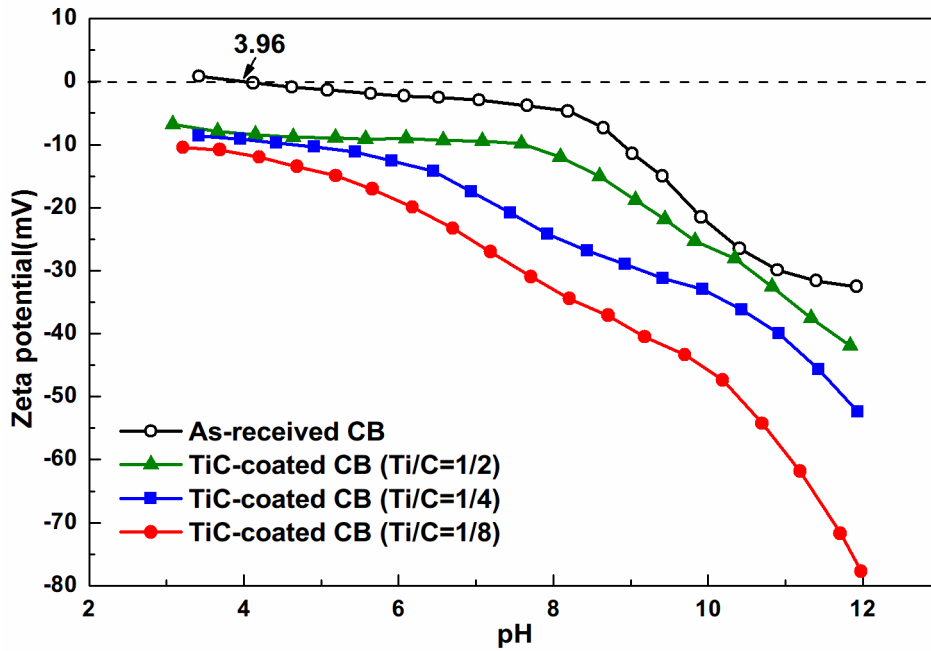


Fig. 6.1 Effect of coating thickness (Ti/C ratio) and pH on zeta potential.

Fig. 6.2 shows zeta potential-pH profiles of uncoated and SiC-coated CBs. The absolute value of zeta potential in the case of uncoated CB was small (<10 mV) at $\text{pH} < 8.5$, although it started to increase upon increasing the pH to > 8.5 . In contrast to this, a much greater zeta potential value was also seen in the case of SiC coated CB at a given pH. In this case, the zeta potential (SiC-coated CB (Si/C=1/8)) increased continuously from ~ 20.4 to ~ 58.0 mV with increasing pH from 3.6 to 12.0. It is also noted that with decreasing SiC thickness, zeta potential increased slightly, which is similar to the case of TiC-coated CB (Fig. 6.1). In principle, with the same coatings on particles, the measured zeta potentials should be the same. However, CB coated with thicker coatings had higher density (as indicated in Fig. 5.17) and thus they readily settled down in aqueous suspensions under gravity. So fewer charged particles were detected between two testing electrodes of zeta potential probe and consequently lower zeta potential values were obtained.

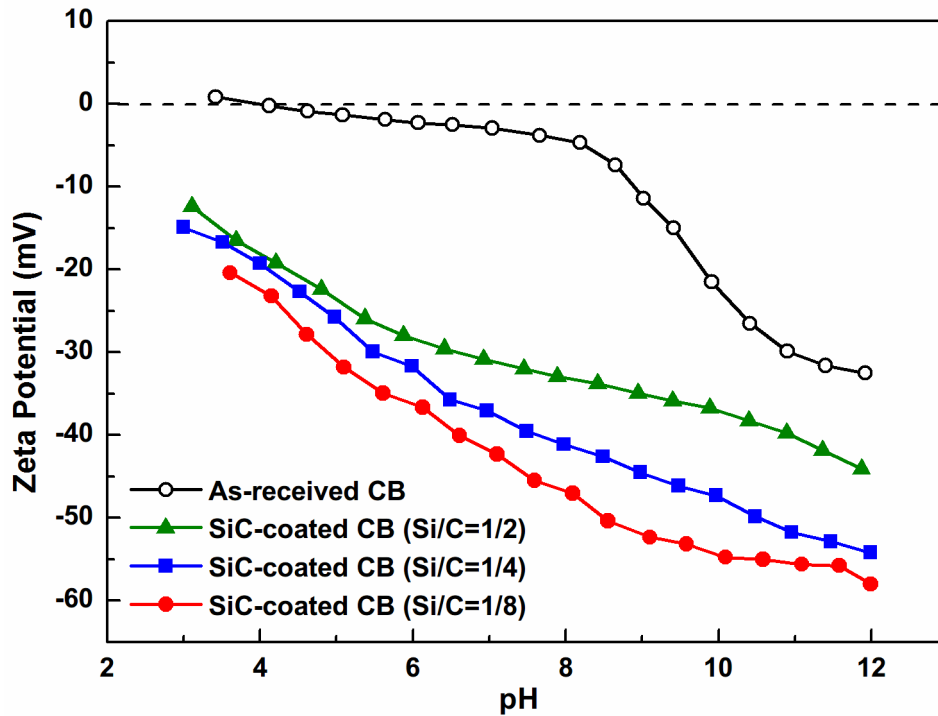


Fig. 6.2 Effect of coating thickness (Si/C ratio) and pH on zeta potential.

These results indicate that SiC-coated CB particles had many more negative charges on their surfaces, which would be beneficial to their dispersion/distribution when used in future castable systems. The much greater zeta potential in this case is believed to be related to the increased functional groups on the CB surface, such as hydrophilic carboxylate group (COOH) and silanol group (SiOH). The mechanism behind this will be discussed in detail in Chapter 8.

The zeta potential of SiC/SiO₂-coated CB particles in aqueous solution was also measured. As shown in Fig. 6.3, compared with SiC-coated CB, higher zeta potentials were obtained at various pH (3 to 10) for CB coated with SiC/SiO₂ composite coatings. For example, at pH=10, zeta potential of the former was ~54.7 mV, whereas that of the latter was ~65.9 mV. This is because outer SiO₂ coatings resulted in more functional silanol groups (Si-OH) on CB particles in water.

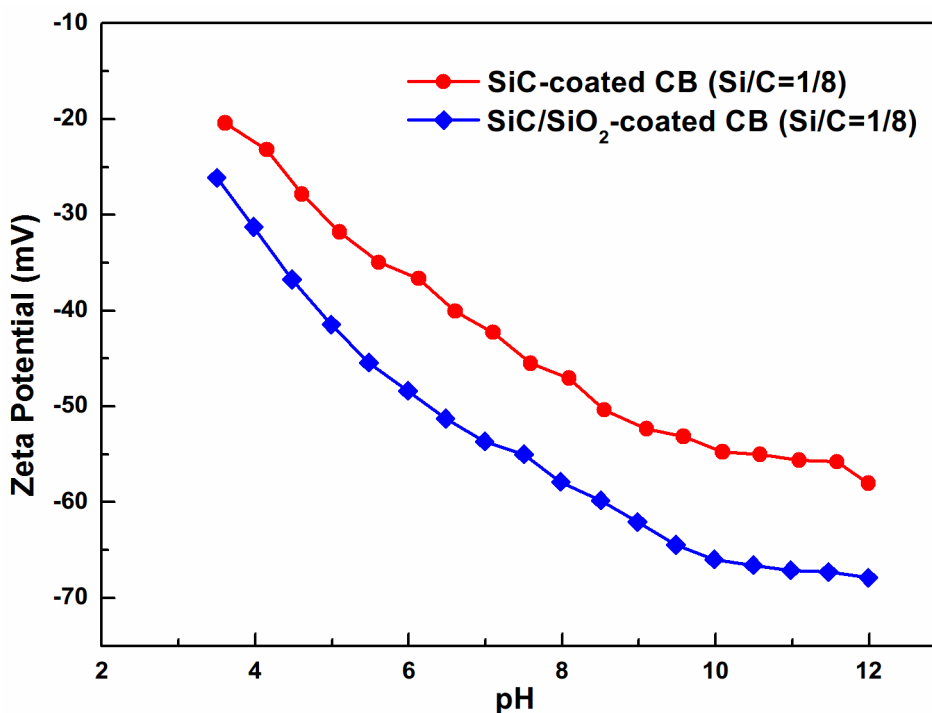


Fig. 6.3 Zeta potential as a function of pH for SiC-coated CB and SiC/SiO₂-coated CB spheres.

6.2 Sedimentation testing

The differences in wetting and dispersing behaviours of uncoated and coated CB particles were also demonstrated by sedimentation testing. For example, ~1 gram as-received CB and TiC-coated CB powders were dispersed in distilled water, respectively and their wetting and dispersing behaviours were recorded. As illustrated by Fig. 6.4a, most of the as-received uncoated CB particles were hardly wetted by water and consequently floated on the surface of water, whereas TiC-coated CB particles were much better wetted and dispersed in water. After agitating for 1 minute and subsequently setting aside for 5 minutes, there still was a large amount of uncoated CB particles floating on the top whilst some of agglomerated clusters settled down under the action of gravity. In contrast, CB particles coated with either thin or thick TiC coatings (in Ti/C molar ratio of 1/8 to 1/2) were homogeneously dispersed in water judging from their uniform black appearances. The above distinct phenomena indicated that carbide coatings significantly improved the water-wettability of CB particles and their dispersion property.

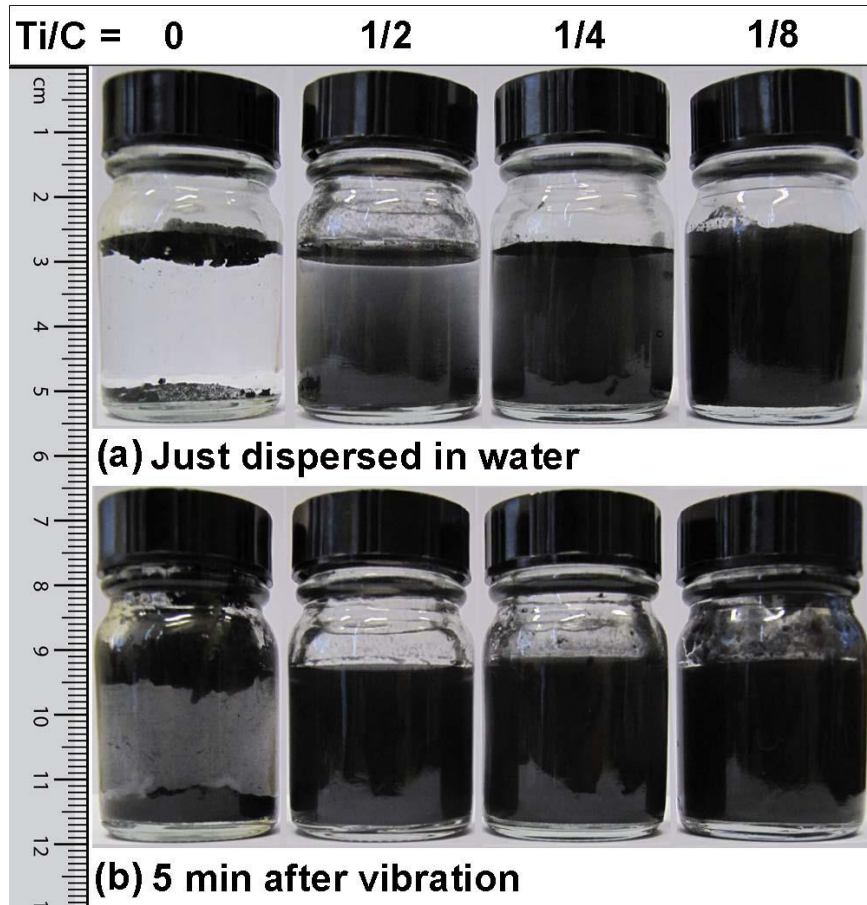


Fig. 6.4 Photographs comparing the dispersions of uncoated and coated CB particles in water.

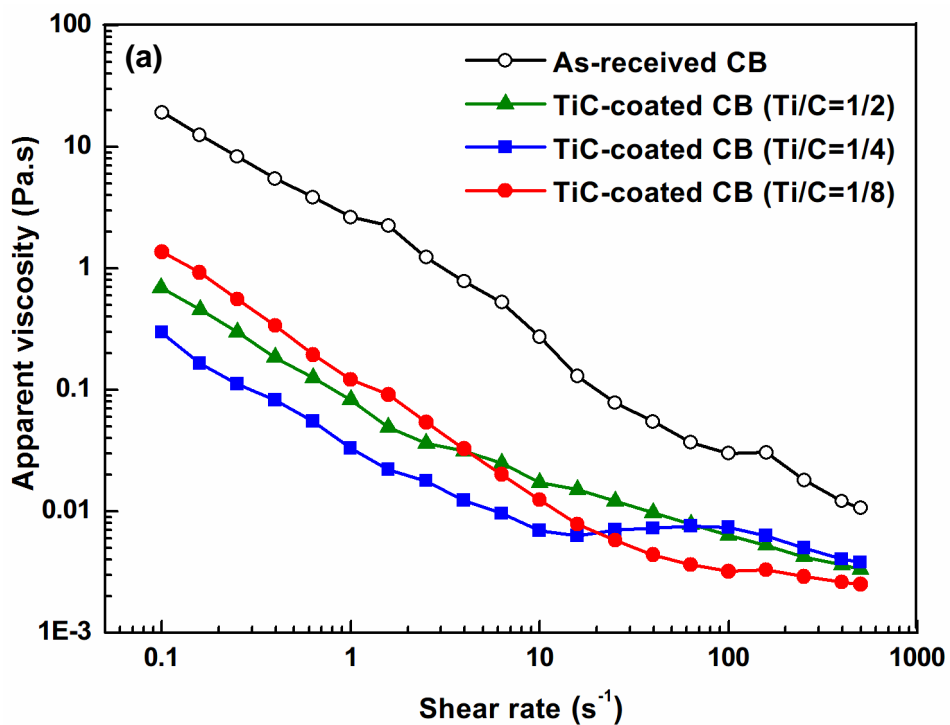
6.3 Rheological behaviour

6.3.1 TiC coated CBs

Fig. 6.5a presents apparent viscosity values of water suspensions containing 25 wt% as-received uncoated or TiC-coated CB particles subject to different shear rates. The viscosity in the former was two orders of magnitude higher than in the latter at a low shear rate and nearly one order of magnitude higher at a high shear rate. This is believed to be related to the improved water-wettability and dispersivity as shown in Fig. 6.1 and 6.4. Moreover, under a given shear rate, there was no obvious difference in the viscosity between CB particles with different thickness TiC coatings, indicating little effect of coating thickness on the flowability of CB in water.

Fig. 6.5b shows the relationship between shear stress and shear rate for water suspensions containing 25 wt% uncoated and TiC-coated CB particles, respectively. A major feature is that the yield shear stress of the former was evidently higher than

that of the latter over the whole range of shear rates (0.1 to 500 s^{-1}), indicating suspensions containing coated CB particles flow more easily when subject to an equal external force. In addition, despite the overall trend of shear stress for uncoated CB-containing suspension increased with shear rate, an evident fluctuation (black line, a typical curve from three parallel test) occurred in the range of shear rate of 1 to 100 s^{-1} , which was mainly due to the instability of uncoated CB suspensions. High degree of agglomeration likely occurred in the case of uncoated CB, because small repel forces were formed between uncoated CB particles, which were reflected on low zeta potential values (Fig. 6.2).



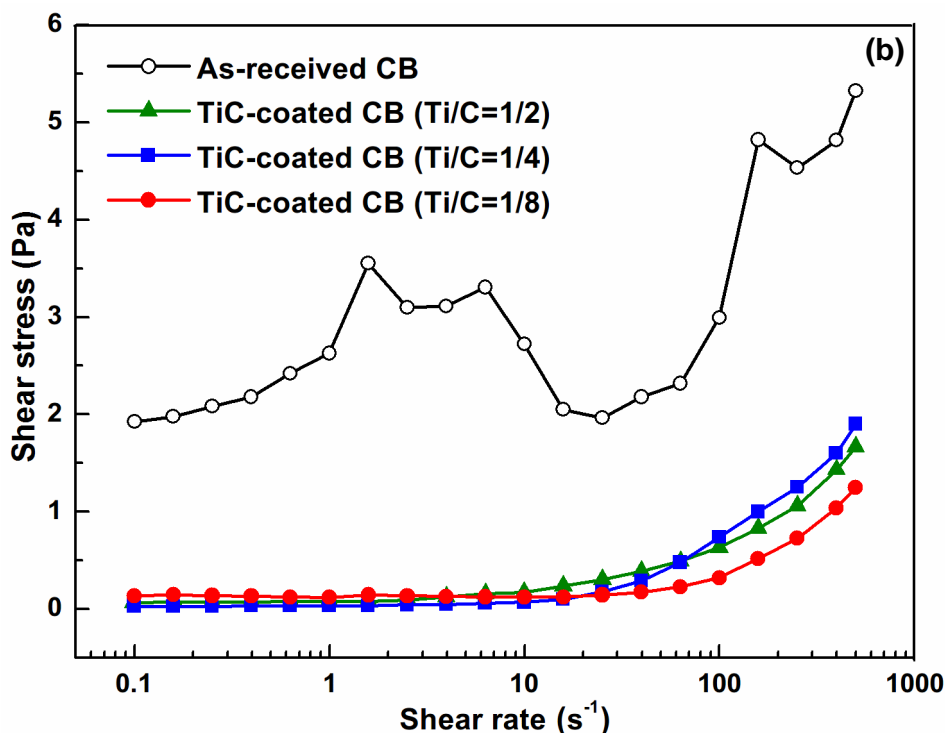


Fig. 6.5 (a) Apparent viscosity and (b) shear stress of water suspensions (pH=10) containing 25 wt% uncoated and TiC-coated CB as a function of shear rate.

6.3.2 SiC-coated CBs

Rheological behaviour of CB particles after SiC coating (Si/C=1/8) was also changed. Fig. 6.6, as an example, shows variations in the apparent viscosity of water suspensions containing uncoated and SiC coated CBs respectively with the shear rate. Suspensions containing either uncoated CB or SiC coated CB both exhibited a shear thinning behaviour, i.e., they became more stable and were subjected to less stress upon increasing the shear rate. Nevertheless, the suspension containing SiC coated CB (pH=10) showed much lower apparent viscosity than the suspension containing uncoated CB (pH=10) at a given shear rate, two orders of magnitude lower at a low shear rate (<10 s⁻¹) and about one order lower at a high shear rate (>10 s⁻¹). This suggests that SiC-coated CB particles would have better flowability in a real castable system than their uncoated counterparts.

On the other hand, pH affects apparent viscosity of suspensions. The rise in apparent viscosity was dramatic for uncoated CB-containing suspension, one order of magnitude higher at pH=6 than that at 10. However, only a slight increase in the viscosity of suspensions containing SiC-coated CB occurred at low shear rate, and nearly no change observed at high shear rate when pH was reduced from 10 to 6.

This is because more negative charges formed on particle surface in basic environment and less in acidic environment as indicated by zeta potential measurement (Fig. 6.2). This change caused by pH was more significant for uncoated CB, for example, ~ 2.3 mV detected at pH=6 and ~ 22.7 mV at pH=10. Enriched negative charges lead to high repel force between particles and thus result in low viscosity and improved flowability.

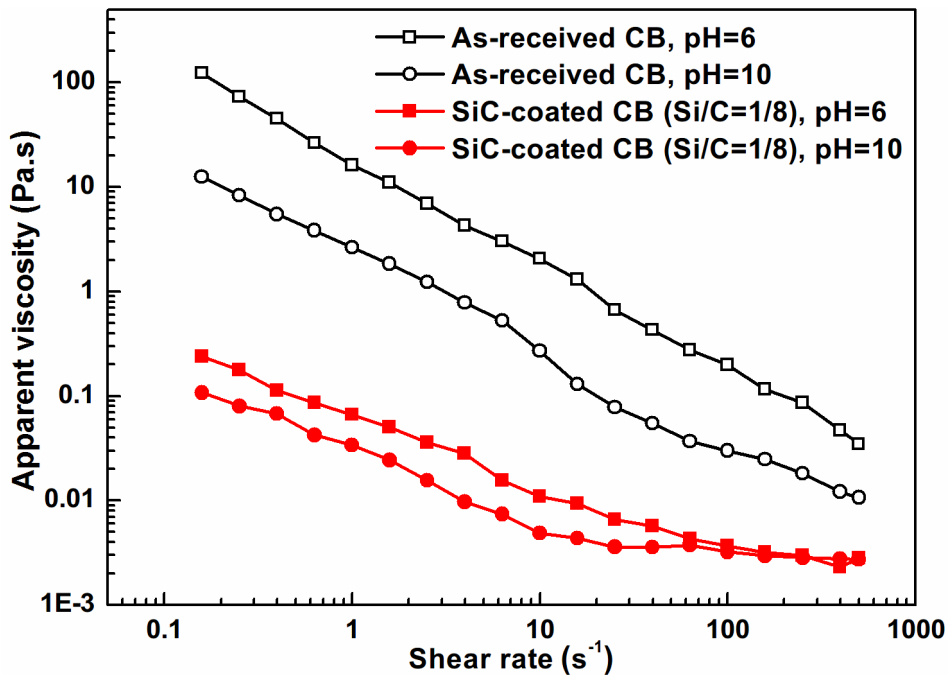


Fig. 6.6 Apparent viscosity of water suspensions containing 25 wt% as-received CB and SiC coated CB, respectively, at various shear rates (pH=6 and 10).

The apparent viscosity was also associated with solid content of the suspension. For instance, when the solid content in SiC-coated CB suspension was increased to 35 wt% (Fig. 6.7), the viscosity was dramatically increased, over two orders of magnitude higher than that of suspension containing 25 wt% coated CB particles. This gives us a clue that high level of CB addition in castable would cause poor flowability and high water demand.

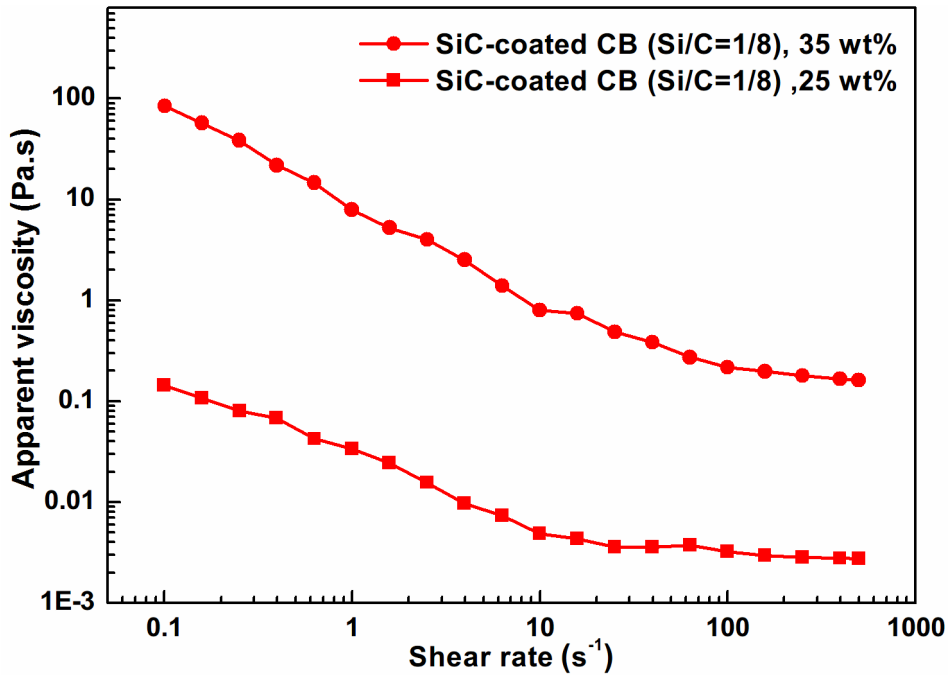


Fig. 6.7 Apparent viscosity of SiC-coated CB suspensions (pH=10) with different solid loadings as a function of shear rate.

The flowability of CB-containing water suspensions can be further improved by formation of SiC/SiO₂ composite coatings on them. As shown in Fig. 6.8, the apparent viscosity of water suspension containing SiC/SiO₂-coated CB was lower than that of the suspension containing SiC-coated CB particles over a wide range of shear rate, indicating that the formation of SiC/SiO₂ composite coatings on CB is effective to enhance flowability of CB particles in water.

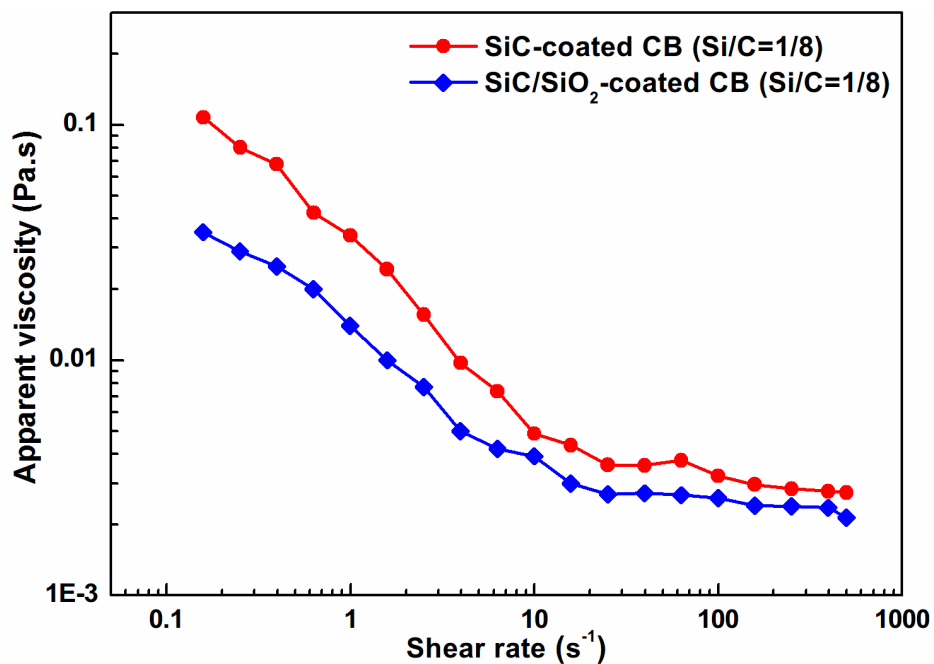


Fig. 6.8 Apparent viscosity of water suspensions (pH=10) containing 25 wt% SiC or SiC/SiO₂ composite coatings at various shear rates.

6.4 Oxidation resistance

6.4.1 Post-treatment of carbide coated CB (Annealing)

6.4.1.1 Annealing of TiC-coated CB

In order to improve oxidation resistance of TiC-coated CB particles, they were annealed in Ar and N₂ atmospheres, respectively. Fig. 6.9 shows the phase changes before and after annealing at 1300 °C for 4 hours in Ar and N₂. After heat-treatment in Ar, no new phases were seen, but the TiC peaks became slightly higher and sharper, indicating a slight increase in its crystallinity and/or crystal size. However, the annealing in N₂ at 1300 °C caused TiC peaks shifting right to higher two-theta angles and approaching the locations of TiN characteristic peaks (ICCD card [38-1420]). This indicates that the nitrogen might be incorporated into TiC crystal structure, forming a TiCN solid solution.

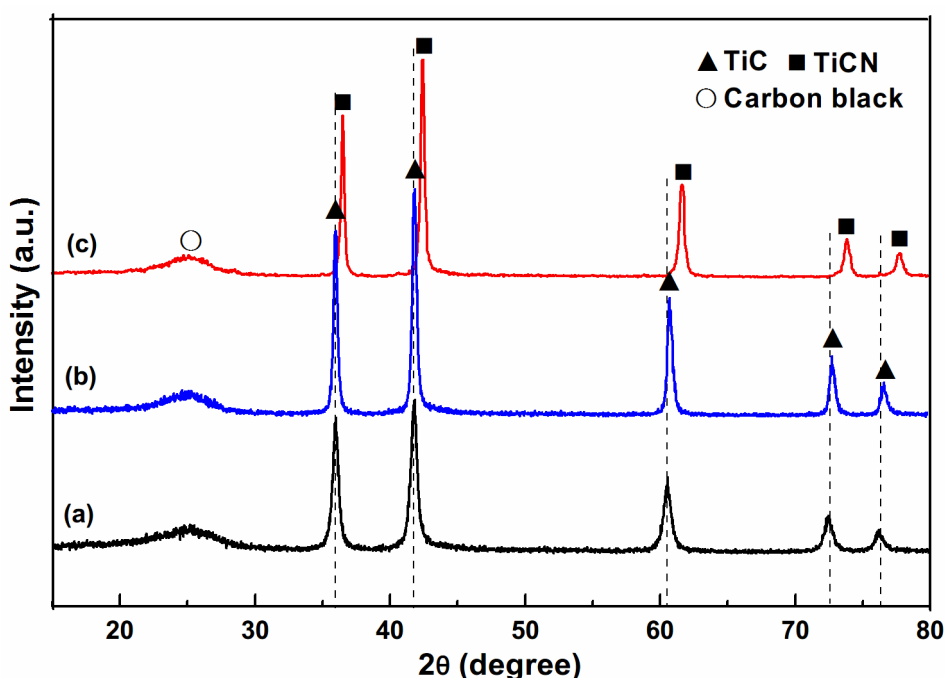


Fig. 6.9 XRD of as-prepared TiC-coated CB (Ti/C=1/8) (a) before and after annealing at 1300 °C for 4 hours in (b) Ar and (c) N₂, respectively.

By peak calibration and refinement and corresponding calculations, the lattice constants (referred as 'A' hereafter) were obtained for these samples. As shown in Table 6.1, the lattice constant of as-prepared TiC coating was 4.3247 Å, very close to that of perfect TiC crystals (A=4.3274 Å, (ICCD card [38-1420])). Nevertheless, it dropped to 4.2505 Å after annealing in N₂, which is close to cell parameter of TiN (A=4.2417).

The TiCN phase was modelled as a perfect $\text{TiC}_{1-X} - \text{TiN}_X$ solid solution, $0 \leq X \leq 1$, with a NaCl type crystal lattice.[206] In accordance with Vegard's rule,

$$A_{\text{TiCN}} = X_{\text{C}} \cdot A_{\text{TiC}} + X_{\text{N}} \cdot A_{\text{TiN}} \quad (6.1)$$

$$\text{Where } X_{\text{C}} = 1 - X_{\text{N}} \quad (6.2)$$

$$\text{So } X_{\text{N}} = (A_{\text{TiC}} - A_{\text{TiCN}}) / (A_{\text{TiC}} - A_{\text{TiN}}) \quad (6.3)$$

According to Equation 6.3, the atomic percentage of carbon and nitrogen atoms could be estimated from parameter A_{TiCN} . The specific composition of TiCN phase was listed in Table 6.1.

Table 6.1 Cell parameter and Specific composition of as-prepared TiC and TiCN phases

| TiC_xN_y | TiC | As-prepared TiC | After annealing in N_2 | TiN |
|--------------------------|--------|-----------------|----------------------------------|--------|
| A (Å) | 4.3274 | 4.3247 | 4.2505 | 4.2417 |
| X | 1 | | 0.1027 | 0 |
| 1-X | 0 | | 0.8973 | 1 |
| | TiC | TiC | $\text{TiC}_{0.1}\text{N}_{0.9}$ | TiN |

The morphologies and chemical compositions of the heat-treated powders were examined by SEM and EDS. Fig. 6.10 a and b show SEM images of TiC-coated particles after annealing at 1300 °C in Ar and N_2 , respectively. They showed similar morphologies and size to TiC-coated particles without such a post-treatment. EDS (Fig. 6.10c) shows TiC-coated particles treated in N_2 at 1300 °C comprised nitrogen in addition to C and Ti. This, along with phase analysis (Fig. 6.9c) revealed that titanium carbonitride ($\text{TiC}_{0.1}\text{N}_{0.9}$) coatings were formed on CB particles by annealing treatment in N_2 .

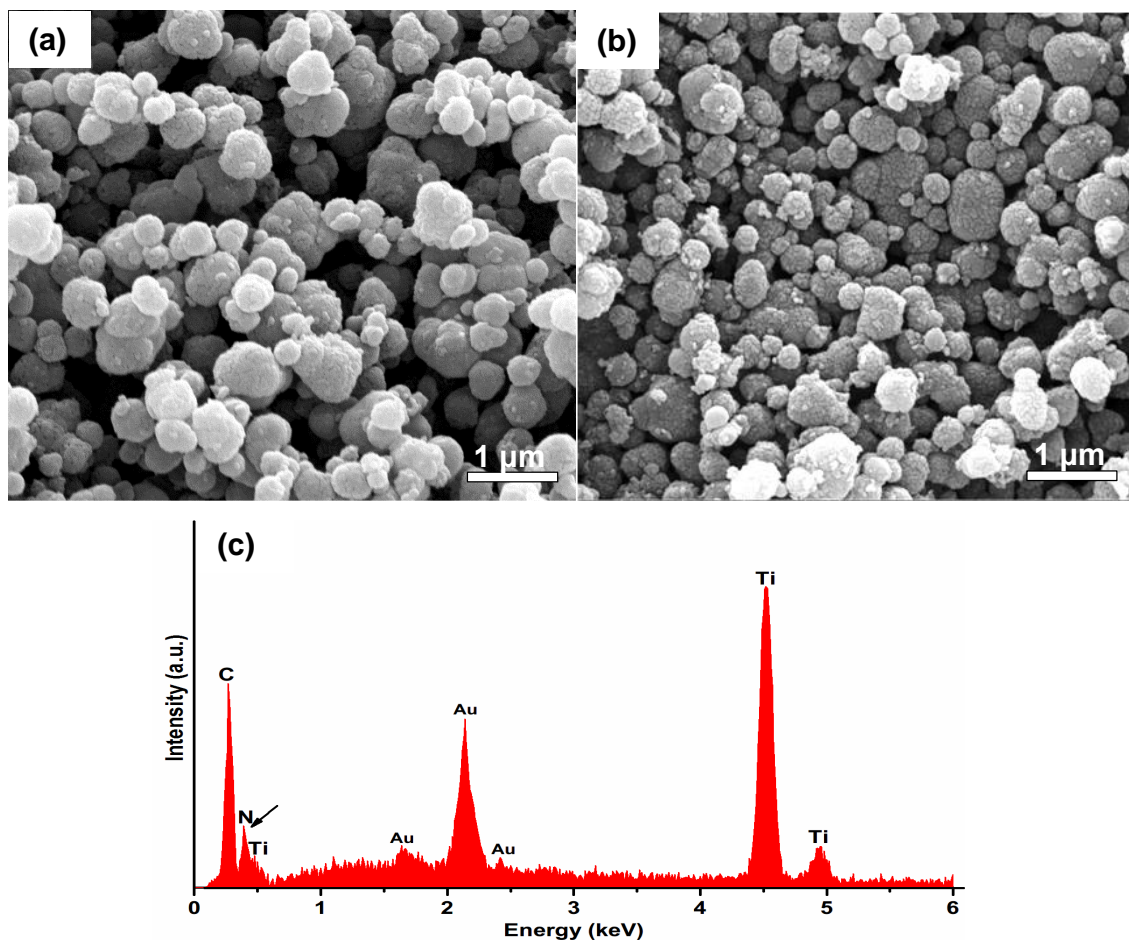


Fig. 6.10 SEM images of TiC-coated CB particles after annealing at 1300 °C for 4 hours in (a) Ar and (b) N₂, and EDS spectrum obtained from (b) showing its chemical composition.

6.4.1.2 Annealing of SiC-coated CB

As-prepared SiC-coated CBs were heat-treated in Ar at 1200 and 1500 °C for 4 hours, respectively. Similarly to the case of TiC-coated CB, no new phases were detected (Fig. 6.11) after annealing in Ar, but the intensities of SiC characteristic peaks gradually increased with annealing temperature from 1200 to 1500 °C. The width of XRD peaks decreased, indicating the increase in crystal size of SiC. This change was further verified by microstructure observation on SiC coatings. As shown in Fig. 6.12, SiC-coated CB particles after post-treatment still remained dispersive and the size of SiC nanocrystals appeared to increase compared with as-prepared SiC-coated CB (Si/C=1/8, formed at 1100 °C for 6 hours) (Fig. 5.6). Moreover, the SiC coatings after annealing seemed to be denser than the one before annealing.

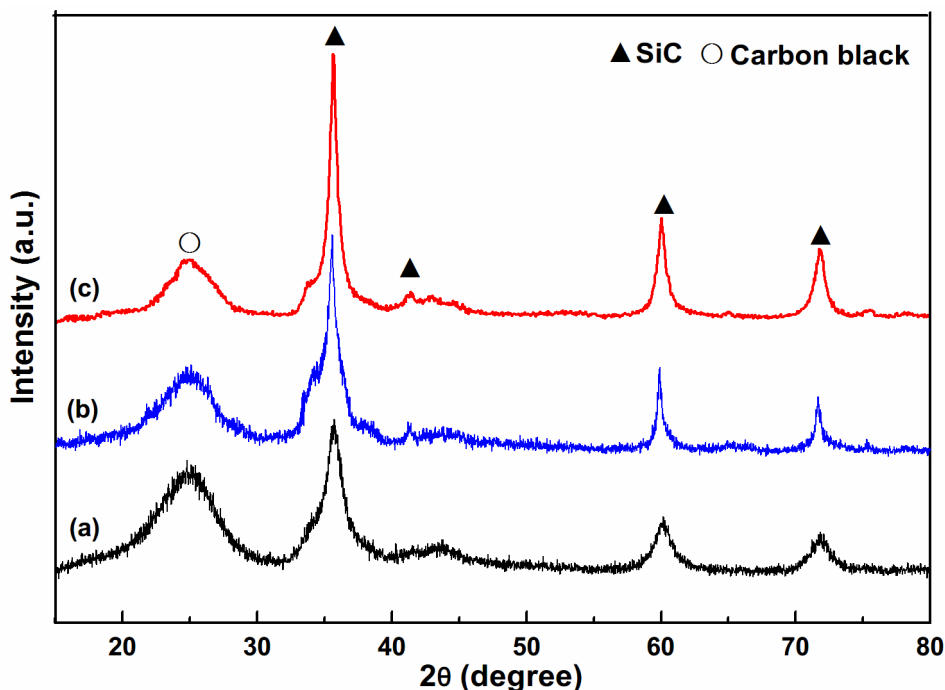


Fig. 6.11 XRD of as-prepared SiC-coated CB (a) before and (b) after annealing in Ar for 4 hours at (b) 1200 °C and (c) 1500 °C.

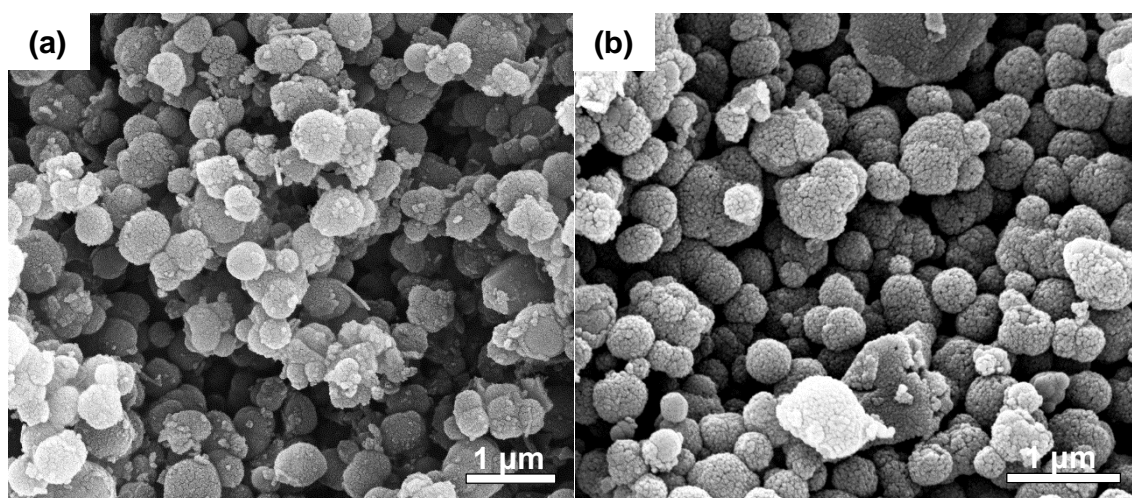


Fig. 6.12 SEM of as-prepared SiC-coated CB after annealing in Ar for 4 hours at (a) 1200 °C and (b) 1500 °C.

6.4.2 Thermogravimetry analysis (TGA)

6.4.2.1 TiC-coated CBs

Fig. 6.13 shows TG curves of uncoated and TiC-coated CB particles prepared from different Ti/C molar ratios of 1/8 to 1/2 (TiC thickness ranging from ~ 10.4 to ~ 50.3 nm as described in Fig. 4.9) at 850 °C for 4 hours. As it can be seen, CB particles were prone to be oxidized in air, starting losing weight at ~ 472 °C. The oxidation process began to accelerate at ~ 600 °C and eventually ended up at ~ 678 °C,

remaining 0.38% ash after combustion completed. As for CB coated with thin TiC coatings ($\text{Ti/C}=1/8$), a weight gain was observed at $\sim 400\text{--}500\text{ }^\circ\text{C}$ (which was attributed to oxidation of TiC coatings at early oxidation stage), followed by a dramatic weight loss at $\sim 500\text{--}700\text{ }^\circ\text{C}$. It shows uncoated and TiC-coated CB ($\text{Ti/C}=1/8$) were completely oxidized at nearly the same temperature, however, the oxidation of CB was slightly retarded by TiC coatings in terms of the rate of weight loss judging by the decreased slope of TG curve in the period of weight loss. Such retardation in CB oxidation was more evident in the TG curves of the samples with thick TiC coatings. For example, the weight loss of TiC-coated CB (with Ti/C molar ratio of $1/4$ and $1/2$) ended up at $\sim 748\text{ }^\circ\text{C}$, about $70\text{ }^\circ\text{C}$ postponement in carbon oxidation.

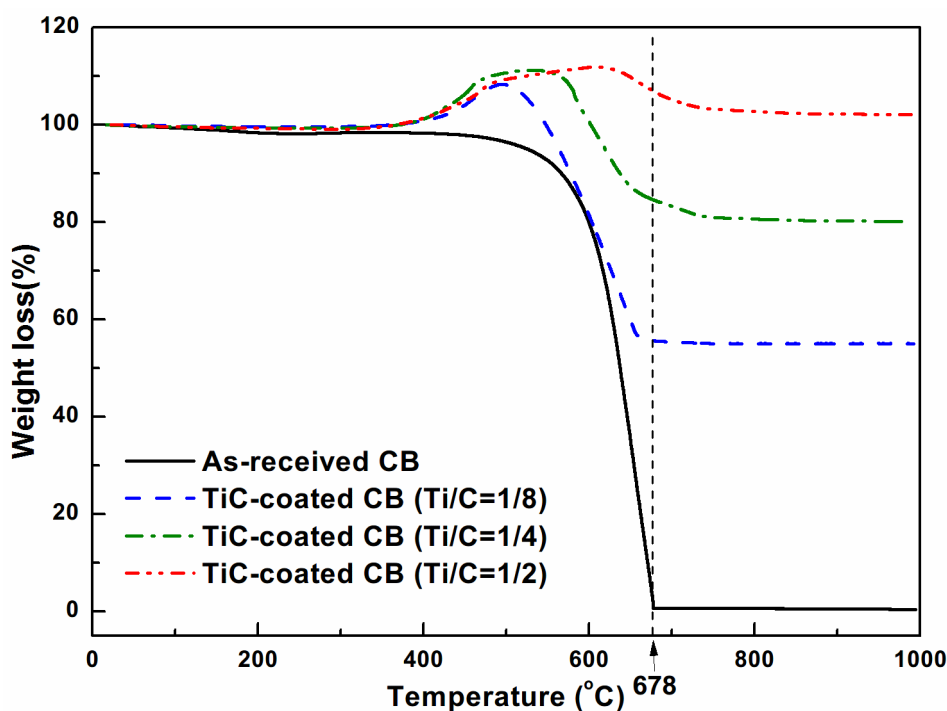


Fig. 6.13 TG curves of uncoated CB and TiC-coated CB with Ti/C molar ratio of $1/8$, $1/4$ and $1/2$.

However, the oxidation resistance of TiC-coated CB was significantly improved by annealing at $1300\text{ }^\circ\text{C}$ in either Ar or N_2 atmosphere. Fig. 6.14 shows that TG curves of TiC-coated CB (with Ti/C molar ratio of $1/8$) after heat-treatment are right shifted to higher oxidation temperatures. The weight gain for the sample treated in Ar and N_2 was postponed, reaching the highest point at $\sim 532\text{ }^\circ\text{C}$ for the former and $\sim 635\text{ }^\circ\text{C}$ for the latter compared with $\sim 495\text{ }^\circ\text{C}$ obtained from the sample before annealing. The rate of weight loss after weigh again for these three samples was almost the same, however, TiC-coated CB after annealing in Ar lost all carbon at $\sim 821\text{ }^\circ\text{C}$ and

the one treated in N_2 terminated its weight loss at ~ 838 °C, about 150 °C higher than that without heating treatment (~ 688 °C). Such retardation in weight loss implies annealing treatment is effective to improve oxidation resistance of TiC-coated CB particles.

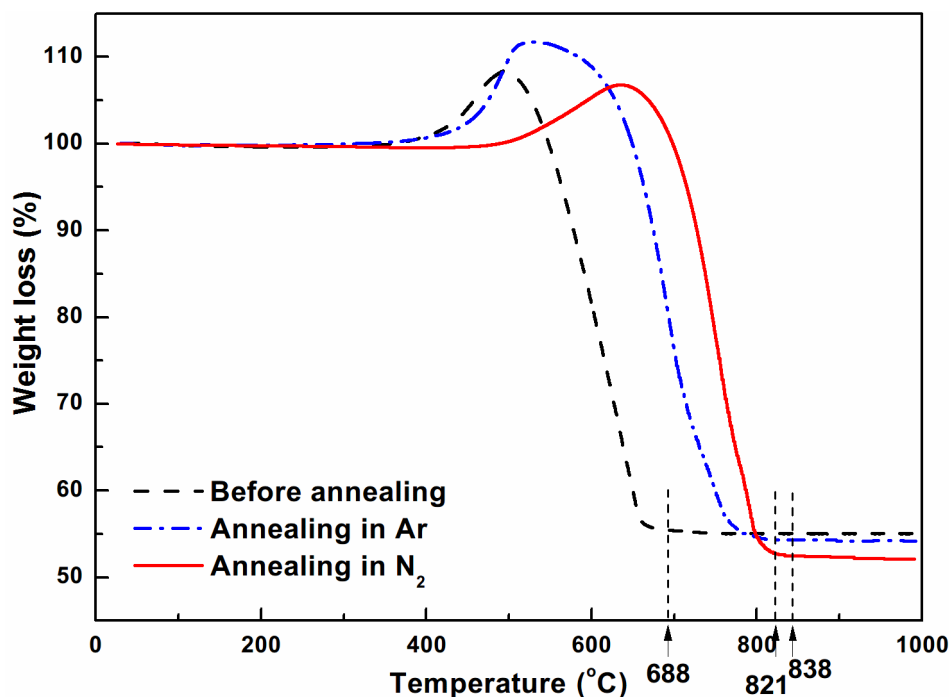


Fig. 6.14 TG curves of TiC-coated CB (with Ti/C molar ratio of 1/8) before and after annealing in Ar and N_2 at 1300 °C, respectively.

6.4.2.2 SiC-coated CBs

The effect of SiC coatings on oxidation resistance of CB was also investigated by TGA. Fig. 6.15 shows the weight loss against temperatures for uncoated and SiC-coated CB particles prepared in different Si/C molar ratios (1/8, 1/4 and 1/2). Slightly different to pristine CB (which commenced oxidation at ~ 472 °C), SiC-coated CB (Si/C=1/8) began to lose weight at ~ 510 °C, and ~ 543 °C and ~ 554 °C for 'thick' SiC coatings prepared in Si/C molar ratio of 1/4 and 1/2, respectively. This implies CB oxidation was postponed gradually with increasing SiC coating thickness. However, the TG curves of pristine CB and SiC-coated CB with Si/C molar ratios 1/8 and 1/4 nearly overlapped in the range of ~ 500 to 650 °C, indicating the latter did not effectively protect CB from oxidation at the elevated temperature.

Unlike TiC-coated CB, a weight gain at ~ 400 – 500 °C (which was due to TiC oxidation) was not seen in this case, because SiC normally have higher oxidation

temperature. However, small amounts of SiC indeed have been oxidised during the process of carbon oxidation, which was verified by XRD in Section 5.1.3.2. The formation of SiO_2 would balance the weight loss resulted from carbon combustion. For example, for SiC coated carbon black prepared from Si/C molar ratio of 1/8, the weight fraction of carbon is calculated as 67.7 wt%. So it might remain 32.3 wt% after carbon is completely oxidized, however, it was determined as 45.3 wt% experimentally. Such an increase in weight is mainly due to the conversion of SiC to SiO_2

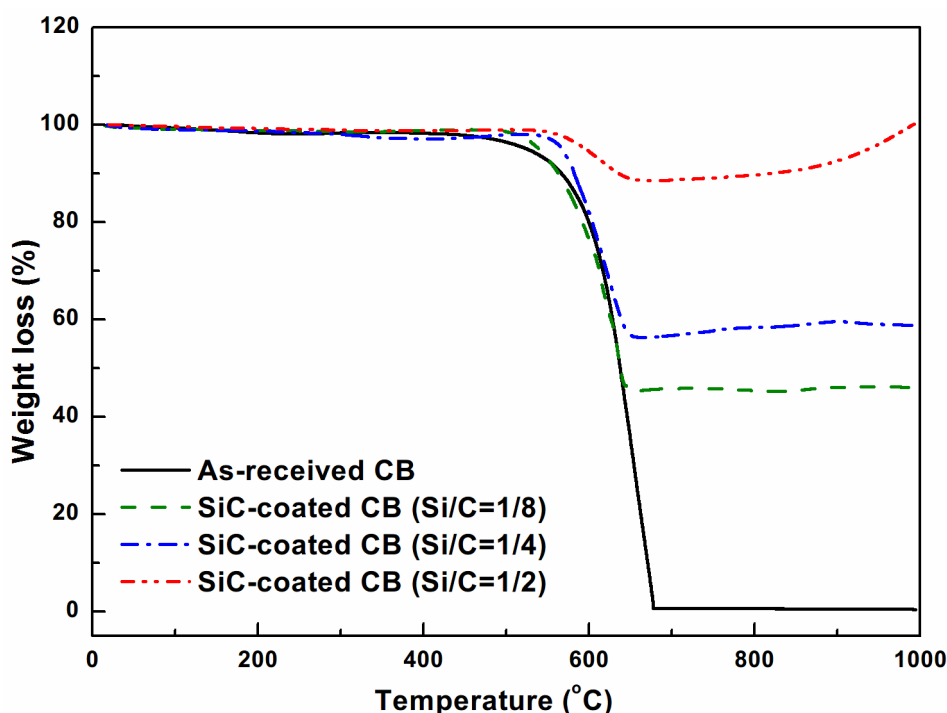


Fig. 6.15 TG curves of uncoated CB and coated CB with different thickness of SiC coatings prepared from initial Si/C molar ratio of 1/8, 1/4 and 1/2, respectively.

As indicated in Section 6.4.2.1, the annealing treatment is beneficial to the improvement in oxidation resistance of carbide-coated CB. Fig. 6.16 gives TG profiles of SiC-coated CB (Si/C=1/8) before and after annealing in Ar at 1200 and 1500 °C. Compared with as-prepared SiC-coated CB which commenced losing weight at ~510 °C and ended up at ~649 °C, SiC-coated CB after annealing 1200 °C started being oxidized at 577 °C and ended at 774 °C, over 100 °C higher than that of the former. Upon further increasing annealing to 1500 °C, the finishing point of carbon combustion was at 866 °C, indicating carbon oxidation was postponed remarkably. Since the chemical composition of coated CB particles was not changed during annealing treatment, the shift of TG curves to higher temperature directly reflects their improved oxidation resistance. In addition, higher annealing

temperature results in better oxidation resistance. For example, at 774 °C, SiC-coated CB after annealing at 1200 °C nearly lost all carbon materials, but there still remained more than 15 wt% (61.5-46.5 wt%) carbon in the sample annealed at 1500 °C.

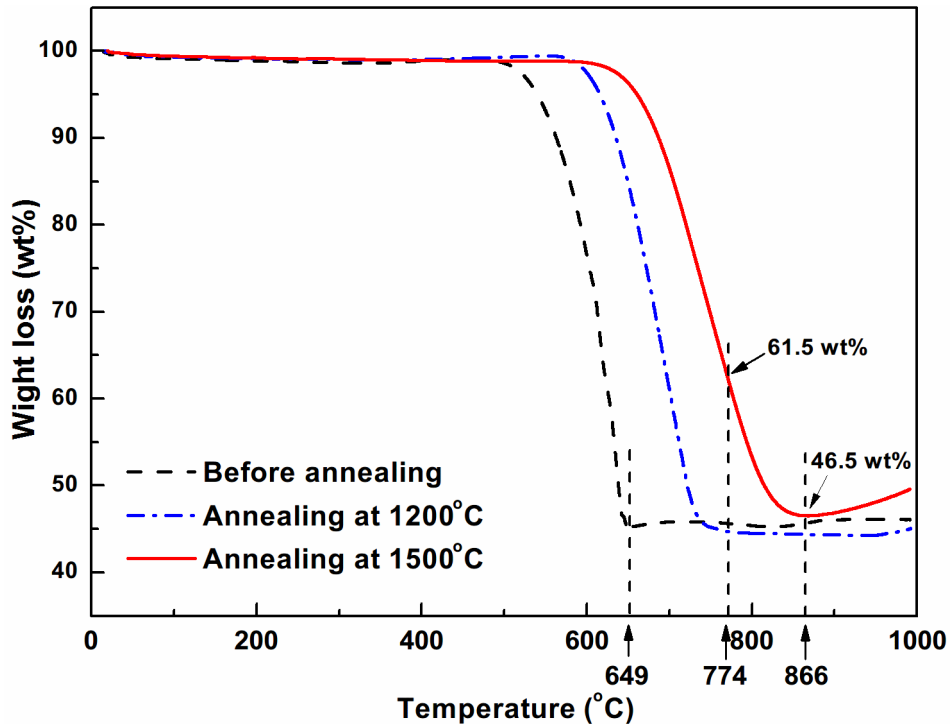


Fig. 6.16 TG profiles of SiC-coated CB before and after annealing at 1200 and 1500 °C in Ar.

6.4.3 Oxidation process

The oxidation behaviour of as-prepared TiC or SiC coated CB before and after annealing at high temperature was investigated by SEM and EDS in order to clearly demonstrate the oxidation process of carbide coated CB. Fig. 6.17a, as an example, shows SEM image of as-prepared TiC-coated CB particles in air 500 °C for 30 minutes. The spherical shape of particles remained, but high level of oxygen was detected on particle surface by EDS (Fig. 6.17d). However, only minor oxygen was found in the sample annealed in Ar (Fig. 6.17b, e) when they were exposed to the same oxidation conditions. For TiC-coated CB after annealing in N₂, the spheres remained almost the same to the one before oxidation at 500 °C, and elemental oxygen was hardly found (Fig. 6.17 c, f). This observation is consistent with the comparisons in weight loss characterized by TGA (Fig. 6.14).

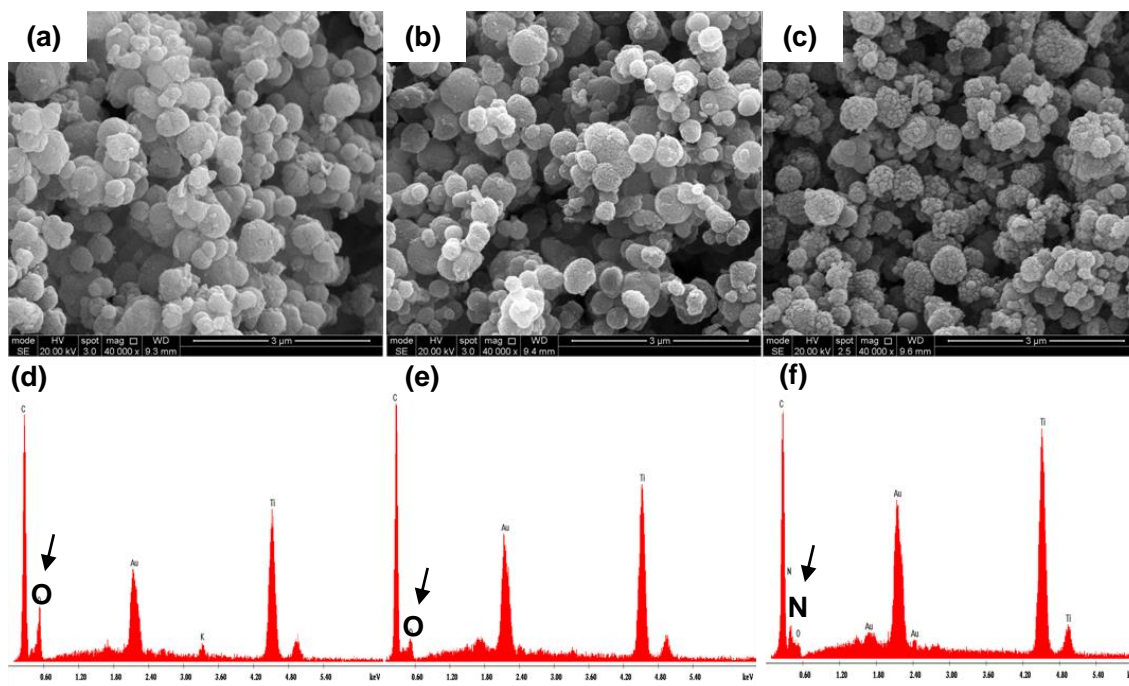


Fig. 6.17 SEM images of TiC-coated CB (Ti/C=1/8) (a) before and after annealing at 1300 °C in (b) Ar and (c) N₂. (d-f) are EDS spectra corresponding to (a-c). All these samples were characterised after firing in air at 500 °C.

Analogously, SiC-coated CB after annealing at high temperatures showed better oxidation resistance than the one without heat-treatment. Firing in 600 °C for 30 minutes, carbon was oxidised and SiC coatings were damaged to some extent. Some cracked spheres (as indicated by black arrows in Fig. 6.18a) were seen in the sample of SiC-coated CB without any treatment. Furthermore, the increase in oxygen intensity (Fig. 6.18b) was significant compared with the one before oxidation (Fig. 5.7b). In contrast, SiC-coated CB after annealing at 1500 °C remained the same as the one before oxidation, including undamaged SiC coatings and oxygen content on CB. Such a different performance under oxidation shows that annealing treatment is useful to improve oxidation resistance of SiC-coated CB, due to the formation of denser SiC coatings after post-treatment. This will be discussed in detail in later chapter.

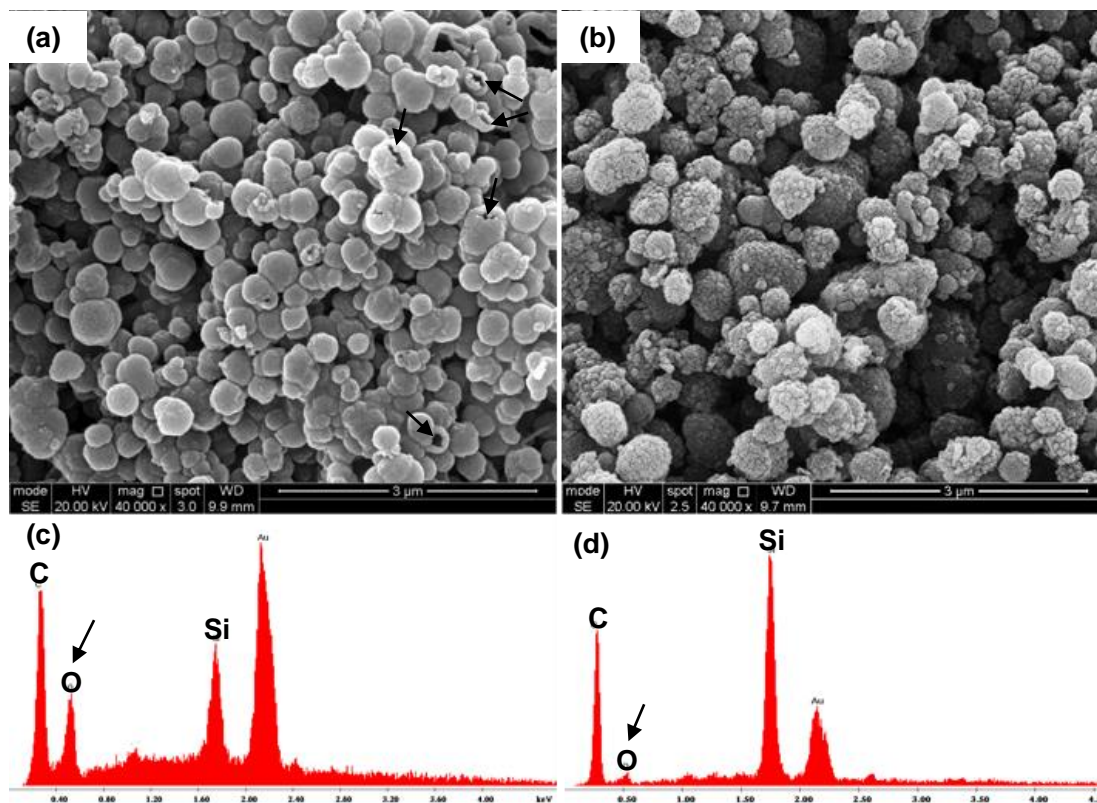


Fig. 6.18 SEM images of SiC-coated CB (Si/C=1/8) (a) before and (b) after annealing at 1500 °C, and their corresponding EDS spectra (c) and (d). Both of these two samples were characterised after firing in air at 600 °C for 30 minutes.

Chapter 7 $\text{Al}_2\text{O}_3\text{-C}$ castables

This chapter will be mainly focused on the applications of TiC or SiC coated carbon materials (GF and CB) in model low cement high alumina castables. Comparisons were made on water demand and flowability for uncoated and carbide-coated carbon containing castables during casting and placement. Their physical and mechanical properties, in terms of bulk density (BD), apparent porosity (AP), permanent linear change (PLC) cold crushing strength (CCS) and cold modulus of rupture (CMOR) were investigated after drying at 110 °C and coking at 1500 °C, respectively. Oxidation resistances of carbon-containing castables as well as their microstructures after oxidation testing were also examined.

7.1 Kg-scale production of carbide-coated CB and GF

For large scale trials of carbide-coated carbon materials in alumina castable systems, carbide-coated CB and GF particles were produced in kg-scale in a large vertical furnace (Fig. 3.4). Since the use of salts was significantly reduced for kg-scale production of coated CB and GF (the weight ratio of salt/reactants was reduced to 2/1 from 20/1 as described in Table 3.11), the coating quality of TiC and SiC was re-examined by SEM before their incorporation in castables. Fig. 7.1 shows typical SEM images of coated carbon particles prepared under such preparation conditions. Unreacted Ti and Si powders were not seen in the fired samples (Fig. 7.1a, b) and TiC-coated CB and SiC-coated CB particles appeared highly dispersed and showed the similar morphologies and sizes to the one prepared in small scale shown in Fig 4.2c and 5.6, indicating equivalent high quality of coated CB particles were produced with less salt consumption and lower cost. Meanwhile, TiC and SiC coated GF were also prepared for applications in $\text{Al}_2\text{O}_3\text{-C}$ low cement castables in order to investigate the effect of carbon types on their flowability, physical and mechanical properties. As shown in Fig. 7.1c and d, TiC was uniformly coated on GF, however, SiC coatings could not fully cover up all graphite flakes. This is consistent with the report by Liu [26].

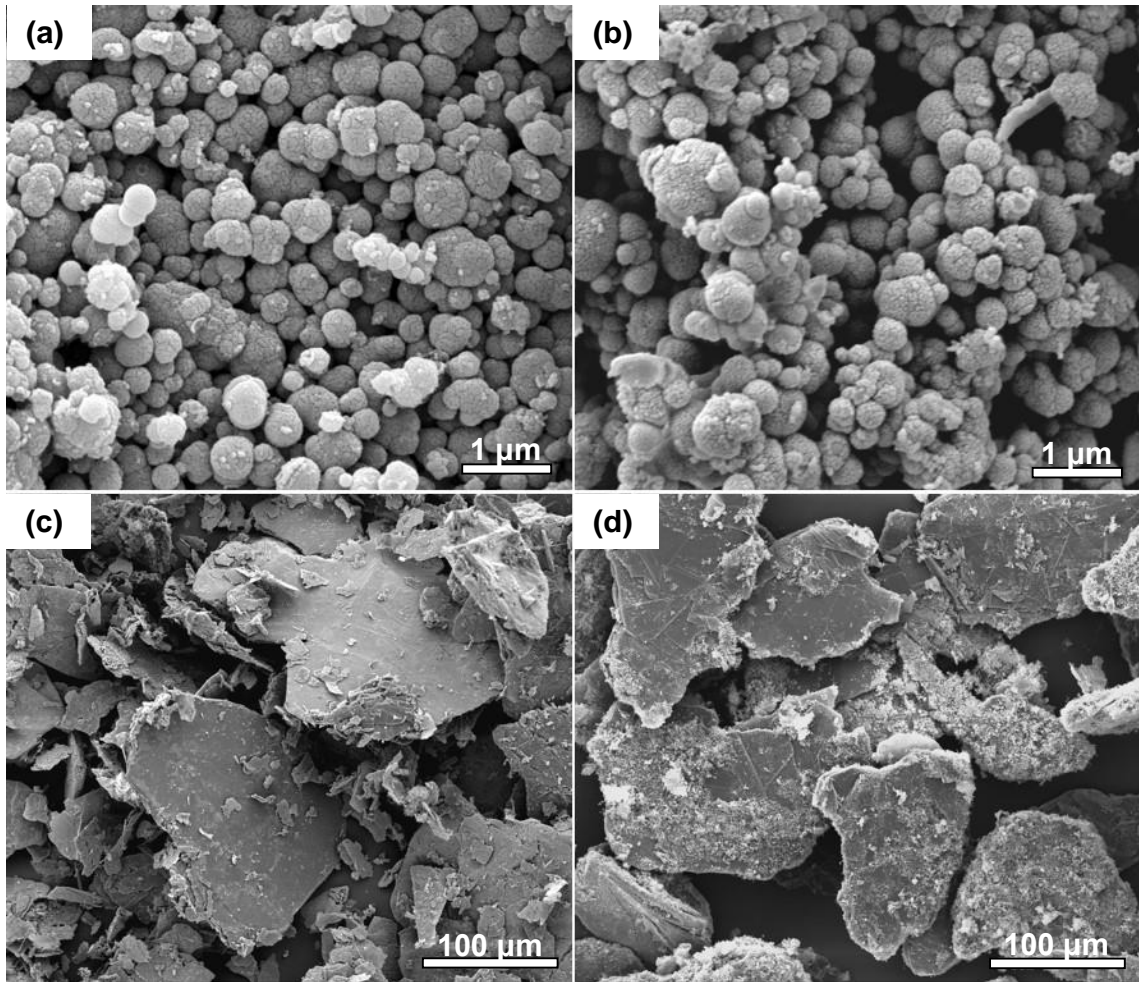


Fig. 7.1 SEM images of (a) TiC-coated CB, (b) SiC-coated CB, (c) TiC-coated GF and (d) SiC-coated GF prepared in a large vertical furnace.

7.2 Water demand and flowability

The water demand and flowability of castables were determined based on standard testing method ASTM C1445-99 (as described in Section 3.3.3.1). The criterion for good flowability (flow value) in this work was set as 140-150 mm where water addition was recorded.

Firstly, the effect of commercial sodium sulfonate-based carbon dispersant (referred to as 'SS' hereafter) on dispersion and flowability of GF in castables was investigated. Due to limited amounts of as-prepared coated GF, 2.5 kg-scale castables were prepared in this case. As shown in Fig. 7.2, castable without GF achieved a flow value of 150 mm at only 5 wt% water addition, however, it required more water (8 wt%) to make castable paste flow properly when 5 wt% GFs were added. The dramatic increase in water addition is due to GF's poor wettability and dispersion in water (as addressed in Section 2.3.1). When carbon dispersant, SS, was incorporated along with GFs into alumina-based castable, the flowability of castable at 8 wt% water addition, on the contrary, was slightly decreased compared with GF-containing castable (referred as GF castable hereafter), indicating SS has almost no positive effect on improving flowability of castable and reducing water demand correspondingly. Nevertheless, such a carbon dispersant is beneficial to the homogenous dispersion of GF in castables. Fig. 7.3, as an example, shows the surface of castable specimens after casting in cubic moulds. A number of clusters of shining GFs (as indicated by black arrows) were seen in the GF castable without SS (Fig. 7.3a), whereas GFs were homogeneously dispersed in the castable containing SS (Fig. 7.3b).

As for TiC-coated GF containing castables (referred to as GF-TiC castables hereafter) either in the presence of SS or not, it required 6.25-6.5 wt% water to achieve similar flow value to GF-castable (Fig. 7.2), indicating a reduction of 1.5 wt% in water addition was achieved for castable preparation. This shows TiC coatings on GF are beneficial to improve flowability of castables and reduce their water demand.

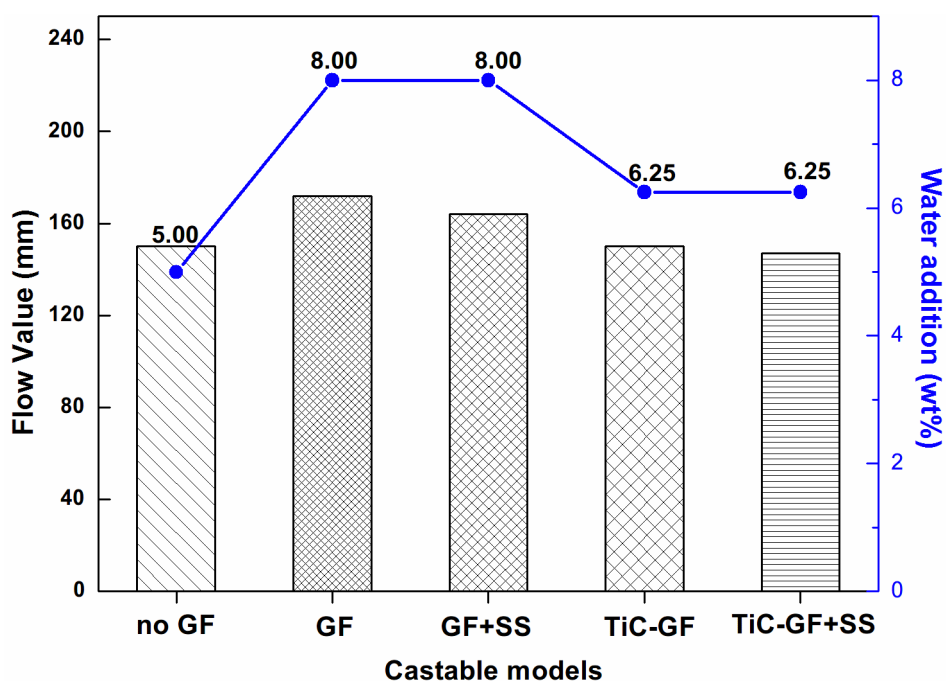


Fig. 7.2 Flow value and water addition of castables containing uncoated and TiC-coated GF (2.5 kg-scale batch).

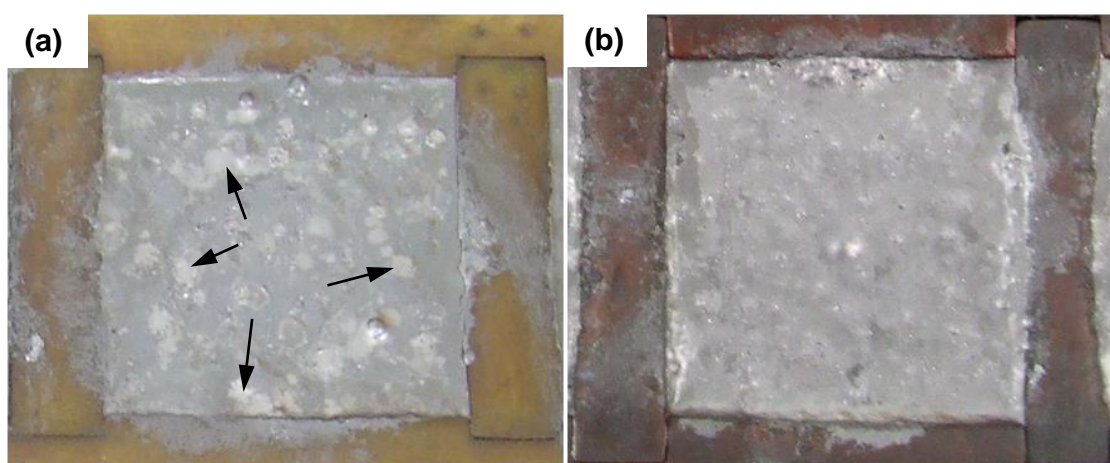


Fig. 7.3 Photos of GF-containing castables (a) without and (b) with SS after casting in cubic moulds with assistance of vibration.

Based on the above investigation, it can be concluded that carbon dispersant (SS) was not capable of reducing water addition effectively for preparation of carbon-containing castables. So carbon dispersant was not added in all castable batches prepared hereafter. Thus, standard trials (5.5kg for each batch) were carried out to investigate the effect of carbide coatings, carbon types and carbon content on water demand for castable casting.

Fig. 7.4 shows that GF castable required the highest water level (9.7 wt% water addition) to achieve the standard flow value (140-150 mm in the present work),

however, SiC-CB castable showed the lowest requirement for water, only 6.5 wt% at an equivalent level of carbon addition (5 wt%). Compared with GF castable, TiC-GF castable only required 7.0 wt%, showing 2.7 wt% reduction in water addition level. However, SiC-GF castable did not show a significant improvement, due to low quality of SiC coatings formed on GF. In terms of amorphous carbon, castable containing 5 wt% uncoated CB showed better flowability and less water demand (8.5 wt%) than that containing GF. It is believed that it results from spherical shape of CB particles and a few functional groups on their surface. With carbide coating on CB, the water demand for castable achieving standard flow was further reduced, only 7.0 wt% for TiC-CB castable and 6.5 wt% for SiC-CB castable. The remarkable reduction in water addition would lead to less apparent porosity and better mechanical properties (See 7.3). When increasing SiC-CB content in castable from 5 to 8 wt%, more water (7.5 wt%) was needed to reach the same flow value.

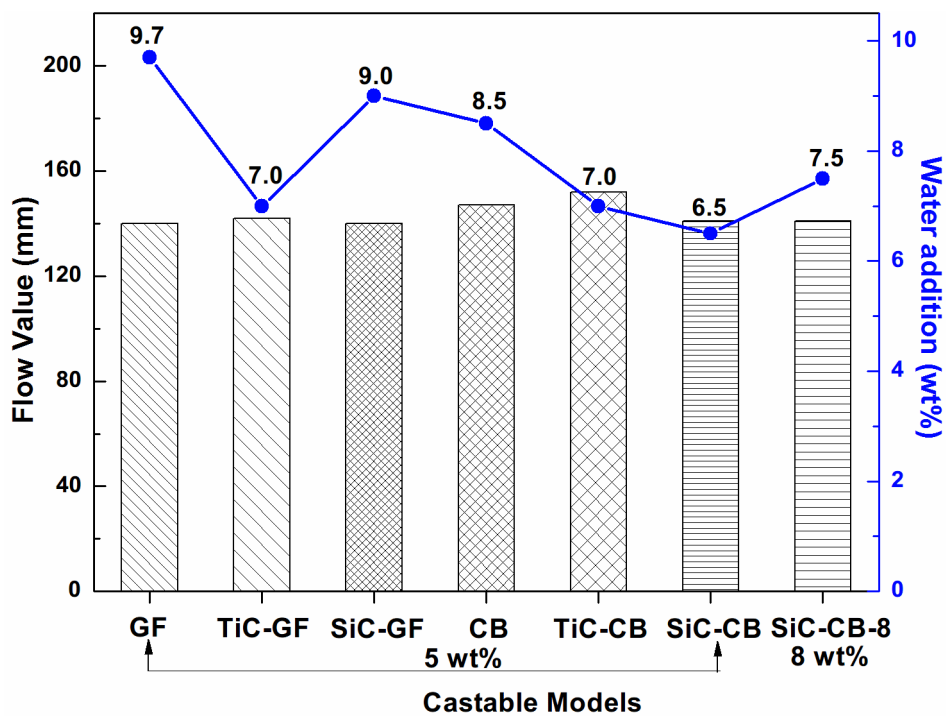


Fig. 7.4 Flow value and water addition of castables containing different carbon sources (standard 5.5 kg-scale batch).

7.3 Physical and mechanical properties

7.3.1 Bulk density, Apparent porosity and Permanent linear change

The apparent porosity (AP) and bulk density (BD) of castables after drying at 110 °C and coking at 1500 °C were measured respectively. As shown in Fig. 7.5, apparent porosity of castables containing various carbon particles after coking at 1500 °C appeared to be higher than that just after drying without high-temperature treatment. The increase is obviously caused by the loss of chemically combined water molecular which were not driven off at 110 °C and evaporation of free water which were trapped in closed pores.[207] The rise in AP from 110 to 1500 °C was dramatic for castables containing uncoated carbon particles (22.6% to 26.5% for GF and 24.6% to 29.8% for CB). High level of water addition required for casting GF or CB containing castables is responsible for such a significant increase in AP after coking at 1500 °C.

In the cases of TiC-coated GF and TiC-coated CB containing castables, similar flowability (Fig. 7.4) was achieved when equivalent water (7 wt%) was added in both castables, but the latter exhibited slightly higher AP than the former. Castable with TiC-GF showed the lowest AP of only 17.2% at 110 °C and 19% at 1500 °C which was lower than that of spinel-coated GF containing castable (over 22% at 1500 °C) investigated by Mukhopadhyay et al [140]. Compared with model TiC-CB castable, SiC-CB containing castable showed ~2% lower in AP than the former.

In terms of bulk density, castables with carbide-coated GF or CB generally had higher BD than with uncoated counterpart, exhibiting denser structure. For example, TiC-GF castable had bulk density as high as 3.0 g/cm³, but the one with CB had the lowest BD (2.5 g/cm³ after coking) among these castables. Low apparent porosity is mainly responsible for high bulk density, however, the contribution of carbide coatings to density increase cannot be ignored. Furthermore, when increasing SiC-CB content from 5 to 8 wt%, the bulk density of corresponding castable was decreased, for instance, from 2.88 to 2.71 g/cm³ at 1500 °C, which is attributed not only to increased water addition and AP but also to the increased addition of SiC-CB particles with lower density (2.23 g/cm³, see Fig. 5.17) compared to aggregate grains (e.g. Al₂O₃, ≥ 3.50 g cm³). In addition, showing the opposite trend of apparent porosity, the bulk density of castables after coking 1500 °C increased slightly, mainly

due to shrinkage in dimensions or volumes as shown in Table 7.1.

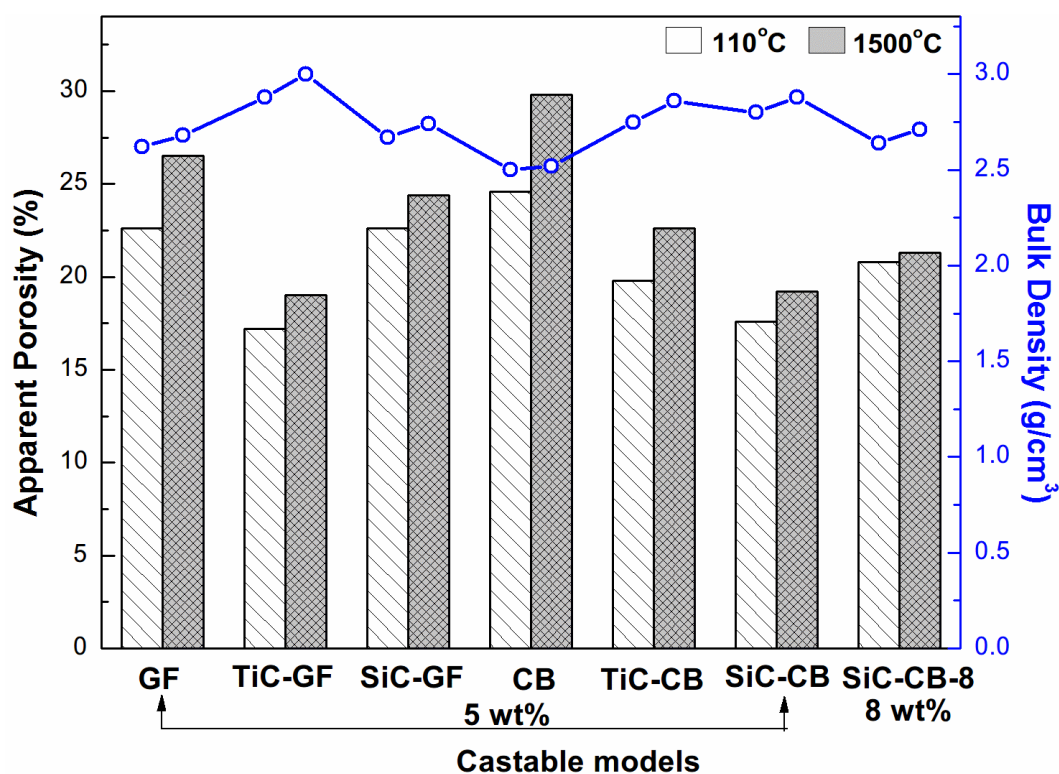


Fig. 7.5 Apparent porosity and bulk density of castables containing different carbon materials.

Permanent linear (or volume) changes (PLC or PVC) were also determined to evaluate the dimension changes and suitability of refractories in ranges of working temperatures. The changes were recorded before and after coking at 1500 °C. Table 7.1 shows PLC and PVC of castables containing different carbon particles. In all these castables, shrinkage occurred to some extent, which is most likely due to consequence of sintering at high temperature. Some liquid phases such as CaO-Al₂O₃-SiO₂ (CAS or CAS₂) would also contribute to the volume reduction.

As for control sets, uncoated GF containing castable showed greater linear change than uncoated CB containing castable. Although GF and CB were incorporated at the same addition level (by weight percentage), CB possessed more numbers of particles due to the smaller size. It means more carbon particles were distributed in CB castables and consequently contributed more to keep stable in dimensions at elevated temperature. In addition, the highest shrinkage took place on castable with TiC-GF, while the lowest shrinkage on the one with SiC-CB. Despite the shrinkage occurred after firing at 1500 °C, the PLC of each model castable was in the range of -0.46% to -1.42% which is tolerated for practical use (less $\pm 2.5\%$)[117].

Table 7.1 Permanent linear change and permanent volume change of castables containing different carbon materials.

| | GF | TiC-GF | SiC-GF | CB | TiC-CB | SiC-CB | SiC-CB-8 |
|-------------------|-------|--------|--------|-------|--------|--------|----------|
| PLC on Firing (%) | -1.05 | -1.42 | -1.02 | -0.59 | -1.40 | -0.46 | -0.62 |
| PVC on Firing (%) | -3.10 | -4.19 | -3.01 | -1.76 | -4.14 | -1.37 | -1.86 |

7.3.2 Cold crushing strength and cold modulus of rupture

Mechanical properties such as cold crushing strength (CCS) and cold modulus of rupture (CMOR) were investigated on both green castables just after drying at 110 °C and castables after coking in a reducing atmosphere (CO) at 1500 °C for 5 hours. Fig. 7.6 shows cold crushing strength of castables containing different carbon materials. It can be seen that castables incorporated with TiC or SiC coated carbon particles (GF and CB) showed 6 times higher in CCS than uncoated GF or CB containing castables. Among coated carbon containing castables, TiC-GF castable after coking at 1500 °C was able to withstand higher crushing strength than TiC-CB counterpart, mainly due to its lower AP. Moreover, specific layer-structured graphite enabled TiC-GF castable to resist high compression stress. However, SiC-GF castable showed less crushing resistance than corresponding SiC-CB castable, due to evidently low AP caused by high water demand for proper flow (Fig. 7.4). When the content of SiC-CB was increased to 8 wt%, CCS slightly decreased, since part of alumina grains were replaced by SiC-CB particles.

Interestingly, the crushing strength did not show a consistent increase for all castable specimens after firing and sintering at 1500 °C in CO environment. It must have to be the consequence of intensive competition between increased unfavourable apparent porosity (Fig. 7.5) and formation of strong ceramic bindings such as dehydrated CA binding phases, solidified CAS phases and formed mullite phase at high temperature.

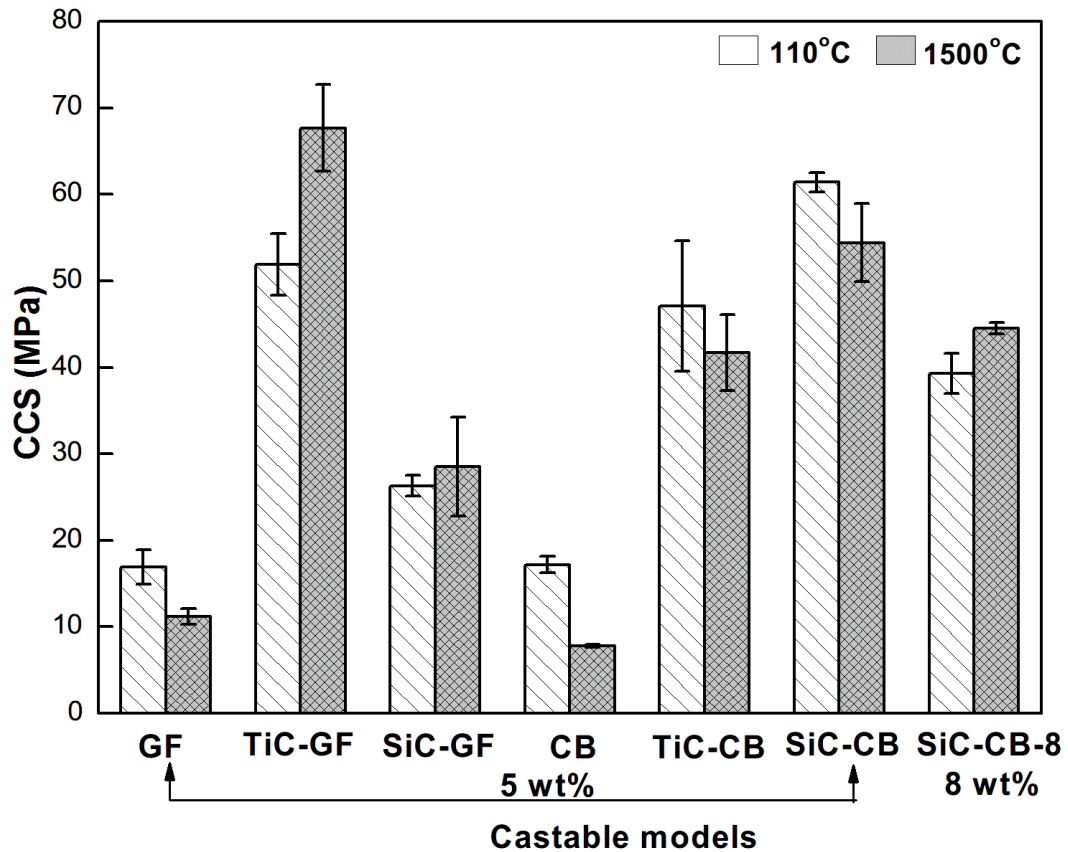


Fig. 7.6 CCS as a function of different carbon materials incorporated castables.

However, the increase in bending strength of castables after coking at 1500 °C was quite evident compared with that of green castables, and such a trend was followed by all model castables as shown in Fig. 7.7. Overall, the bending strength after high temperature sintering was almost doubled for uncoated carbon containing castables but even tripled for coated carbon containing castables. Consistent with results of cold crushing strength, uncoated CB or GF containing castable showed the lowest bending strength, for example, only 1.6 MPa at 110 °C and 3.5 MPa at 1500 °C for CB castable. In contrast, the rupture strength could reach 13.8 MPa for TiC-CB castable and 18.3 MPa for SiC-CB castable at 1500 °C. TiC-GF castable exhibited the highest rupture strength after coking, reaching 22.1 MPa which is over four times higher than that of GF castable.

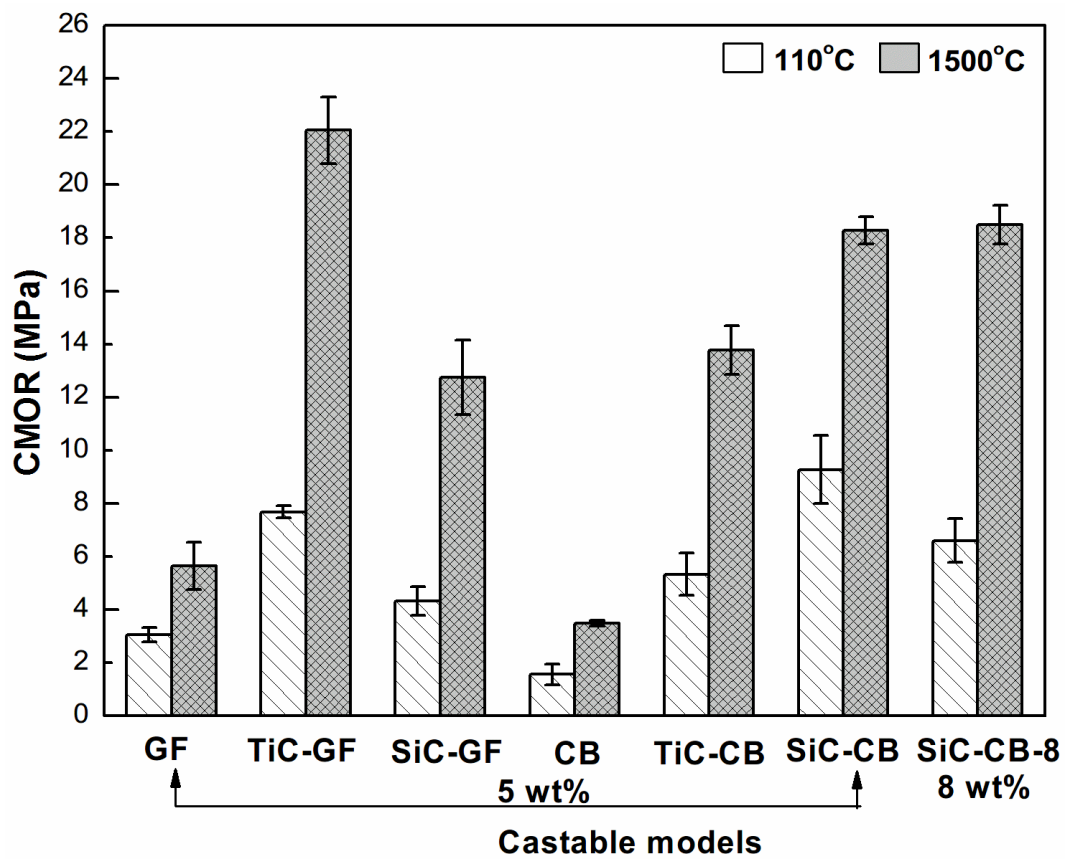


Fig. 7.7 CMOR as a function of different carbon materials incorporated castables.

7.4 Oxidation resistance

In this work, antioxidants such as Al, Si or B₄C were not added to the castables in order to investigate the effect of carbide coatings alone on the oxidation resistance of carbon particles in carbon-containing castables at elevated temperatures. The oxidation test was initially performed at 1000 °C for 30 minutes. Fig. 7.8 shows the cross-sections of uncoated GF and CB castables after oxidation under the conditions. It can be seen that the oxidation was not so severe and only a thin oxidation layer (white zone as shown in Fig 7.8) was obtained.

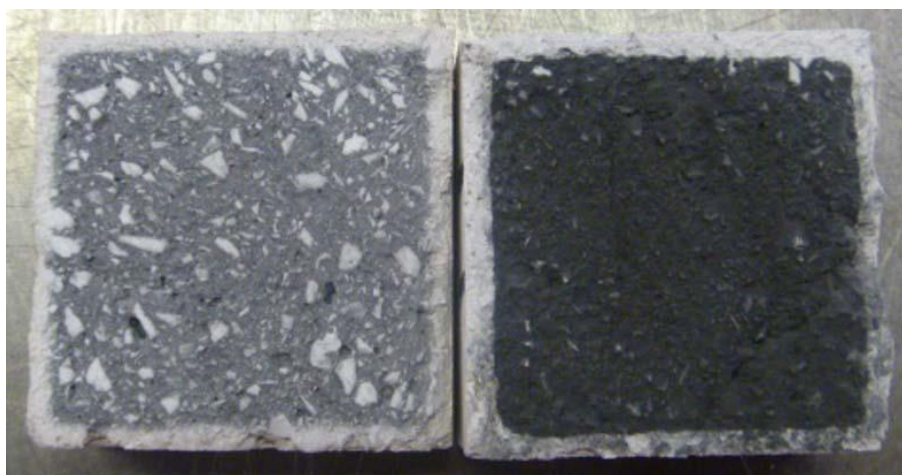


Fig. 7.8 Preliminary oxidation test of castable samples containing uncoated GF (left) and uncoated CB (right) performed at 1000 °C for 30 minutes.

To increase evident oxidation extent, the oxidation of carbon-containing castables at 1000 °C was extended to 3 hours in air. Fig. 7.9 demonstrates the cross-sections of oxidized castables, showing more severe oxidation was obtained compared to Fig. 7.8. Overall, there were more unoxidised carbon materials (indicated by black area in the centre of cubes) left in carbide coated GF or CB containing castables than uncoated GF or CB containing castable, indicating carbide coatings show a positive effect on oxidation resistance of carbon in the castable applications.

The oxidation of carbon-containing castables was commonly indexed by decarbonized depth and corresponding oxidation area. Fig. 7.10 shows the decarbonized depth of TiC-GF castable was 6.28 mm, much less than that of uncoated GF castable (7.90 mm). CB castable was severely oxidized and showed the decarbonized depth of 10.48 mm, whereas TiC-CB castable's decarbonized depth was 6.82 mm. Furthermore, SiC-CB castable exhibited even better oxidation resistance with a decarbonized depth of 6.35 mm.

As shown in Fig. 7.9f, the oxidised area of SiC-CB castable appeared light grey rather white colour, indicating unoxidised SiC-coated CB particles or SiC shells remained after oxidation. This is because SiO₂ would be formed from oxidation of black SiC coatings and thus appeared white in oxidized area, similar to TiO₂ containing oxidized area shown in Fig 7.9e. More details will be revealed by microstructural observation in later section.

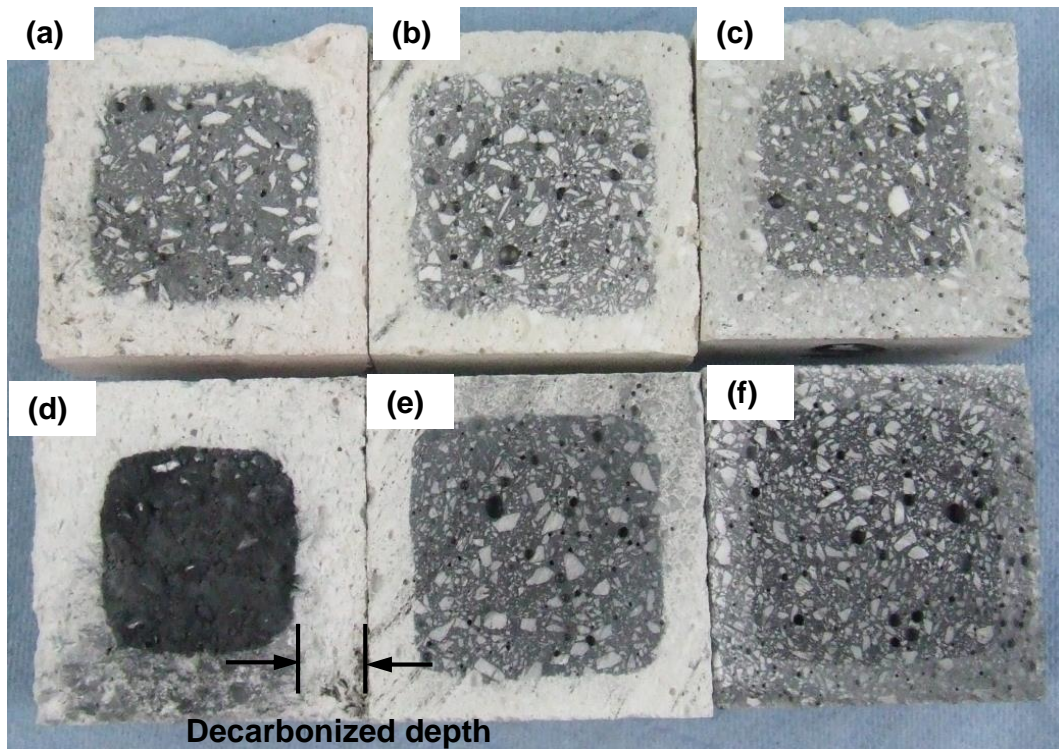


Fig. 7.9 Cross-sections of Al₂O₃-C castables containing 5 wt% (a) GF, (b) TiC-coated GF, (c) SiC-coated GF, (d) CB, (e) TiC-coated CB, and (f) SiC-coated CB, respectively, after oxidation in air at 1000 °C for 3 hours.

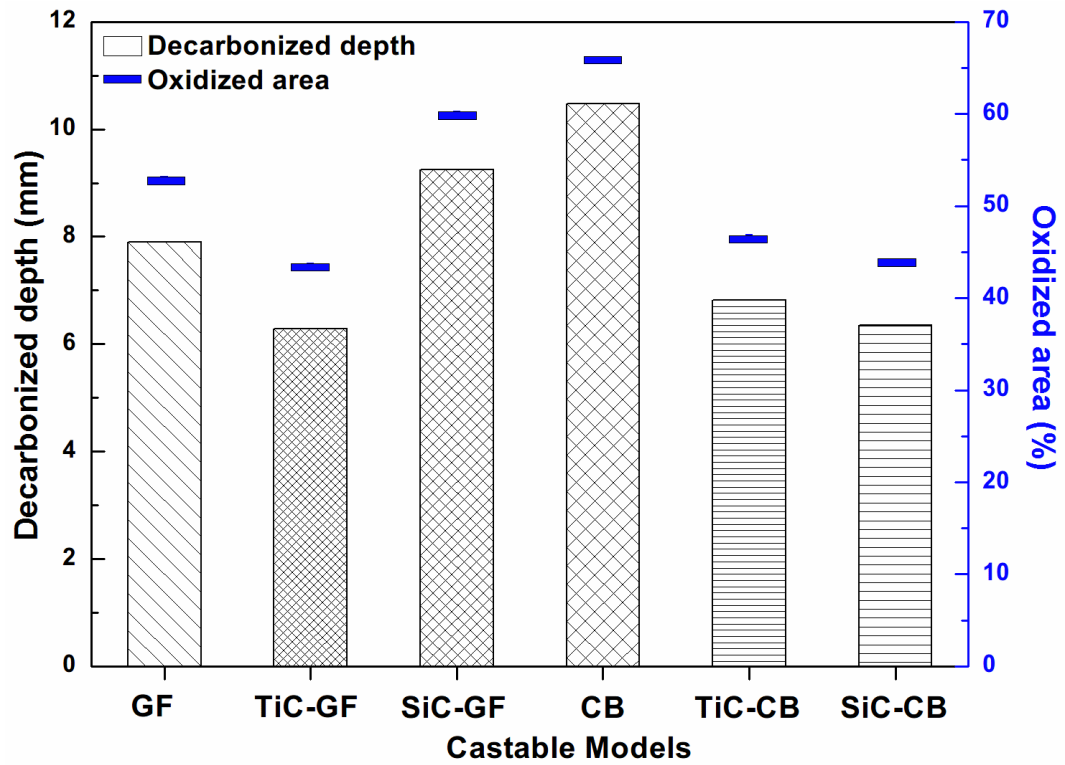


Fig. 7.10 Decarbonized depth and oxidation area of various castable models after oxidation at 1000 °C for 3 hours.

7.5 Microstructural examination

7.5.1 Castable specimens after coking at 1500 °C

All castable specimens were embedded in coke and fired at 1500 °C for 5 hours in air where CO-rich atmosphere was produced by reaction of the coke with oxygen. Since GF castable was highly porous (Fig. 7.5) and showed low mechanical properties (as indicated in Figs 7.6 and 7.7), it was difficult to obtain high quality polished surface of samples for microstructural examination. Fig. 7.11a shows a typical back-scattered image (BEI) of fracture surface of GF castables. Flaky graphites (dark contrast) were dispersed in the matrix and several pores (> 100 µm) were seen. Fig. 7.11b shows BEI of the polished surface of TiC-GF castable. In addition to large tabular alumina (TA) grains, TiC-coated GF (bright phase surrounding dark stripe-like substance as indicated by white arrows) were closely embedded in the matrix. TiO₂ was not formed in this case, since the Gibbs free energy of reaction between TiC and CO at 1500 °C was +70.4 kJ. In addition, low melting calcium aluminium silicate (CAS) liquid formed in the matrix leaving bright CAS-rich regions. The CAS phase was further verified by secondary-scattered imaging (SEI) (Fig. 7.11c) and EDS analysis (Fig. 7.11d, Spot A) in which Al, Ca, Si and O elements were detected. Moreover, it was noticed that the solidified CAS liquid bonded all matrix and additives (e.g. TiC-GF) together, providing mechanical strength for the castables. The EDS analysis (Fig. 7.11d, Spot B) showed TiC coatings still remained on GF (as indicated by black arrows in Fig. 7.11c) and not destroyed after vigorous mixing with aggregates and firing in CO at 1500 °C.

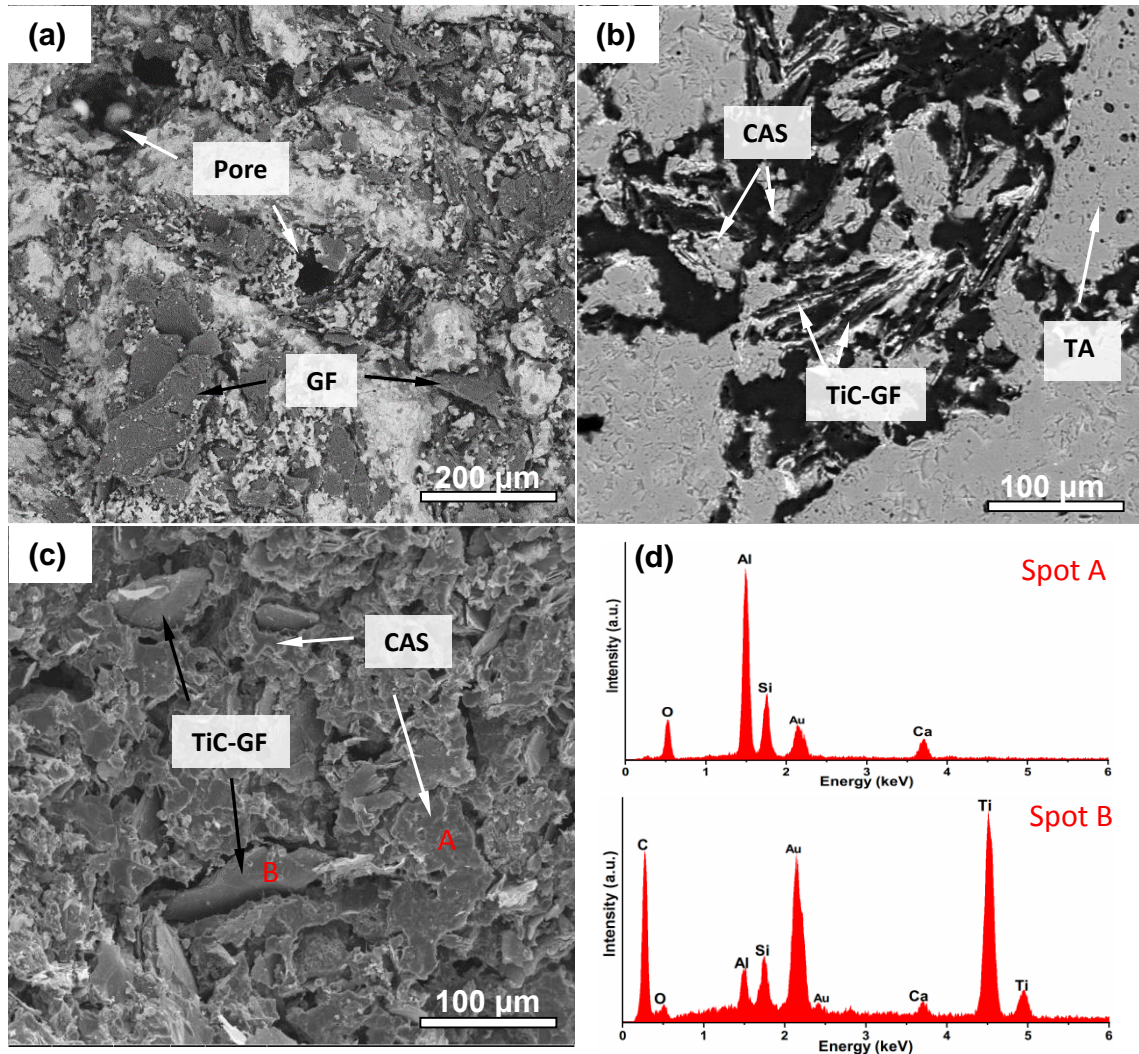


Fig. 7.11 BEI of (a) GF castable and (b) TiC-GF castable after coking at 1500 °C; (c) SEI of TiC-GF castable after coking at 1500 °C; (d) EDS spectra detected from spot A and B in (c). (CAS- $\text{CaO}\cdot\text{Al}_2\text{O}_3\cdot\text{SiO}_2$ ternary phase; TA- Tabular alumina)

Given the high mean atomic weight of TiC, TiC-CB spheres with bright contrast were observed in BEI shown in Fig. 7.12a. Most of TiC-CB spheres were well dispersed in the matrix (Fig. 7.12c), but a few of the spheres were agglomerated (as indicated black arrows in Fig. 7.12a). The slightly dark agglomerates of TiC-CB spheres, implying that CB with TiC coating can be well mixed with fine gradients in the castable. As for SiC-CB containing castable (Fig. 7.12b), part of SiC-coated CB spheres appeared as dense phase in the microstructure. The EDS confirmed that the agglomerates (Spot A) also contained Al₂O₃, SiO₂, and CaO phases or their combinations with unidentified ratios. It could be speculated that SiC-coated CB spheres was compatible with cement and microsilica so that they were bonded together as clusters and sintered at high temperature. The morphology of SiC-CB containing castable (Fig. 7.12d) shows that despite of a few clusters, SiC-CB

spheres were dispersed homogeneously in the matrix. In addition, a large number of well-developed mullite (Mu) crystals (Fig 7.12b, Spot B) formed inside alumina agglomerates suggesting that the microsilica reacted with the alumina forming aluminosilicates at 1500 °C. EDS (Fig 7.12b, Spot B) shows a Al/Si ratio of 3/1, consistent with mullite ($3\text{Al}_2\text{O}_3 \cdot 2\text{SiO}_2$, A_3S_2) composition. Mullite formation is quite common for silica-containing high alumina castables in which microsilica reacts with alumina at above 1200 °C.[208, 209]. The presence of mullite can contribute to the physical, chemical and mechanical properties of refractory castables.

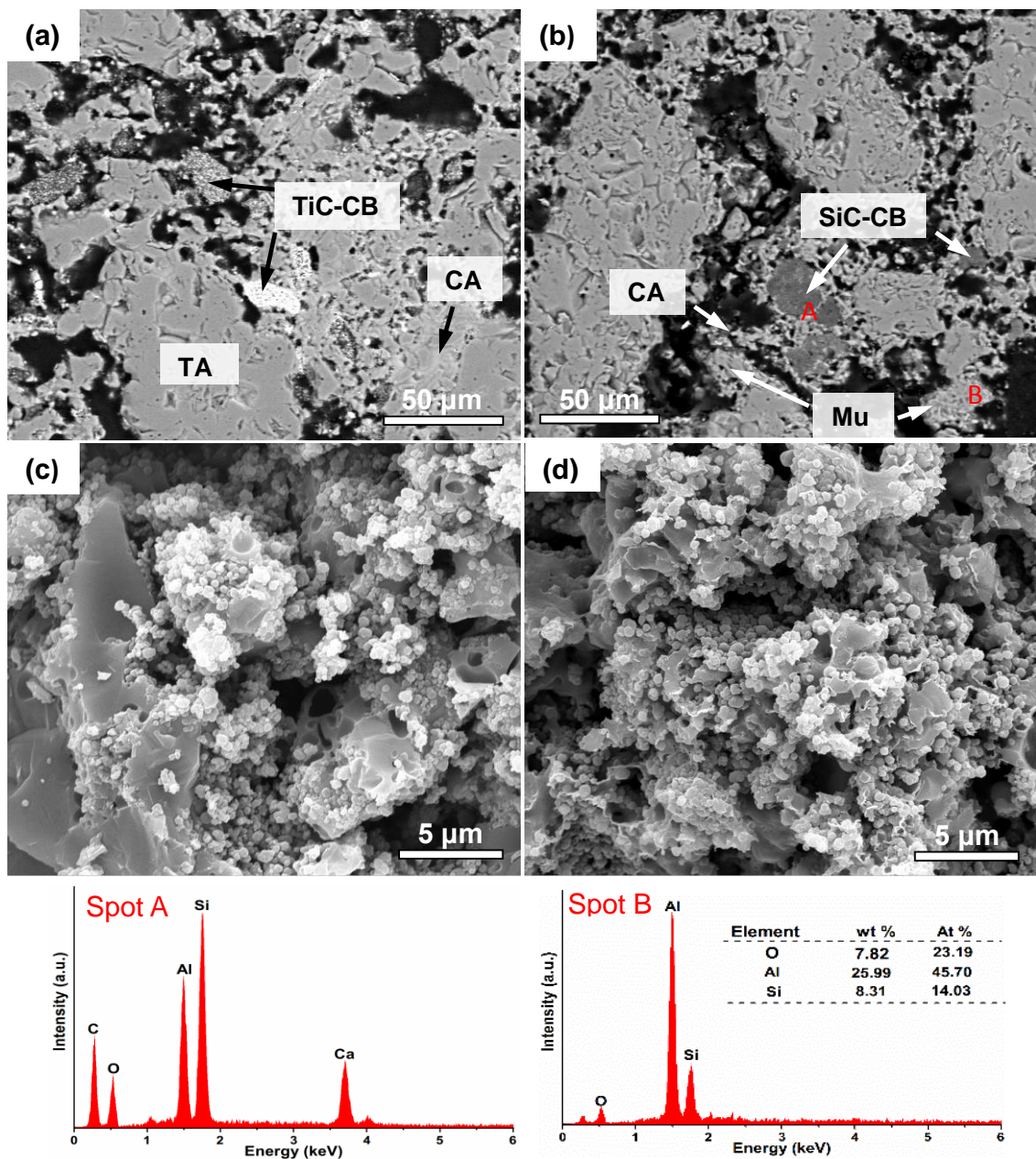


Fig. 7.12 BEI of castables containing (a) TiC-CB and (b) SiC-CB, SEI of castable containing (c) TiC-CB and (d) SiC-CB. The EDS spectra on spot A and B were also given at the bottom. (CA- $\text{CaO} \cdot \text{Al}_2\text{O}_3$ calcium aluminate; Mu- $3\text{Al}_2\text{O}_3 \cdot 2\text{SiO}_2$)

7.5.2 Castable specimens after oxidation test

7.5.2.1 Uncoated and coated GF containing castables

Fig. 7.13 shows BEI of unoxidised and decarbonized areas after oxidation of GF castable at 1000 °C for 3 hours. Several large pores were seen from this poor texture before oxidation (Fig. 7.13a), which further verified its high apparent porosity (Fig. 7.5) caused by high level of water addition for proper castable flow. The graphite flakes were observed as stripe-like shape when viewed from lateral side of flaky graphite. After oxidation (Fig. 7.13b), GFs were burnt out and left cavities with a GF's shape. However, sintering was not started at 1000 °C, leading to even higher porosity. As a result, oxygen readily diffused through newly-formed pores and aggravated carbon oxidation.

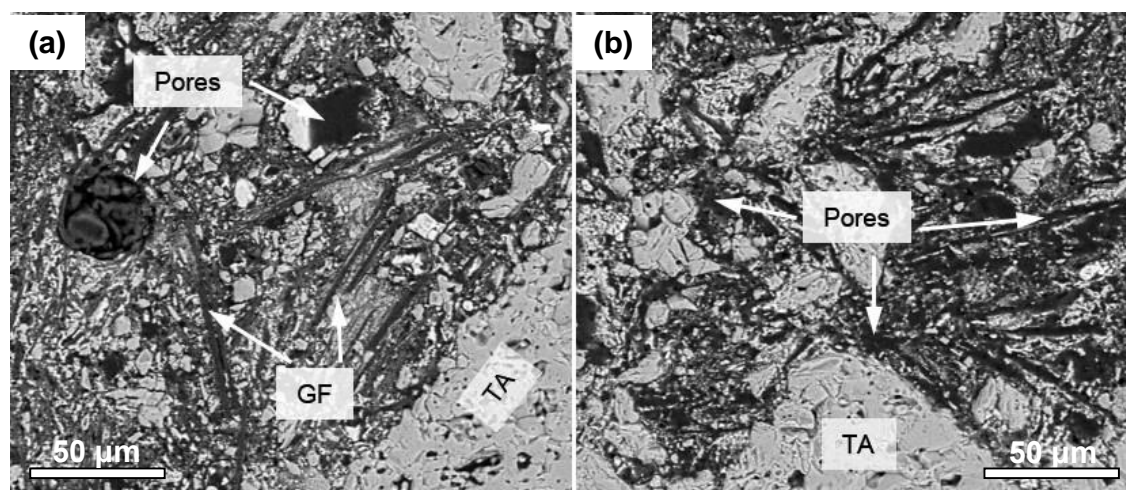


Fig. 7.13 BEI of (a) unoxidised and (b) decarbonized areas after oxidation of GF castable at 1000 °C for 3 hours.

Compared with GF castable (Fig. 7.13a), aggregates, fine powders and GF were closely packed (Fig. 7.14a). In the unoxidised area, the bright phase surrounding black GF was identified as TiC by EDS (Fig. 7.14c), indicating that TiC coating remained when subjected to vigorous mixing during castable preparation. Two graphite flakes stuck together with Al₂O₃ and SiO₂ fine powders clipped between them, forming a sandwich structure. As indicated by red dotted circle in Fig. 7.14a, the graphite flakes were tightly bonded with matrix, which was not seen in uncoated GF containing castable. The phenomenon implies that GFs coated with TiC are highly compatible with oxide matrix, forming compacted bulk composite. After firing in air atmosphere, in addition to oxidation of GF, TiC was converted to TiO₂ (Fig. 7.14b), which was evidenced by EDS (Fig. 7.14d). The formation of TiO₂ consumed

part of O₂ and thus reduce carbon oxidation to some extent. On the other hand, the voids generated by graphite oxidation were filled with TiO₂, further decreasing the oxygen diffusion into the internal of castable and consequently retarding further oxidation.

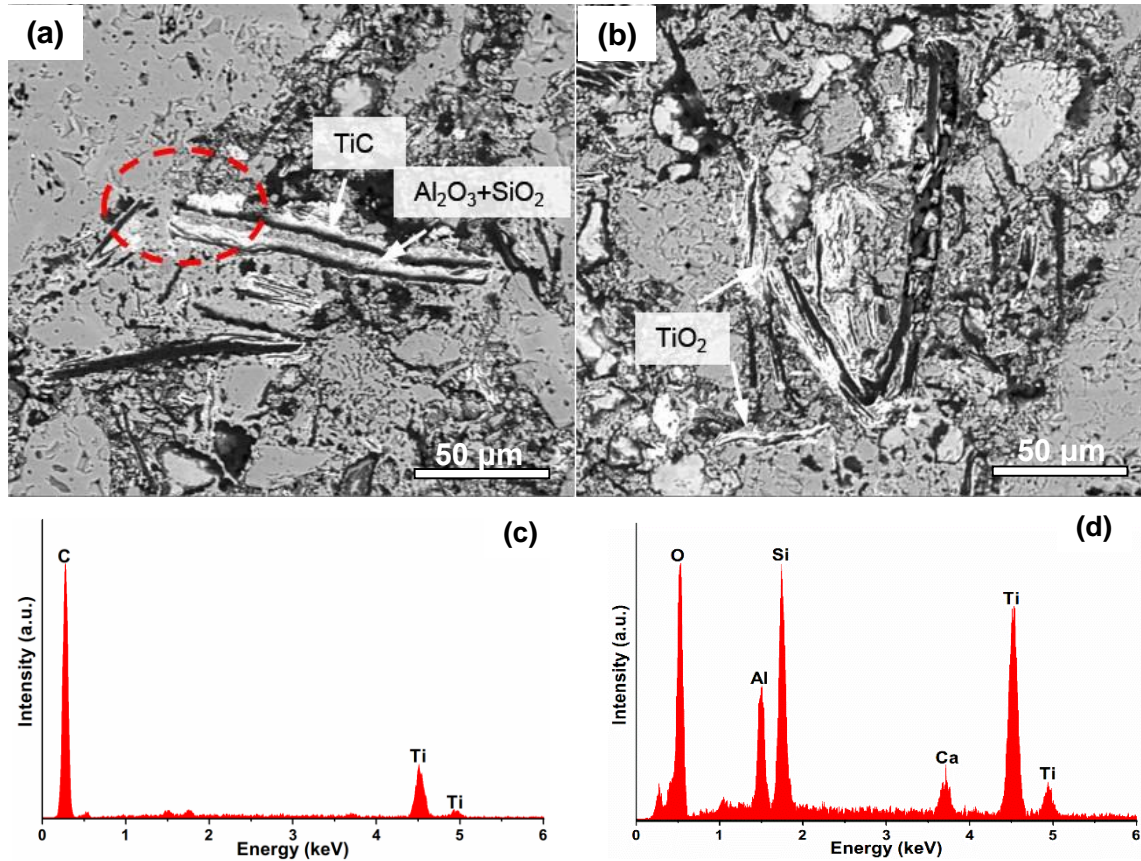


Fig. 7.14 BEI of (a) unoxidised area and (b) oxidized area in TiC-GF castable; (c) EDS on graphite surface shown in (a), and (d) EDS of bright phase indicated by arrows shown in (b).

7.5.2.2 uncoated and coated CB containing castables

Compared with uncoated CB-containing castable, TiC-CB castable showed over 3.6 mm less in the thickness of decarbonized layer than that in the case of the former (Fig. 7.9d, e), exhibiting much better oxidation resistance. This is mainly attributed to much lower apparent porosity and closely packed structure. Fig. 7.15 shows the microstructures of TiC-CB castable in unoxidised and decarbonized area, respectively. There was no major difference in the texture and phase compositions except the conversion of TiC to TiO₂. EDS (Fig. 7.15c) shows the clusters in unoxidised area (slightly bright contrast as indicated by black arrows) comprised C, Ti, O, Al and Si, showing the clusters were the mixtures of TiC-CB, Al₂O₃ and SiO₂. After oxidising the castable, bright TiO₂ area as well as cement phase (dehydrated

CA) was seen in Fig. 7.15b, which was further verified by XRD (Fig. 7.16)

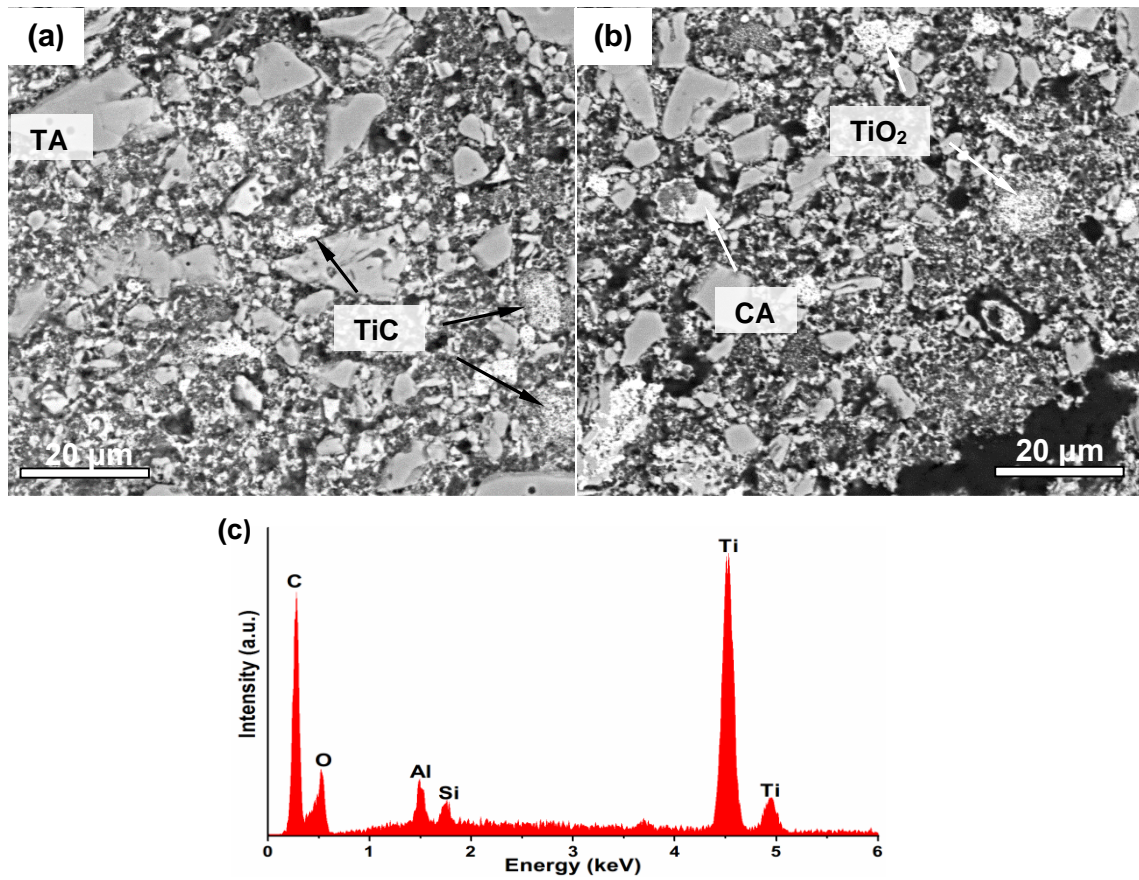


Fig. 7.15 BEI of (a) unoxidised and (b) decarbonized area in TiC-CB castable after oxidation at 1000 °C for 3 hours; (c) EDS of bright powder clusters shown in (a).

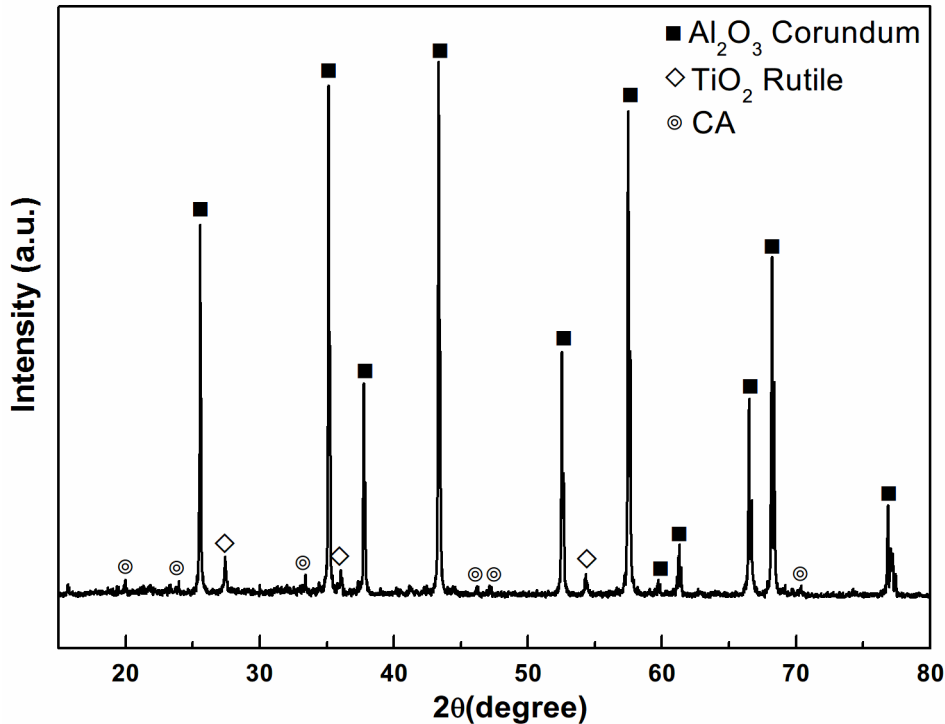


Fig. 7.16 XRD of decarbonized area of TiC-CB castable.

Fig. 7.17 shows the differences in the microstructure of unoxidised and oxidized area in SiC-CB castable after oxidation at 1000 °C. Differently from TiC-CB castable, in addition to dispersed SiC-coated CB particles in castable, a number of dark grey clusters in the range of ~5-20 μm were observed in Fig. 7.17a. As identified by EDS (Fig 7.12), they were most likely to be the mixture of SiC-coated CB particles, Al₂O₃ fine powders fumed silica and calcium aluminate cement which were clearly seen in the high magnification BEI shown in Fig. 7.17c. Furthermore, the decrease in amounts of these grey clusters after oxidation at 1000 °C verified that SiC-coated CB particles were certainly contained in the clusters. This means that SiC coating not only changes the wetting behaviour of carbon in water, but also enhanced compatibility with oxide aggregate and other oxide additives. Moreover, as shown in Fig. 7.17d, the porous-like cluster still appeared to be grey under SEM observation and its corresponding EDS spectrum (insert in Fig. 7.17d) shows a certain level of Si and C elements still remained after oxidation, indicating SiC coatings were not completely oxidised to form SiO₂.

In addition, dehydrated cement agglomerates CA were also seen in SiC-CB castable after heating in 1000 °C (Fig. 7.17a, b). EDS shown in Fig. 7.17e confirmed the bright CA phase was only consisted of Al, Ca and O, along with Al/Ca ≈2, verifying the CA composition to be CaO·Al₂O₃. Meanwhile, CA₂ shown in an insert

in Fig 7.17b were formed in the cement agglomerates due to reaction of CA with alumina, which also observed in Sarpoolaky's research work [209]. EDS (Fig. 7.17f) verified that the Al/Ca molar ratio was increased to ~4/1 ($\text{CaO}\cdot 2\text{Al}_2\text{O}_3$).

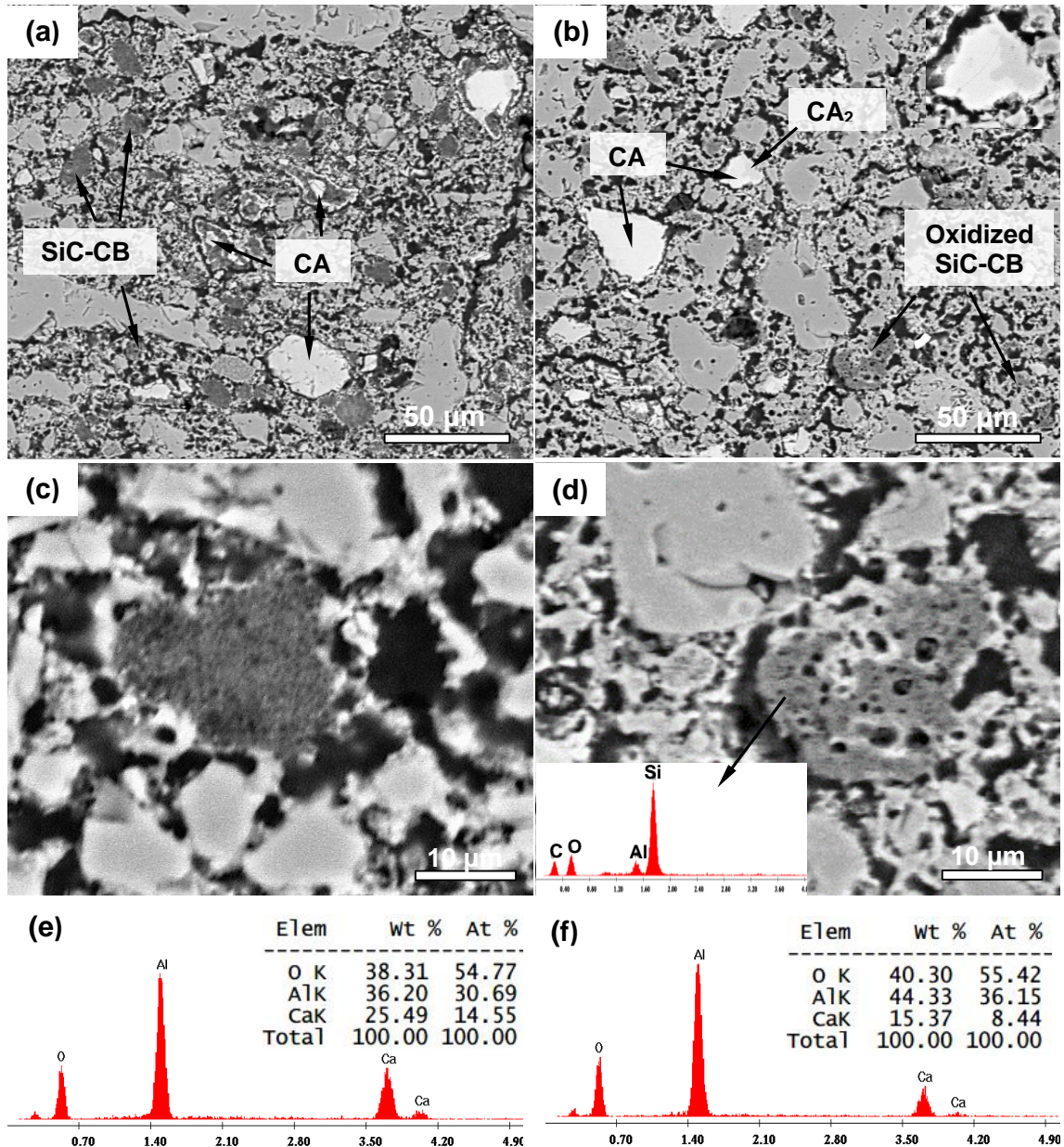


Fig. 7.17 BEI of (a) unoxidised and (b) oxidised area in SiC-CB castable after oxidation at 1000 °C, with their corresponding high magnification BEI (c) and (d); (e) and (f) are EDS spectra of bright phases (CA and CA₂) shown in (b).

It was also noticed that the boundary between decarbonised area and unoxidised area was blurred. The bulk sample appeared light grey on the external surface rather than white colour. (After oxidation test it should show as white appearance as TiC-CB castable.) Thus, the external surface of SiC-CB castable after oxidation was characterised by SEM (Fig. 7.18). Interestingly, it appeared quite dense on the top

surface with only a few cracks. In contrast, a number of large pores and cracks were seen on the top surface of uncoated CB-containing castable after oxidation and alumina grains seemed to be peeled off during oxidation test. In this case, oxygen gas was able to readily go through pores and cracks and burn off all carbon materials at high temperature.

As shown in the high magnification SEM (Fig. 7.18c), it seemed a layer of continuous liquid phase was coated on the surface, and micron-pores were hardly found. EDS (Fig. 7.18c) verified that the surface was mainly composed of elemental Al, Si and O, as well as a small amount of Ca. Their corresponding compounds might be CA, Al₂O₃ and SiO₂ or their combinations. The dense layer on the top surface of SiC-CB castable after oxidation was further identified by XRD. Fig. 7.19 shows in addition to high intensive Al₂O₃ corundum, sillimanite (Al₂O₃·SiO₂) peaks were also shown up. Fig. 7.18d shows the morphology of the area underneath top surface of SiC-CB castable after oxidation. It was found that after carbon core was oxidised and SiO₂ shells remained in the composites as indicated by the arrow. Although carbon was oxidised, the space was still occupied by SiO₂ shell, which might be able to slow down the inward diffusion of air to some extent and reduce carbon oxidation. In addition, it was believed that the formed dense surface is responsible for excellent oxidation resistance of castables.

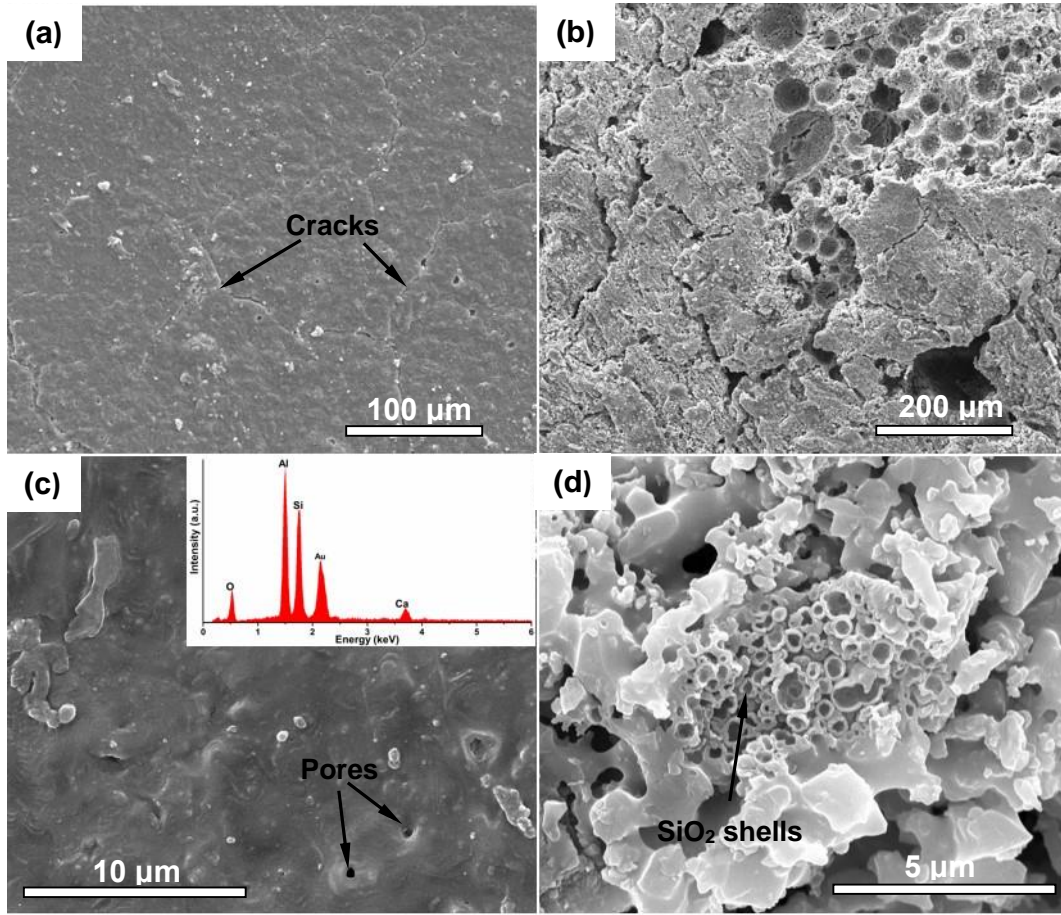


Fig. 7.18 SEM images of top surface of (a) SiC-CB castable and (b) CB castable after oxidation at 1000 °C; (c) high magnification SEM and EDS shown in (a); (d) SEM of the oxidized area underneath top surface of SiC-CB castable.

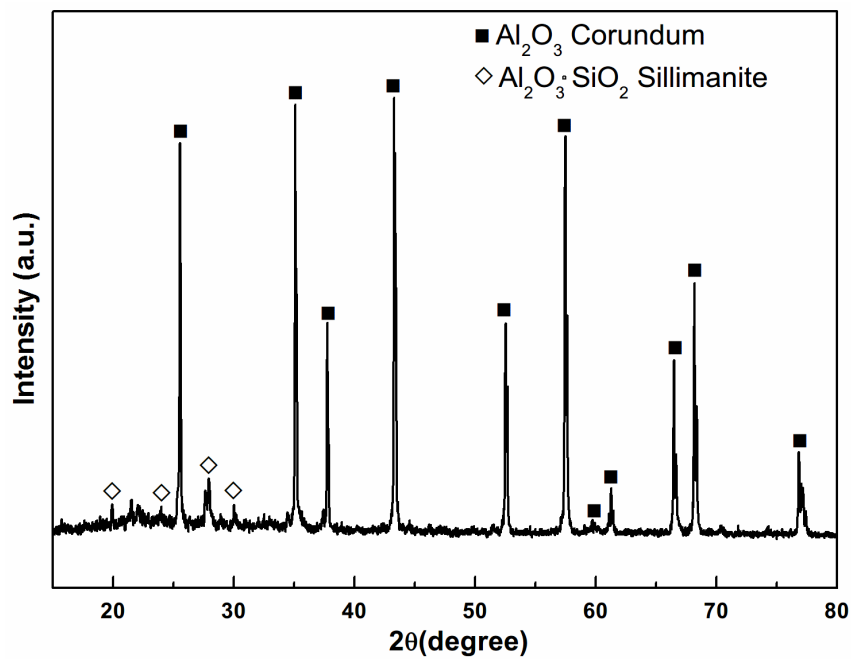


Fig. 7.19 XRD of denser layer on the top of SiC-CB castable after oxidation at 1000 °C for 3 hours.

Chapter 8 Further discussions

As described and discussed in the previous chapters, novel carbon materials, carbide coated CB particles, can be successfully prepared by using the low temperature MSS technique. Herein, the effects of key processing parameters such as synthesis temperature, metal/carbon molar ratios and molten salt, will be discussed in more detail. The synthesis mechanism of carbide coating formation will be clarified based on characteristics of MSS and solid experimental evidences.

Carbide-coated CB exhibited significantly improved water-wettability, dispersion property and flowability, and excellent oxidation resistance. In this chapter, the reasons for good water-affinity of carbide coatings and better oxidation resistance of carbide-coated CB will be revealed. In addition, the promising results showing the potential application of coated carbon materials (GF and CB) in actual castable systems will be highlighted. The effects of carbide coatings on flowability, oxidation resistance, and physical and mechanical properties of carbon-containing castables will be further discussed.

8.1 Factors affecting molten salt synthesis of carbide coatings

8.1.1 Synthesis temperature

Synthesis temperature is one of the most critical parameters influencing the formation of high quality carbide coatings on CB particles. It relates to reaction time, diffusion rate of atoms, and crystal nucleation and growth. The synthesis temperatures for formation of TiC and SiC were preliminarily predicted by thermodynamic calculations. The standard Gibbs free energy changes for formation of TiC and SiC from metallic powders (Ti or Si) and carbon are given below.

$$\text{TiC: } \Delta G^0 = -184100 + 12.16T \text{ (J)} \quad (8.1)$$

$$\text{SiC: } \Delta G^0 = -73220 + 7.95T \text{ (J)} \quad (8.2)$$

From above equations, we can find that the Gibbs free energy for formation of TiC or SiC compound is obviously negative at even room temperature ($T=293\text{K}$), indicating that the reaction can take place in an ambient environment without any exterior energy input. However, for some kinetic reasons, for example, low contact area between Ti or Si with C, and slow atom diffusion rate at room temperature, it is not

possible for such a reaction to proceed at room temperature.

When firing the mixture of Ti powders and CB particles at 850 °C for 4 hours, XRD shown in Fig. 4.12 revealed that unreacted Ti remained in the fired sample though part of TiC was formed, indicating higher temperature or longer holding time would be required for completion of the reaction. In addition, none of SiC was formed after firing Si-CB mixture at 1100 °C for 6 hours (Fig. 5.18), implying that SiC formation was not even initiated at this temperature and higher temperature (>1100 °C) was required. In contrast, the reaction between metallic powders and CB particles in molten salt initiated at 650 °C for TiC (Fig. 4.1) and 1000 °C for SiC (Fig. 5.2), however, full conversion of reactants to carbides required as low as 750 °C for TiC and 1100 °C for SiC. The dramatic decrease in synthesis temperature in the presence of molten salt is mainly attributed to the liquid reaction medium formed by melting chloride or fluoride salts at target temperatures. The salt-solution medium facilitates the transport or diffusion of reactant species, Ti, Si and CB in this case, increasing the possibility of the contact between reactants during reaction. One of typical examples is that the mobility of oxide species in the solid state is 1×10^{-18} cm²/s whereas it is increased to 1×10^{-5} – 1×10^{-8} cm²/s in the molten salt.[151] Secondly, the interaction of metallic Ti or Si with molten salt at reaction temperatures resulted in dissolution of micron-sized metal particles and formation of highly active species (Fig. 4.14 and 5.20) which could be readily diffused onto CB surface through the molten salt, forming carbide coatings.

Compared with other reported methods for TiC and SiC synthesis shown in Table 8.1, molten salt synthesis offers a low temperature synthesis route of refractory carbide coatings. It is advantageous to reduce the energy consumption and save fabrication cost of TiC and SiC coatings.

Table 8.1 Comparisons in synthesis temperature required for TiC and SiC formation.

| Carbide | Synthesis methods | Starting materials | Temperature (°C) | Reaction products |
|------------------------|--|---|------------------|--|
| TiC | Molten salt synthesis | Ti + CB/GF | 750-950 | TiC |
| | Chemical vapour deposition | TiCl ₄ + H ₂ + CH ₄ | 1000-1200 | TiC [210] |
| | Sol-gel & Microwave carbothermal reduction | C ₁₆ H ₃₆ O ₄ Ti | 1200-1300 | TiC [211] |
| | Carbothermal reduction | TiO ₂ + C(C ₃ H ₆) | 1550 | TiC, TiC _x O _y [212] |
| | Self-propagating Synthesis | Ti + C | 1400-1650 | TiC _x [213] |
| | Thermal plasma processing | Ti+CH ₄ | - | TiC [214] |
| SiC | Molten salt synthesis | Si + CB/GF | 1100-1200 | β-SiC |
| | Chemical vapour deposition | CH ₃ SiCl ₃ + H ₂ | 1100 | β-SiC [215] |
| | | SiCl ₄ -CH ₄ -H ₂ | 1250 | β-SiC [216] |
| | | SiH ₄ + CH ₄ + H ₂ | 1200-1400 | β-SiC [217] |
| | Vapour solid synthesis | SiO + CO/CNT | 1250-1550 | β-SiC [218] |
| | Sol-gel & carbothermal reduction | Si(OC ₂ H ₅) ₄ + CF | 1400-1650 | β-SiC [219] |
| Carbothermal reduction | SiO ₂ + Si + CF | 1500-1800 | β-SiC [220] | |

Note: CB=carbon black, GF=graphite flakes, CF=carbon fibres

As for molten salt synthesis of carbide coatings, the synthesis temperature was also dependent on reactants including metallic powders and carbon types, and molar ratio of metal/carbon. Their relationship was illustrated in Fig. 8.1. It can be seen that it normally required higher synthesis temperature (> 300 °C higher) for formation of SiC than TiC, mainly owing to their difference in intrinsic reactivity. As

shown in Figs. 4.1 and 5.2, part of TiC was formed from Ti and CB at 650 °C, whereas Si did not show any sign of reaction with CB at even 900 °C. In terms of carbon source, it can be found that preparation of TiC and SiC coatings on GF required a slightly higher temperature than that on CB. For example, SiC-coated CB was prepared at 1100 °C for 6 hours (Fig. 5.2) and the reaction of Si with GF took place at 1200 °C for 8 hours (Fig. 7.1). This indicates that CB particles exhibit higher reactivity than GF, due to smaller size and amorphous nature of carbon. In addition, depending on molar ratio of metal/carbon, the required synthesis temperatures were slightly different. For example, the completion of reaction between Si and CB in NaF-NaCl occurred at 1150 °C for Si/C of 1/2 and 1/4, and 1100 °C for 1/8. Therefore, synthesis temperature of carbide coating in molten salt is mainly dependent on reactivity of reactants and their initial molar ratios.

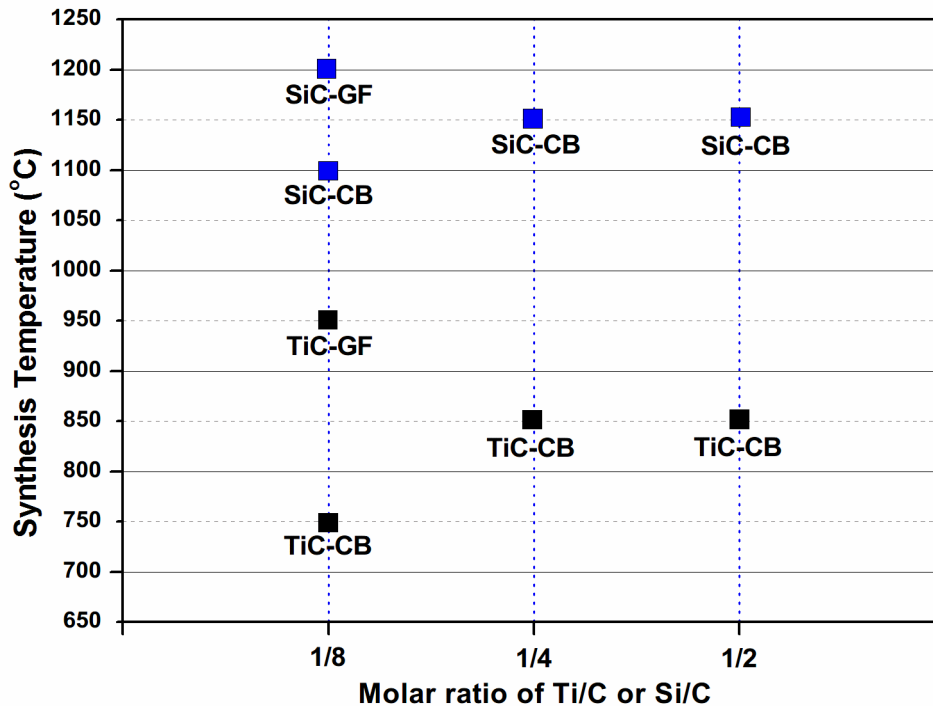


Fig. 8.1 Synthesis temperatures required for formation of TiC and SiC coatings on CB and GF in various Ti/C and Si/C molar ratios (Holding time for complete reaction: 4 hours for TiC-CB and TiC-GF, 6 hours for SiC-CB and 8 hours for SiC-GF).

8.1.2 Metal/Carbon ratio

In the case of chemical vapour deposition, SiC coating thickness can be tailored by controlling flow rate of gaseous precursor and reaction time [221], and in the case of vapour-solid preparation, it can be tailored by controlling silicization degree [202]. Different from these, the thickness of carbide coatings prepared by using the MSS technique could be readily tailored by simply adjusting the molar

ratio of metal/carbon (described in Chapters 4 and 5). In addition to variation in thickness of SiC coatings, the particle density and carbon content also changed with metal/carbon molar ratios. As summarised in Table 8.2, the thickness of carbide coatings and corresponding particle density of coated CB increased with increasing metal/carbon ratios, whereas the carbon content decreased adversely.

Table 8.2 TiC/SiC coated CB prepared with different initial metal/C ratios.

| Metal/C initial ratio (by mole) | Carbon content | | Particle density (g/cm ³) | Coating thickness** (nm) | |
|---------------------------------|----------------|---------------|---------------------------------------|--------------------------|------|
| | By volume* (%) | By weight (%) | | | |
| TiC-CB | 1/2 | 40.44 | 16.67 | 3.70 | 50.3 |
| | 1/4 | 62.79 | 37.50 | 3.02 | 23.7 |
| | 1/8 | 76.93 | 58.33 | 2.59 | 10.4 |
| SiC-CB | 1/2 | 32.58 | 23.08 | 2.78 | 66.3 |
| | 1/4 | 56.64 | 47.37 | 2.46 | 36.5 |
| | 1/8 | 74.05 | 67.74 | 2.23 | 18.4 |
| | 1/12 | 80.82 | 76.74 | 2.14 | 12.2 |

*Volume percentage was calculated based on measured particle density of carbide-coated CB spheres.

** The thickness of TiC coating was estimated based on particle density, and SiC coating thickness was measured from TEM images of SiC-coated CB spheres.

As shown in Table 8.2, the metal/carbon molar ratio is such a critical parameter for preparation of carbide-coated carbon particles that it should be carefully controlled when the coated carbon powders are used for refractory castable applications. Firstly, it is responsible for coating quality. If metal/carbon ratio is too high, for example, Ti/C or Si/C = 1/1, all carbon would be consumed and converted to carbide (e.g. TiC and SiC nanorods as reported in Ref [148] [149]). On the other hand, if it is too low, i.e., the metal is not sufficient, coatings on carbon templates would be discontinuous. Fig 8.2, as an example, shows that high quality TiC coatings (uniform and crack-free) were obtained from initial Ti/C molar ratio of 1/8, whereas uncoated

GF surface was still seen when Ti/C molar ratio was reduced to 1/16. Secondly, it is necessary to prepare carbide coatings with an appropriate thickness for improving oxidation resistance of carbon particles. Li [146] and Xie [156] suggested that TiC and SiC coatings with a thickness of >200 nm could effectively protect carbon fibre from oxidation in air at elevated temperature. In the present study, the results indicate (Fig 6.13 and 6.15) that thicker carbide coatings (~30-60 nm) were able to improve oxidation resistance of CB. Thirdly, a high molar ratio of metal/carbon leads to high particle density (Table 8.2) which would narrow the density gap between carbon and other oxide grains (e.g. MgO and Al₂O₃) in future castable systems, assisting more homogeneous distribution/dispersion of carbon in the castable systems. However, free carbon content would be reduced in the case of using a high metal/carbon molar ratio, which might adversely affect the functionality of carbon in improving carbon-containing refractories' thermal shock and corrosion resistance.

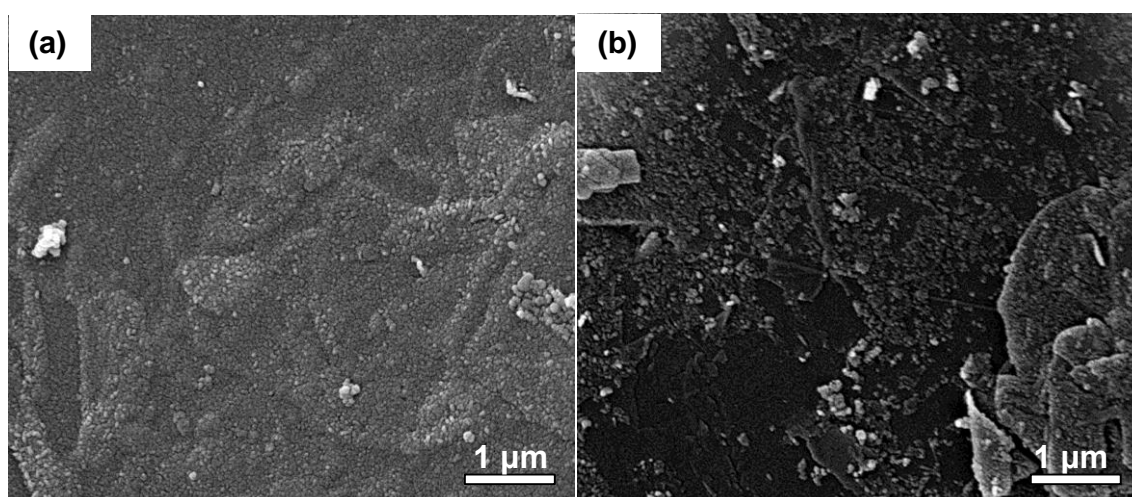


Fig. 8.2 SEM images of TiC coatings on GF prepared from Ti/C molar ratio of (a) 1/8 and (b) 1/16.

8.1.3 Molten salt

Molten salt played an important role in carbide coating formation. Firstly, it provides liquid environment for metal/carbon reaction. Under this condition, reactants were well mixed and contact possibility of them was increased, and consequently reactions were accelerated from kinetic aspect. This was supported by the fact that TiO₂ was reduced by carbon to sub-titanium oxides at 950 °C in the presence of KCl, whereas it was not the case in the absence of molten salt at the same temperature (Fig. 4.15).

Secondly, molten salt enables metallic powders to dissolve in it upon heating to

above melting temperature. Similarly to the dissolution of oxides in molten salt [153, 154], metals also dissolve into molten salt to some extent. Despite of unavailable data on solubilities of metal particles in molten salt, dissolution was verified experimentally in this work. Micron-sized Ti was fired alone in KCl at 850 °C and the size and shape of particles changed considerably (Fig. 4.14). The presence of nano-sized Ti particles after interaction between Ti and molten salt is owing to 'dissolution-precipitation' process [156] in which micron-sized Ti dissolves in KCl and precipitates out of the salts upon cooling. Wei and Li [222, 223] suggested that dissolved Ti might be in form of mobile cations and delocalized electrons, an unstable intermediate state between ionic and metallic. The dissolution phenomenon of Ti in molten salt was also confirmed by Liu and Xie [155, 156]. Likewise, micron-sized Si powder have a certain solubility in NaF or NaF-based salts (Fig. 5.20). Since the coefficients of diffusion of reactants in liquid state are much higher than those in the solid state [224], the dissolved Ti or Si species will be fast delivered to carbon surface in liquid environment. The dissolution of metal in molten salt not only decreases the synthesis temperature compared with other methods (Table 8.1), but also realizes *in-situ* formation of carbide.

In the case of molten salt synthesis of carbide coatings, the use of an appropriate salt is the key. For example, among chloride salts, KCl is the best salt candidate for TiC coating formation, and NaF is essential for SiC formation at >1100 °C. Generally, the salt selection for molten salt synthesis of carbide is determined by three factors, viscosity of molten salt, carbon's wettability in molten salt, and solubility of metallic powders in molten salt.[156, 225] The relevant data of viscosity of molten salt and their contact angle on carbon surface are listed in Table 8.3. LiCl shows the lowest viscosity among these salts but with the worst wettability with graphite. NaCl has similar viscosity to that of KCl after melting, but also exhibits poor wettability. Based on these two factors, KCl might be the most suitable candidate for reaction of Ti or Si with CB. However, metallic powders have different solubilities in specific salts. For example, as shown in Fig. 5.20, micron-sized Si powders were evidently dissolved in a single NaF at 1100 °C and appeared as nano-sized Si particles when extracting from the solidified salt after cooling to room temperature. In contrast, Si powders changed very little after firing in a single NaCl under the same conditions, indicating Si has an extreme low solubility in NaCl at 1100 °C. Therefore, all these factors (viscosity of molten salt, carbon's wettability in molten salt, and solubility of

metallic powders in molten salt) should be taken into considerations when choosing the salts for molten salt synthesis of carbides.

Table 8.3 Viscosity of single molten salt at 850 °C and its corresponding contact angle with graphite.[226, 227]

| Single salt | Viscosity at 850 °C (mPa·s) | Contact angle with graphite |
|-------------|-----------------------------|-----------------------------|
| LiCl | 0.9244-0.9250 | 127-137 (900-1100 °C) |
| KCl | 1.0210-1.0226 | 73-78 (780-950 °C) |
| NaCl | 1.0460-1.0470 | 113-128 (810-950 °C) |
| NaF | — | 115-127 (1000-1100 °C) |

In some cases, salt assemblies were used for molten salt synthesis, since salt assemblies could provide lower melting temperature (also called eutectic melting temperature). For instance, the LiCl-KCl binary salt starts to melt at as low as 353 °C when 45 wt% LiCl and 55 wt% KCl (referred to as 45%LiCl-KCl hereafter) are mixed together, whereas single KCl melts at temperatures as high as 771 °C (Fig. 8.3). In the case of TiC formation by MSS, 45%LiCl-KCl instead of single KCl was used to synthesise TiC at as low as 750 °C. Although TiC coatings were obtained, as-prepared TiC-coated CB appeared slightly heavier agglomeration (Fig. 4.2d). This might be due to the reaction of Ti and C occurring in molten salt at low temperature (<750 °C) when the viscosity was high but homogenous dispersion of CB particles had not been achieved. So the ratio between LiCl and KCl should be readjusted, for example, 15 wt% LiCl and 85 wt% KCl.

It is also noticed that NaF content in the NaF-NaCl salt assembly was reduced to 2.5-5 wt% from 20 wt% for the synthesis of SiC coatings on CB. Fig. 5.3 and 5.6 show almost the same high quality SiC coatings were obtained when NaF was reduced. This not only reduces the use of environmentally-unfriendly fluoride but also reduces the evaporation of the salt mixture. As shown in Fig. 8.4, the evaporated salts increased with NaF content (from 0 to 20 wt%) in the salt assembly. This is because eutectic melting temperature increased with less NaF (< 20 wt%) in the salt mixtures.

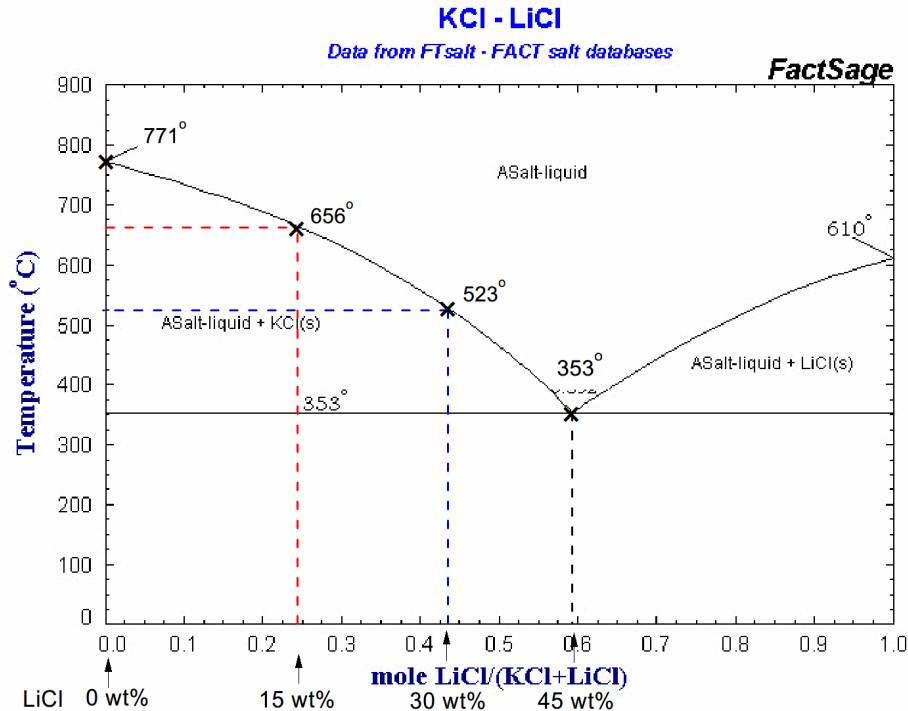


Fig. 8.3 Phase diagram of KCl-LiCl.[228]

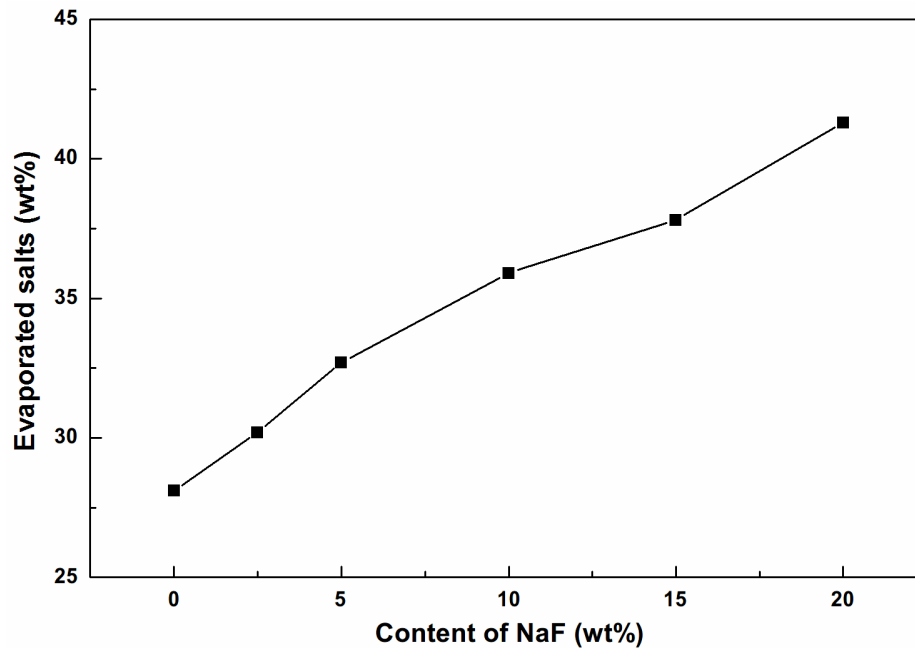


Fig. 8.4 The weight percentage of recycled salts separated from solidified resultant samples after firing at 950 °C for 4 hours as function of content of NaF in the salt assembly.

8.1.4 Template growth mechanism

Attributed to the use of molten salt in the reaction, carbide formation occurred at relatively low temperature, 750-850 °C for TiC and 1100-1200 °C for SiC (Fig. 8.1). Furthermore, as-prepared carbide coated CB retained the similar morphologies and sizes to uncoated CB spheres (Fig. 4.2 and 5.6), indicating the formation of carbide

coatings was dominated by the template growth mechanism in which carbon sources acted as hard templates for carbide growth. Such a mechanism was also verified by previous studies such as carbide formations on carbon fibre [146] [147] [146,147], carbon nanotube [148] [149] and natural cotton [156] and wood [161]. Herein, the template growth mechanism was further discussed to illustrate the formation and growth of carbide coating based on more experimental evidences. It is vital to understand how active Ti and Si species react with carbon, thus using this understanding to precisely control the reaction process and reduce the defects created during formation.

The template formation and growth of carbide comprise two main steps, dissolution and diffusion, as schematically illustrated in Fig. 8.4. The dissolution of metallic reactants in molten salt is the prerequisite to *in-situ* formation of carbide coatings on carbon templates. As evidenced in Fig. 4.13, irregularly micron-sized TiC clusters rather than TiC coatings were obtained after firing the mixture of Ti powders and CB particles in the absence of molten salt. In this case, formation of TiC is based on solid-solid reaction and the reaction occurred on the template of micron-sized Ti powders. In contrast, the dissolution of metallic powders (discussed in Section 8.1.3) in molten salt not only increases the reactivity and activity of metal species, but also increases the motion rate of metallic reactants. Nevertheless, carbon materials are quite stable in the molten salt, neither size nor shape changed after interaction at reaction temperature [156]. Thus, CB particles acted as templates in the reaction.

The formation and growth of carbide coatings are mainly based on diffusion of Ti and Si through molten salt and their inter-diffusion of carbon and Ti/Si through TiC or SiC thin films. The specific details are stated bellow. When active Ti or Si species reach the top surface of carbon particles, carbide compounds are formed immediately and an initial thin carbide coating (shown as cross-section of a layered structure at diffusion step in Fig. 8.5) is formed. Since the first layer of carbides blocks the direct contact of reactants (Ti or Si with C), the reaction rate slows down. The subsequent reaction will proceed by inward diffusion of silicon or titanium atoms and outward diffusion of carbon atoms through pre-formed carbide coating. The inter-diffusion will continue until all metallic reactants are consumed. For this reason, formation of thick coatings normally required slightly higher temperature or longer reaction time (Fig. 8.1), allowing the completion of slow inter-diffusion of Ti or Si and C through increased TiC or SiC coating layer.

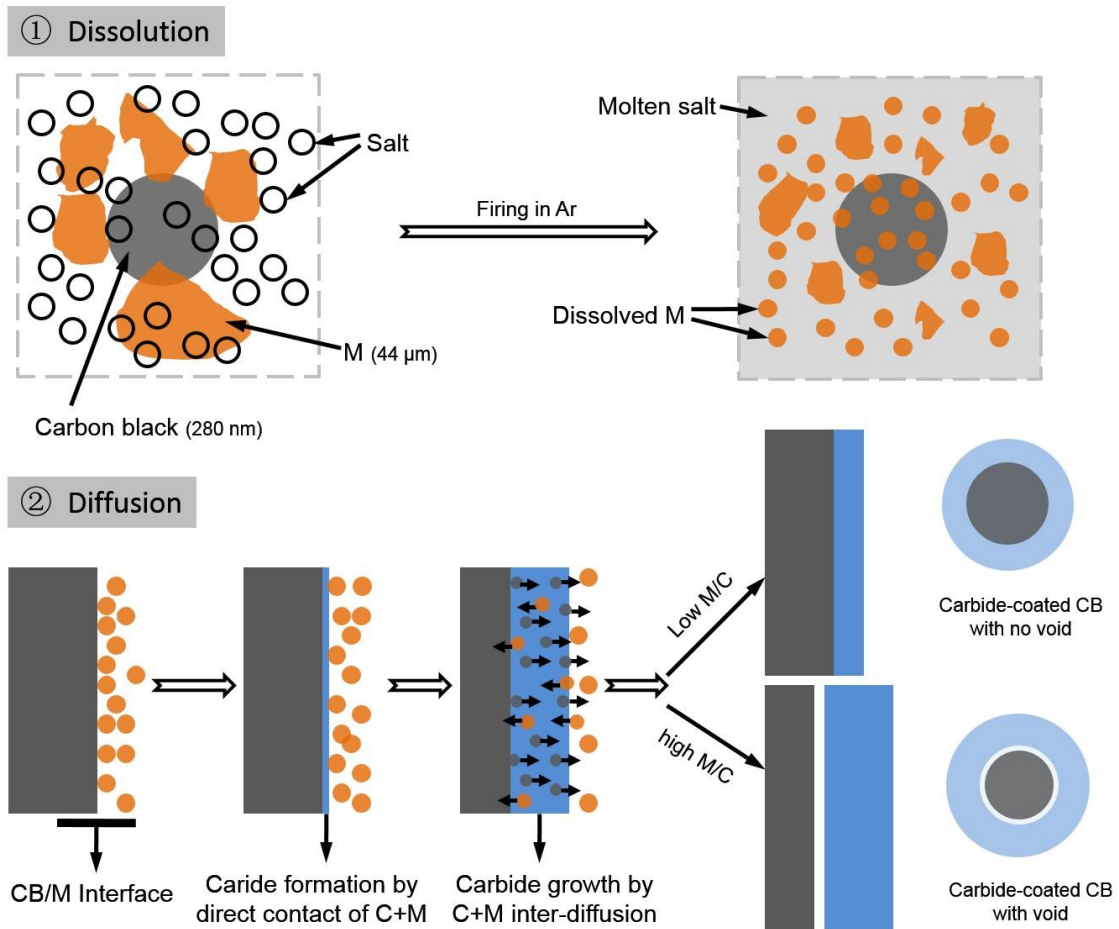


Fig. 8.5 A Schematic diagram of template growth (dissolution-diffusion) mechanism for carbide coating formation. The cross-sections in the second step showing the interface between carbon top surface and as-formed SiC coating. (M= Ti or Si)

So the diffusion coefficients of Ti or Si and C in carbide will be critical to the growth of carbide coatings. The extensive studies [229-232] reveal that carbon diffuses faster than Si in the lattice of β -SiC, that is $D_c > D_{Si}$. So when a low content of Si is added (low Si/C in this case), thin SiC coatings are formed on carbon core within a short time mainly by direct contact reaction. However, when high Si/C molar ratio is used, most of SiC is formed by inter-diffusion through pre-formed SiC. It will take longer for Si to go through thick SiC shell, whereas C atoms can go through SiC by outward diffusion using less time, due to its higher diffusion coefficient. As a result, voids or gaps (white zone indicated in Fig 8.5) at the interface between carbon core and SiC shell were formed. The analysis and conclusion were verified by TEM observation of SiC-coated CB prepared in high Si/C molar ratio (1/4 to 1/2) (Table 5.2). It showed the higher the Si/C molar ratio used, the larger the void formed. When Si/C was made as 1/1 and all carbon was consumed and converted to SiC, hollow structure (Fig. 5.21) was formed. This phenomenon is also called Kirkendall

effect.[204]

It also should be noticed that the dissolution of metal in molten salt and reaction of metal with carbon occurred simultaneously. Since the solubility of Ti or Si in molten salt is small (reflected from only part of Ti or Si powders were dissolved in molten salt as shown in Fig. 4.14 and 5.20), dissolution is easy to reach saturation. When dissolved Ti and Si species are consumed making the molten salt unsaturated with Ti or Si again, metallic powders will continue to dissolve in molten salt until all reactants are reacted eventually. Such a conclusion was also supported by analysis on equilibrium concentration of reactants in molten salt.[150]

Taking advantages of the template growth mechanism of MSS, different structures of carbide coated carbon or carbides could be readily configured based on different carbon templates, showing the variability and simplicity of MSS technique. This will be beneficial to extend the use of molten salt synthesis in synthesis of other functional ceramics.

8.2 Water-wettability and oxidation resistance of carbide-coated carbon materials

8.2.1 Effects of carbide coatings on wettability, dispersivity and flowability

8.2.1.1 Water-wettability

Although the water-wettability values of uncoated and carbide-coated CB were not quantitatively determined in this work, the improvement in water-wettability for coated CB was clearly demonstrated by straightforward dispersion of carbon particles in water. As shown in Fig. 6.4, TiC-coated CB particles, as an example, were immediately wetted by water and well dispersed in water either with assistance of vibration or not, whereas most of uncoated CB particles remained on the top of water. Such a change in wetting behaviour was also observed by Liu [155]. In her work, the contact angle for natural graphite with water was measured as 101° (considered as hydrophobic when contact angle greater than 90°), whereas contact angle for TiC or SiC-coated GF was $\sim 60^\circ$, indicating TiC and SiC coatings were hydrophilic.

The improvement in water-wettability was further discussed and explained from the following three aspects which are responsible for the wettability of solid surface. [233]: physical surface tension (or interfacial free energy), geological microstructure and chemical composition. As reported from literature [234], the interfacial free energy between TiC and water is 2768.6 mJ/m^2 , about 44 times higher than that between carbon and water (63.1 mJ/m^2). According to Young's theory [235], contact angle is inversely proportional to interfacial free energy between solid surface and liquid. Thus, theoretically, TiC (or SiC) should show smaller contact angle and more wettable with water than carbon.

Based on the observations from SEM and TEM images (Fig. 4.3, 4.5, 5.7 and 5.11), carbide-coated CB showed a rough surface, due to the formation of carbide nanocrystals on the surface. Liu [26] also clearly characterised the surface of TiC-coated GF by using AFM, revealing the roughness of carbon surface was increased after TiC coating. According to Johnson's model [236, 237], the wettability will be enhanced by the increased roughness when contact angle is smaller than 90° . So carbide-coated CB is proven to be water-wettable in terms of the change in geological microstructure of solid surface.

Another factor to influence the wettability of solid surface is the chemical composition. As for carbon materials without any oxidation or other treatments, there are very limited hydrophilic functional groups such as $-\text{COOH}$ or $-\text{OH}$ attached on the surface. Thus, no hydrophilic bond could be formed with water and this makes carbon difficult to be dispersed in an aqueous environment.[238] However, after coating with carbide materials, the surface chemical composition of CB has been changed. TiC surface is found to be Ti terminated.[239] These Ti terminals are believed to be unsaturated, existing in the form of $\equiv\text{Ti}^+$ which are unstable and will easily combine oxygen from their surroundings.[134] The existence of TiO_2 was experimentally proved by Zhang and Tan [240] by using XPS element analysis. They found that around 86% of titanium content on the surface combined with oxygen, forming TiO_2 . They also suggested that TiO_2 tended to coordinate with water molecules to form $\equiv\text{Ti}-\text{OH}$ which could enhance the water affinity with TiC coated carbon materials. Similarly, a thin layer of SiO_2 was observed on the surface SiC when exposed to air.[149, 200] As well known, SiO_2 is very hydrophilic and tends to form functional silanol group ($\text{Si}-\text{OH}$) in the presence of water. In addition, Adar et al. [241] and Cerovie et al. [242] suggested that Si-C bonds could interact with water, forming carboxylate group (COO^-). Thus, with a great number of silanol groups and carboxylate groups on the surface, SiC-coated carbon could be readily wetted and dispersed.

8.2.1.2 Dispersion property

The dispersion property of uncoated and carbide-coated CB were compared in sediment tests (Fig. 6.4), showing better dispersion property was achieved for coated CB. This was also verified by zeta potential measurement. The higher value, the better dispersion ability. The plots of zeta potential versus pH for uncoated and coated CB in water (shown in Fig. 6.1 and 6.2) are integrated in one figure (Fig. 8.6) and used to compare with uncoated and TiC-coated GF. The common feature is that zeta potential values of coated carbon particles were higher than those of uncoated ones, indicating improved dispersion property for CB coated with carbides. Moreover, coated CB showed higher zeta potential than coated GF, for example, at $\text{pH}=10$, ~ 46 mV for TiC-coated CB and ~ 54 mV for SiC-coated CB, whereas only ~ 13 mV for TiC-coated GF. In addition, better dispersion property of carbide-coated carbon was obtained in basic environment ($\text{pH}>8$). This enables them to homogeneously disperse in oxide-based refractory castables, as Al_2O_3 or

MgO-based systems are usually basic (pH=10.5) [58].

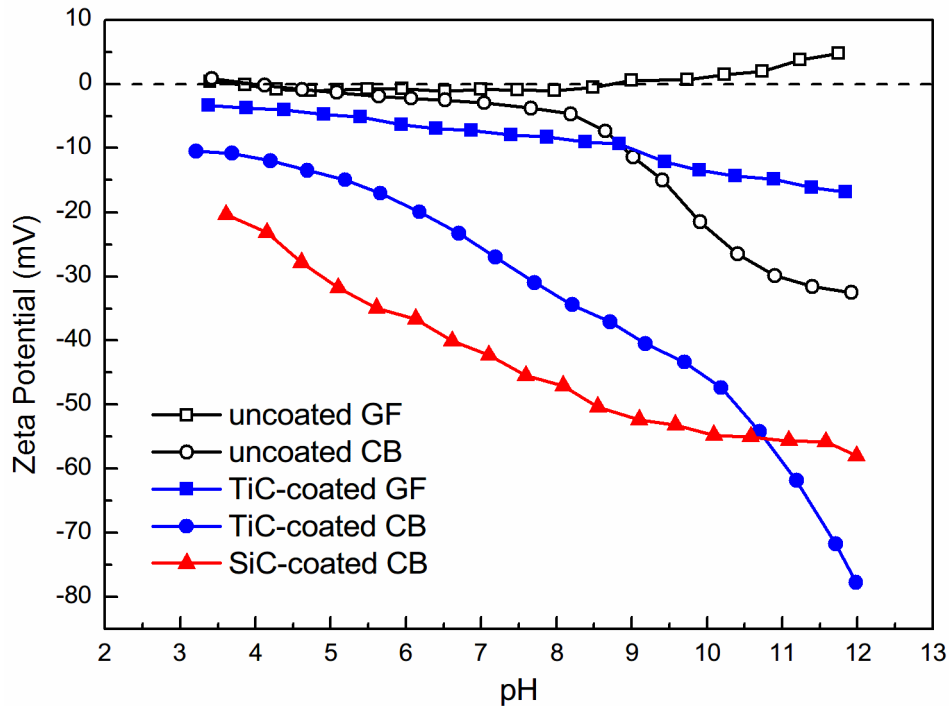


Fig. 8.6 Zeta potential as a function of pH for uncoated and coated carbon particles in water.

The reason for high zeta potential value and much improved dispersion of coated carbon particles is that there are more negative charges formed on particle surface than in the case of uncoated one. As discussed in above section, Ti-OH and Si-OH are usually formed on TiC and SiC surface in the presence of water. The dissociative chemisorption of water molecules led to a hydroxylated surface, which can specifically adsorb H^+ and OH^- according the following equations [243]:



When H^+ is dominant, it is beneficial to form $Ti-OH_2^+$ and $Si-OH_2^+$ (Equation 8.3 and 8.5). When more OH^- was added into suspensions, the formation of $Ti-OH_2^+$ and $Si-OH_2^+$ is suppressed and the surface will be surrounded by more negative charges ($Ti-O^-$ and SiO^-) (Equation 8.4 and 8.6). Therefore, for TiC and SiC coating, high pH will enable surfaces with more negative charges and it is helpful to disperse carbon particles in water. However, for uncoated carbon, in particle for graphite, pH value has little influence on their dispersion due to the lack of charged sites.

8.2.1.3 Flowability

The rheological behaviours of uncoated and coated carbon containing suspensions were extensively studied and described in Chapter 6, and their plots of apparent viscosity vs shear rate are shown together in Fig. 8.7. It can be seen that uncoated GF containing suspension exhibited the highest viscosity and worst flowability, nearly two orders of magnitude higher than that of uncoated CB. Despite the flowability of GF in water was improved by TiC coatings, the former still appeared more viscous than the latter. This indicates that nanosized spherical CB particles are more flowable than micron-sized flaky graphite. The flowability of uncoated CB was further improved by TiC and SiC coating, almost two orders of magnitude higher than that in the former at a low shear rate and nearly one order of magnitude higher at a high shear rate. The decrease in apparent viscosity is associated with the improved water-wettability and dispersivity as discussed above. With TiC or SiC coating, there are a number of negative charges on the carbon surface due to formation of Ti-O^- and Si-O^- , in particular, in alkaline environment. This will generate strong repulsive forces between particles in suspensions and consequently prevent agglomeration or flocculation during suspension flow.[244, 245] As a result, the apparent viscosity decreased. The phenomenon of agglomeration or flocculation of uncoated CB was observed in Fig. 6.6b, showing unstable shear stress detected with increasing shear rate.

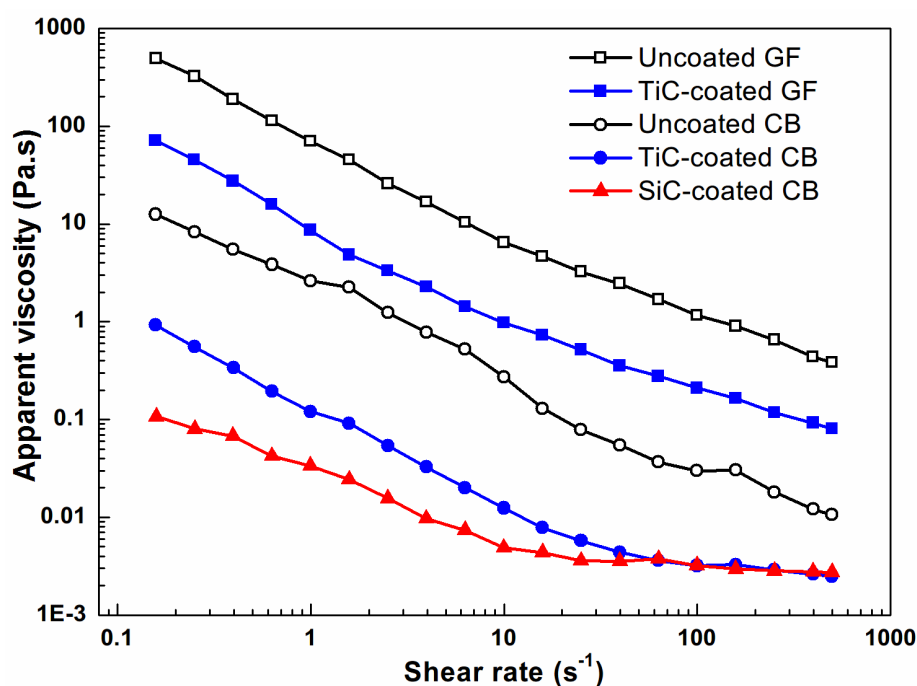


Fig. 8.7 Apparent viscosity of water suspensions (pH=10) containing 25 wt% uncoated and carbide coated CB as a function of shear rate.

The rheological behaviours of carbon suspensions are also highly related to pH. Fig. 6.6 gives us a clue that in alkaline suspensions, low apparent viscosity of carbide coated CB was obtained. This is because at high pH, carbide surface was surrounded with more negative ions, generating even more repulsive forces between particles. This explanation was supported by zeta potential measurement that at high pH, high value of zeta potential was obtained.

8.2.2 Effect of carbide coatings on oxidation resistance

8.2.2.1 As-prepared carbide coatings

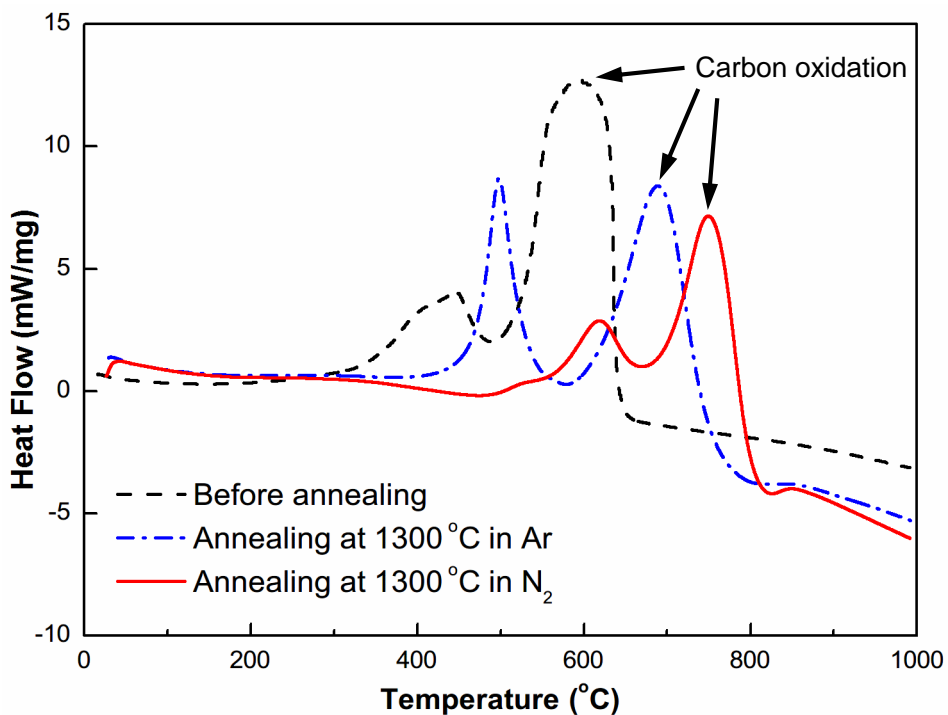
The oxidation resistances of uncoated and coated CB were investigated by TG (Section 6.4.2) in which both of them were exposed to air flow at elevated temperature up to 1000 °C. As shown in Figs. 6.13 and 6.15, the oxidation resistance of CB particles was only slightly improved by carbide coatings. The retardation in carbon oxidation was more evident in the TG curves of the samples with thick TiC or SiC coatings, indicating thicker carbide coating is beneficial to increase carbon's oxidation resistance.

The limitation in improving oxidation resistance of carbon particles is attributed to two aspects. One reason is that the coating layer is too thin. The thickness of TiC coating at Ti/C=1/8 was estimated as only ~10 nm, and ~50 nm at Ti/C=1/2. The thin TiC coating was effective to improve water affinity of carbon particles, however, it was still not thick enough to protect carbon from oxidation. As reported in Literature [146], the oxidation resistance of carbon fibre was improved by TiC coating with a thickness reaching above ~200 nm. The second reason is that as-prepared carbide coatings were not dense enough. For example, it can be clearly seen from high resolution SEM of the individual TiC-coated CB sphere (Fig. 4.3) that there were some nanopores between TiC nanocrystals (~10nm) though TiC coating was continuous. Thus, small oxidising gas molecules (e.g. O₂) would readily penetrate through these open nanopores and consequently oxidise carbon and TiC simultaneously from both inside and outside of TiC coatings. So thin TiC or SiC coatings cannot act as barriers to oxidation and thus cannot effectively improve oxidation resistance of CB.

8.2.2.2 Effect of annealing treatment

Based on above analysis, there are two ways to further improve the oxidation

resistance of carbide-coated CB: One is to increase coating thickness and the other is to make coating denser. Since a reasonable level of carbon content needs to remain after carbide coating, it is not possible to further increase metal/carbon molar ratio to over 1/2. As a result the formation of thicker coatings (e.g. >60 nm) cannot be realised. However, denser carbide coatings can be achieved just simply by high-temperature annealing. Figs. 6.14 and 6.16, as examples, show an evident retardation in oxidation of the annealed samples at elevated temperature, indicating improved oxidation resistance after annealing treatment at 1200-1500 °C. Such a significant improvement was also verified by a shift of exothermic peaks of carbon oxidation (indicated by black arrows shown in Fig. 8.8) to higher temperatures.



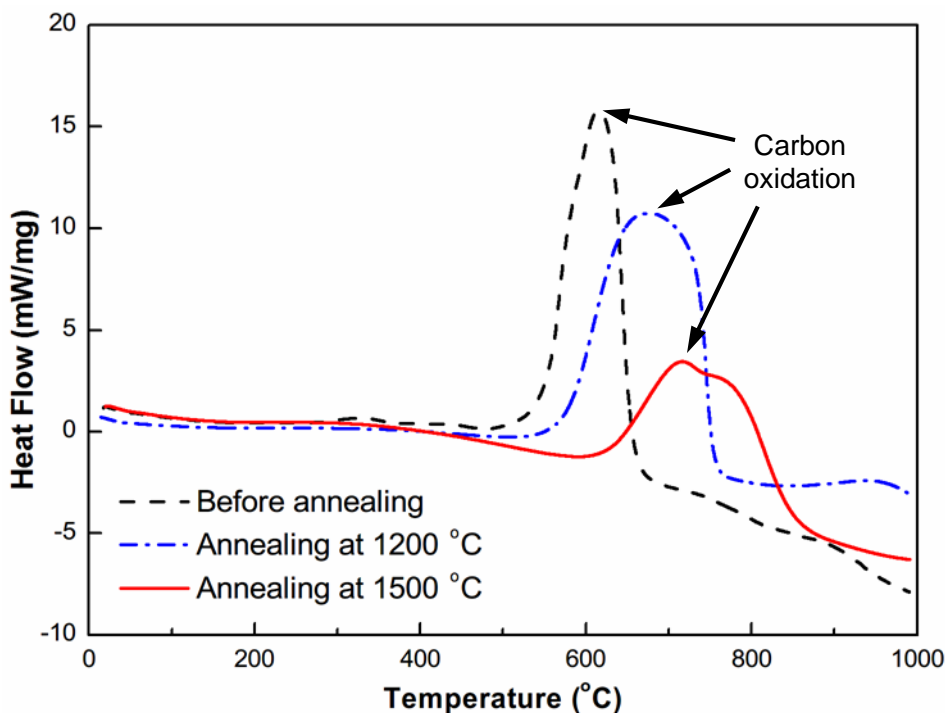


Fig. 8.8 DSC curves of (a) TiC-coated CB before and after annealing in Ar and N₂ at 1300 °C, and (b) SiC-coated CB before and after annealing in Ar at 1200 and 1500 °C

As for TiC-coated CB, the sample after annealing in N₂ exhibited slightly better oxidation resistance than that after annealing in Ar, due to the formation of TiCN solid solution during annealing process (Figs. 6.9 and 6.10 and Table 6.1). On the other hand, the oxidation resistance of carbide-coated CB is also associated with annealing temperature. Figs. 6.16 and 8.18b verify that higher annealing temperature resulted in better oxidation resistance. This is because at higher temperature, carbide coatings became denser than that before annealing treatment. The changes in phases and microstructures of carbide coatings before and after heating-treatment was further analyzed by XRD and SEM. As shown in Fig. 8.9 (left), the XRD intensity of the main peak of β -SiC at $2\theta \approx 35.65^\circ$ increased dramatically after annealing and reached the highest at 1500 °C, indicating the increase in crystallinity of SiC phase. SEM images of SiC coatings on CB (Fig. 8.9) show that, with the growth of nanocrystals, nanopores in the SiC coatings were gradually eliminated and coating layer became denser during annealing treatment.

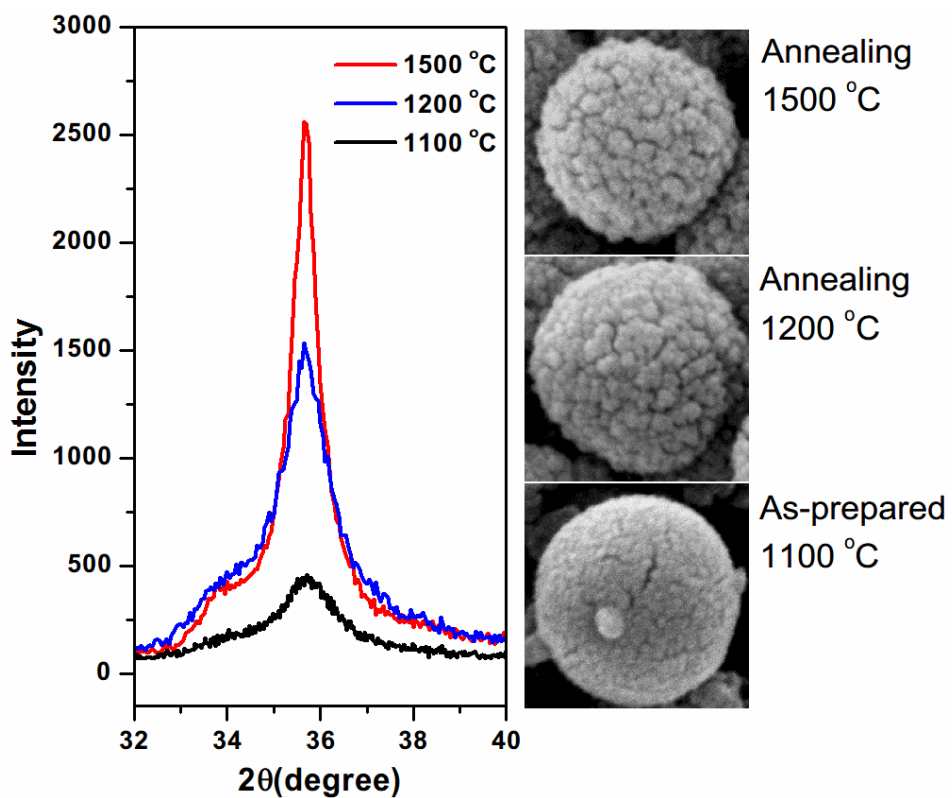


Fig. 8.9 Refined XRD profiles of main peak of β -SiC ((111) plane) before (as-prepared at 1100 °C) and after heat-treatment at 1200 and 1500 °C (Left figure) and their corresponding SEM image of individual SiC coated CB sphere on the right hand.

8.3 Carbon-containing high alumina castables

8.3.1 Effects of carbide coatings on water demand and flowability

As described in the literature review (Chapter 2), the major difficulty in developing carbon-containing castable is the poor wettability of carbon materials, since high water demand is required to achieve a reasonable flow value when carbon particles are incorporated. This was also addressed in this work. In the preliminary experiments, it witnessed a remarkable increase in water addition after adding uncoated GF into model castables, from 5 wt% to 8 wt% to reach the flow value equivalent to that of carbon-free castable (Fig. 7.2). Zhou [117] proposed a mechanism/model to explain the increase in water addition when GF were added into oxide-based castables. As shown in Fig. 8.17, a thin water film is formed on the surface of oxides to make a castable flow. When the added GF contacts with oxides, the continuous water film is destroyed. However, the new continuous water film is not able to form because of non-wettability of GF with water. Under this circumstance, a proper flow of particles including oxides and graphite is hard to achieve. Consequently, high water addition is required to separate GF and oxide particles and rebuild the continuous water film.

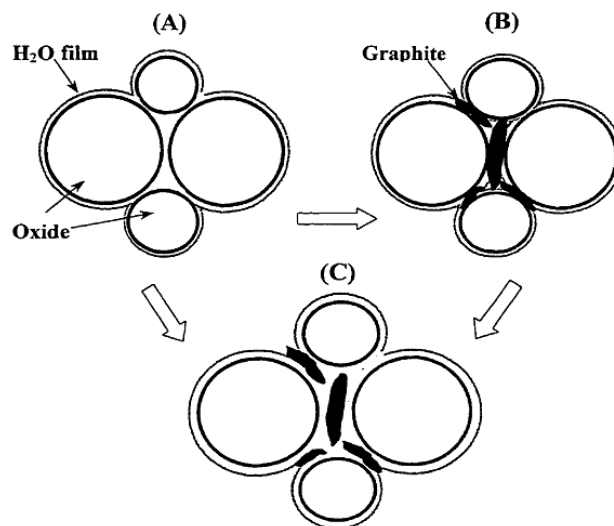


Fig. 8.10 Schematic diagram of the water wetting on Oxide-GF surface.[117]

In the experiment, a carbon dispersant, SS, was added in the model castable as a comparison set. However, it did not work effectively to reduce the water demand. 8 wt% water was added into GF containing castables with and without SS, but the flow value of SS-containing castable decreased adversely (172 mm for castable without SS, and 164 mm for SS added with castable). The function of the carbon dispersant

should be that the non-polar end of the macromolecule attaches on the carbon surface, and the ionic end (for example, $-\text{SO}_3^-$ in this case) faces towards the external. So the GF coated with SS would be negatively charged, similarly to SiO_2 and Al_2O_3 in the alkaline aqueous environment. One reason of the dispersant not working on GF might be that the SS was consequently not firmly attached on GF surface and GF's water-wettability was not improved. Secondly, it is probably due to the interaction of negative SS with some of cations, Ca^{2+} and Al^{3+} , released from cement.

In contrast, carbide coatings could significantly reduce water demand when carbon was incorporated into castables. As for standard 5.5kg-scale batch (Fig. 7.4), coated-carbon containing castable required only 6.5-7.0 wt% water, however, it required 8.5 wt% water for uncoated CB castable and 9.7 wt% water for uncoated GF castable. When increasing SiC-coated CB content from 5 to 8 wt%, only 7.5 wt% water was needed to reach the same flow value. The improvement in reducing water demand is more significant than that achieved by previous research. For example, the water addition was as high as 8.5 wt% when spinel coated GF prepared by sol-gel technique was incorporated into castables.[140]

So the advantages of carbide coating on carbon were fully demonstrated during castable making. Firstly, the water-wettability of carbon particles was improved by carbide coatings. As discussed in Section 8.2.1, TiC and SiC showed excellent water-affinity, due to the formation of Ti-OH and Si-OH on the surface in contact with water. So carbide coated carbon particles were readily wetted by water. Secondly, the dissociation of Ti-OH and Si-OH in alkaline solutions imparted the particles with negative charges (TiO^- and SiO^-) (demonstrated as high zeta potential in Chapter 6) which generate strong repel forces between particles and prevent carbon agglomeration during mixing. Thirdly, the carbide coatings were able to increase the density of carbon materials, making them more comparable with oxide aggregates. It also enables carbon particles to distribute uniformly in the castable matrix.

8.3.2 Effect of carbide coatings on oxidation resistance

As no antioxidants were added into castables, the results of oxidation tests performed at 1000 °C could directly reflect the effect of carbide coatings on oxidation resistance of carbon-containing castables. As shown in shown in Figs. 7.9 and 7.10, castables containing carbide-coated carbon particles (except SiC-coated

GF) showed much less decarbonised depth (6.28-6.82 mm) than that containing uncoated carbon particles (7.90-10.48 mm), indicating the improved oxidation resistance was achieved by carbide coatings. The oxidation resistance of castables was presented in order of TiC-GF>SiC-CB>Ti-CB>GF>Si-GF>CB. Overall, there are two aspects responsible for the improvement in oxidation resistance of carbon-containing castables. One is attributed to the decreased apparent porosity (Fig. 7.5). Higher porosity enabled oxidising gas to diffuse readily into the inside of castables and promote the oxidation of carbon materials. So it was effective to retard carbon oxidation by decreasing porosity. Secondly, such an improvement comes from the contribution of high-quality carbide coatings. TiC and SiC on carbon particles acted as a barrier to prevent direct contact with oxidising gases and consequently slowed down the oxidation rate. Moreover, the oxidation of TiC and SiC would consume part of oxidising gases and thus their concentration or pressure during oxidation process decreased, similar to the performance of antioxidants like metallic Al and Si in carbon-containing bricks [108]. In addition, TiO₂ and SiO₂ remained in the generated pores after carbon oxidation (Fig. 7.14 and 7.15) and decreased the porosity to some extent. In the case of SiC-CB castable, the formation of aluminosilicate dense layer on the external surface of castable also help prevent the further invasion of oxygen.

8.3.3 Effect of phase evolution on mechanical properties

Unlike shaped and pre-fired refractory composites in which the mechanical strength is provided by carbon networks derived from pyrolysed pitches or phenolic resins, castables, Al₂O₃-C castable in this case, was bonded by inorganic binders such as hydraulic calcium aluminate cements (CACs).

As for green castables just after placement (110 °C), the mechanical strength was developed by hydration of CAC cement with water and subsequent formation of stable hydrated compounds C₃AH₆ and AH₃ [80] when temperature rose to above 35 °C. The mechanical strength of green castables was generally very low (Fig. 7.7) After coking at 1500 °C, the bending strength was remarkably increased, even doubled or tripled at 1500 °C for castables containing carbide-coated CB compared with that at 110 °C. This is due to the formation of strong ceramic bonding phases such as mullite and CAS at high temperature.[208, 209]

In addition, it was found that coated-carbon castables exhibited higher mechanical

strengths than uncoated-carbon castables at both 110 °C and 1500 °C. This is mainly attributed to the decreased apparent porosity of castables. The apparent porosity (Fig. 7.5) was followed in the order of CB>GF>SiC-GF>TiC-CB>SiC-CB>TiC-GF. Correspondingly, the mechanical strengths of carbon-containing castables (Fig. 7.6 & Fig. 7.7) was presented in the order of TiC-GF>SiC-CB>TiC-CB>SiC-GF>GF>CB. It reveals that mechanical properties of castables are highly dependent on their apparent porosity. On the other hand, from microstructures of castables (Fig. 7.11 and 7.15), it can also be seen that coated carbon particles were tightly bonded by calcium aluminate phase and closely surrounded by oxides. This verifies that carbide-coated carbon particles are more compatible than the uncoated ones in oxide-based matrix. This fact could be additionally contributes to the improved mechanical strength in the cases using carbide coated carbon.

Chapter 9 Conclusions and Future work

9.1 Conclusions

In this study, a molten salt synthesis technique has been further developed and employed to prepare carbide coatings (TiC and SiC) on carbon black particles. The water-wettability, dispersivity and oxidation resistance of CB were effectively improved by carbide coating. As a result, low water demand and improved flowability were achieved when carbide-coated carbon particles were incorporated into the castables. The resulting castables exhibited lower apparent porosity, much improved mechanical properties and oxidation resistance compared with castables using uncoated-carbon. Based on the results and discussions presented in the previous chapters (Chapters 4-8), the main conclusions can be drawn as follows.

9.1.1 Preparation of carbide-coated CB

The preparation of TiC or SiC coated CB was optimised by varying synthesis conditions, for example, firing temperature, holding time, salt assembly, and Ti/C or Si/C molar ratios. The morphology of the resulting powders and microstructure of coated particles were characterised by SEM, EDS, TEM and SAED. The main findings from these are given below.

- 1) Homogeneous TiC coatings were prepared on CB particles by firing them with Ti powders in KCl or KCl-LiCl for 4 hours at 750-850 °C which is 100–200 °C lower than that required for preparation of TiC coatings on GF. It was also feasible to use a combination of Ti and TiO₂ as a titanium source to reduce the preparation cost of TiC coatings. High quality TiC coatings were obtained when firing the mixture of TiO₂ and Ti (in molar ratio of 1/3) at 950 °C for 4 hours.
- 2) High quality SiC coatings were prepared on CB spheres after firing them with Si powders in a binary NaCl-NaF salt for 6 hours at 1100 °C which is much lower than that required by vapour-solid reaction (1350-1550 °C) for SiC coating formation. NaF was proven to be essential in the molten salt synthesis of SiC and its optimal amount was 2.5-5 wt% in the binary NaCl-based salt. In addition, graded SiC/SiO₂ composite coatings were also prepared by controlled oxidation of SiC-coated CB in air at 450 °C for 90 minutes to further improve their water-wettability.

- 3) The core/shell structure of carbide-coated CB spheres was clearly verified by SEM and TEM. The thickness of the TiC and SiC coating (shell) prepared in the metal/carbon molar ratio of 1/8 was estimated as ~10 and ~12 nm respectively. By controlling the metal (Ti or Si) to CB ratio in the initial batch mixture, the carbide coating thickness could be readily tailored to meet practical requirements in real castable systems. The increase in particle density of CB after carbide coating would narrow the density difference between carbon and other aggregates of castable (e.g. Al₂O₃ and MgO), thus additionally improving the dispersion/distribution of carbon particles in castables.
- 4) Molten salt synthesis of carbide coatings from metallic powders and carbon particles was dominated by the template growth mechanism. The dissolution of Ti or Si in molten salt not only increased their reactivity and accelerated the reaction but also enabled active Ti or Si active species to fast deliver to the surface of carbon particles and form carbide coatings on the template. The growth of carbide coatings was dependent on the inward diffusion of Ti or Si and outward diffusion of carbon through a pre-formed carbide coating layer. Since the diffusion coefficient of carbon is greater than that of metals, (e.g. $D_c > D_{Si}$), defects such as voids would emerge when thick carbide coatings were attempted to form.

9.1.2 Water-wettability and oxidation resistance of carbide-coated CB

The water-wettability and relevant dispersion property of uncoated and coated CB were evaluated by zeta potential measurements and visual observation of carbon dispersion in water. The rheological behaviours of suspensions containing carbon particles were investigated by measuring apparent viscosity against shear rate. In addition, oxidation resistance of as-received and carbide-coated CB was examined and compared by TGA and DSC. The main points are concluded as below.

- 1) The water-wettability of CB particles was significantly improved after carbide coating. Compared with uncoated CB, the sediment test showed carbide-coated CB could be rapidly wetted by water and well dispersed in water within a short time. It was also found that carbide-coated CB particles exhibited better dispersion property and flowability in water, in particular, in an alkaline environment. Zeta potential values of carbide-coated CB were much higher than that of uncoated CB, for example, at pH=10, ~46.1 mV for TiC-coated CB, ~54.7

mV for SiC-coated CB and ~65.9 mV for SiC/SiO₂-coated CB but only ~22.6 mV for uncoated CB. Moreover, the apparent viscosity of suspensions containing 25 wt% coated CB was over one order of magnitude lower than that containing the same level of as-received CB. This is attributed to the formation of TiO₂ and SiO₂ thin film layers on the surface of carbide-coated carbon. A number of hydrophilic Ti-OH and Si-OH groups were generated in contact with water. Consequently, negative charges Ti-O⁻ and Si-O⁻ formed on the particle surface at high pH prevented carbon from agglomeration and imparted them excellent dispersion properties and flowability.

- 2) TGA and DSC verified that the improvement in oxidation resistance of carbon after carbide coating was limited, due to formation of nanopores in carbide coatings. However, the annealing treatment at 1200-1500 °C could promote the growth of carbide nanocrystals and make the carbide coating denser, thus evidently improving their oxidation resistance. The TG curves of carbide-coated CB after post-treatment were right shifted to higher temperatures and the completion of carbon oxidation was postponed. For example, as-received CB was completely oxidized at ~678 °C, but TiC-coated CB after annealing at 1300 °C in N₂ lost all carbon at ~838 °C, and annealed (1200-1500 °C) SiC-coated CB at ~800-866 °C. The observation of microstructure and elemental changes of carbide-coated CB during the oxidation process indicated annealing atmosphere and temperature were influential to their oxidation resistance.

9.1.3 Application of carbide-coated carbon in castables

Both uncoated and coated carbon particles (including CB and GF) were incorporated into model castables to investigate the effects of carbide coatings on water addition, flowability, mechanical properties, and oxidation resistance of carbon-containing castables. The results indicated that carbide coatings had positive influences on all these aspects, and the main conclusions based on this part of work can be made as follows.

- 1) The water addition was reduced by over 20%, from 8.5-9.7 wt% required for uncoated carbon containing castables to 6.5-7.0 wt% for coated carbon containing castables (to achieve the similar flow values). In other words, flowability or workability of castables was improved when the same amount of water was added. The dramatic decrease in water addition led to a considerable

drop in apparent porosity (e.g. 24.6% to 17.2% at 110 °C, and 29.8% to 19.2% at 1500 °C for uncoated and coated CB) and an increase in bulk density (e.g. 2.52 to 2.88 g/cm³ at 1500 °C for uncoated and coated CB).

- 2) The mechanical properties of castables have benefited from decreased apparent porosity when carbide-coated carbon particles were incorporated. Castables containing carbide-coated carbon particles after coking at 1500 °C showed over 6 times higher compression strength and 3-5 times higher bending strength than that containing uncoated carbon particles. For example, an uncoated CB containing castable resisted crushing at 7.8 MPa and bending at 3.5 MPa, whereas SiC-coated CB containing castable crushed at 54.4 MPa and ruptured at 18.28 MPa, respectively. In addition, oxidation resistance of carbon-containing castables was improved significantly. A CB castable was severely oxidized and showed a decarbonized depth of 10.48 mm, whereas TiC-CB castable's decarbonized depth was 6.82 mm and that of a SiC-CB castable was 6.35 mm.

9.2 Future work

The research work presented in this thesis has made a big progress in terms of improving carbon's water-wettability and reducing water demand for preparation of carbon-containing castables. As a result, apparent porosity was decreased and mechanical properties and oxidation resistance were correspondingly increased. However, much effort is still needed to make to further improve the process of coating synthesis and castable preparation, eventually realizing the wide commercial applications of carbon-containing castables in the iron and steel industry for example.

- 1) High quality TiC coatings have been successfully prepared on amorphous carbon black and graphite flakes, however, it was very difficult to obtain equivalently high quality SiC coatings on natural crystalline graphite flakes. It is necessary to readjust the synthesis conditions or modify the graphite surface before SiC coating.
- 2) The production efficiency of carbide-coated carbon particles needs to increase. In this work, only 100g samples were produced from each run by using an enlarged graphite crucible and furnace. This cannot meet the high demand of

carbon materials for applications in refractory castables. So more efficient production apparatus and processes are required to make coated carbon commercially available.

- 3) By incorporating a dispersant specially designed for dispersion of carbides in aqueous suspensions (e.g. tetramethyl ammonium hydroxide (TMAH) for dispersion of SiC), a much lower water addition for making castables might be achieved.
- 4) Appropriate antioxidants such as Si and B₄C are required for further improving the oxidation resistance of carbon-containing castables. Meanwhile, high temperature mechanical properties and slag corrosion tests should be carried out to make a comprehensive assessment of the use under industrial conditions.

References

- [1] Rothenberg GB. Refractory Materials, ndc, Noyes Data Corporation, 1976.
- [2] Carniglia SC, Barna GL. Handbook of industrial refractories technology: principles, types, properties, and applications, Noyes Publications, 1992.
- [3] Schacht C. Refractories handbook, Taylor & Francis, 2004.
- [4] Routschka G. Refractory Materials: Pocket manual: design, properties, testing, Vulkan-Verlag, 2008.
- [5] Ewais EMM. Carbon based refractories *Journal of the Ceramic Society of Japan* 2004; 112(1310):517-32.
- [6] Staff BSI. Classification of dense shaped refractory products. Alumina-silica products. In: Standard B-AE, editor.: B S I Standards; 1999.
- [7] ASTM. Classification of shaped heat-insulating refractory products C155-88(92): ASTM; 1992.
- [8] Classification of dense shaped refractory products-Special products. 1999.
- [9] Semler CE. Reflections on Refractories, 1989-2009 *Refractories application and news* 2010; 15(1):4.
- [10] Oguchi Y, Mori J. *Taikabutsu Overseas* 1993; 13(4):7.
- [11] Malagawa H, Y. Nakamura, K.Sawano, Tamura S, Tsutsui N, Nakamura H. UNITECR. New Orleans, LA, USA 1997. p. 203-12.
- [12] Zhang S, Lee WE. UNITECR. Cancun, Mexico 2001. p. 65-67.
- [13] Lee WE, Moore RE. Evolution of in situ refractories in the 20th century *Journal of the American Ceramic Society* 1998; 81(6):1385-410.
- [14] Zhang S, Lee WE. Carbon containing castables: current status and future prospects *British Ceramic Transactions* 2002; 101(1):1-8.
- [15] Kawasaki H, Yoshitomi J, Shikano H, Hayashi T. Surface treatment of graphite for monolithic refractories *Taikabutsu Overseas* 1991; 11(4):46-47.
- [16] Rigaud M, Palco S, Zhou N. Alumina and magnesia-based castables containing graphite: comparison *Iron and Steelmaker (USA)* 2002; 29(10):45-51.
- [17] Kitahara A, Ema T, Kobayashi K, Osawa T. Graphite granulated product for amorphous refractory. In: Patent J, editor. Japan,1991.
- [18] Sharif ShM, Golestani-Fard F, Sarpoolaky H. Improvement of water/resin wettability of graphite using carbon black nano particles coating via ink media *Journal of Alloys and Compounds* 2009; 482(1-2):361-65.
- [19] Yu J, Ueno S, Hiragushi K. Improvement in flowability, oxidation resistance and water wettability of graphite powders by TiO₂ coating *Journal of the Ceramic Society of Japan* 1996; 104(6):481-85.

References

- [20] Sunwoo S, Kim J, Lee K, Kim H. Preparation of ZrO₂ coated graphite powders *Journal of Materials Science* 2000; 35(14):3677-80.
- [21] Zhang S, Lee WE. Improving the water-wettability and oxidation resistance of graphite using Al₂O₃/SiO₂ sol-gel coatings *Journal of the European Ceramic Society* 2003; 23(8):1215-21.
- [22] Ansar SA, Bhattacharya S, Dutta S, Ghosh S, Mukhopadhyay S. Development of mullite and spinel coatings on graphite for improved water-wettability and oxidation resistance *Ceramics International* 2010; 36(6):1837-44.
- [23] Saberi A, Golestani-Fard F, Sarpoolaky H, Willert-Porada M, Gerdes T, Simon R, et al. Development of MgAl₂O₄ spinel coating on graphite surface to improve its water-wettability and oxidation resistance *Ceramics International* 2009; 35(1):457-61.
- [24] Ono Y, Matsumoto T, Amemiya Y. Development of the basic monolithic refractories containing hydrophilic graphite *Rep Res Lab Asahi Glass Co Ltd* 1993; 43(1):35–46.
- [25] Sakamoto S, Ono Y. Graphite containing unshaped refractories *Taikabutsu Overseas* 1994; 14(1):47-51.
- [26] Liu X, Zhang S. Low-temperature preparation of titanium carbide coatings on graphite flakes from molten salts *Journal of the American Ceramic Society* 2008; 91(2):667-70.
- [27] Liu X, Wang Z, Zhang S. Molten salt synthesis and characterization of titanium carbide-coated graphite flakes for refractory castable applications *International Journal of Applied Ceramic Technology* 2011; 8(4):911-19.
- [28] Routschka G. Refractory base materials: Pocket manual refractory materials, Vulkan-Verlag; 1997. p. 2-2.
- [29] Lee WE, Vieira W, Zhang S, Ahari KG, Sarpoolaky H, Parr C. Castable refractory concretes *International Materials Reviews* 2001; 46(3):145-67.
- [30] Lee WE, Rainforth WM. Ceramic microstructures: property control by processing, Springer, 1994.
- [31] Refractories. Pittsburgh, PA, USA: The Refractories Institute; 1987.
- [32] Dickson T. The refractories industry worldwide 2012-2017- A market/technology report. TAK Industrial Mineral Consultancy; 2013. p. 400.
- [33] Refractories materials for steelmaking. Brussels: International iron and steel institute; 1985.
- [34] Steel production 2012. Worldsteel Association; 2013.
- [35] Naruse Y. Trends of Steelmaking Refractories *Transactions of the Iron and Steel Institute of Japan* 1984; 24(10):783-98.
- [36] Banerjee S. Recent developments in steel-making refractories. UNITECR & 7th Biennial Worldwide Congress 2001. p. 1033-41.

References

- [37] Nakashima H, Sudo S, Takahashi I, Konishi E. UNITECR. Kyoto, Japan 1995. p. 205-13.
- [38] Stewart W. *British Ceramic Transactions* 1994; 93(6):3.
- [39] Sugita K. Status of Refractories and Steel Technology in Japan: Progress during the Past Half Century. UNITECR. Kyoto, Japan 1995. p. 103-32.
- [40] Zhang S, Lee W. Carbon containing castables: current status and future prospects *British Ceramic Transactions* 2002; 101(1):1-8.
- [41] Hideaki Nishio IU, Shigeo Yoshino. Carbon-containing refractory. In: Patent U, editor. US: Shinagawa Refractories Co., Ltd; 1984.
- [42] Teranishi H, Yasui K, Imai I. *Taikabutsu Overseas* 1998; 18(1):5.
- [43] Amin MH, Amin-Ebrahimabadi M, Rahimipour MR. The effect of nanosized carbon black on the physical and thermomechanical properties of Al₂O₃-SiC-SiO₂-C composite *Journal of Nanomaterials* 2009; 2009:1.
- [44] Bag M, Adak S, Sarkar R. Study on low carbon containing MgO-C refractory: Use of nano carbon *Ceramics International* 2012; 38(3):2339-46.
- [45] Li N, ZW J. Carbon containing refractories. China, Science Press, 1990.
- [46] Kelly BT. Physics of Graphite, Applied Science Publishers, 1981.
- [47] Cooper C, Alexander I, Hampson C. The role of graphite in the thermal shock resistance of refractories *Transactions and journal of the British Ceramic Society* 1985; 84(2):57-62.
- [48] Silva SRP, INSPEC. Properties of amorphous carbon. London, UK, INSPEC, 2003.
- [49] Heidenreich RD, Hess W, Ban L. A test object and criteria for high resolution electron microscopy *Journal of Applied Crystallography* 1968; 1(1):1-19.
- [50] Niedermeier W, Raab H, Stierstorfer J, Kreitmeier S, Göritz D. The microstructure of carbon black investigated by atomic force microscopy *Kautschuk Gummi Kunststoffe* 1994; (47):799-805.
- [51] Donnet JB, Bansal RC, Wang MJ. Carbon Black: Science and Technology, Dekker, 1993.
- [52] Jain PL. Principles of Foundry Technology. India, Tata McGraw-Hill, 2003.
- [53] Zawrah M. Effect of zircon additions on low and ultra-low cement alumina and bauxite castables *Ceramics International* 2007; 33(5):751-59.
- [54] Hart LRD, Lense E. Alumina chemicals: science and technology handbook, American Ceramic Society, 1990.
- [55] Bier TA, Parr C, Revais C, Fryda H. Chemical interactions in calcium aluminate cement based castables containing magnesia. UNITECR. New Orleans, LA, USA 1997. p. 15-21.

References

- [56] Salomão R, Pandolfelli VC. Magnesia sinter hydration–dehydration behavior in refractory castables *Ceramics International* 2008; 34(8):1829-34.
- [57] Soudie J. Understanding and optimization of MgO hydration resistance and spinel formation mechanisms for increasing performance of DVM used in crucible induction furnaces melting steel. UNITECR. Orlando, USA, 2005.
- [58] Birchal V, Rocha S, Ciminelli V. The effect of magnesite calcination conditions on magnesia hydration *Minerals Engineering* 2000; 13(14):1629-33.
- [59] Durán T, Pena P, De Aza S, Gómez–Millán J, Alvarez M, De Aza AH. Interactions in calcium aluminate cement (CAC) - Based castables containing magnesia. Part I: Hydration - dehydration behavior of MgO in the absence of CAC *Journal of the American Ceramic Society* 2011; 94(3):902-08.
- [60] Yoshida A, Kaneyasu A. Evaluation method for hydration resistance of magnesia fine powder and effect of B₂O₃ content in magnesia raw materials. UNITECR. Osaka, Japan 2003. p. 433-36.
- [61] Phillips V, Kolbe J, Opperhauser H. Effect of pH on the growth of Mg (OH)₂ crystals in an aqueous environment at 60 °C *Journal of Crystal Growth* 1977; 41(2):228-34.
- [62] Amaral L, Oliveira I, Salomao R, Frollini E, Pandolfelli V. Temperature and common-ion effect on magnesium oxide (MgO) hydration *Ceramics International* 2010; 36(3):1047-54.
- [63] Salomão R, Pandolfelli VC. The role of hydraulic binders on magnesia containing refractory castables: Calcium aluminate cement and hydratable alumina *Ceramics International* 2009; 35(8):3117-24.
- [64] Odegard C, Myhre B. Magnesia-silica-hydrate bonded MgO castables. UNITECR. Cancun, Mexico 2001.
- [65] Souza T, Braulio M, Luz A, Bonadia P, Pandolfelli V. Systemic analysis of MgO hydration effects on alumina–magnesia refractory castables *Ceramics International* 2012; 38(5):3969-76.
- [66] Durán T, Pena P, De Aza S, Gómez–Millán J, Alvarez M, De Aza AH. Interactions in Calcium Aluminate Cement (CAC) - Based Castables Containing Magnesia—Part II: Hydration - Dehydration Behavior of CAC and their Mixtures with Dead - Burned and Reactive - Grade MgO *Journal of the American Ceramic Society* 2011; 94(3):909-17.
- [67] Elkem. Products information. 2013.
- [68] Myhre B. The effect of microsilica additions on flow and strength of tabular alumina based refractory castables. The American Ceramic Society, 95th Annual Meeting in Cincinnati. Ohio, USA 1993.
- [69] Myhre B. Tabular Alumina Based Refractory Castables Part I : The effect of microsilica additions on low and cold strength of tabular alumina based low and ultra low cement castables. Norway: Elkem Materiels; 1992.
- [70] Fumo DA, Segadaes AM. Effect of silica fume additions on the hydration

behavior of calcium aluminates. UNITECR. New Orleans, LA, USA 1997. p. 1325-33.

[71] Myhre B. Tabular Alumina Based Refractory Castables Part III : Reactions in the bond-phase of microsilica containing refractory castables Part I-III: Synopsis. Norway: Elkem Materiels; 1992.

[72] Myhre B. Hot strength and bond-phase reactions in low and ultralow-cement castables. UNITECR '93/XXII ALAFAR Congress. São Paulo, Brazil 1993.

[73] Myhre B. Microsilica in alumina based ultralow-cement castables. The effect of microsilica additions on flow. The XXIII ALAFAR Congress. Puerto Vallarta, Mexico 1994.

[74] Kriechbaum GW, Laurich JO, Garsel DV, Gnauck V, Heijden JCD. The matrix advantage system, new raw materials for low moisture, self-levelling, and vibration placed alumina and magnesium aluminate spinel castables. UNITECR. New Orleans, LA, USA 1997. p. 645-55.

[75] Krietz LP, Fisher RE, Beetz JG. Evolution and status of refractory castable technology entering the 1990s *American Ceramic Society Bulletin* 1990; 69(10):1690-93.

[76] Banerjee S. Recent developments in monolithic refractories *American Ceramic Society Bulletin* 1998; 77(10):59-63.

[77] Sorrentino D, Sorrentino F, George M. Mechanisms of hydration of calcium aluminate cements *Mater Sci Concrete IV, Ed J Skalny, S Mindess, Am Ceram Soc, Weterville, Ohio* 1995:41-90.

[78] Scrivener KL, Cabiron J-L, Letourneux R. High-performance concretes from calcium aluminate cements *Cement and Concrete Research* 1999; 29(8):1215-23.

[79] An L, Chan HM, Soni KK. Control of calcium hexaluminate grain morphology in in-situ toughened ceramic composites *Journal of Materials Science* 1996; 31(12):3223-29.

[80] Calcium aluminate cements in construction: A re-assessment. Slough, UK: The Concrete Societ; 1997.

[81] Hongo Y. ρ -Alumina bonded castable refractories *Taikabutsu Overseas* 1988; 9(1):35-38.

[82] Vance M, Moody K. Use of hydratable alumina binders in refractory compositions and related applications *Pittsburgh: Alcoa Industrial Chemicals, Internal Report* 1995.

[83] Teranishi H, kawamura T, yashi K, Imai I. *Taikabutsu Overseas* 1998; 18(1):5.

[84] Mišta W, Wrzyszc J. Rehydration of transition aluminas obtained by flash calcination of gibbsite *Thermochimica Acta* 1999; 331(1):67-72.

[85] Vaidya S, Thakkar N. Effect of temperature, pH and ageing time on hydration of rho alumina by studying phase composition and surface properties of transition alumina obtained after thermal dehydration *Materials Letters* 2001; 51(4):295-300.

[86] Ma W, Brown PW. Mechanisms of reaction of hydratable aluminas *Journal of the*

American Ceramic Society 1999; 82(2):453-56.

[87] Ghanbari Ahari K, Sharp J, Lee W. Hydration of refractory oxides in castable bond systems—I: alumina, magnesia, and alumina–magnesia mixtures *Journal of the European Ceramic Society* 2002; 22(4):495-503.

[88] Cardoso FA, Innocentini MD, Miranda MF, Valenzuela FA, Pandolfelli VC. Drying behavior of hydratable alumina-bonded refractory castables *Journal of the European Ceramic Society* 2004; 24(5):797-802.

[89] Ismael M, Anjos R, Salomão R, Pandolfelli V. Colloidal silica as a nanostructured binder for refractory castables *Refractories Applications & News* 2006; 11(4):16-20.

[90] Xiong JQ, Peng YT, Xie DY, Mao XS. The characteristics of silica-sol combining refractories *Advanced Materials Research* 2012; 396:288-91.

[91] Alireza S, Fatemeh K, Hossein S. Improving thermo-mechanical properties of tubular alumina castables via using nano structured colloidal silica 2011.

[92] Iler RK. The chemistry of silica: solubility, polymerization, colloid and surface properties, and biochemistry, 1979.

[93] Nouri-Khezrabad M, Braulio M, Pandolfelli V, Golestani-Fard F, Rezaie H. Review: Nano-bonded refractory castables *Ceramics International* 2012.

[94] Myhre B. Microsilica in refractory castables- surface properties and set. IREFCON. Kolkata, India, 2010.

[95] Hommer H. Interaction of polycarboxylate ether with silica fume *Journal of the European Ceramic Society* 2009; 29(10):1847-53.

[96] Hommer H, Wutz, K. and von Seyerl, J. The effect of polycarboxylate ethers as deflocculants in castables *Interceram Refractories Manual* 2007:3.

[97] Seyerl JV. Use of polycarboxylate ethers to improve workability of castables *Ceram Forum Int* 2007; 9.

[98] Otrój S, Bahrevar MA, Mostarzadeh F, Nilforoshan MR. The effect of deflocculants on the self-flow characteristics of ultra low-cement castables in Al₂O₃–SiC–C system *Ceramics International* 2005; 31(5):647-53.

[99] Studart AR, Pandolfelli VC, Tervoort E, Gauckler LJ. Selection of dispersants for high-alumina zero-cement refractory castables *Journal of the European Ceramic Society* 2003; 23(7):997-1004.

[100] Schmitz J, Pegelow U, Schulte HG and Hofer RA. new concept for dispersing agents in aqueous coatings *Progress in Organic Coatings* 1999; 35:6.

[101] Liu T, Jia S, Kowalewski T, Matyjaszewski K, Casado-Portilla R, Belmont J. Water-dispersible carbon black nanocomposites prepared by surface-initiated atom transfer radical polymerization in protic media *Macromolecules* 2006; 39(2):548-56.

[102] Gokce A, Gurcan C, Ozgen S, Aydin S. The effect of antioxidants on the oxidation behaviour of magnesia–carbon refractory bricks *Ceramics International* 2008; 34(2):323-30.

References

- [103] Zhang S, Marriott N, Lee W. Thermochemistry and microstructures of MgO–C refractories containing various antioxidants *Journal of the European Ceramic Society* 2001; 21(8):1037-47.
- [104] Zhang SW, Hashimoto S, Lee WE. Hydration of aluminum powder in magnesia-containing water *Journal of the American Ceramic Society* 2005; 88(4):1057-59.
- [105] Zhang S, Lee W, Zhu B, Li N. Improving hydration resistance of Al powder for carbon containing castables using inorganic–organic hybrid coatings *Advances in applied ceramics* 2005; 104(2):79-82.
- [106] Yamaguchi A, Zhang S. Synthesis and some properties of Al₄SiC₄ *Nippon seramikusu kyokai gakujutsu ronbunshi* 1995; 103(1):20-24.
- [107] Wang T, Yamaguchi A. Oxidation protection of MgO–C refractories by means of Al₈B₄C₇ *Journal of the American Ceramic Society* 2001; 84(3):577-82.
- [108] Luz AP, Miglioli MM, Souza TM, Hashimoto S, Zhang S, Pandolfelli VC. Effect of Al₄SiC₄ on the Al₂O₃SiCSiO₂C refractory castables performance *Ceramics International* 2012; 38(5):3791-800.
- [109] Luz A, Valenzuela F, Domiciano V, Brito M, Pandolfelli V. Improved oxidation resistance of high-carbon-containing castables via antioxidant blend *American Ceramic Society Bulletin* 2009; 88(3):40.
- [110] Ono Y. Development of the basic monolithic refractories containing hydrophilic graphite. Rep Res Lab Asahi Glass Co Ltd.; 1993. p. 35-46.
- [111] Contescu CI. Selection and characterization of carbon black and surfactants for development of small scale uranium oxycarbide kernels. Oak Ridge, TN: Oak Ridge National Laboratory; 2005.
- [112] Hayashi T. In: Patent J, editor. Japan1990.
- [113] Kitahara A. In: Patent J, editor. Japan1989.
- [114] Kawasaki H, Shikano H, Hayashi T. *Taikabutsu Overseas* 1989; 41:3.
- [115] Kawasaki H, Shikano H, Hayashi T. Surface treatment of graphite for monolithic refractories. *Taikabutsu Overseas* 1991; 11(4):2.
- [116] K. Isomura MK, M. Takagi, S. Goto, M. Nomura, K. Jono, Y. Tiritani and S. Tanaka. Development of graphite containing alumina castable and its application to BF trough. 3rd International Symposium on Refractories. Beijing, China 1998.
- [117] Zhou N. Elaboration of Al₂O₃-based graphite containing castables PhD thesis: Université de Montréal; 2000.
- [118] Rigaud N. Proc Electric Furnace Conf. Pittsburgh, PA, USA1998. p. 131-42.
- [119] Zhang H-L, Liu S-H, Li F, Bai S, Liu C, Tan J, et al. Electrochemical performance of pyrolytic carbon-coated natural graphite spheres *Carbon* 2006; 44(11):2212-18.
- [120] Ding Y-S, Li W-N, Iaconetti S, Shen X-F, DiCarlo J, Galasso FS, et al.

References

Characteristics of graphite anode modified by CVD carbon coating *Surface and Coatings Technology* 2006; 200(9):3041-48.

[121] Yoshio M, Wang H, Fukuda K, Hara Y, Adachi Y. Effect of carbon coating on electrochemical performance of treated natural graphite as lithium - ion battery anode material *Journal of the Electrochemical Society* 2000; 147(4):1245-50.

[122] Wang H, Yoshio M. Carbon-coated natural graphite prepared by thermal vapor decomposition process, a candidate anode material for lithium-ion battery *Journal of Power Sources* 2001; 93(1):123-29.

[123] Segal D. Sol-gel processing: routes to oxide ceramics using colloidal dispersions of hydrous oxides and alkoxide intermediates *Journal of Non-Crystalline Solids* 1984; 63(1):183-91.

[124] Pierre AC. Introduction to sol-gel processing, Kluwer Academic Publishers, 1998.

[125] Von DC, Bradley RCM, Gaur DP. Metal alkoxides New York, San Francisco, Academic Press, London, 1978.

[126] Brinker CJ, Scherer GW. Sol-gel science: the physics and chemistry of sol-gel processing, Academic Press, 1990.

[127] Sakka S. Handbook of sol-gel science and technology. 1. Sol-gel processing, Kluwer Academic Publishers, 2005.

[128] Livage J, Ganguli D. Sol-gel electrochromic coatings and devices: a review *Solar Energy Materials and Solar Cells* 2001; 68(3):365-81.

[129] Hench LL, West JK. The sol-gel process *Chemical Reviews* 1990; 90(1):33-72.

[130] Corriu RJ, Leclercq D. Recent developments of molecular chemistry for sol - gel processes *Angewandte Chemie International Edition in English* 1996; 35(13 - 14):1420-36.

[131] Yoshimatsu H, Fujiwara S, Konishi R, Miyawaki M, Miura Y. Wettability by water and oxidation resistance of alumina-coated graphite powder *Journal of the Ceramic Society of Japan* 1995; 103:929-34.

[132] Yilmaz E, Yilmaz S. Investigation of properties of boehmitic sol coated graphite added alumina-low cement castables *Journal of Ceramic Processing Research* 2010; 11(1):56-60.

[133] Yilmaz S, Kutmen-Kalpakli Y, Yilmaz E. Synthesis and characterization of boehmitic alumina coated graphite by sol-gel method *Ceramics International* 2009; 35(5):2029-34.

[134] Yu J, Ueno S, Hiragushi K. Improvement in flowability, oxidation resistance and water wettability of graphite powders by TiO₂ coating *Nippon seramikusu kyokai gakujuutsu ronbunshi* 1996; 104(6):481-85.

[135] Kawabata K, Yoshimatsu H, Fujiwara K, Mihashi H, Hiragushi K, Osaka A, et al. Oxidation resistance of graphite powders coated with Al₂O₃-based oxides *J Ceram Soc Jpn* 1999; 107(9):832-37.

References

- [136] Kawabata K, Yoshimatsu H, Fujii E, Hiragushi K, Osaka A, Miura Y. Fluidity of a slurry of the graphite powder coated with Al_2O_3 -based metal oxides *Journal of Materials Science Letters* 2001; 20(9):851-53.
- [137] Li D-X, Thomson WJ. Kinetic mechanisms for mullite formation from sol-gel precursors *Journal of Materials Research* 1990; 5(9):1963-9.
- [138] Mukhopadhyay S, Ansar SA, Paul D, Bhowmick G, Sengupta S. Characteristics of refractory castables containing mullite and spinel coated graphites *Materials and Manufacturing Processes* 2012; 27(2):177-84.
- [139] Saberi A, Golestani-Fard F, Willert-Porada M, Simon R, Gerdes T, Sarpoolaky H. Improving the quality of nanocrystalline MgAl_2O_4 spinel coating on graphite by a prior oxidation treatment on the graphite surface *Journal of the European Ceramic Society* 2008; 28(10):2011-17.
- [140] Mukhopadhyay S, Dutta S, Ansar SA, Das S, Misra S. Spinel-coated graphite for carbon containing refractory castables *Journal of the American Ceramic Society* 2009; 92(8):1895-900.
- [141] Mukhopadhyay S. Improved sol gel spinel (MgAl_2O_4) coatings on graphite for application in carbon containing high alumina castables *Journal of Sol-Gel Science and Technology* 2010; 56(1):66-74.
- [142] Mukhopadhyay S, Das G, Biswas I. Nanostructured cementitious sol gel coating on graphite for application in monolithic refractory composites *Ceramics International* 2012; 38(2):1717-24.
- [143] Jian-Feng H, Xie-Rong Z, He-Jun L, Xin-Bo X, Ye-wei F. Influence of the preparation temperature on the phase, microstructure and anti-oxidation property of a SiC coating for C/C composites *Carbon* 2004; 42(8-9):1517-21.
- [144] Wang Y-Q, Zhou B-L, Wang Z-M. Oxidation protection of carbon fibers by coatings *Carbon* 1995; 33(4):427-33.
- [145] Sakamoto SOY. Graphite containing unshaped refractories *Taikabutsu Overseas* 1994; 14(1):5.
- [146] Li X, Dong Z, Westwood A, Brown A, Zhang S, Brydson R, et al. Preparation of a titanium carbide coating on carbon fibre using a molten salt method *Carbon* 2008; 46(2):305-09.
- [147] Xie W, Mirza Z, Möbus G, Zhang S. Novel synthesis and characterization of high quality silicon carbide coatings on carbon fibers *Journal of the American Ceramic Society* 2012; 95(6):1878-82.
- [148] Li X, Westwood A, Brown A, Brydson R, Rand B. A convenient, general synthesis of carbide nanofibres via templated reactions on carbon nanotubes in molten salt media *Carbon* 2009; 47(1):201-08.
- [149] Xie W, Möbus G, Zhang S. Molten salt synthesis of silicon carbide nanorods using carbon nanotubes as templates *Journal of Materials Chemistry* 2011; 21(45):18325-30.
- [150] Kimura T. Molten Salt Synthesis of Ceramic Powders. In: Sikalidis C, editor. *Advances in Ceramics - Synthesis and Characterization, Processing and Specific*

Applications: INTECH; 2011.

[151] Arendt R, Rosolowski J, Szymaszek J. Lead zirconate titanate ceramics from molten salt solvent synthesized powders *Materials Research Bulletin* 1979; 14(5):703-09.

[152] Zhang S. Low temperature synthesis of complex refractory oxide powders from molten salts *J Pakistan Materials Society* 2007; 1(2):49-53.

[153] Li Z, Zhang S, Lee WE. Molten salt synthesis of LaAlO_3 powder at low temperatures *Journal of the European Ceramic Society* 2007; 27(10):3201-05.

[154] Jayaseelan DD, Zhang S, Hashimoto S, Lee WE. Template formation of magnesium aluminate (MgAl_2O_4) spinel microplatelets in molten salt *Journal of the European Ceramic Society* 2007; 27(16):4745-49.

[155] Liu X. Molten salt synthesis and characterisation of carbide-coated graphite. PhD thesis, Sheffield: The University of Sheffield; 2010.

[156] Xie W. Molten salt synthesis and characterisation of novel carbide materials. PhD thesis, Sheffield: The University of Sheffield; 2011.

[157] Kerridge DH, Polyakov EG. Refractory metals in molten salt: their chemistry, electrochemistry and technology. Boston, Kluwer academic, Dordrecht, 1998.

[158] Hassine N, Binner J, Cross T. Synthesis of refractory metal carbide powders via microwave carbothermal reduction *International Journal of Refractory Metals and Hard Materials* 1995; 13(6):353-58.

[159] Vyshnyakova K, Yushin G, Pereselentseva L, Gogotsi Y. Formation of porous SiC ceramics by pyrolysis of wood impregnated with silica *International Journal of Applied Ceramic Technology* 2006; 3(6):485-90.

[160] Ye J, Zhang S, Lee WE. Novel low temperature synthesis and characterisation of hollow silicon carbide spheres *Microporous and Mesoporous Materials* 2012; 152:25-30.

[161] Ding J, Deng CJ, Yuan WJ, Zhu HX, Li J. Preparation of porous TiC/C ceramics using wooden template in molten salt media *Advances in applied ceramics* 2013; 112(3):131-35.

[162] Pierson HO. Handbook of refractory carbides & nitrides: properties, characteristics, processing and applications, Elsevier Science, 1996.

[163] Santhanam AT. Application of transition metal carbides and nitrides in industrial tools. In: Oyama ST, editor. Chemistry of transition metal carbides and nitrides: Springer; 1996.

[164] Qin X, Li Y, Hong X, Wu Y, Li Y. Effect of Ti(C,N) content on properties of low carbon MgO-C brick *Journal of Wuhan University of Science & Technology* 2008; 31(2):4.

[165] Yousheng Li, Weijun Tong, Nan Li. Influence of Ti(C,N) on properties of corundum based castables *Naihuo Cailiao* 2006; 40(5):3.

[166] Zawrah M, Khalil N. High alumina castables reinforced with SiC *Advances in*

applied ceramics 2005; 104(6):312-17.

[167] Matsui T, Goto K, Yamada Y, Taki N. Characteristics and applications of nano tech magnesia carbon bricks *USA: Proc of the Untecr 2005*:176-79.

[168] Ochiai T. Development of refractories by applying nano-technology *Journal of Technical Association of Refractories Japan* 2005; 25(1):4-11.

[169] Almatiss. GP-RCP_001_Tabular_T60_T64_0812. Almtis; 2013.

[170] Nabaltec. NABALOX_1xx-7xx_Datasheet_EN. 2013.

[171] Almatiss. RP-EU_RCP_007_Aluminas_for_Refractories_0811. Almatiss; 2013.

[172] Elkem. Microsilica-Grade-971-pds. 2013.

[173] Kerneos. Secar71. 2013.

[174] Kerneos. Brochure_REF_SECAR-Range_UK_20110803_LD. 2013.

[175] Cancarb. 034 Basic Carbon Refractories II. 2013.

[176] Von Seyerl J. Use of Polycarboxylate ethers to improve workability of castables. CFI Ceramic forum international: Göller; 2007.

[177] Hommer H. The effect of polycarboxyl ethers as deflocculants in microsilica containing castables. 10th Biennial Worldwide Congress on Refractories. Dresden, Germany, 2007. p. 401-04.

[178] Myhre B. The effect of particle-size distribution on flow of refractory castables. Proceedings of the Thirtieth Annual Symposium on Refractories, The St Louis Section of The American Ceramic Society, St Louis March, 1994. p. 19-22.

[179] Myhre B, Hundere AM. The use of particle size distribution in development of refractory castables. Proc XXV Congreso ALAFAR, Bariloche, Argentina 1996. p. 33-42.

[180] Andreasen JA. Ueber die Beziehung zwischen Kornabstufung und Zwischenraum in Produkten aus losen Körnern (mit einigen Experimenten) *Kolloid-Zeitschrift* 1930; 50:217-28.

[181] Hong Peng, Myhre B. Improved flow of refractory castables by optimised particle size distribution. The 55th International Colloquium on Refractories. Aachen, Germany 2012.

[182] Cullity BD. Elements of X-Ray Diffraction, Addison-Wesley, 1978.

[183] SEM-EDX. Scanning Electron Microscopy & Energy Dispersive X-Ray Spectroscopy. 2013.

[184] Ammf. Australian Microscopy & Microanalysis Research Facility; 2013.

[185] Griffiths P, De Haseth JA. Fourier Transform Infrared Spectrometry, Wiley, 2007.

[186] Nicolet T. Introduction to Fourier Transform Infrared Spectrometry. 2001.

References

- [187] Keng EYH. Method and apparatus for volume measurement. US Patents 1969.
- [188] Instruments M. Zetasizer nano series user manual. In: theory Zp, editor. Worcestershire: Malvern Instruments Ltd, 2004.
- [189] Barnes HA, Hutton JF, Walters K. An introduction to rheology, Elsevier, 1989.
- [190] West AR. Basic solid state chemistry, John Wiley & Sons, 1999.
- [191] ASTM. Measuring consistency of castable refractory using a flowtable (C1445-99). 2005.
- [192] ASTM. Standard test methods for apparent porosity, liquid absorption, apparent specific gravity, and bulk density of refractory shapes by vacuum pressure. ASTM 2011.
- [193] ASTM. Standard practice for calculating areas, volume, and linear change of refractory shapes. ASTM; 2011.
- [194] ASTM. Standard test methods for cold crushing strength and modulus of rupture of refractories. ASTM; 2008.
- [195] Yuan Q, Zheng Y, Yu H. Mechanism of synthesizing nanocrystalline TiC in different milling atmospheres *International Journal of Refractory Metals and Hard Materials* 2009; 27(4):696-700.
- [196] Arvieu C, Manaud JP, Quenisset JM. Interaction between titanium and carbon at moderate temperatures *Journal of Alloys and Compounds* 2004; 368(1–2):116-22.
- [197] Razavi M, Rahimipour MR, Kaboli R. Synthesis of TiC nanocomposite powder from impure TiO₂ and carbon black by mechanically activated sintering *Journal of Alloys and Compounds* 2008; 460(1–2):694-98.
- [198] Pujar VV, Cawley JD. Effect of stacking faults on the X-ray diffraction profiles of β -SiC powders *Journal of the American Ceramic Society* 1995; 78(3):774-82.
- [199] Pujar VV, Cawley JD. Computer simulations of diffraction effects due to stacking faults in β -SiC: II, experimental verification *Journal of the American Ceramic Society* 2004; 84(11):2645-51.
- [200] Raharnan MN, Boiteux Y, Johghe L. Surface characterization of silicon nitride and silicon carbide powders *American Ceramic Society Bulletin* 1986; 65(8):6.
- [201] Zhang Y, Shi E, Chen Z, Li X, Xiao B. Large-scale fabrication of silicon carbide hollow spheres *Journal of Materials Chemistry* 2006; 16(42):4141-45.
- [202] Liu ZY, Ci LJ, Jin-Phillipp NY, Ruhle M. Vapor-solid reaction for silicon carbide hollow spherical nanocrystals *Journal of Physical Chemistry C* 2007; 111(34):12517-21.
- [203] Qian J, Wang J, Qiao G, Jin Z. Preparation of porous SiC ceramic with a woodlike microstructure by sol-gel and carbothermal reduction processing *Journal of the European Ceramic Society* 2004; 24(10-11):3251-59.
- [204] Yin Y, Rioux RM, Erdonmez CK, Hughes S, Somorjai GA, Alivisatos AP. Formation of hollow nanocrystals through the nanoscale Kirkendall Effect *Science*

2004; 304(5671):711-14.

[205] Wang W, Dahl M, Yin Y. Hollow Nanocrystals through the Nanoscale Kirkendall Effect *Chemistry of Materials* 2012; 25(8):1179-89.

[206] Monteverde F, Medri V, Bellosi A. Synthesis of ultrafine titanium carbonitride powders *Applied Organometallic Chemistry* 2001; 15(5):421-29.

[207] Lee W, Vieira W, Zhang S, Ahari KG, Sarpoolaky H, Parr C. Castable refractory concretes *International Materials Reviews* 2001; 46(3):145-67.

[208] Zawrah M, Khalil N. Effect of mullite formation on properties of refractory castables *Ceramics International* 2001; 27(6):689-94.

[209] Sarpoolaky H, Ahari KG, Lee W. Influence of in situ phase formation on microstructural evolution and properties of castable refractories *Ceramics International* 2002; 28(5):487-93.

[210] Popovska N, Streitwieser DA, Xu C, Gerhard H. Paper derived biomorphic porous titanium carbide and titanium oxide ceramics produced by chemical vapor infiltration and reaction (CVI-R) *Journal of the European Ceramic Society* 2005; 25(6):829-36.

[211] Zhang H, Li F, Jia Q, Ye G. Preparation of titanium carbide powders by sol-gel and microwave carbothermal reduction methods at low temperature *Journal of Sol-Gel Science and Technology* 2008; 46(2):217-22.

[212] Koc R, Folmer JS. Carbothermal synthesis of titanium carbide using ultrafine titania powders *Journal of Materials Science* 1997; 32(12):3101-11.

[213] Lohse BH, Calka A, Wexler D. Synthesis of TiC by controlled ball milling of titanium and carbon *Journal of Materials Science* 2007; 42(2):669-75.

[214] Tong L, Reddy RG. Synthesis of titanium carbide nano-powders by thermal plasma *Scripta Materialia* 2005; 52(12):1253-58.

[215] Cheng L, Xu Y, Zhang L, Yin X. Preparation of an oxidation protection coating for C/C composites by low pressure chemical vapor deposition *Carbon* 2000; 38(10):1493-98.

[216] Zhu Y-C, Ohtani S, Sato Y, Iwamoto N. The improvement in oxidation resistance of CVD-SiC coated C/C composites by silicon infiltration pretreatment *Carbon* 1998; 36(7-8):929-35.

[217] Pai CH, Koumoto K, Takeda S, Yanagida H. Preparation of SiC hollow particles by gas-phase reaction in the SiH₄-CH₄-H₂ system *Journal of Materials Science* 1989; 24(10):3679-85.

[218] Morisada Y, Maeda M, Shibayanagi T, Miyamoto Y. Oxidation resistance of multiwalled carbon nanotubes coated with silicon carbide *Journal of the American Ceramic Society* 2004; 87(5):804-08.

[219] Vix-Guterl C, Ehrburger P. Effect of the properties of a carbon substrate on its reaction with silica for silicon carbide formation *Carbon* 1997; 35(10-11):1587-92.

[220] Lee Y-J. Formation of silicon carbide on carbon fibers by carbothermal

References

reduction of silica *Diamond and Related Materials* 2004; 13(3):383-88.

[221] Yao Y, Long C, Li Q, Li G, Li Y, Pan Y, et al. Preparation and characteristic of chemical vapour deposition C + SiC on graphite *Journal of Nuclear Materials* 1994; 212–215, Part B(0):1552-56.

[222] Wei P, Qiliang H, Jian C, Juan C, Huang Y. Mechanism of titanium deposition on Al₂O₃ ceramic surface by molten salt reaction *Materials Letters* 1997; 31(3–6):317-20.

[223] Li C-H, Lu H-B, Xiong W-H, Chen X. Diamond and graphite coated with polyalloys by an immersion method *Surface and Coatings Technology* 2002; 150(2):163-69.

[224] Bondioli F, Bonamartini Corradi A, Leonelli C, Manfredini T. Nanosized CeO₂ powders obtained by flux method *Materials Research Bulletin* 1999; 34(14–15):2159-66.

[225] Liu X, Wang Z, Zhang S. Molten Salt Synthesis and Characterization of Titanium Carbide - Coated Graphite Flakes for Refractory Castable Applications *International Journal of Applied Ceramic Technology* 2011; 8(4):911-19.

[226] Brockner W, Torkklep K, Oye H.A. Viscosity of molten alkali chlorides *Journal of Chemical and Engineering Data* 1981; 26:4.

[227] Baumli P, Kaptay G. Wettability of carbon surfaces by pure molten alkali chlorides and their penetration into a porous graphite substrate *Materials Science and Engineering: A* 2008; 495(1):192-96.

[228] FactSage. Phase diagram. 2013.

[229] Ghoshtagore RN, Coble R. Self-diffusion in silicon carbide *Physical Review* 1966; 143:623-26.

[230] Hong JD, Davis RF, Newbury DE. Self-diffusion of silicon-30 in α -SiC single crystals *Journal of Materials Science* 1981; 16(9):2485-94.

[231] Hong JD, Davis RF. Self - diffusion of carbon - 14 in high - purity and N - Doped α -SiC single crystals *Journal of the American Ceramic Society* 1980; 63(9 - 10):546-52.

[232] Hon M, Davis R. Self-diffusion of 14C in polycrystalline β -SiC *Journal of Materials Science* 1979; 14(10):2411-21.

[233] Mittal KL. Contact Angle, Wettability and Adhesion, VSP, 2009.

[234] Hugosson HW, Eriksson O, Jansson U, Ruban AV, Souvatzis P, Abrikosov I. Surface energies and work functions of the transition metal carbides *Surface Science* 2004; 557(1):243-54.

[235] Young T. An essay on the cohesion of fluids *Phil Trans Roy Soc (London)* 1805; 95:65-88.

[236] Arthur WA, Gast AP. Physical Chemistry of Surfaces, 6th edition, Wiley, 1997.

References

- [237] Johnson R, Dettre RH. Contact angle hysteresis. I. Study of an idealized rough surface *Advances in chemistry, Series* 1964; 43(112):1964.0065-2393.
- [238] Pavese M, Musso S, Bianco S, Giorcelli M, Pugno N. An analysis of carbon nanotube structure wettability before and after oxidation treatment *Journal of Physics: Condensed Matter* 2008; 20(47):474206.
- [239] Tan K, Finnis M, Horsfield A, Sutton A. Why TiC (111) is observed to be Ti terminated *Surface Science* 1996; 348(1):49-54.
- [240] Zhang JX, Jiang DL, Tan SH, Gui LH, Ruan ML. Aqueous processing of titanium carbide green sheets *Journal of the American Ceramic Society* 2001; 84(11):2537-41.
- [241] Adair JH, Mutsuddy BC, Drauglis E. Stabilization of silicon carbide whisker suspensions: I. Influence of surface oxidation in aqueous suspensions *Advanced Ceramic Materials;(USA)* 1988; 3(3):231-34.
- [242] Cerovic LS, Milonjić SK, Kostić-Gvozdenović L. Intrinsic Equilibrium Constants of beta-Silicon Carbide Obtained from Surface Charge Data *Journal of the American Ceramic Society* 1995; 78(11):3093-96.
- [243] Schindler PW. Surface complexes at Oxide-Water interfaces. In: Anderson MA, Rubin AJ, editors. Adsorption of inorganics at Solid-Liquid interfaces: Ann Arbor Science Publishers; 1981.
- [244] Lewis JA. Colloidal processing of ceramics *Journal of the American Ceramic Society* 2000; 83(10):2341-59.
- [245] Moraru V, Lebovka N, Shevchenko D. Structural transitions in aqueous suspensions of natural graphite *Colloids and Surfaces A: Physicochemical and Engineering Aspects* 2004; 242(1):181-87.